



MONASH University

**Fracturing of hard rocks by
microwave treatment and potential
applications in mechanised tunnelling**

YANLONG ZHENG
(Doctor of Philosophy)

A thesis submitted for the degree of *Doctor of
Philosophy* at Monash University in 2017
(Department of Civil Engineering)

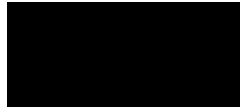
Copyright notice

© Yanlong Zheng (2017).

Declaration

This thesis contains no material which has been accepted for the award of any other degree or diploma at any university or equivalent institution and that, to the best of my knowledge and belief, this thesis contains no material previously published or written by another person, except where due reference is made in the text of the thesis.

Signature:

A solid black rectangular box used to redact the signature.

Print Name: Yanlong Zheng

Date: 25 December 2017

ABSTRACT

TBM tunnelling in hard rocks has unparalleled advantages over conventional drilling and blasting techniques in terms of higher advance rates and better working conditions. However when tunnelling through very hard and abrasive rocks, the performance of TBMs can be significantly hampered, resulting in excessive cutter wear, low advance rates and cost/schedule overruns. Alternative methods or assisted techniques must be found to cope with those rocks. The preceding microwave treatment of rocks followed by mechanical breakage operations is recognised as a promising technique. The objectives of this PhD research are to examine the microwave-rock interaction mechanisms by quantifying the dielectric properties of basic rock forming minerals (which translate as the ability in absorbing microwave energy), to assess the influence of microwave treatment on the physical and mechanical properties of hard and abrasive rocks and to study the feasibility of using microwave on hard rock TBMs.

This thesis measures the dielectric properties of gabbro and granite from 1 MHz to 2 GHz and from room temperature to 300 °C using the parallel plate technique. The influence of temperature and frequency on the dielectric properties of rocks are examined and compared to those in the literature. The thesis then measures the heating rates of 8 rock forming minerals using a 2 kW industrial microwave system. The order of the heating rates from low to high is olivine, quartz, muscovite, diopside, plagioclase, orthoclase, biotite and hornblende. They are classified into three categories: good microwave absorbers including hornblende and biotite, intermediate microwave absorber including orthoclase and poor microwave absorbers including quartz, diopside, olivine, muscovite and plagioclase. It then proposes a new method to derive the loss factors of minerals. The method combines the microwave heating tests, the effective medium theory and numerical simulations. The order of the dielectric loss factors from low to high is quartz, olivine, muscovite, diopside, plagioclase, orthoclase, biotite and hornblende. The method can also be used to predict the dielectric properties of natural rocks.

The thesis investigates the effect of microwave treatment on the heating rate, spatial temperature distribution, ultrasonic wave velocities, elastic modulus and compression peak loads of three igneous rocks (i.e. gabbro, monzonite and granite). The crack pattern and crack density are also studied using the petrographic thin-section observations. Experiments results indicate that the single-mode microwave system can effectively and efficiently weaken the three rocks by generating cracks or melting/shattering the specimens. The heating rates and thermal gradients increase as either exposure time or power levels increases. When heated at 2

kW for 120 s, the P-wave velocities of gabbro and monzonite can be reduced to 44 % and 51 %, respectively, S-wave velocities reduced to 34 % and 62 %, Young's modulus reduced to 13 % and 27 %, loading capacity reduced to 34 % and 43 %. By contrast, granite specimens are more prone to catastrophic failures. Petrographic observations imply that the dominant crack types in gabbro, monzonite and granite are intergranular and transgranular cracks, intergranular cracks and transgranular cracks, respectively.

An investigation on the application of microwave on TBMs indicates that installation of microwave applicators on the cutterhead is technically feasible. The main challenge comes from a rotating cutterhead which results in a very short exposure time of rocks on the periphery. The horn applicator is proved to be the most suitable to be installed on the TBM cutterheads. The analysis indicates that microwave may be favourable in weakening quartz-rich rocks such as granite and quartzite. It is estimated that one third of the total installed power of the TBM cutterhead needs to be added/allocated to microwave applicators.

Publications during enrolment

Zheng Y.L., Zhang Q.B. and Zhao J., 2017. Effect of microwave treatment on thermal and ultrasonic properties of Gabbro. *Applied Thermal Engineering* 127, 359-369.

Zheng, Y.L., Zhang, Q.B., Zhao, J., 2016. Challenges and opportunities of using tunnel boring machines in mining. *Tunnelling and Underground Space Technology* 57, 287-299.

Liu Z.H, Du C.L*, **Zheng Y.L.**, et al, 2017. Effects of nozzle position and waterjet pressure on rock-breaking performance of roadheader [J]. *Tunnelling and Underground Space Technology* 69: 18-27.

Zhao J, **Zheng Y.L.**, Zhang Q.B., Zhao X.B, 2017. New Technologies Assisting Hard Rock Cutting in TBMs. TBMDiGs Wuhan Keynote paper.

Zheng Y.L., Zhang Q.B., Zhao X.B., Zhao J. A comparative study of microwave treatment of three igneous rocks. *Geothermics*. To be submitted.

Zheng, Y., Gong, Q., Li, J. and Zhao, J, 2014. A review of the applications of tunnel boring machines in mines, in *Proceedings 15th Australasian Tunnelling Conference 2014*, pp 691–704.

ACKNOWLEDGEMENT

This PhD topic is a challenging undertaking as it is interdisciplinary and there is a long learning curve. I would like to acknowledge lots of people, without whose help the thesis would not have been possible.

I would like to express my greatest and foremost gratitude to my supervisors, *Prof. Jian Zhao* and *Dr. Qianbing Zhang* for their invaluable supervision, support and encouragement during my four-year candidature at Monash. Help from *Prof. Yun Bai*, *A/Prof. Xiaobao Zhao* and *A/Prof. Mohan Yellishetty*, *Prof. Lei He*, *Prof. Qiuming Gong*, *Prof. Xiaoli Liu* and *Mr. Huanlin Gou* at a certain point of the research, academically or mentally, is also acknowledged.

I am also very grateful to *Prof. Grigori Torgovnikov* and *Dr. Graham Brodie* at University of Melbourne, *Dr. Nguyen Tran* at Microwave Power Component Pty, and *Prof. Mohan Jacob* at James Cook University for their help in the early stage of the research.

I am indebted to *Dr. Caroline Venn*, *Mr. Junnel Alegado*, *Mr. Massino Raveggi*, and *Ms. Rachelle Pierson* from the School of Earth, Atmosphere and Environment, Monash University for their support in the mineral processing and petrographic thin section studies of the research. Technical support from *Mr. Long Goh*, *Mr. Mike Leach*, *Mr. Jeffery Doddrell*, *Mr. Philip Warnes* and *Mr. Sarvan Mani* in the Civil Lab is also highly appreciated.

I would like to thank all my office mates, *Md Faizal*, *Michael Von't Steen*, *Asgar Ali*, *Md Rouf*, *Louis King*, *Albert Ao*, *Xiaogang Zhang*, *Guanglei Zhang*, and *Zhaoyang Ma* for the happy time we spent together. Thanks also go to fellow students in our research group: *Xing Li*, *Yang Zou*, *Haozhe Xing*, *Kai Liu*, *Wei Xiong*, *Minghe Ju*, *Jack Wu*, *Tingwen Sun*, *Zenghui Liu*, *Jincheng Fan*, *Xiaoxuan Kong*, *Fuping Zhang*, *Pengfei Liu*, *Xiaofeng Li* for their help in my life and research.

A special thank you goes to the administrative staff at the Department of Civil Engineering, *Mrs. Jenny Manson*, *Mrs. Irene Sgouras*, *Ms. Tara Fry* and *Ms. Noi Souvandy*.

The financial support from the China Scholarship Council and the Faculty of Engineering, Monash University is acknowledged.

Finally, I would like to thank my parents and sisters for their endless support and love throughout my pursuit of the PhD degree.

TABLE OF CONTENTS

ABSTRACT.....	i
ACKNOWLEDGEMENT	v
TABLE OF CONTENTS.....	vii
LIST OF FIGURES	xi
LIST OF TABLES.....	vii
LIST OF ACRONYMS	ix
CHAPTER 1 Introduction.....	1
1.1 Research motivations	1
1.2 Research objectives and roadmap	3
1.3 Thesis structure	3
Reference	5
CHAPTER 2 A Review of Novel Assisting Rock Breakage Methods	7
2.1 Hard rock TBM tunnelling.....	7
2.2 Problems associated with hard rock tunnelling.....	9
2.3 Improvement of TBM capacity.....	13
2.3.1 High performance disc cutters	14
2.3.2 Optimised machine design	15
2.4 Assisting rock breaking methods	15
2.4.1 Waterjet.....	19
2.4.2 Laser.....	24
2.4.3 Microwave and infrared irradiation	31
2.5 Technical and economical comparison	38
2.6 Concluding remarks	41
Reference	41
CHAPTER 3 Fundamentals of Microwave Interactions with Minerals and Rocks.....	47
3.1 Introduction.....	47
3.2 What is microwave?.....	47
3.3 Polarisation mechanisms.....	49
3.3.1 Electronic polarisation	49
3.3.2 Atomic polarisation.....	50
3.3.3 Dipolar (orientation) polarisation.....	50
3.3.4 Ionic polarisation.....	51
3.3.5 Interfacial polarisation	51
3.4 Dielectric properties of minerals.....	52

3.4.1 Definitions of dielectric properties	52
3.4.2 Microwave heating and weakening mechanisms	53
3.4.3 Factors influencing the dielectric properties of minerals and rocks.....	53
3.5 Dielectric properties measurement techniques.....	58
3.5.1 Resonant cavity technique	58
3.5.2 Coaxial probe technique.....	60
3.5.3 Free space technique	61
3.5.4 Parallel plate technique	61
3.5.5 Dielectric properties of minerals and rocks	62
3.6 Common microwave systems	63
3.6.1 Microwave basic components	63
3.6.2 Industrial multimode microwave	64
3.6.3 Industrial single mode microwave	64
3.6.4 Other applicators	66
3.7 Measurement of the dielectric properties of gabbro and granite.....	66
3.7.1 Sample preparation	66
3.7.2 Parallel plate measurement system	66
3.7.3 Test procedures	67
3.7.4 Measurement results and discussion	68
3.8 Research gaps.....	77
3.9 Concluding remarks	78
Reference	78
CHAPTER 4 Heating Rates and Dielectric Properties of Low Loss Rock Forming Minerals.....	83
4.1 Introduction.....	83
4.2 Literature review on heating rates of minerals.....	83
4.2.1 Literature review on mineral heating rates.....	83
4.2.2 Problems of existing research	87
4.3 Materials and methodologies	88
4.3.1 Minerals	90
4.3.2 Crushing an grinding facility	91
4.3.3 Energy-dispersive X-ray spectroscopy	93
4.3.4 Industrial microwave system	94
4.3.5 Temperature measurement	95
4.3.6 Solid density measurement	96
4.3.7 Design of experiment	97
4.4 Test results and discussions	98
4.4.1 Element compositions of minerals.....	98

4.4.2 Heating rates of pure minerals	102
4.4.3 Effect of power level on heating rates.....	105
4.4.4 Effect of grain size on heating rates	107
4.4.5 Derivations of loss factors of minerals.....	109
4.4.6 Heating rates of mineral mixtures (comparing with the pure ones)	114
4.4.7 Further discussions.....	117
4.5 Conclusions.....	118
Reference	119
CHAPTER 5 Experimental Study of Microwave Treatment of Igneous Hard Rocks.....	121
5.1 Introduction.....	121
5.2 Materials and sample preparation	121
5.2.1 Rock type selection	121
5.2.2 Rock descriptions.....	122
5.2.3 Sample preparation	124
5.3 Experimental facilities and procedures	125
5.3.1 Microwave system setup and temperature measurement	125
5.3.2 Crack extraction techniques	125
5.3.3 Thin section preparation.....	126
5.3.4 Petrographic microscopy observation.....	128
5.3.5 P-wave velocity measurement	128
5.3.6 Compression testing machine	129
5.3.7 Test procedures	130
5.4 Test results and discussions	131
5.4.1 General observations.....	131
5.4.2 Temperature vs exposure time	138
5.4.3 Temperature vs power level.....	141
5.4.4 Temperature distribution.....	143
5.4.5 P-wave velocity reduction at different locations.....	145
5.4.6 Local and overall P-wave velocity reduction.....	146
5.4.7 Overall S-wave velocity.....	146
5.4.8 Dynamic elastic modulus	148
5.4.9 Reductions in loading capacity	149
5.4.10 Crack pattern	151
5.4.11 Crack density	159
5.4.12 Correlation between parameters.....	164
5.5 Limitation of the research	167
5.6 Conclusions.....	168

Reference	169
CHAPTER 6 Application of Microwave on Tunnel Boring Machines	171
6.1 Introduction.....	171
6.2 Typical cutterhead designs of hard rock TBMs	171
6.3 Conceptual designs of using microwave on TBMs.....	173
6.4 Study on use of open ended waveguide applicators.....	177
6.4.1 Waveguide applicators	177
6.4.2 Horn applicators	178
6.5 Power requirement estimation	179
6.5.1 Exposure time	179
6.5.2 Power requirement of microwave applicators.....	181
6.5.3 Conventional cutterhead	184
6.6 Expected difficulties	185
6.7 Conclusions.....	186
Reference	186
CHAPTER 7 Conclusion and Future Work.....	189
7.1 Conclusions.....	189
7.2 Limitation and future work	191
CURRICULUM VITAE.....	193

LIST OF FIGURES

CHAPTER 1

Fig. 1.1 Roadmap of the thesis research.

CHAPTER 2

Fig. 2.1 Rockburst during TBM tunnelling: (a) Strainburst in hard rock due to stress concentrations (modified from Ortlepp and Stacey (1994)); (b) Rockbursting at Jinping II hydropower station in China (Home, 2009).

Fig. 2.2 TBM thrust as a function of rock strength with 17 inch disc cutters (Frenzel et al., 2008).

Fig. 2.3 Correlation of TBM cutter life (17 inch disc cutter), UCS and CAI for some common hard rock types (Reproduced from Maidl et al. (2008)).

Fig. 2.4 Disc cutter wipeout when cutters become blocked (Roby et al., 2008).

Fig. 2.5 Relative wear volumes of 19-inch and 20-inch disc rings (Smading, 2017a).

Fig. 2.6 Assisted TBM tunnelling concept (modified from Maurer (1980)).

Fig. 2.7 Kerfing strategies when using assisting methods: (a) Shallow kerfing; (b) Deep kerfing (modified from Carstens et al. (1970)).

Fig. 2.8 Electric thermal breakage methods and conceptual applications in tunnelling. (a) Schematic of electric rock breakage (Segsworth and Kuhn, 1977); (b) Schematic of plasma blasting (Hamelin et al., 1993); (c) Thermal tunnelling with plasma torches (Poole and Thorpe, 1973); (d) Tunnelling using plasma blasting (Kitzinger and Nantel, 1992).

Fig. 2.9. Applications of waterjet in TBM tunnelling: (a) Mechanically assisted waterjet cutting (modified from Knickmeyer and Baumann (1983)); (b) Waterjet assisted mechanical cutting (modified from Fenn et al. (1985)).

Fig. 2.10. Cutting forces of a disc cutter with and without 40 MPa waterjet assistance: Thrust force reductions; (b) Rolling force reductions (Reproduced from Fenn et al. (1985)).

Fig. 2.11 Groove geometries of (a) mechanical cutting and (b) waterjet assisted cutting (Ciccu and Grosso, 2014)

Fig. 2.12 Waterjet assisted TBM tunnelling. (a) The 2.65 m diameter Wirth TBM with waterjet nozzles, (b) Penetration rate with/without waterjet assistance (Knickmeyer and Baumann (1983).

Fig. 2.13 Interaction between laser and rock (after Maurer (1980)).

Fig. 2.14 Strength reduction of granite specimens subjected to laser irradiation (reproduced from Williamson et al. (1968)).

Fig. 2.15 Cross section of laser cut rocks. Laser power equal to 16.5 kW. Kerfing speed from left to right: 125, 100, 75, 50, 25 cm/mm (Jurewicz, 1976).

- Fig. 2.16 Laser gage kerfing concept applied to tunnelling (modified from Jurewicz (1976)).
- Fig. 2.17 Laser assisted linear cutting tests: (a) Cutting pattern; (b) Normalised muck volume under different conditions (Carstens et al., 1970).
- Fig. 2.18 A conceptual design of a laser assisted hard rock TBM (Carstens et al., 1970).
- Fig. 2.19 Principles of microwave weakening of rocks.
- Fig. 2.20 Cracking of a 38 mm diameter Harcourt granite in the microwave waveguide after 5 seconds heating at 5kW. (a) Thermal shattering in the waveguide, (b) cross-section of the crack surface.
- Fig. 2.21 The electromagnetic machine used in a USSR hard rock mine (Hoekstra, 1976).
- Fig. 2.22 Performance comparison between an electrothermal excavator and a mechanical excavator. (a) Advance rates vs rock strength; (b) Energy consumption vs rock strength (Gushchin et al., 1973).
- Fig. 2.23 Two designs of TBMs assisted with infrared generators in the Soviet Union. (a) The 450 kW PK-8ETM tunnelling machine (Gushchin et al., 1979); (b) The 380 kW Yasinovatets-2ETM tunnelling machine (Protasov et al., 1984).
- Fig. 2.24 Specific energy of different excavation methods (Bieniawski et al., 2012).

CHAPTER 3

- Fig. 3.1 Wavelength and frequency spectrum of electromagnetic waves.
- Fig. 3.2 Generation of electromagnetic waves by the acceleration of a charge (Chabay and Sherwood, 2015)
- Fig. 3.3 Four basic polarisation mechanisms of dielectric heating (Agilent, 2004).
- Fig. 3.4 Polarisation of mineral crystals under an external electric field: (a) Polarisation of the quartz crystal; (b) Displacement of atoms in a barium titanate unit cell.
- Fig. 3.5 Dielectric properties of water as a function of microwave frequency at different temperatures. (a) Dielectric constant; (b) loss factor (Barba and d'Amore, 2012).
- Fig. 3.6 Dielectric properties of low loss minerals as a function of microwave frequency. (a) Dielectric constant, (b) loss factor (Data from Nelson et al. (1989)).
- Fig. 3.7 Variation of loss factor of different rock types from 1.6 GHz to 16 GHz (reproduced from Ulaby et al. (1988)).
- Fig. 3.8 Dielectric properties of some rock types as a function of temperature at 35 GHz. (a) Dielectric constant, (b) loss factor (reproduced from Campbell and Ulrichs (1969)).
- Fig. 3.9 Dielectric properties of some minerals as a function of temperature at the frequency of 2.216 GHz. (a) Dielectric constant, (b) loss factor (Data from Cumbane (2003)).
- Fig. 3.10 Structures of molecules of water and ice.

- Fig. 3.11 Dielectric properties measurement using the resonant cavity perturbation technique. (a) Measurement setup using the short-circuited method, (b) methods recommended by the ASTM-D2520 (ASTM, 2013).
- Fig. 3.12 Shift of resonant frequency and quality factor after insertion of a dielectric.
- Fig. 3.13 The coaxial probe technique for dielectric properties measurement. (a) Measurement setup composing a coaxial probe, a network analyser and a computer, (b) Immersion of the probe into the materials under test.
- Fig. 3.14 Measurement of the dielectric properties using the free space technique. (a) Setup at Monash University, (b) Schematic of the technique (Agilent, 2004).
- Fig. 3.15 Graphical representation and its equivalent circuit model of parallel plate methods (Agilent, 2004).
- Fig. 3.16 Key components of an industrial microwave system (Courtesy of Richardson Electronics).
- Fig. 3.17 Power density (E²) distribution in a TE₃₂₄ mode in a 35 cm × 30 cm × 25 cm cavity at 2.45 GHz. (a) Cavity and plane of observation in the middle of the height; (b) Contour plot of the electric field strength; (c) Three-dimensional plot (Mehdizadeh, 2015).
- Fig. 3.18 Schematic of a single mode cavity. (a) Cavity adapted from a WR340 waveguide in the TE₁₀₃ mode, (b) electric field distribution (Mehdizadeh, 2015).
- Fig. 3.19 Preparation of sheet samples. (a) IsoMet 4000 precision saw; (b) A 13mm drill core and 1 mm thick sheet samples.
- Fig. 3.20 Measurement of the dielectric properties using the parallel plate technique. (a) Photo of the measurement setup; (b) Schematic of the Quatro Cryosystem; (c) Schematic of the RF sample cell BDS 2200 (Courtesy of Novocontrol Technologies).
- Fig. 3.21 Calibration sets for the Novocontrol RF cell (from left to right: 50 Ohms capacitor, low loss capacitor, short circuited ends).
- Fig. 3.22 Dielectric properties of the Austral Black Gabbro Sample No.4 as a function of frequency and temperature. (a) Dielectric constant vs frequency; (b) loss factor vs frequency; (c) dielectric constant vs temperature; (d) loss factor vs temperature.
- Fig. 3.23 Dielectric properties of the Austral Black Gabbro Sample No.5 as a function of frequency and temperature. (a) Dielectric constant vs frequency; (b) loss factor vs frequency; (c) dielectric constant vs temperature; (d) loss factor vs temperature.
- Fig. 3.24 Dielectric properties of the Austral Black Gabbro Sample No.6 as a function of frequency and temperature. (a) Dielectric constant vs frequency; (b) loss factor vs frequency; (c) dielectric constant vs temperature; (d) loss factor vs temperature.
- Fig. 3.25 Average dielectric properties of the Austral Black Gabbro as a function of frequency (samples 4-6). (a) Dielectric constant; (b) Loss factor.
- Fig. 3.26 Average dielectric properties of the Austral Black Gabbro as a function of temperature at selected frequencies. (a) Dielectric constant; (b) Loss factor.

Fig. 3.27 Dielectric properties of the Austral Black Gabbro as a function of temperature at 2 GHz.

Fig. 3.28 Dielectric properties of the granite sample No.2 as a function of frequency and temperature.

(a) Dielectric constant vs frequency; (b) loss factor vs frequency.

Fig. 3.29 Dielectric properties of the granite sample No.3 as a function of frequency and temperature.

(a) Dielectric constant vs frequency; (b) loss factor vs frequency.

Fig. 3.30 Dielectric properties of the granite sample No.5 as a function of frequency and temperature.

(a) Dielectric constant vs frequency; (b) loss factor vs frequency.

Fig. 3.31 Average dielectric properties of granite as a function of frequency and temperature. (a)

Dielectric constant vs frequency; (b) loss factor vs frequency.

Fig. 3.32 Dielectric properties of the granite as a function of temperature at 1.43 GHz.

CHAPTER 4

Fig. 4.1 Schematic of the microwave system used for heating rate tests by Chen et al. (1984).

Fig. 4.2 Microwave system used for heating rates measurement by McGill et al. (1995). (a) Domestic microwave oven with a 1 litre water load at 1 kW; (b) Waveguide applicator for varying power levels from 0.5 kW to 2 kW.

Fig. 4.3 Surface temperature of 11 rock-forming minerals after microwave treatment for 3 mins at 2 kW (Lu et al., 2017).

Fig. 4.4 The classification of igneous rocks and the rock forming minerals (Tarbuck et al., 2016). Fine grained rocks are volcanic and coarse grained rocks are intrusive.

Fig. 4.5 Optical images of the 8 rock forming minerals before crushing and milling. (a) quartz, (b) muscovite, (c) plagioclase, (d) orthoclase, (e) olivine, (f) diopside, (g) biotite and (h) hornblende.

Fig. 4.6 Equipment used for crushing and grinding. (a) Jaw crusher, (b) Agate mill, (c) Sieve shaker.

Fig. 4.7 Minerals after crushing and milling crushing and grinding (grain size smaller than 75 μ m). (a) quartz, (b) muscovite, (c) plagioclase, (d) orthoclase, (e) olivine, (f) diopside, (g) biotite and (h) hornblende.

Fig. 4.8 EDS analysis of minerals. (a) The FEI Quanta scanning electron microscope (SEM); (b) Carbon coated specimens on stubs.

Fig. 4.9 Schematic of the experimental setup of microwave treatment of rocks.

Fig. 4.10 Thermometers used for temperature measurement. (a) ULIRVision TI160 IR camera; (b) INT-2013IR shotgun.

Fig. 4.11 Quantachrome multipycnometer for the measurement of solid density.

Fig. 4.12 Olivine of different grain sizes in the 10 ml quartz beakers.

Fig. 4.13 EDS spectrums of the 8 rock forming minerals. (a) quartz, (b) olivine, (c) muscovite, (d) plagioclase, (e) diopside, (f) orthoclase, (g) biotite and (h) hornblende.

Fig. 4.14 Melting of hornblende when heated at 1 kW for 20s.

Fig. 4.15 Heating rates of seven rock forming minerals at 1 kW.

Fig. 4.16 Heating rates of Category 3 minerals at (a) 1 kW and (b) 2 kW.

Fig. 4.17 Difference in chemical compositions of pyroxenes.

Fig. 4.18 Heating rates of (a) quartz, (b) diopside, (c) olivine, (d) muscovite, (e) plagioclase, (f) orthoclase, (g) biotite and (h) hornblende at different power levels.

Fig. 4.19 Heating rates of olivine of different grain sizes at (a) 1 kW and (b) 2 kW.

Fig. 4.20 Heating rates of diopside of different grain sizes at (a) 1 kW and (b) 2 kW.

Fig. 4.21 Light (microwave) transmission and scattering in (a) glass, (b) coarse powder, (c) fine powder. Wave reflection, scattering and transmission are illustrative only.

Fig. 4.22 Numerical simulation setup with geometries and boundary conditions.

Fig. 4.23 Electric field strength (V/m) in the cavity (a) before and (b) after the insertion of samples.

Fig. 4.24 Heating rates of minerals at different power levels.

Fig. 4.25 Calculated loss factors of minerals at different power levels.

Fig. 4.26 Heating rates of plagioclase-orthoclase mixture (simulated monzonite) at (a) 1 kW and (b) 2 kW.

Fig. 4.27 Heating rates of plagioclase-diopside mixture (simulated gabbro) at (a) 1 kW and (b) 2 kW.

Fig. 4.28 Heating rates of orthoclase and quartz mixture at (a) 1 kW and (b) 2 kW.

Fig. 4.29 Heating rates of orthoclase, quartz and biotite mixture (simulated granite) at (a) 1 kW and (b) 2 kW.

Fig. 4.30 Dependence of loss factor on chemical compositions.

CHAPTER 5

Fig. 5.1 Selected rock types in the QAPF diagram for plutonic rocks (highlighted in dark blue).

Fig. 5.2 X-ray diffraction (XRD) pattern of the Austral Black Gabbro.

Fig. 5.3 Petrographic microscopy images of the Austral Black Gabbro under (a) PPL and (b) XPL. Pl- plagioclase; Cpx - clinopyroxene; Opx – orthopyroxene; Bt-biotite.

Fig. 5.4 Petrographic microscopy images of the monzonite under (a) PPL and (b) XPL.

Fig. 5.5 Petrographic microscopy images of the granite under (a) PPL and (b) XPL.

Fig. 5.6 Schematic of the experimental setup of microwave treatment of rocks.

Fig. 5.7 Thin section preparation facilities. (a) Vacuum desiccator; (b) Hot plates; (c) Trim saw; (d) Diamond grinder; (e) Flat glass; (f) Slide mounting jig; (g) Thin section saw and grinder; (h) Microscopy and ultrasonic cleaner.

Fig. 5.8 Petrographic microscopies utilised. (a) Nikon Optiphot2 microscopy; (b) Zeiss Axio microscopy.

Fig. 5.9 Measurement of P-wave velocity. (a) Measurement setup (ISRM); (b) Measurement locations.

Fig. 5.10 300 kN Shimadzu AGS-X Series testing machine.

Fig. 5.11 Microwave treatment of granite specimens. (a)-(c) show a specimen heated at 1 kW for 10 seconds; (d)-(f) show a specimen heated at 2 kW for 1 second; (g) shows a specimen heated at 1 kW for 50 seconds; (h) shows a specimen heated at 2 kW for 3 seconds; (i) shows a specimen heated at 1.5 kW for 90 seconds.

Fig. 5.12 Influence of exposure time on temperature of gabbro specimens at four power levels. (a) Maximum temperature (T_M); (b) Average temperature (T_A).

Fig. 5.13 Influence of exposure time on temperature of monzonite specimens. (a) Maximum temperature (T_M); (b) Average temperature (T_A).

Fig. 5.14 Influence of exposure time on temperature of granite specimens. (a) Maximum temperature (T_M); (b) Average temperature (T_A).

Fig. 5.15 Influence of power level on temperature. (a) Maximum temperature (T_M) of gabbro; (b) Average temperature (T_A) of gabbro; (c) Maximum temperature (T_M) of monzonite; (d) Average temperature (T_A) of monzonite; (e) Maximum temperature (T_M) of granite; (f) Average temperature (T_A) of granite.

Fig. 5.16 Temperature distribution along the centreline of gabbro specimens at 1 kW: (a) 30 seconds; (b) 60 seconds; (c) 90 seconds; (d) 120 seconds.

Fig. 5.17 Temperature distribution along the centrelines. (a) Gabbro specimens heated at 1 kW; (g) Gabbro specimens heated for 90 seconds; (a) Monzonite specimens heated at 1 kW; (g) Monzonite specimens heated for 90 seconds; (a) Granite specimens heated at 1 kW; (g) Granite specimens heated for 90 seconds.

Fig. 5.18 Normalised P-wave velocities at three locations of the specimens heated at 1 kW: (a) Gabbro; (b) Monzonite; (c) Granite.

Fig. 5.19 Normalised P-wave velocity as a function of exposure time. (a) V'_{Pm}/V_{Pm} of gabbro; (b) V'_P/V_P of gabbro; (c) V'_{Pm}/V_{Pm} of monzonite; (d) V'_P/V_P of monzonite; (e) V'_{Pm}/V_{Pm} of granite; (f) V'_P/V_P of granite.

Fig. 5.20 Normalised S-wave velocities (V'_S/V_S) after microwave treatment of (a) gabbro, (b) monzonite and (c) granite.

Fig. 5.21 Normalised elastic moduli of (a) gabbro specimens, (b) monzonite specimens and (c) granite specimens (data at 2 kW not available).

Fig. 5.22 Compression test results of gabbro and monzonite specimens treated at 2 kW. (a) Load-displacement curves of gabbro; (b) Load-displacement curves of monzonite; (c) Peak load and destruction work of gabbro and monzonite.

- Fig. 5.23 Thin section images of Austral Black Gabbro after microwave treated at 2 kW for 30 seconds (Size of view: 60mm by 40mm). (a) Image under plane-polarised light; (b) Image under cross-polarised light; (c) Image under UV light; (d) Binarised crack extraction.
- Fig. 5.24 Thin section images of Austral Black Gabbro after microwave treated at 1.5 kW for 120 seconds (Size of view: 60mm by 40mm). (a) Image under plane-polarised light; (b) Image under cross-polarised light; (c) Image under UV light; (d) Binarised crack extraction.
- Fig. 5.25 Thin section images of Austral Black Gabbro after microwave treated at 2 kW for 90 seconds (Size of view: 60mm by 40mm). (a) Image under plane-polarised light; (b) Image under cross-polarised light; (c) Image under UV light; (d) Binarised crack extraction.
- Fig. 5.26 Crack patterns of Austral Black Gabbro after microwave treatment. (a) and (b) are images of trans-granular cracks along the cleavage planes of the plagioclase and intergranular cracks along feldspar-pyroxene grain boundaries (specimens heated at 2 kW for 30 seconds); (c) and (d) are images of cracks along the lamellar twinning plane of an orthoclase and transgranular cracks under PPL and XPL (specimen heated at 1.5 kW for 120 seconds); (e) and (f) are images of inter-granular, trans-granular and intra-granular cracks under PPL and XPL (specimen heated at 1.5 kW for 90 seconds).
- Fig. 5.27 Thin section images of a monzonite specimen after microwave treated at 2 kW for 90 seconds (Size of view: 60mm by 40mm). (a) Image under plane-polarised light; (b) Image under cross-polarised light; (c) Image under UV light; (d) Binarised crack extraction.
- Fig. 5.28 Thin section images of a monzonite specimen after microwave treated at 2 kW for 120 seconds (Size of view: 60mm by 40mm). (a) Image under plane-polarised light; (b) Image under cross-polarised light; (c) Image under UV light; (d) Binarised crack extraction.
- Fig. 5.29 Crack patterns in monzonite thin sections after microwave treatment. (a) and (b) are PPL and XPL images showing inter-granular cracks along feldspar-quartz grain boundaries (specimens heated at 2 kW for 90 seconds); (c) and (d) are PPL and XPL images showing the predominant intergranular cracks along the grain boundaries under (specimen heated at 1.5 kW for 120 seconds).
- Fig. 5.30 Thin section images of a granite specimen after microwave treated at 1 kW for 90 seconds (Size of view: 60mm by 40mm). (a) Image under plane-polarised light; (b) Image under cross-polarised light; (c) Image under UV light; (d) Binarised crack extraction.
- Fig. 5.31 Crack patterns in granite thin sections after microwave treatment. (a) and (b) are PPL and XPL close-up images showing transgranular cracks (specimens heated at 1 kW for 90 seconds); (c) and (d) are PPL and XPL images showing the predominant trans-granular cracks along the grain boundaries (specimen heated at 1 kW for 60 seconds).
- Fig. 5.32 Skeletonised cracks on microwave treated gabbro surfaces (specimens treated at 0.5 kW). (a) 30 seconds; (b) 60 seconds; (c) 90 seconds; (d) 120 seconds.

- Fig. 5.33 Skeletonised cracks on microwave treated gabbro surfaces (specimens treated at 2 kW). (a) 30 seconds; (b) 60 seconds; (c) 90 seconds; (d) 120 seconds.
- Fig. 5.34 Crack density as a function of exposure time for (a) gabbro, (b) monzonite and (c) granite.
- Fig. 5.35 Crack density extraction based on the Underwood Method using equivalent distance grid.
- Fig. 5.36 Estimated crack density after microwave treatment. (a) in the middle of the gabbro specimens; (b) overall of gabbro specimens; (c) in the middle of the monzonite specimens; (d) overall of monzonite specimens; (e) in the middle of the granite specimens; (f) overall of granite specimens.
- Fig. 5.37 Temperature and crack distribution of a gabbro specimen heated at 2 kW for 90 seconds. (a) Temperature distribution using multiphysics numerical simulation; (b) Cracks in the front surface; (c) Cracks in the mid-thickness cross section; (d) Cracks at the back surface.
- Fig. 5.38 Correlations between normalised P-wave velocity and energy output. (a) Gabbro; (b) Monzonite; (c) Granite.
- Fig. 5.39 Correlations between normalised P-wave velocity and temperature. (a) Gabbro; (b) Monzonite; (c) Granite.
- Fig. 5.40 Correlations between normalised P-wave velocity and crack density. (a) Gabbro; (b) Monzonite.
- Fig. 5.41 Temperature change in the microwave heating and natural cooling process (gabbro heated at 1.5 kW for 120 seconds).

CHAPTER 6

- Fig. 6.1 Cutterhead designs of (a) a main beam TBM and (b) a single shield TBM (The Robbins Company). Boxes in figures illustrate the position of microwave applicators with respect to disc cutters.
- Fig. 6.2 Configurations of microwave applicators with respect to TBM disc cutters. (a) Applicators ahead of disc cutters in the cutting trajectories (Hassani et al., 2016), (b) applicator parallel to disc cutter by a certain distance.
- Fig. 6.3 Commercially available microwave applicator types (modified after Mehdizadeh (2015)). (a) Waveguide with a flange, (b) waveguide with a horn, (c) focusing waveguide.
- Fig. 6.4 Distance from the excavation face to the cutterhead equipped with 19 inch disc cutters.
- Fig. 6.5 Electric field (V/m) distribution of (a) a waveguide antenna, (b) a horn applicator and (c) a focusing antenna cut at the shorter dimension at an output power of 2 kW.
- Fig. 6.6 Electric field (V/m) distribution of (a) a waveguide antenna, (b) a horn applicator and (c) a focusing antenna cut at the broader dimension at an output power of 2 kW.
- Fig. 6.7 Electric field strength along the centreline of the applicators. (a) From microwave port to a distance of 300 mm, (b) 5 cm from the aperture to 300 mm.

- Fig. 6.8 Electric field distribution in the materials contacted with a rectangular open-ended waveguide (Habash, 1994; Mehdizadeh, 2015).
- Fig. 6.9 Geometry of the horn application showing a propagating wave front in the flare (Brodie et al., 2015).
- Fig. 6.10 Temperature distribution vs. depth into the stack of basalt slabs after 60s of microwave treatment at six distances from the antenna and 15 kW power (Nekoovaght, 2015).
- Fig. 6.11 Cracking of a 38 mm diameter 80 mm long Harcourt granite after 10 seconds of microwave heating at 2.5 kW. (a) Thermal shattering, (b) cross-section of the crack surface.
- Fig. 6.12 Electric field strength along the centreline of the applicators with rock mass in front at 15 kW. (a) Distance of 50 mm, (b) Distance of 100 mm.
- Fig. 6.13 Temperature in the rock mass with a distance of 5 cm at 15 kW. (a) Temperature after 3 seconds of heating, (b) temperature increase as a function of exposure time.
- Fig. 6.14 Temperature in the rock mass with a distance of 10 cm at 15 kW. (a) Temperature after 3 seconds of heating, (b) temperature increase as a function of exposure time.
- Fig. 6.15 Maximum temperature in the rock mass with a distance of 5 cm and 10 cm and at 30 kW.

LIST OF TABLES

CHAPTER 1

Table 1.1 PhD and master's theses on microwave treatment of rocks.

CHAPTER 2

Table 2.1 World records of TBM advance rates in hard rocks (Courtesy of The Robbins Company).

Table 2.2 TBM projects with exceedingly hard and abrasive rock problems.

Table 2.3 Development history of disc cutters (Roby et al., 2008).

Table 2.4 Comparison between two TBMs of the same diameter (Rauer, 2014).

Table 2.5 Lasers used for rock cutting and drilling (after Graves et al. (2002)).

Table 2.6 Comparison of specific energy of Berea Sandstone using four laser types (Graves et al., 2002).

Table 2.7 Field experiments using electrothermal and electrothermomechanical rock destruction.

Table 2.8 Review of microwave treatment of hard rocks in the laboratory (modified after Zheng et al. (2017)).

Table 2.9 Comparison of SE in the Barre Granite using different methods (modified after Graves et al. (2002)).

CHAPTER 3

Table 3.1 Common dielectric properties measurement techniques (After Agilent (2004)).

Table 3.2 Dielectric properties of minerals at 2.45GHz and room temperature.

Table 3.3 PhD and master's theses on microwave treatment of ores.

Table 3.4 PhD and master's theses on microwave treatment of non-ore rocks.

CHAPTER 4

Table 4.1 Minerals transparent to microwave irradiation (Chen et al., 1984).

Table 4.2 Heating of natural minerals at 1 kW using a domestic oven (Walkiewicz et al., 1988).

Table 4.3 Physical and dielectric properties of the selected minerals (specific heat capacity data from Waples and Waples (2004) and Krupka et al. (1985); reference in the table are for the dielectric properties of minerals).

Table 4.4 Specifications of infrared camera and gun.

Table 4.5 Solid density of the powdered minerals (grain size smaller than 75µm).

Table 4.6 Elemental compositions of the minerals from the EDS analysis.

Table 4.7 Heating rates ($^{\circ}\text{C}/\text{min}$) of pure minerals at four power levels.

Table 4.8 Heating rates ($^{\circ}\text{C}/\text{min}/\text{g}$) of pure minerals at four power levels.

Table 4.9 Predicted and measured heating rates of minerals by Harrison (1997).

Table 4.10 Calculated electric field strength at different power levels using numerical simulations.

Table 4.11 Derivations of loss factors using Equations 3.17 and 4.4.

Table 4.12 Comparison between measured and predicted heating rates ($^{\circ}\text{C}/\text{min}$) of mineral mixtures at 1 kW and 2 kW

CHAPTER 5

Table 5.1 Observations of gabbro specimens heated at 2 kW for different durations.

Table 5.2 Microcrack extraction in gabbro specimens after microwave treatment using the fluorescent resin technique.

Table 5.3 Observations of monzonite specimens heated at 2 kW for different durations.

Table 5.4 Crack extraction in monzonite specimens after microwave treatment using the fluorescent resin technique.

Table 5.5 Crack extraction in granite specimens after microwave treatment using the fluorescent resin technique.

Table 5.6 Linear regression of maximum and average temperature with exposure time ($T = kt + b$) at the four power levels for the gabbro specimens.

Table 5.7 Linear regression of maximum and average temperature with exposure time ($T = kt + b$) for the monzonite specimens.

Table 5.8 Linear regression of maximum and average temperature with exposure time ($T = kt + b$) for the granite specimens.

LIST OF ACRONYMS

ASTM	American Society of Testing methods
BDS	Broadband spectroscopy
BTS	Brazilian tensile strength
BWI	Bond work index
CAI	Cherchar abrasivity index
CSM	Colorado School of Mines
CT	Computed tomography
D&B	Drilling and blasting
DP	Dielectric properties
DR	Drilling rate
DRI	Drilling rate index
EM	Electromagnetic
ET	Electrothermal
ETM	Electrothermomechanical
IR	Infrared
IRSM	International Society for Rock Mechanics
ISM	Industrial, scientific and medical
MAWC	Mechanically assisted waterjet cutting
MCT	Microwave cavity type
MLA	Mineralogical analysis
MW	Microwave
PL	Power level
PLS	Point load strength
PPL	Plane polarised light
RF	Radio frequency
RPM	Revolution per minute
SCB	Semi-circular bending
SE	Specific energy
SEM	Scanning electron microscopy
SKE	Specific kerfing energy
TBM	Tunnel boring machine
TE	Transverse electric field
TGA	Thermogravimetric analysis
UCS	Uniaxial compressive strength
UPV	Ultrasonic pulse velocity

UV	Ultraviolet
WAMC	Waterjet assisted mechanical cutting
XPL	Cross polarised light
XRD	X-ray diffraction analysis

CHAPTER 1

Introduction

This chapter provides an overview of the research motivations, the research objectives and the thesis structure.

1.1 Research motivations

Tunnel boring machine (TBM) tunnelling in hard rocks for civil and mining projects offers many unparalleled advantages over the conventional drill and blast (D&B) method when operating in compatible grounds. The advantages include higher advance rates, higher safety level, less ground disturbance and possible cost saving (Cigla et al., 2001; Maidl et al., 2008). However, tunneling in extremely hard and abrasive rocks has historically been troublesome and now emerges as one of the greatest challenges that must be properly addressed. It is clear that when those demanding rocks are encountered, the consequences can be very severe, ranging from excessive cutter wear, low advance rates to even project terminations (Bilgin et al., 2016; Du, 2017a; Tarkoy and Marconi, 1991).

ISRM (1981) defined rocks with a uniaxial compressive strength (UCS) of over 250 MPa as extremely high strength rocks. For massive hard rocks with a UCS of about 200 MPa, they may also have boreability problems. Massive rock mass could be defined as the rock mass that are without discontinuities or with very few discontinuities with a joint spacing of 1 m and over (Wickham et al., 1972). In this thesis, extremely hard rocks are defined as rocks with a UCS of over 200 MPa. The abrasiveness of rocks comes from both strength and the equivalent quartz contents (West, 1989) and is usually characterised by the Chechar Abrasivity Index (CAI) and Drilling Rate Index (DRI). Even though there are different excavators, i.e. TBMs, roadheader, continuous miners and mobile miners, to choose from for tunnel excavation, only TBMs are barely capable of boring through such rocks (Rostami, 2011). However, when tunnelling through very hard and abrasive rocks, the performance of TBMs can be significantly hampered. Alternative methods or assisting techniques must be developed to cope with such kinds of rocks.

Microwave assisted hard rock breakage has been demonstrated as a promising technique to either individually break rocks or work as an assistance to mechanical excavators (Hartlieb and Grafe, 2017; Hoekstra, 1976; Lindroth et al., 1993; Santamarina, 1989). Since the 1970s, a number of field and laboratory works have been conducted to treat rocks by microwave and to study the effect of microwave treatment on the physical and mechanical properties of rocks and the increase in penetration rates of mechanical excavators. Table 1.1 summarises the master's and doctorate theses on microwave treatment of rocks since 2000. Although those researches provide insight the microwave weakening of rocks, there is still a great lack of knowledge for microwave to be used in assisted TBM tunnelling in hard rocks.

Table 1.1 PhD and master's theses on microwave treatment of rocks.

Author	Thesis	Test Conditions	Main work and findings
Nekoovaght (2015)	Physical and mechanical properties of rocks exposed to microwave irradiation: Potential application to tunnel boring (D)	f: 915 MHz to 10 GHz PL: 1-5 kW, 10 kW t: 15-120s MCT: multi-mode	(1) Measured the DPs of 10 rock types using a coaxial probe (2) UCS, BTS, CAI tests of 10 rock types before and after MW radiation (3) T distribution in dry and wet rocks using stacked slices (4) Development a MW antenna for rock treatment
Wang (2016)	Microwave heating effects on formation damages in tight gas sands (D)	f: 2.45 GHz PL: 1.05 kW t: up to 10 mins MCT: multi-mode	(1) Measured the DPs of sandstone from 1MHz to 3GHz (2) Porosity and permeability of sandstone after microwave increases.
Nejati (2014)	Analysis of physical properties and thermo-mechanical induced fractures of rocks subjected to microwave radiation (D)	f: 200 MHz to 20 GHz T: 23-80 °C PL: 1-5 kW t: 5-30s MCT: multi-mode	(1) Dependence of the DPs of basalt on frequency, temperature, water content and the optimal frequency range (2) Effect of MW exposure time & PL on fracture toughness of basalt using SCB tests (3) Surface Fracture growth path using normal camera and SEM (4) DEM simulation of strength reduction of rock after MW radiation
Jin (2015)	The impact of water on heat distribution and mechanical properties of basalt after microwave treatment (M)	f: 2.45GHz PL: 3kW t: 40s, 60s, 80s MCT: multi-mode	Water did not affect heat distributions and mechanical properties of basalt after MW heating
Liu (2015)	Exploration of microwave-assisted breakage of rocks: The effect of size, shape, and internal discontinuity of rock on microwave distribution (M)	f: 2.45 GHz PL: N/A t: 90s MCT: multi-mode	Temp distribution of stacked basalt with different ratio of diameter and height. The results contradict with the research of Kobusheshe (2010).
Nekoovaght (2009)	An investigation on the influence of microwave energy on basic mechanical properties of hard rocks (M)	f: 2.45 GHz PL: 0.8, 1.25, 3kW ET: 15, 30, 60, 120, 240s MCT: multi-mode	(1) CAI and UCS decrease by 30 % as PL increases. (2) BTS of basalt can reduce by up to 80 %.
Satish (2005)	Exploring microwave assisted rock breakage for possible space mining applications (M)	f: 2.45 GHz PL: 1 W/g t: 60, 120, 180, 240s MCT: multi-mode	(1) PLS and UCS decreases with increasing MW exposure time. (2) FEM simulations indicated fractures take place at the boundaries of MW absorbing pyrite and MW transparent calcite.

Note: BTS-Brazilian tensile strength; BWI- Bond work index; CAI-Cerchar Abrasivity Index; D- Doctoral thesis; t-exposure time; M-Master thesis; MCT-cavity type; MLA-mineralogical analysis; PL-power level; PLT-point load test; SCB-semi-circular bending; SEM-Electron Scanning microscopy; T-temperature; TGA-Thermogravimetric Analysis; UCS-uniaxial compressive strength.

1.2 Research objectives and roadmap

This thesis aims to understand the challenges posed by extremely hard and abrasive rocks on TBM tunnelling. It then reviews the historical research and development on the novel methods to assist TBM excavation in those rocks. By conducting the techno-economical comparisons of those methods, the reason for performing microwave rock treatment is justified. The thesis then tries to understand whether and how microwave weakens different hard rocks by characterising the heating rates and dielectric properties of basic rock forming minerals using a newly proposed method and by microwave treatment of hard rocks. The effect of microwave treatment on the physical and mechanical properties of three igneous rocks is investigated in a comprehensive manner. The thesis also explores the mechanisms of microwave rock weakening by performing multi-physics numerical simulation. The applications of microwave on TBMs are also studied. The roadmap of the research can be found in [Figure 1.1](#).

1.3 Thesis structure

After this introductory chapter, **Chapter 2** reviews and highlights the challenges of hard and abrasive rocks on TBM tunnelling and then presents an extensive review of the state-of-the-art research on the novel rock breakage techniques. Special attention is paid to waterjet, laser, infrared and microwave. Their technical advantages and disadvantages in applications to TBM tunnelling are compared. The reason for performing microwave rock treatment is well justified.

Chapter 3 summarises the theories of microwave dielectric heating, the dielectric property measurement techniques and the dielectric properties of rock forming minerals and rocks at the microwave frequency and previous research on the effect of microwave treatment on the physical and mechanical properties of rocks. The parallel plate technique is then used to measure the dielectric properties of gabbro and granite from 1 MHz to 2 GHz and from room temperature to 300 °C. The influence of temperature and frequency on the dielectric properties of rocks is discussed. Research gaps when using microwave for assisted TBM tunnelling are identified.

In **Chapter 4**, the heating rates of the 8 basic rock forming minerals at the frequency of 2.45 GHz are presented. It then presented the derivations of the loss factors of those minerals at the microwave frequency of 2.45 GHz using a new method, which combines the microwave heating tests, the effective medium theory and the numerical simulations. The method is then used to predict the heating rates of mineral mixtures (simulated rocks) and compared with the values from experiments.

Chapter 5 presents in a detailed manner the microwave treatment of three igneous rocks. A description of the rock properties, research methodology and the experimental results are discussed. The effect of power level and exposure time on the heating rate, spatial temperature distribution, ultrasonic wave velocity, crack generation and strength reductions are investigated. The results indicate that microwave can effectively and efficiently weaken the three igneous rocks.

Chapter 6 discusses the technical considerations when using microwave on TBMs, which include the selection of the open-ended microwave applicators, the configurations of the applicators on the cutterhead with respect to the disc cutters, the power requirements and the expected difficulties.

Chapter 7 presents the conclusions drawn from the work and the work to be performed in the future.

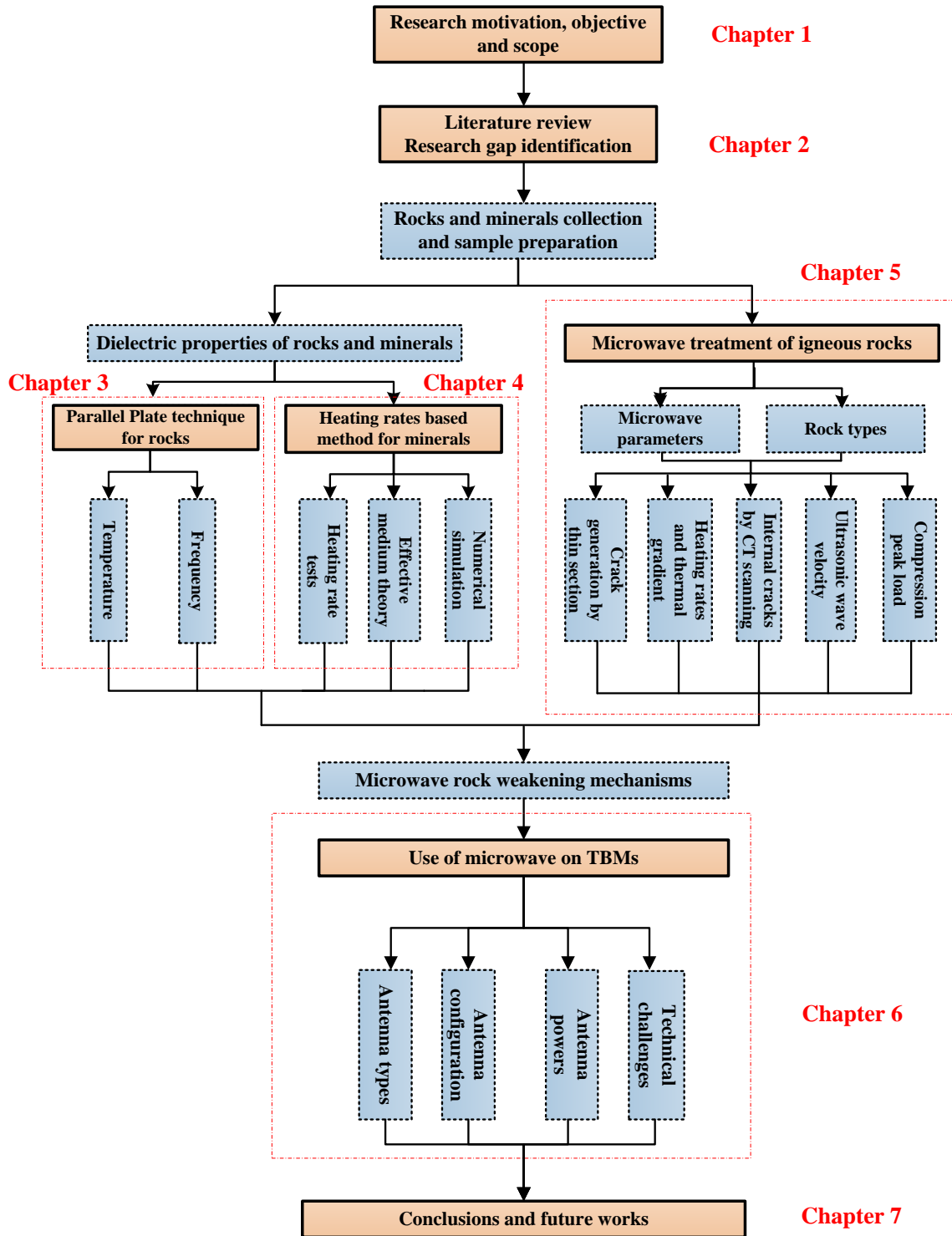


Fig. 1.1 Roadmap of the thesis research.

Reference

- Bilgin, N., Copur, H., Balci, C., 2016. Effect of high strength rocks on TBM performance, TBM Excavation in Difficult Ground Conditions. Wiley-VCH Verlag GmbH & Co. KGaA, pp. 211-223.
- Cigla, M., Yagiz, S., Ozdemir, L., 2001. Application of tunnel boring machines in underground mine development, International Mining Congress, Ankara, Turkey.
- Du, L., 2017. Building long tunnels at great depth using TBMs: Status quo, challenges and mitigation measures, 6th International Bridges and Tunnels Technical Congress & Exhibition, Shanghai, China.
- Hartlieb, P., Grafe, B., 2017. Experimental study on microwave assisted hard rock cutting of granite. BHM Berg- und Hüttenmännische Monatshefte, 1-5.
- Hoekstra, P., 1976. Rock, frozen soil and ice breakage by high-frequency electromagnetic radiation: A review. Department of Defense, Department of the Army, Corps of Engineers, Cold Regions Research and Engineering Laboratory, p. 17.
- ISRM, 1981. Rock characterization, testing and monitoring: ISRM suggested methods. Pergamon Press.
- Jin, L., 2015. The impact of water on heat distribution and mechanical properties of basalt after microwave treatment, Department of Mining and Materials. McGill University.
- Kobusheshe, J., 2010. Microwave enhanced processing of ores, Department of Chemical and Environmental Engineering, Faculty of Engineering. University of Nottingham.
- Lindroth, D.P., Berglund, W.R., Morrell, R.J., Blair, J.R., 1993. Microwave-assisted drilling in hard rock. Tunnels and Tunnelling 25, 24-27.
- Liu, F., 2015. Exploration of microwave-assisted breakage of rocks: The effect of size, shape, and internal discontinuity of rock on microwave distribution, Department of Mining and Materials.
- Maidl, B., Schmid, L., Ritz, W., Herrenknecht, M., 2008. Hardrock tunnel boring machines. Wiley.
- Nejati, H., 2014. Analysis of physical properties and thermo – mechanical induced fractures of rocks subjected to microwave radiation, Department of Mining and Materials. McGill.
- Nekoovaght, P.M., 2009. An investigation on the influence of microwave energy on basic mechanical properties of hard rocks. Concordia University.
- Nekoovaght, P.M., 2015. Physical and mechanical properties of rocks exposed to microwave irradiation: Potential application to tunnel boring, Department of Mining and Materials. McGill University.
- Rostami, J., 2011. Mechanical rock breaking, in: Darling, P. (Ed.), SME Mining Engineering Handbook, Third Edition, 4 ed. SME, USA, pp. 417-434.
- Santamarina, J.C., 1989. Rock excavation with microwaves: A literature review, in: Kulhawy, F.H. (Ed.), 1989 Foundation Engineering Conference. ASCE, Evanston, Illinois, United States, pp. 459-473.
- Satish, H., 2005. Exploring microwave assisted rock breakage for possible space mining applications, Department of Mechanical Engineering. McGill University.
- Tarkoy, P.J., Marconi, M., 1991. Difficult rock comminution and associated geological conditions, Tunnelling '91. Elsevier Applied Science, London, England, pp. 195-207.
- Wang, H., 2016. Microwave heating effects on formation damages in tight gas sands, Department of Petroleum Engineering, Faculty of Science and Engineering. Curtin University, Curtin.
- West, G., 1989. Rock abrasiveness testing for tunnelling. International Journal of Rock Mechanics and Mining Sciences & Geomechanics Abstracts 26, 151-160.
- Wickham, G.E., Tiedemann, H.R., Skinner, E.H., 1972. Support determination based on geologic predictions, 1972 North America Rapid Excavation and Tunnelling Conference. American Institute of Mining, Metallurgical, and Petroleum Engineers, Chicago, Illinois, USA, pp. 43-64.

CHAPTER 2

A Review of Novel Assisting Rock Breakage Methods

This chapter summarises the challenges of hard and abrasive rocks on the TBM tunneling in the civil and mining industry through case studies. It then briefly introduces the advancement of TBM technologies in dealing with hard rocks, and presents in a detailed manner the efforts on assisting rock breakage methods. The methods reviewed include waterjet, laser, microwave, and infrared irradiation. Their pros and cons are compared from technical and economic perspectives. This chapter serves to provide the state of the art review of the solutions to hard rocks.

2.1 Hard rock TBM tunnelling

Tunnel boring machines (TBMs) are mechanized tunnelling devices that automatically excavate and support circular/noncircular tunnels of different diameters, through a variety of ground conditions (Maidl et al., 2008). Since the modern hard rock TBMs are developed in the 1950s, they have undergone tremendous technological innovations and have become one of the dominant tunnelling techniques, especially for long tunnels. At present different TBM types with varying excavation and support features, e.g. gripper (also called main beam), single shield, double shield, hybrid TBMs and crossover TBMs, are available to cope with different rock mass conditions (Bäppler, 2016; Home, 2016; Maidl et al., 2008). TBMs have been extensively deployed in civil engineering for the construction of traffic tunnels for road, rail and subway, and utility tunnels for gas, power, water supply and sewage as well as hydraulic tunnels for water diversion (Bilgin et al., 2013; Liu et al., 2016). On the other hand, the mining industry is also regaining interests in using TBMs for mine drift construction (Brox, 2013; Home and Askildrud, 2011; Zheng et al., 2016). TBM tunnelling offers many unparalleled advantages over the conventional drilling and blasting (D&B) methods. TBMs well operated in compatible grounds bring about the following benefits (Cigla et al., 2001; Gertsch, 1994; Maidl et al., 2008; Robbins, 1987):

- Higher advance rates. The advance rates of TBMs are approximately 3-6 times that of D&B. Table 2.1 shows the world records of hard rock TBM performance. An advance rate of over 600 m/month has become the norm in not too bad rock masses. The construction time could be dramatically reduced, lending itself very attractive to build long tunnels.
- Higher safety level. Fewer crews are in the tunnel at any given time (usually less than 15) and crews are working under the protection of the TBM shield/canopy. Moreover, no explosives are used in the excavation. The risks and casualties can then be significantly reduced.
- Better configurations and less support requirement. The overbreak can easily be controlled and the grounds are less disturbed. Thus no/less temporary/permanent support is required, further reducing the overall cost.

Table 2.1 World records of TBM advance rates in hard rocks (Courtesy of [The Robbins Company](#)).

	Best day	Best week	Best month	Monthly average
3.01 – 4.00 m diameter				
Record	172.4 m	703 m	2066 m	1189 m/month
Make and model	Robbins Mk 12C	Robbins Mk 12C	Robbins MB 104-121A	Robbins Mk 12C
Project	Katoomba Carrier, Australia	Katoomba Carrier, Australia	Oso Tunnel, USA	Katoomba Carrier, Australia
4.01 – 5.00 m diameter				
Record	128.0 m	477.0 m	1822 m	1352 m/month
Make and model	Robbins MB 146-193-2	Robbins MB 146-193-2	Robbins DS 1617-290	Robbins DS 155-274
Project	SSC No. 4, Texas, USA	SSC No. 4, Texas, USA	Yellow River Tunnels 4 and 5, China	Yellow River Lot V, China
5.01 – 6.00 m diameter				
Record	99.1 m	562 m	2163 m	1095 m/month
Make and model	Robbins MB 1410-251-2	Robbins MB 1410-251-2	Robbins MB 1410-251-2	Robbins DS 1811-256
Project	Little Calumet, Chicago, USA	Little Calumet, Chicago, USA	Little Calumet, Chicago, USA	Yindaruqin, China
6.01 – 7.00 m diameter				
Record	124.7 m	515.1 m	1754 m	1187 m/month
Make and model	Robbins MB 203-205-4	Robbins MB 203-205-4	Robbins MB 203-205-4	Robbins, MB 222-183-2
Project	Indianapolis DRT, USA	Indianapolis DRT, USA	Indianapolis DRT, USA	Dallas Metro, USA
7.01 – 8.00 m diameter				
Record	115.7 m	428 m	1482 m	770 m/month
Make and model	Robbins MB 236-308	Robbins MB 236-308	Robbins MB 321-200	Robbins MB 321-200
Project	Karahnjukar Hydroelectric, Iceland	Karahnjukar Hydroelectric, Iceland	TARP, Chicago, USA	TARP, Chicago, USA
8.01 – 9.00 m diameter				
Record	75.5 m	428 m	1719 m	873 m/month
Make and model	Robbins 271-244	Robbins 271-244	Robbins 271-244	Robbins 271-244
Project	Channel Tunnel, U.K.	Channel Tunnel, U.K.	Channel Tunnel, U.K.	Channel Tunnel, U.K.
9.01 – 10.00 m diameter				
Record	105.6 m	435 m	1600 m	715 m/month
Make and model	Herrenknecht S-373	Herrenknecht S-373	Herrenknecht S-373	Robbins 321-199
Project	La Cabrera, Spain	La Cabrera, Spain	La Cabrera, Spain	TARP, USA
10.01 – 11.00 m diameter				
Record	48.8 m	235 m	841.8 m	–
Make and model	Robbins 354-253	Robbins 332-335	Robbins 332-335	–
Project	TARP, Chicago, USA	West Qinling, China	West Qinling, China	–
11.01 – 13.00 m diameter				
Record	49.7 m	248.8 m	787.8 m	–
Make and model	Herrenknecht	Herrenknecht	Herrenknecht	–
Project	Legacy Way, Australia	Legacy Way, Australia	Legacy Way, Australia	–
13.01 m and over				
Record	–	153 m	468 m	–
Make and model	–	Robbins 471-316	Robbins 471-316	–
Project	–	Niagara, Canada	Niagara, Canada	–

However, the performance of TBMs could be greatly compromised if unfavourable ground conditions are encountered (Sharifzadeh and Hemmati Shaabani, 2006). Adverse ground conditions include changing geology (Yamamoto et al., 2006; Zhao et al., 2007), mixed-face grounds (Ma et al., 2015; Tóth et al., 2013), squeezing grounds (Palmströ, 1995; Ramoni and Anagnostou, 2008), blocky grounds (Delisio et al., 2013), high in-situ stressed grounds (Gong et al., 2012; Yin, 2013), extremely hard and abrasive grounds (Gehring, 1994; Liu and Liang, 2000), large/huge groundwater inrush (Font Capó, 2012; Li et al., 2015), highly fractured and faulted grounds (Barton, 2000; Paltrinieri, 2015) and gassy grounds (Copur et al., 2012; Taherian, 2015).

TBM tunnelling in such difficult grounds might cause unwanted delays and cost overruns, sometime leading to unacceptable project terminations and personnel casualties. A better understanding of the challenges and proposing of corresponding counter-measures are imperative for the success of a TBM project. Therefore, those ground conditions have attracted tremendous attention from the academics and engineers. Their successfully resolutions turn challenges into great opportunities and provide boosts to the design, manufacture and operation of TBMs.

2.2 Problems associated with hard rock tunnelling

Of those challenging grounds, extremely hard and abrasive rocks have historically been troublesome and now emerge as one of the greatest challenges that must be properly addressed. Table 2.2 provides a non-exhaustive list of the TBM projects with exceedingly hard and abrasive rock problems. It is clear that when those demanding rocks are encountered, the consequences can be very severe, ranging from excessive cutter wear, low advance rates to even project terminations.

(a) Rockburst

Rockburst is one of the most common problems encountered when TBM tunnelling in massive and hard rocks, particularly where the in-situ stress is high. It refers to the damage to an excavation that occurs in a sudden or violent manner and is associated with a seismic event (Kaiser et al., 1996). An excellent explanation of the rockburst mechanisms in tunnels and shafts is presented in Ortlepp and Stacey (1994). Of the six mechanisms, strainbursting is the most common damage observed in machine tunnelling, reasons being that there is a high chance of a local stress build-up due to the absence of joints and fractures and the less disturbance from excavation. It is most likely to occur from half a diameter to three diameters behind the face, but may also occur from the face itself (Ortlepp and Stacey, 1994). Strainbursting may cause significant problems to TBMs, leading to high/abnormal cutter wear, possible cutter wipeout and cutterhead jamming, conveyor and mucking chute damage, gripping and support difficulties, and consequently a low utilization factor and penetration rate (Gong et al., 2012).

Table 2.2 TBM projects with exceedingly hard and abrasive rock problems.

Year	Project	TBM type	Dia. (m)	Tunnel length (km)	Geology	Hard rock associated problems	Solutions/consequences
1977	Fosdalen Bergverk mine haulage tunnel, Norway (Hansen, 1998)	Main beam	3.15	0.67	Tough and massive quartz keratophyre	Low penetration rates, very high cutter cost	Boring terminated.
1977	Floskefonn transfer tunnel, Norway (Hansen, 1998)	Main beam	3.25	0.35	Granitic gneiss UCS up to 270MPa	Three main bearing failures	Boring terminated.
1986	Kiena Gold Mine, Canada (Vanin, 1987)	Gripper	2.18	0.514	Competent andesite and basalt UCS: 41–252 MPa	Cutterhead cracking due to rock hardness, mechanical malfunction, excessive cutter wear and low advance rate (5.6 m/d)	Boring terminated.
1995	Midmar project, South Africa (Hansen, 1998)	Main beam	3.5	6.5	Dolerite UCS: up to 420 MPa	Cutter wear and change	Development of heavy duty cutter rings to sustain cutter load and reduce wear
1997	Qinling rail tunnel, China (Liu and Liang, 2000)	Gripper	8.8	18.45	Granite and gneiss UCS: 150-250 MPa, Max. 325MPa	Low advance rates (reduced from 3.5 m/hr to 1 m/hr), Higher cutter wear (37.3 m ³ /cutter) compared to desired 100 m ³ /cutter)	No special solutions adopted.
2007-2009	Beykoz-Istanbul Sewage Tunnel, Turkey (Bilgin et al., 2016)	Hybrid EPBM	3.1	4.1+3	Silty clay to shale to limestone, Quartzite UCS: 110-225 MPa	Very low penetration rate (1 mm/rev)	Replacing CCS disc cutters with V-type disc cutters in quartzite
2008-present	AMR water transfer tunnel, India (Robbins, 2017)	Double shield	10	43.5	Granite UCS: 160-190 MPa Quartzite: up to 450 MPa Quartz content: 35-70 %	Very low cutter life index (3.8-5.5), Cutterhead wear plates worn out	Ongoing development of harder, more durable cutter rings, 3 cutterhead refurbishments
2012-2014	Corbalis to Fox Mill Water Main Project, USA (Robbins, 2014)	Double shield	2.2	1.89	Diabase rock UCS: exceeding 345 MPa	High rock strength stopped the first contractor using a Lovat machine. Low advance rate (3.7-4.0 m/day) High cutter wear	No solutions put forward.
2013-2015	Røssåga hydropower project, Norway (Log et al., 2017)	Gripper	7.23	7	Mica schist, gneiss, marble/dolomite layers UCS: 100-280 MPa	Low cutter life, a damaged gripper shoe, main bearing replacement	Change of heat treatment process to improve cutter performance
2015-present	Yinhanjiwei Water Diversion Project, China (Xue et al., 2016)	Gripper TBM	8.02	18.3	Quartzite, Granite, Diorite and Fault-cataclasite, Mylonite UCS: 100- 240 MPa Quartz content: 43.67-92.6 %	Low advance rates (170 m/month) High cutter wear (58 m ³ /cutter)	Worldwide selection of suitable cutters
2016-present	Bahce-Nurdag High Speed Rail Tunnel, Turkey (Robbins, 2017)	Single shield	8	7.2+7.2	Interbedded sandstone, quartzite, and mudstone to highly weathered shale and dolomitic limestone. UCS up to 223 MPa	Very low advance rates	Project ongoing Solutions not available

A comprehensive review on the rockburst during TBM tunnelling in hard rock and coal mines is presented in [Zheng et al. \(2016\)](#). One of the notable projects of rockbursting in the mining industry is the Star Gold Mine, Idaho (USA) where a TBM is chosen for drilling exploratory and development drifts in 1969. The lithology consists of quartzite with a UCS of 69–351 MPa and a hardness of 83–225. During TBM tunnelling at a depth of 2310 m, extremely serious stress-induced rockbursting, popping and slabbing are encountered while penetration rates are far below what is reasonable with available cutter loads ([Tarkoy and Marconi, 1991](#)).

For railway and hydropower engineering where the overburden is large, rockburst is a more severe and prominent problem. [Figure 1.1\(a\)](#) illustrates the mechanism of the strainburst in massive hard rock masses, while [Figure 1.1\(b\)](#) shows the rockbursting and slabbing at Jinping II Hydropower Plant in China which can be explained by the strainburst mechanism ([Home, 2009](#)).

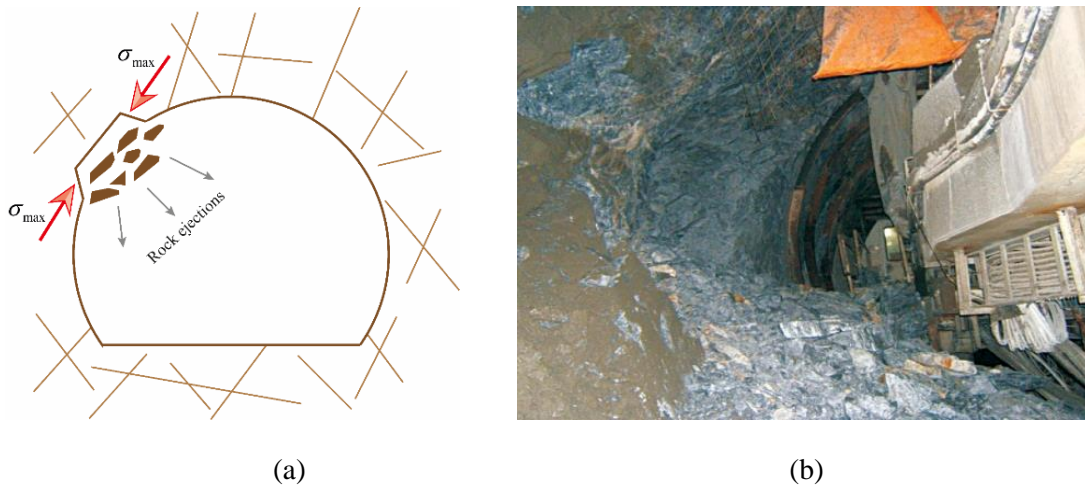


Fig. 2.1 Rockburst during TBM tunnelling: (a) Strainburst in hard rock due to stress concentrations (modified from [Ortlepp and Stacey \(1994\)](#)); (b) Rockbursting at Jinping II hydropower station in China ([Home, 2009](#)).

(b) Low penetration rates

In massive and hard rock mass, the penetration rate decreases exponentially as the rock strength increases. [Figure 2.2](#) shows the thrust, torque and penetration rate of TBMs with 17 inch disc cutters in rocks of different strengths ([Frenzel et al., 2008](#)). It indicates that to achieve a reasonable penetration rate a critical load must be exceeded. As the rock strength increases, the critical load may not be easily exceeded, resulting in a very poor rock breaking performance. According to [Du \(2017b\)](#), in the Yinhanjiwei Water Diversion Project in China where massive and hard granite, quartzite and diorite are encountered, the penetration rate of an 8.2 m diameter TBM is 2.4 m/h in rock mass with a UCS of 120 MPa. However, the penetration rate dropped to 1.3 m/h at 160 MPa and 0.6 m/h at 200 MPa.

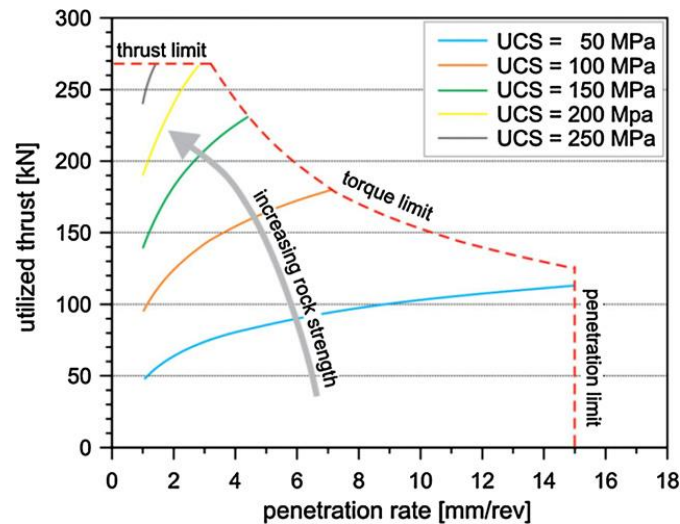


Fig. 2.2 TBM thrust as a function of rock strength with 17 inch disc cutters (Frenzel et al., 2008).

In the Qinling Rail Tunnel Project, the penetration rate decreased from 3.5 m/h to 1 m/h when extremely hard rocks are encountered (Liu and Liang, 2000). In the Beykoz-Istanbul Sewage Tunnel in Turkey, the penetration rate is 1 mm/revolution in quartzite (Bilgin et al., 2016), far below the acceptable value of 2-2.5 mm/revolution (Barla and Pelizza, 2000). Low boreability issues are also reported in the AMR Water Diversion Project in India and Bahce-Nurdag High Speed Rail Tunnel in Turkey, etc. More projects with boreability problems and the counter-measures can be found in Table 2.2.

(c) Excessive cutter wear and low TBM utilisation

According to West (1989) and Plinninger et al. (2003), the cutter wear is highly correlated to the Young's modulus (or UCS) and equivalent quartz content of the rock. Figure 2.3 presents a rough correlation between of TBM cutter life, UCS, and CAI for some common hard rock types (Maidl et al., 2008). As also shown in Table 2.2, the most abrasive rock types are igneous and metamorphic rocks with a high mechanical strength and equivalent quartz content, for instance, granite and quartzite. In those rocks, the cutter wear and cost can be unacceptably high. Home and Askilrud (2011) presented that in soft to medium-hard sedimentary rocks such as limestone and other nonabrasive rock types, cutter costs are typically as low as US\$ 1.00/m³ or less. However, in hard, massive quartzite, they can reach US\$ 20/m³. As shown in Table 2.2, the cutter life in the Qinling Rail Tunnel Project and the Yinhanjiwei Project is 37.3 m³/cutter and 58 m³/cutter, respectively. These fall into the region of extremely high cutter wear. In the Yinhanjiwei Project, 1626 cutters are replaced in a distance of 1891 m, corresponding to 1.16 m/cutter (Du, 2017b). As a result, significant cost overruns and schedule delays occurred.

(d) Cutter wipe-out

In the case there are large wedges stemming from strainburst or large chips, one disc cutter may be blocked and stop rotating. Considering the load on cutters are close to their maximum allowable value,

blocking one cutter will lead to the over-loading of adjacent cutters. The over-loading of disc cutters may also result from the vibration of the boring process. This could possibly lead to a wipe-out of a group of adjacent disc cutters (Figure 2.4). In the worst scenarios, the cutterhead structure may also be damaged.

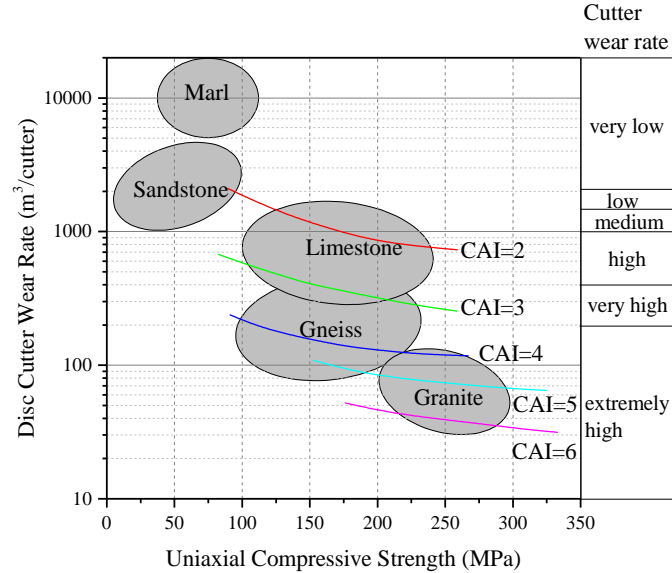


Fig. 2.3 Correlation of TBM cutter life (17 inch disc cutter), UCS and CAI for some common hard rock types (Reproduced from Maidl et al. (2008)).



Fig. 2.4 Disc cutter wipeout when cutters become blocked (Roby et al., 2008).

2.3 Improvement of TBM capacity

Since the 1970s and 1980s, a great number of researches have been conducted to improve the performance of TBMs in those challenging grounds. Researches are carried out from two different ways. One is to improve the capacities of the machines by developing more powerful and resistant cutters, the other being to pre-condition rocks before excavation or to assist rock breakage while mechanical cutting.

2.3.1 High performance disc cutters

To dig in ever-harder rocks and/or to cope with ever-larger tunnel diameters, the capacity of disc cutters has been constantly improved since it was invented in the 1950s (Deering et al., 1991). Table 2.1 shows development history of the Robbins disc cutters. It can be found that the diameter of disc cutters has increased from 11 inch (280 mm) in 1961 to 20 inch (508 mm) in 2006, with the loading capacity increased from 85 kN to 312 kN (Roby et al., 2008). With an increased ring diameter, a higher thrust, torque and revolution could be applied to effectively break hard rocks. Moreover, a larger diameter also means a larger wear volume. For instance, the wear volume of the 20-inch cutters is 1.6 times that of the 19-inch cutters (Figure 2.5), meaning a significant improvement of cutter life. According to Smading (2017a), field tests show that machines with 20 inch disc cutters have on average a 24 % better monthly advance rate than those with 19 inch cutters. The cutter wear is also significantly improved thanks to the use of more wear-resistant materials and special heat treatment techniques (Smading, 2017b). Cutters today can either incorporate hard, fine grained carbides into the matrix of the disc material or apply a hardened coating of alloy powder on the steel substrate of the disc to help avoid rapid cutter destruction such as ring chipping and spalling (Ozdemir, 2002). The bearing, seal, and lubricants are also continually improved to prolong the disc cutter life. Moreover, by implementing real-time cutter wear monitoring, the conditions of cutters can be determined which could help to schedule cutter wear maintenance (Mosavat, 2017).

Table 2.3 Development history of disc cutters (Roby et al., 2008).

Diameter (inch)	Diameter (mm)	Peak load (kN)	Year introduced
11	279	85	1961
12	305	125	1969
13	330	145	1980
14	356	165	1976
15.5	394	200	1973
16.25	413	200	1987
17	432	215	1983
19	483	312	1989
20	508	312	2006

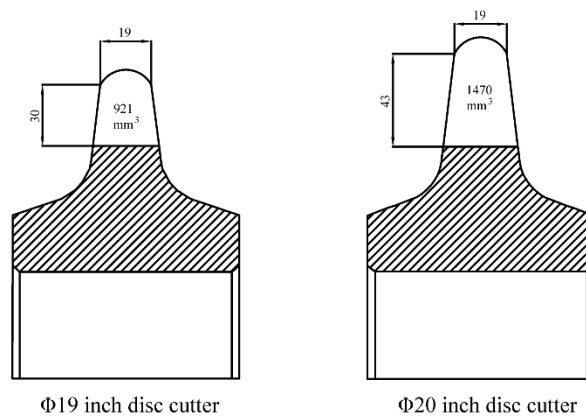


Fig. 2.5 Relative wear volumes of 19-inch and 20-inch disc rings (Smading, 2017a).

2.3.2 Optimised machine design

Based on a detailed geotechnical baseline report, the cutterhead design of hard rock TBMs can be optimised by conducting full-scale linear cutting tests. [Rostami and Ozdemir \(1993\)](#) proposed a method to calculate the thrust forces based on the linear cutting tests, however, the rock strength tested ranged from 70 to 200 MPa. [Bilgin et al. \(2013\)](#) and [Bilgin et al. \(2017\)](#) reported the linear cutting tests on rocks with strength of over 200 MPa (maximum 327 MPa) to provide design data and select proper TBM(s). TBM performance parameters, such as thrust and torque values per penetration are compared with the predicted values based on the tests. It is concluded that the field and predicted parameters are very close in values.

With the improvement of the reliability of key TBM components such as main bearings, the utilisation rate has been significantly increased ([Nelson, 1993](#)). Utilisation rates of over 50 % are now possible in hard rocks. [Table 2.4](#) compares the specifications of two TBMs of the same diameter but used at different time, from which one can understand how technologies in terms of rock breaking and support have advanced in the past four decades.

Table 2.4 Comparison between two TBMs of the same diameter ([Rauer, 2014](#)).

Parameters	White Pine Copper Mine (1971)	Stillwater Copper Mine (2011)
TBM type	Main beam	Main beam
TBM diameter (m)	5.49	5.49
Disc cutter diameter (mm)	279 (11 inch)	483 (19 inch)
Maximum cutter loading capacity (kN)	85	312
Cutter power (kW)	895	1,968
Cutterhead torque (Nm)	2,332,767	3,095,000
Machine thrust (kN)	7,031	10,898
Machine weight (metric tonnes)	205	227
Ground support	Two rotary percussive roof drill	McNally slat support system, two roof bolt drill, probe drill ring, core drills, ring beam erectors
Tunnel length (m)	1,783	6,975
Advance rate (m/h)	1	4.8

2.4 Assisting rock breaking methods

In the 1970s and early 1980s, a considerable amount of research on assisting rock breaking methods was conducted worldwide. Those work have been reviewed by [Maurer \(1980\)](#), [Murray et al. \(1994\)](#), [NRC \(1994\)](#), [Pierce et al. \(1996\)](#), [Res et al. \(2003\)](#) and [Vogt \(2016\)](#). In the context of assisted TBM tunnelling, the concept is shown in [Figures 2.6 and 2.7](#). As shown in [Figure 2.6](#), the concept involves cutting parallel kerfs on the excavation face using assisting methods, then cutting the rock between two

adjacent kerfs by mechanical tools (normally disc cutters). If the kerfs are shallow, the mechanical tool plays a dominant in the rock breakage. In contrast, if they are deep, the kerfing techniques are the primary means for rock breakage. Concepts of cutting along treated trajectories have also been proposed and tested. Depending on the rock breakage mechanisms, those assisting methods could be grouped into three classifications: mechanical breakage, electromagnetic wave breakage and electrical breakage.

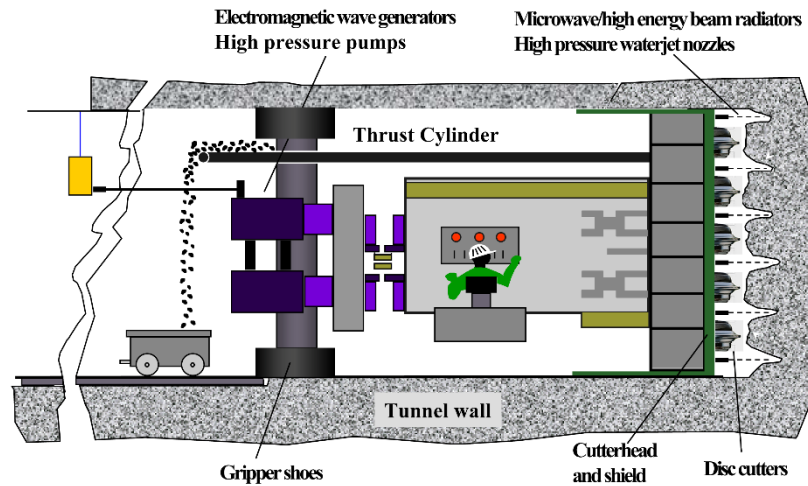


Fig. 2.6 Assisted TBM tunnelling concept (modified from Maurer (1980)).

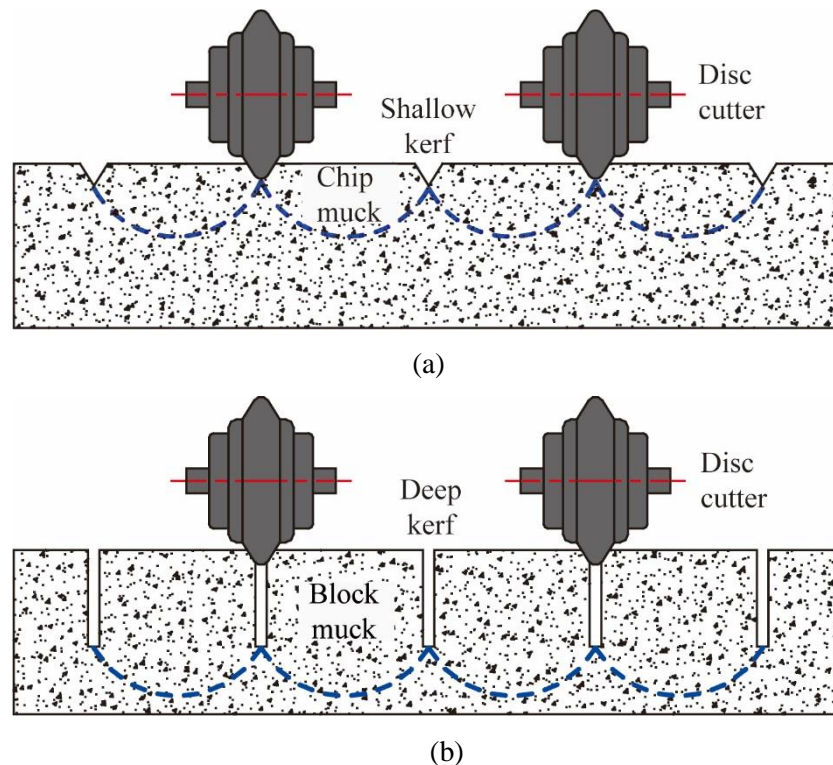


Fig. 2.7 Kerfing strategies when using assisting methods: (a) Shallow kerfing; (b) Deep kerfing (modified from Carstens et al. (1970)).

(a) Mechanical breakage methods

Mechanical breakage is now the dominant rock breaking mechanism for TBM tunnelling and it includes:

- Chisel bit/drag bit, disc cutter
- Percussive jack hammer
- High pressure water jet
- Undercutting technology
- Oscillating disc cutting
- Controlled foam injection
- Combination of two or more above

The mechanism of mechanical breakage is that it generates a stress which exceeds the mechanical strength of rocks, either tensile, shear or compressive. The stress can be either static or dynamic (impulsive). Given the drastic difference in the tensile and compressive strengths, it is preferred that rocks fail in the tensile mode. A majority of the assisting methods aims to provide free surfaces to make use of this difference. State of the art reviews of current and emerging technologies for mechanical rock breakage can be found in [Ramezanzadeh and Hood \(2010\)](#) and [Dehkhoda and Fairhurst \(2017\)](#). The rock breakage principles and merits of mechanical excavators can be found in [Rostami \(2011\)](#).

(b) Electromagnetic (EM) wave breakage

This is in fact thermal treatment of rocks using any form of heat to induce weakening (cracking), spalling, melting and vaporisation of rocks. The heat sources include, but are not limited to:

- Torque heating
- Laser cutting
- Infrared irradiation
- Microwave heating including millimetre wave melting

In principle, the mechanism of thermal breakage using all the sources is the same. The heat sources take up different bands in the EM spectrum, with corresponding frequencies and wavelengths. The heating of rocks, taken as dielectrics, is governed by the interactions between EM waves and rocks, which can be characterised by the dielectric properties of rock forming materials and the electric/magnetic field intensity. The concentration of energy (power density), the depth of penetration and the brittleness of the rocks determine the heating outcomes, being it fracturing, spalling, melting or vaporisation. More theories on dielectric heating could be found in [von Hippel \(1954\)](#) and [Chabay and Sherwood \(2015\)](#) and will be discussed in Chapter 3.

(c) Electrical breakage

This is sometimes grouped into the mechanical breakage classification. However, there is a big difference in that the stresses are generated using high voltage electric currents. It includes:

- Plasma blasting

- Electron beam
- Electric current

Figure 2.8 shows the schematics of electrical rock breakage and plasma blasting and their conceptual applications in tunnelling. In the plasma blasting process, the energy is released in the form of an electric discharge into a small amount of liquid located in a hole drilled in the rock. The electrical discharge rapidly vaporizes, and disintegrates the liquid, thus creating a high pressure plasma confined in the rock. As with chemical explosives, the expanding hot gas generates a shock wave that, in conjunction with cracks propagating from the blast zone, fractures the rock (Hamelin et al., 1993). This method involves pre-drilling of holes and use of blasting probes with survivability problems and is not expected to advance rapidly to be used in tunnelling.

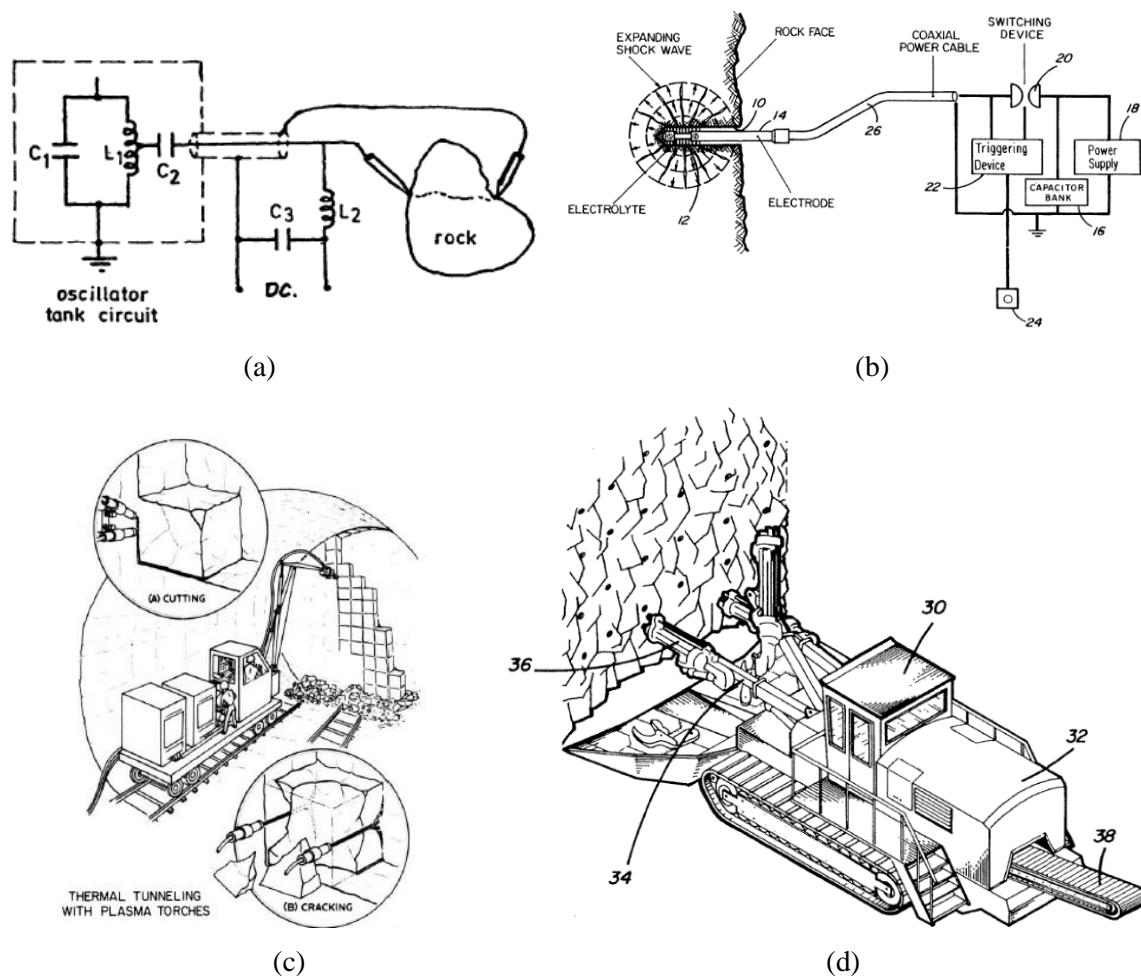


Fig. 2.8 Electric thermal breakage methods and conceptual applications in tunnelling. (a) Schematic of electric rock breakage (Segsworth and Kuhn, 1977); (b) Schematic of plasma blasting (Hamelin et al., 1993); (c) Thermal tunnelling with plasma torches (Poole and Thorpe, 1973); (d) Tunnelling using plasma blasting (Kitzinger and Nantel, 1992).

The principle of breaking rocks by high frequency current involves the formation of a narrow heated channel in a sufficiently short time to create thermal shocks. Initially the power drawn from the source

creates a conducting channel through the rock. Near the completion of this channel, rock will start drawing power from the direct current source. The surge of energy from this source shatters the rock into fragments. (Segsworth and Kuhn, 1977). This method is more suitable for secondary rock breakage.

This chapter does not intend to review all the techniques listed. Only waterjet, laser and microwave assisted TBM tunnelling will be discussed considering the feasibility and the amount of work conducted in those fields.

2.4.1 Waterjet

The waterjet cutting technology has been used to cut rock materials since the 1960s. A great review on its development history and applications in direct and assisted rock cutting can be found in Summers (1995). The cutting mechanism lies in that the high velocity and high pressure jet, with or without abrasives, provides an impact on the target and erodes away materials under attack. In general, a waterjet cutting system consists of a high-pressure pump, a jet nozzle and possibly an abrasive delivery system. Although high pressure waterjet (commercial pressure up to 900 MPa is available) is capable of cutting through rocks of any strength and hardness, mechanical breakage must be performed to remove the adjacent ribs between waterjet cut kerfs in the context of rock excavation (Summers and Henry, 1972). Another benefit of mechanical assistance is that it can substantially reduce the specific energy of the rock breakage process.

Based on which means plays a dominant role in breaking rocks, the methods can be classified as mechanically assisted waterjet cutting (MAWC) and waterjet assisted mechanical cutting (WAMC) (Hood, 1993; Summers, 1995). Figure 2.9 illustrates the two methods when applied to TBM tunnelling. As shown in Figure 2.9(a), MAWC involves cutting parallel/concentric kerfs using high pressure waterjet and then rolling down a mechanical tool (normally a disc cutter) along a central kerf or between two kerfs to break the intervening ribs (Hood et al., 1992). In this method, new surfaces are created to change the rock failure mode from compression to shear and tension. The energy output from waterjetting is about 4-10 times that from mechanical excavators. In contrast, WAMC (Figure 2.9(b)) involves the use of relatively low water pressure with nozzles directed at the rock-cutter interface to either flush away the crushed rocks, and reduce the cutting forces or to penetrate into the mechanically induced cracks to assist their propagation (Dubungnon, 1981; Hood, 1985; Pierce et al., 1996). In WAMC, the energy ratio from waterjetting and mechanical tools is about 1:1 (Ciccu and Grosso, 2010).

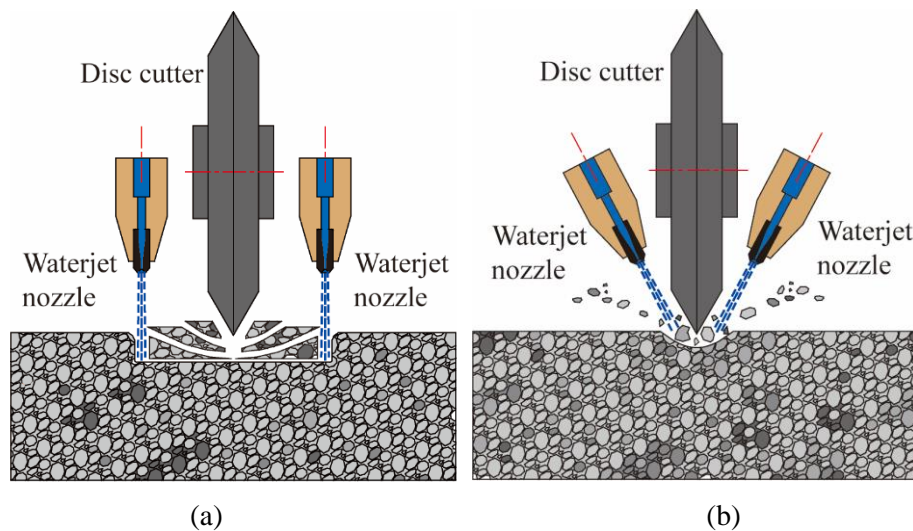


Fig. 2.9. Applications of waterjet in TBM tunnelling: (a) Mechanically assisted waterjet cutting (modified from Knickmeyer and Baumann (1983)); (b) Waterjet assisted mechanical cutting (modified from Fenn et al. (1985)).

In the 1970s and 1980s, laboratory and field research activities were conducted in countries such as the US, Germany, Russia and South Africa in attempts to improve the excavation efficiency of hard rock in mining and civil engineering projects. Those researches were carried out along the course of the development of TBMs and roadheaders (Zheng et al., 2016). Research have demonstrated that waterjet could help in significantly increasing the advance rates, reducing cutting forces and extending the cutter life (Fenn et al., 1985; Henneke and Baumann, 1978; Hood, 1985; Kouzmich and Merzlyakov, 1983; Ozdemir and Evans, 1983; Tecen and Fowell, 1983; Wang and Miller, 1976). Other possible benefits include improved working environment (less dust and heat generation) and lighter and smaller machines (Ciccu and Grosso, 2014; Hood et al., 1992; Ropchan et al., 1980; Summers, 1995).

(1) Laboratory research

The first tests on waterjet assisted cutting were performed at the Bendix Research Labs, sponsored by the US Bureau of Mines (Chadwick, 1973; Chadwick and Kurko, 1972). They used waterjet pressure between 250-560 MPa to cut kerfs in eight hard rock types and rolled down a central kerf. Though waterjet is shown to be effective in kerfing, there were no obvious energy savings compared to unassisted cutting. Fenn et al. (1985) conducted waterjet assisted and unassisted disc cutter excavation on a norite with a UCS of 254 MPa. Two 1.2 mm diameter waterjet nozzles (5 to 40 MPa), one on each side of the disc cutter, were directed at the edge of the cutter with a standoff distance of 35 mm (Figure 2.9(a)). The cutting speed was 0.6 m/s. Figure 2.10 shows some of their work results. It can be found that with the assistance of waterjet the rolling and thrust forces of the disc cutter could be reduced by up to 40 %. Their investigation of jet pressure effect indicated that no additional benefits of any significance could be gained by using pressure greater than 40MPa and that the major benefits occurred

in the 0-5 MPa range. No lab tests on waterjet assisted disc cutting were conducted in the following three decades. The reasons will be explained in the next sections.

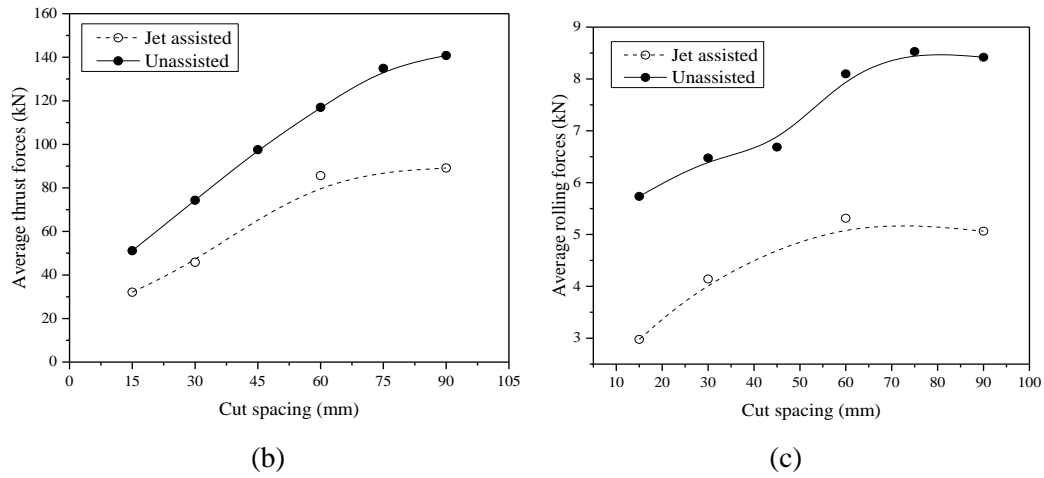


Fig. 2.10. Cutting forces of a disc cutter with and without 40 MPa waterjet assistance: Thrust force reductions; (b) Rolling force reductions (Reproduced from Fenn et al. (1985)).

More recently, Ciccu and Grosso (2014) used a 150 MPa nozzle directed parallel to the edge of the disc cutter to cut rhyolite (UCS 44 MPa). Their test setup and results can be found in Figure 2.11. The standoff distance was 30 mm and cutting speed was 1-2 m/s. They found that penetration rate and excavated volume significant increased while the width of groove on the nozzle side decreased owing to the weakening action of a jet, causing deeper penetration.

Dehkhoda (2011) developed a water pulsing system (microsecond pulses) to break large sized boulders. It is found that the system is able to break 1 m³ sized boulders in less than 1 minute. She believed that the high velocity pulsed waterjet not only directly induces rock damage and rock breakage but also induces stress waves within the target. This technology shows benefits in energy consumption and water usage. More exploratory research should be conducted to apply this technology on mechanical excavators.

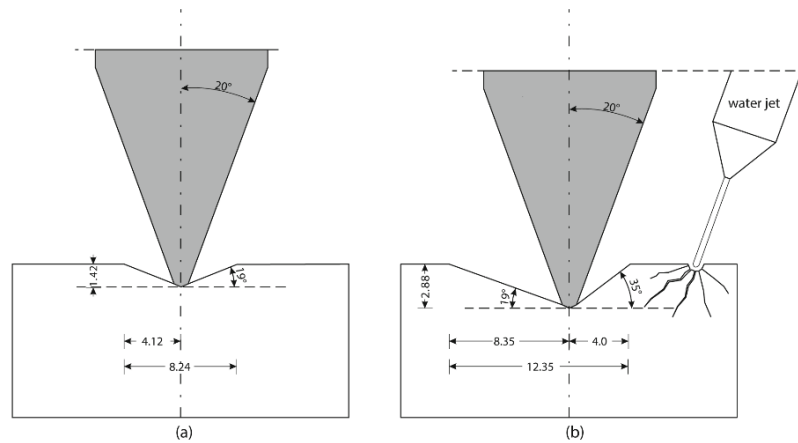


Fig. 2.11 Groove geometries of (a) mechanical cutting and (b) waterjet assisted cutting (Ciccu and Grosso, 2014).

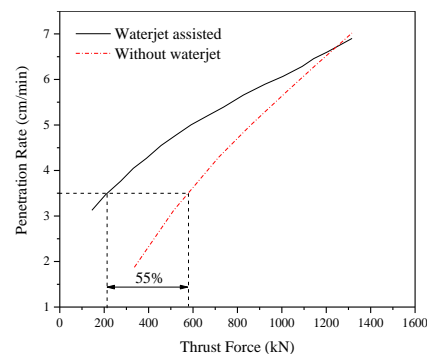
(2) Full scale field tests

Full scale field tests on modified TBMs with waterjet assistance were conducted in the late 1970s and early 1980s in the US and Germany. Wang and Miller (1976) reported the field tests in a US granite quarry using a 2.1 m diameter Robbins TBM equipped with waterjet. The TBM had 16 disc cutters, 31 high-pressure nozzles with an orifice diameter of 0.3 mm and a standoff distance of 37.5 mm. The waterjet pressure was 345 MPa and thrust ranged from 22.4 MPa to 27.6 MPa. The granite rock strength ranged from 159-262 MPa. Their results indicated that advance rates could be increased by 40-48 % when the jets were directed in between the cutters. In contrast, placing the nozzles under the cutters actually reduced the advance rates. They estimated that there could be a cost saving of 14 % to 24 % for 3 m and 6 m TBMs, respectively.

The trial projects of mechanically assisted waterjet cutting in a German quarry is presented in Henneke and Baumann (1978) and Kouzmich and Merzlyakov (1983). They used a 2.65 m diameter Wirth TBM (Figure 2.12(a)) equipped with 100 nozzles (total power 1000 kW) and 14 disc cutters (total power 320 kW). The nozzle orifice diameter was 0.25 mm, working at a pressure of 400 MPa. Nozzle and cutter spacing (as in Figure 2.9(a)) was set at 50 mm and the traverse velocity was 0.125 m/sec. They found that the cutting forces in sandstone could be reduced by up to 50 % to achieve the same advance rates and that should a constant thrust be applied penetration rate of the machine could be doubled. At a waterjet pressure of 360 MPa and a flow rate of 120 l/min, the thrust force to have a penetration rate of 3.5 cm/min could be reduced by 55 % (Figure 2.12(b)). By adding chain polymers to water, the cutting depth could be increased by up to 70 %. Later on, one 6 m diameter Demag TBM was also used in a German coal mine (Baumann and Henneke, 1980). The TBM was equipped with jet nozzles working at a pressure of 400 MPa. The nozzles were installed within the centre of the cutter head and in the calibre section where peak loads and extreme wear were observed. Similar performance improvement (50 %) was observed with waterjet assistance.



(a)



(b)

Fig. 2.12 Waterjet assisted TBM tunnelling. (a) The 2.65 m diameter Wirth TBM with waterjet nozzles, (b) Penetration rate with/out waterjet assistance (Knickmeyer and Baumann (1983)).

(3) Overall evaluation of waterjet assisted TBM tunnelling

In the literature, although most researchers admit that early trials were overall not successful, there are mixed and divided opinions on the fate of the technology. [Hustrulid \(1976\)](#) designed a 7 m diameter TBM based on previous researchers' work. He found that to achieve a penetration rate of 1.2 m/hr in granite, 192 nozzles with an orifice diameter of 0.3 mm, a working pressure of 350 MPa and a total power of 4425 kW are required. He asserted that this would be uneconomical particularly in those conditions where the long-term reliability of the system could not be guaranteed. This was later rebutted by [Summers \(1995\)](#) that many of Hustrulid's assumptions were false and that Hustrulid's prestige and misjudgement cast a significant pall over the future of waterjet-assisted TBM research.

[Ozdemir and Dollinger \(1984\)](#) blamed on the poor reliability of the high pressure pumping equipment, high power cost and personnel safety concern that precluded the immediate acceptance and utilization of the waterjetting technologies by TBM manufacturers. They concluded that the jet pressures would have to reduce substantially to minimize the power requirements, improve equipment reliability and enhance personnel safety.

[Hood \(1985\)](#) attributed the unsatisfactory performance of waterjet cutting to (1) the poor understanding of the mechanism by which the waterjets assist the breaking process, (2) hardware not specially designed for the cutting purpose leading to incompatibility with the working environment and waste of energy.

[Robbins \(1987\)](#) asserted that although laboratory tests of waterjet cutting achieved very promising results, field experiments on TBMs is disappointing. He believed that pure water without abrasive (up to 400 MPa) is effective in medium strength rocks that are no longer a problem to cut with rolling disc cutters. He argued that although low water jets at pressures of 35-70 MPa could be effective in aiding the mechanical rolling cutters by removing cutting chips, perhaps extending fractures and reducing cutting forces, applying high pressure with a large number of nozzles in the field had been proven highly unreliable and trouble-prone.

(4) Research directions

Since the last research boom on waterjet assisted TBM boring in the 1970s and 1980s, very little research has been conducted in the past three decades. This can be explained by the fact that the performance of modern TBMs has been substantially improved and the impact of previous unsuccessful applications. Considering the demonstrated feasibility of waterjet assisted cutting, it is still a possible assistance means to help bore through hard and abrasive rocks if the following issues are properly addressed.

- Development of suitable equipment

As discussed in the last section, the reliability of the high pressure jet delivering system to the excavation face should be improved. High pressure pump and nozzles are now quite mature. However, the greatest challenge comes from the rotary sealing of the shaft. Also the energy consumption of the

combined methods should be evaluated. The technologies such as pulsed jetting should also be further developed.

- Use of abrasives

Use of abrasive materials has been demonstrated to be very beneficial in conventional pure waterjet cutting by reducing water pressure and enhancing cutting performance. However, its impact on the TBM cutter wear must be studied before it can be used for field applications. The economic analysis should also be performed considering the high cost of the unrecoverable abrasives.

- Selection of right water pressure

At the moment, the role of water pressure in TBM rock breakage is still unclear. There is still a controversy in the water pressure selection (high pressure or low pressure) and the direction of waterjet nozzles. A comparative study of MAWC and WAMC should be conducted to better understand the rock breakage process in hard rocks. Also for large diameter TBMs, the impact of the rotational speed on the assistance of cutting of rocks at the periphery should be examined, as the interaction time will be much shorter.

- Excess water

The use of large quantity of water remains to be a problem, particularly when there is already water ingress into the tunnel. Research should be conducted to reduce the quantity of water. Possible solutions include the use of abrasive and pulsating waterjet systems. A further advantage of pulsed waterjets is that less power is used in the jet assist when compared to a continuous jet, significantly lowering the power requirements (Wilson et al., 1997).

2.4.2 Laser

Laser, the acronym for ‘light amplification by simulated emission of radiation’, is a device that generates or amplifies coherent radiation at the frequencies in the infrared, visible, or ultraviolet regions of the EM spectrum (Siegman, 1986). It is in essence an intense beam of photons from excited atoms or molecules. Depending on the energy source, laser can be divided into gas, solid-state, chemical reaction, dye, free electron, excimer lasers, etc. (Weber, 1998). Since the first laser system is invented in 1960, tremendous research on laser (assisted) tunnelling and drilling has been performed (Carstens et al., 1970; Graves et al., 2002; Jurewicz, 1976; Williamson et al., 1968). The mechanism of laser heating, kerfing or drilling is more or less the same as conventional heating (McGarry and Moavenzadeh, 1970). The different heating outcomes lie in the facts that the EM waves are moderately or highly focused thus the energy intensity could be significantly increased and that the wavelength of a laser is in the order of micrometres, interpreting as a small penetration depth into the materials when compared to microwave (wavelength from 1 mm to 1 m). Table 2.5 lists seven laser systems that have been used on rock kerfing and drilling research (Graves et al., 2002). Of those laser systems, CO₂, MIRCAL, COIL and the Nd:YAG are the four most widely used.

Table 2.5 Lasers used for rock cutting and drilling (after [Graves et al. \(2002\)](#)).

Laser systems	Type	Waveform	Wavelength (μm)	Power level (kW)	Comments
HF(DF) - Hydrogen Fluoride (Deuterium Fluoride)	Chemical	CW	2.6-4.2	1200	Mid-Infrared Advanced Chemical Laser (MIRCAL) is this type.
COIL - Chemical Oxygen Iodine Laser	Chemical	CW	1.315	100	Mature technology.
DDL - Direct Diode Laser	Solid state	CW	0.8	4	Energy efficient with low power level. High durability and reliability, great attenuation in optics due to large wavelength. Pulse length can vary between 1-1000 μs.
CO₂ Laser	Gas	CW RP	1-30	1000	
CO Laser	Gas	CW RP	5-6	200	
Nd: YAG - Neodymium : Yttrium Aluminum Garnet	Solid state	RP	1.06	Avg. 4 Max. 32	Low energy efficiency.
FEL – Free Electron Laser	Electron	CW	10 ⁻⁴ - 10 ³	14	Wavelength adjustability allows optimization for such effects as reflection, scattering, absorption, blackbody radiation and plasma screening.
KrF (Excimer) Laser - Krypton Fluoride Excimer	Solid state	RP	0.248	10	Pulse length of 0.1 μs.

Note: CW-Continuous waves; RP - Repetitive pulses.

Figure 2.13 illustrates the interaction between laser and rocks. The focused laser beam with a Gaussian type distribution of laser intensity would melt and vaporise the rock and form a notch or kerf in the centre of the beam, where the laser intensity is the highest. To the sides of the central peak, laser intensity diminishes rapidly and an increasing degree of melting occurs. Due to the very low thermal conductivity of rocks there are great thermal gradients and stresses in the vicinity of liquid-solid boundary, very likely to generate microcracks in the rock solid ([Jurewicz, 1976](#)). Four mechanisms exist in the rock weakening process, weakening by the generation of cracks, spalling, melting and vaporisation. Many people believe that the rock melting should be minimised to save energy while others believe this is an inevitable process ([Carstens et al., 1970](#)). In case the laser is poorly focused, the heating scenario is similar to that of conventional heating.

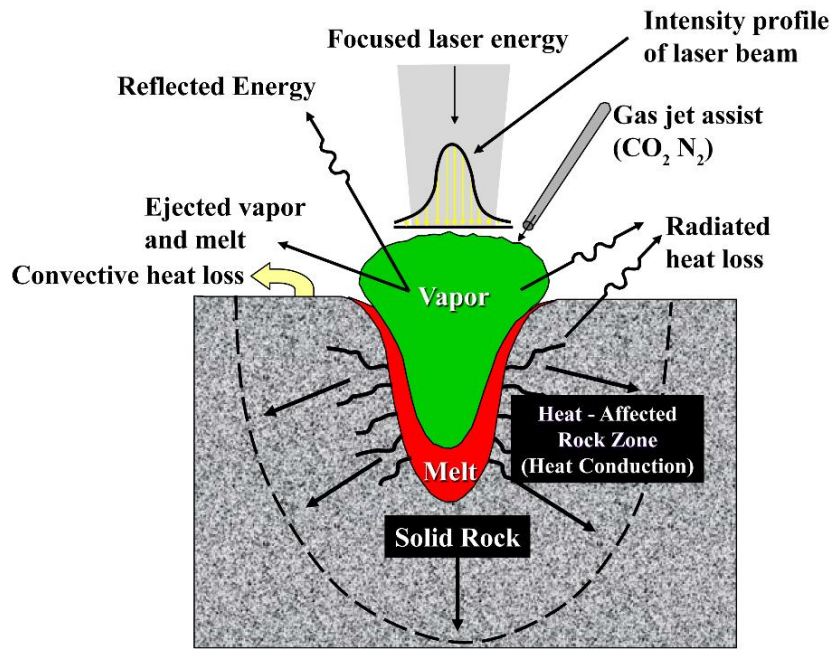


Fig. 2.13 Interaction between laser and rock (after Maurer (1980)).

In the laser-rock interaction, both laser parameters and rock parameters play a critical role (Graves and Bailo, 2005). Laser parameters include power level, wavelength, beam diameter, mode of delivery (continuous wave or repetitive pulses), radiation time (traverse speed). Rock parameters include thermal conductivity, specific heat, porosity, dielectric properties and mechanical strength, etc.

(1) Continuous wave lasers

The effect of laser treatment on the reduction in the mechanical strength of rocks was first explored by Williamson et al. (1968) and Moavenzadeh et al. (1968) at the Massachusetts Institute of Technology. They used a laser to heat rectangular rock specimens, notched or unnotched, at different power levels and durations and then did three point bending to get the modulus of rupture. Williamson et al. (1968)'s results, shown in Figure 2.14, indicate that the modulus of rupture of the Barre Granite (2.5 cm by 2.5 cm by 15 cm) could be reduced by up to 90 %. They also found that the threshold energy input must be exceeded for an improvement in cutting efficiency. Rad and McGarry (1970) used a 750 W CO₂-N₂-He laser to treat the same rock and then excavated the lased rock with a drag bit. They found that laser irradiation could facilitate the excavation and decrease the specific energy. Carstens and Brown (1971) used a 5 kW CO₂ gas laser to treat 7 rock types and one concrete using two different focusing mirrors. They found that the laser is capable of effectively cutting kerfs on and penetrating into all the rocks and concrete except granite where a viscous glassy melt forms. Also as the traverse speed increases, the kerf depth decreases. The gas jet could greatly assist in kerfing and penetrating. Lauriello and Chen (1973) used the same laser setup to irradiate the Barre Granite and found the unfocused laser to be effective in fracturing the granite. It is noteworthy that the laser systems abovementioned are of low

power levels and unfocused. This could to some extent reduce the energy unnecessarily listed in melting and vaporising rocks.

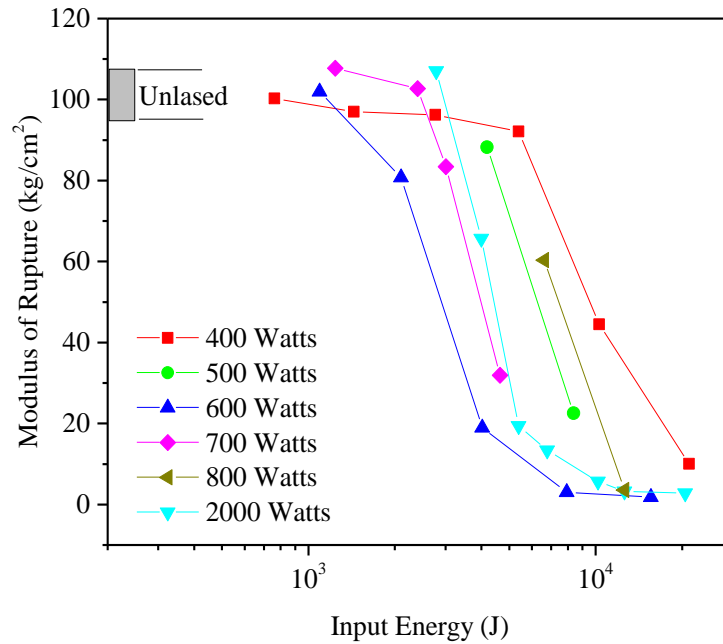


Fig. 2.14 Strength reduction of granite specimens subjected to laser irradiation (reproduced from Williamson et al. (1968)).

To examine the feasibility of laser gage kerfing on TBMs in hard rocks, Jurewicz (1976) used a multi-kW CO₂ laser to cut three rock types: granite, diabase and quartzite. Five traverse velocities (ranging from 25 cm/second to 125 cm/second) and four laser powers (from 5 kW to over 15 kW) were used. Special considerations were paid to factors such as assisting gas pressure, focusing degree of laser and distortion of the focusing mirror of the laser. Figure 2.15 shows the cross-sections of the laser cut kerfs in the three rocks. The kerf depth in granite and diabase are shallower than the theoretical values indicating a large proportion of energy lost in vaporising.

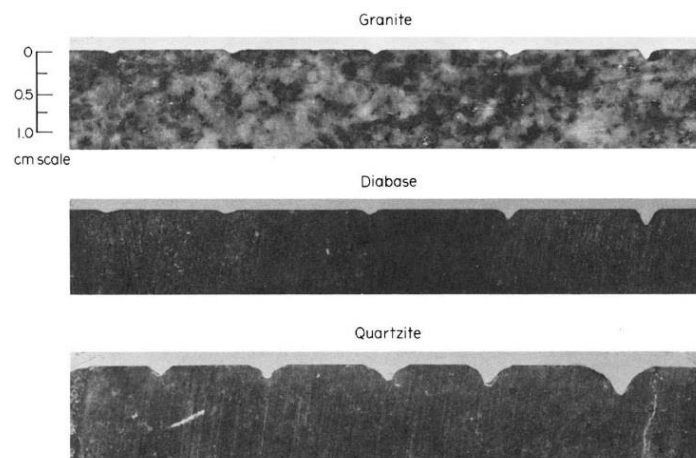


Fig. 2.15 Cross section of laser cut rocks. Laser power equal to 16.5 kW. Kerfing speed from left to right: 125, 100, 75, 50, 25 cm/mm (Jurewicz, 1976).

Jurewicz (1976) then further simulated the laser gage kerfing and mechanically loaded sample with 1 cm deep laser kerfs at a distance of 3 cm (Figure 2.16). He found that concept of tunnel gage kerfing to be both technically and economically feasible in the three rock types.

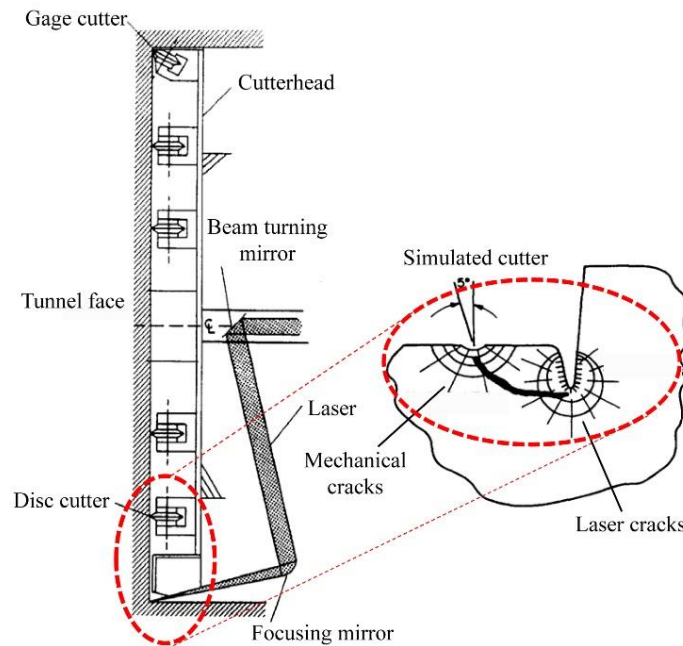


Fig. 2.16 Laser gage kerfing concept applied to tunnelling (modified from Jurewicz (1976)).

Since the late 1990s and early 2000s, there has been a new round of research on laser drilling in petroleum engineering, led by Prof. Graves at Colorado School of Mines (Graves et al., 2002; Graves and Bailo, 2004, 2005; O'Brien et al., 1999). The research demonstrated the feasibility of laser/rock destruction using three U.S. military lasers (MIRCAL, COIL, and CO₂) and two Russian lasers (CO and CO₂). Tests were conducted on 11 different rock types under varying conditions of sample size and shape, saturation, stress, purge gas, lasing time, pulsing etc (Graves et al., 2002). The specific energy of the Berea Sandstone using different laser types are shown in Table 2.6.

(2) Pulsed lasers

Researchers have investigated how high power, pulsed laser beams interacted with matter, and in particular metals, since the 1970s. Montross et al. (1999) reported the use of Q-switched pulsed lasers in weakening basalt by shock waves. The shock waves are induced by laser pulses from a Q-switched near-infrared laser of wavelength 1064 nm and a pulse length of 20 ns. The energies used were 10, 50, and 100 J, all delivered at the rock's surface at an energy density of 300 J/cm² and a power density of 10 GW/cm². The laser system used consisted of two 50 J systems where the beams were overlapped to generate the 100 J energies. They measured the Vickers microhardness and the depth of damage and found that the pulsed laser is able to reduce the hardness by 50 % and that the weakening effect could be enhanced by shock wave interactions. The specific energy of laser cutting they calculated is 294 J/cm³, which is significant less than the values when using continuous wave lasers (See Table 2.6).

The specific energy of pulsed laser cutting is about 10 times that of mechanical cutting. When combined the two methods, the energy consumption is reasonably acceptable. This could have possibly pointed out the research directions of using laser for hard rock breakage.

Table 2.6 Comparison of specific energy of Berea Sandstone using four laser types (Graves et al., 2002).

Laser	Power (kW)	Power density (kW/cm ²)	Specific Energy (kJ/cm ³)
CO ₂ *	10.0	26.0	37.4
CO ₂ *	5.0	13.0	50.4
CO ₂ **	N/A	~1000	34.1
CO	N/A	~1000	22.8
COIL	6.3	123.6	31.8
COIL	5.3	139.6	26.5
COIL	2.8	35.2	6.8
COIL	1.5	16.4	7.2
Nd:YAG	1.2	1.7	31.0
Nd:YAG	1.2	0.9	16.2
Nd:YAG	0.5	0.3	17.5
Nd:YAG	0.5	0.4	22.2

Note: *Wright-Patterson Air Force Base, Ohio, USA;

** Lebedev Radiophysics Institute, Moscow, Russia

(3) TBM applications

The earliest comprehensive research on thermally assisted TBM tunnelling dates back to 1970 when the United Aircraft Corporation started a project entitled “Heat-assisted tunnel boring machines” in an effort to make TBMs more capable of economic operations in relatively hard rock types (Carstens et al., 1970). They used a CO₂-N₂-He continuous laser with an output power of 1 kW to treat the Barre Granite. The traverse velocity varied from 0.25-12.7 cm/s. The interval between the laser swath and disc cutter varied from 0 to 1 inch (Figure 2.17(a)). They conducted the linear cutting tests on the laser treated rock block (single radiation and multiple radiation) using different thrust. Radiant heaters have insufficient power density to effectively heat the rock, and high-temperature jets create serious environmental problems. However, the test program indicated that a more effective way to assist mechanical cutters would be to use concentrated thermal energy to melt shallow slots in the rock between cutter paths (Figure 2.17(b)). Their research concluded that heated assisted TBM tunnelling at that time was technically feasible but economically unattractive.

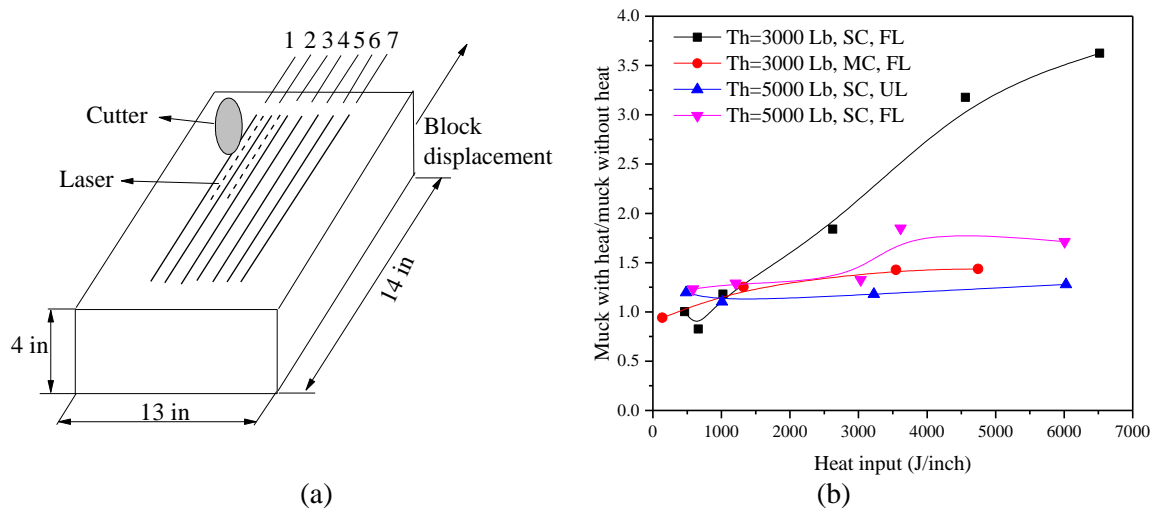


Fig. 2.17 Laser assisted linear cutting tests: (a) Cutting pattern; (b) Normalised muck volume under different conditions (Carstens et al., 1970).

Carstens et al. (1970) also designed the prototype of a laser assisted TBM through a detailed technical investigation (Figure 2.18). On the cutterhead, there are spike areas for the installation of laser irradiators, which will be able to cut kerfs in between disc cutters.

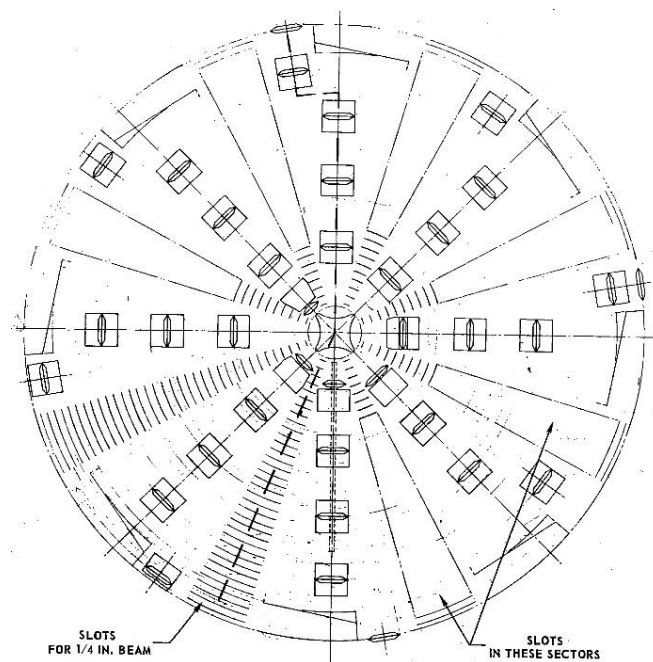


Fig. 2.18 A conceptual design of a laser assisted hard rock TBM (Carstens et al., 1970).

(3) Problem to be solved

The lasers used in the early research had very low power, are difficult to focus, incapable of transmitting power over large distances, non-portable and largely unsafe. However, with the advent of new developing technology in the field of lasers most of the abovementioned problems are put to rest (Pooniwala, 2006). For lasers to be successfully applied, the following problems need to be properly addressed.

(a) High energy consumption and low energy efficiency

Unlike waterjet, which can be directed at the rock-cutter interface, the only technical possibility of using lasers is to cut kerfs to augment mechanical rock cutting (Pierce et al., 1996). Laser kerfing involving the melting and vaporising of rocks is extremely energy intensive. Continuous wave lasing could be prohibitively expensive to use. Also in the process of laser generation, the energy conversion efficiency is as low as 50 %. Efforts should be made to reduce the energy consumption to an acceptable level. One possible way is to reduce the volumes of rocks being melted or vaporised and to induce more spalling failures. Another solution might be to use pulsed laser systems, which is able to generate power levels of gigawatts for a couple of nanoseconds using a limited amount of energy. The pulsed laser technologies have been used in material engineering but are still relatively new in rock mechanics.

(b) Heat problem

Temperature as high as 3000 °C can be generated when using lasers. The heat problem can be alleviated to a certain degree by using gas jetting to cool the lava and by enhancing the ventilation in the excavation chamber. However, the impact of high temperature debris on the cutters, cutterheads and conveyor belts still needs to be systematically assessed.

2.4.3 Microwave and infrared irradiation

Microwave is the collective name of the EM waves with a frequency ranging from 300 MHz to 300 GHz and a corresponding wavelength from 1 m to 1 mm. Millimetre waves cover the frequency spectrum from 30 GHz to 300 GHz and have a wavelength between 10 mm to 1 mm. The infrared radiation occupies the frequency range from 300 GHz to 400 THz (1 mm - 750 nm). In this thesis, infrared radiation is also referred to as microwave for simplicity. EM waves are self-propagating waves characterised by electric (E) and magnetic (H) field components oscillating in phase and perpendicular with each other and also perpendicular to the direction of propagation (Metaxas and Meredith, 1983). In the literature, both microwave and infrared have been used to treat hard rocks. The frequencies set aside for microwave processing of materials are 915 MHz, 2.45 GHz and 5.8 GHz, of which the middle one is the most widely used. Normally, an industrial microwave heating system consists of a high volt power supply, a microwave generator, a circulator to protect the generator, a tuner to match the impedances of the generator and the load, an applicator to hold the sample, water load(s), and other measurement and protection devices. Infrared radiation has almost the same components. The only difference is the frequency of the EM waves generated. Unlike lasers and electron beams, microwave has a larger wavelength and penetration depth thus can bulk heating, rather than surface heating, materials.

Essentially, EM waves heat via dielectric heating which originates from either the ability of the electric field to polarise charges in the material and the inability of this polarisation to follow extremely rapid reversals of the electric field or through direct conduction effects (Metaxas and Meredith, 1983). The

polarisation mechanisms can be divided into ionic, dipolar, atomic and electronic polarisation at different scales, of which the atomic and electronic polarisations play the dominant role in heating dry and polycrystalline rocks (von Hippel, 1954).

Due to the huge difference in dielectric properties of rock minerals, they will be heated at different rates when subjected to microwave irradiation. Figure 2.19 illustrates how the intergranular and transgranular cracks are generated in the rock matrix. The weakening of rocks by microwave will primarily depend on thermal and dielectric properties of minerals (determined by the mineralogical compositions), grain size, mineral dissemination. The best scenario would be that there are 20 % of microwave absorbing minerals enclosed in microwave transparent minerals.

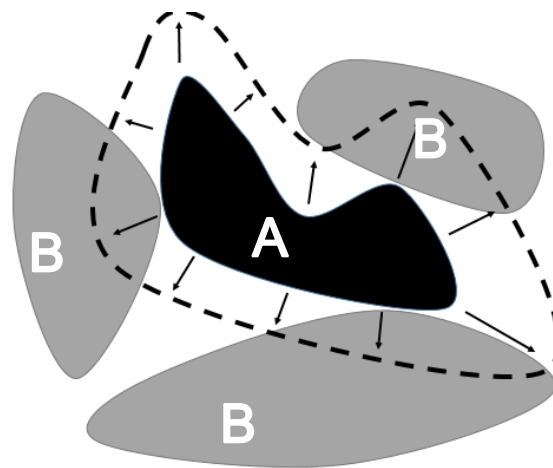


Fig. 2.19 Principles of microwave weakening of rocks.

Figure 2.20 shows the microwave treatment of the Australian Harcourt Granite (38 mm diameter in 80 mm in length) in a WR340 waveguide. The sample shattered into halves after 5 seconds of treatment at a power of 5 kW. Observations of the cross section indicate that the biotite is selectively heated and melted.

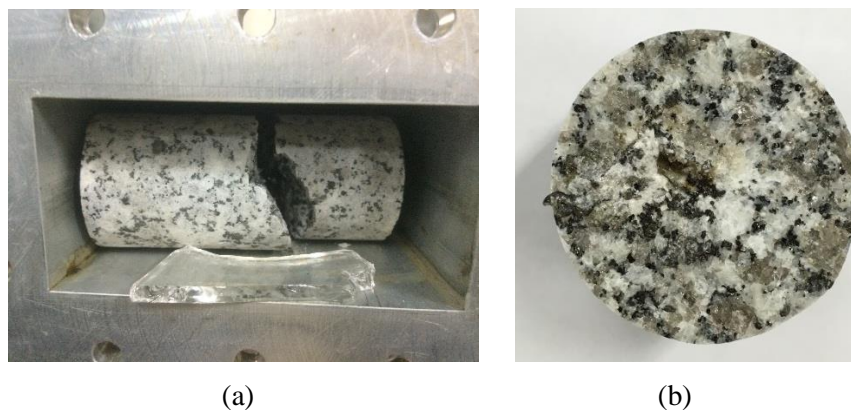


Fig. 2.20 Cracking of a 38 mm diameter Harcourt granite in the microwave waveguide after 5 seconds heating at 5kW. (a) Thermal shattering in the waveguide, (b) cross-section of the crack surface.

(1) TBM applications

Dozens of field experiments on using high frequency EM waves individually (electro-thermal breaking) or as assistance to mechanical tools (electro-thermo-mechanical) to break hard rock and frozen soil were conducted in the former Soviet Union. A brief review of pioneering works in Russian can be found in [Hoekstra \(1976\)](#). The idea stemmed from the need in excavating frozen soil in a faster and less energy intensive way ([Misnik and Nekrasov, 1969](#); [Misnik and Nekrasov, 1973](#)). [Gushchin et al. \(1973\)](#) designed two eletrothermal (ET) drifting machines, one of rectangular shape, the other circular shape ([Figure 2.21](#)), and used them to build tunnels and shafts in an apatite mine. As shown in [Figure 2.22](#), they found that as compressive strength of rocks increases the advance rates using the ET machine increases and the energy consumption decreases. When the rock strength exceeds 150 MPa, the power requirement of an ET machine is comparable to that of a mechanical machine. To make the most use of the two methods, [Gushchin et al. \(1979\)](#) developed an electro-thermo-mechanical (ETM) machine ([Figure 2.23\(a\)](#)) and obtained the advance rates in three different modes, namely mechanical, ET and ETM. The results showed that in the combined mode (ETM mode), the advance rates increased from 0.2 m/h in the mechanical mode and 0.15 m/h in the ET mode to 0.7-0.8 m/h at a reduced energy consumption. [Protasov et al. \(1984\)](#) developed another ETM machine with an EM power of 380 kW ([Figure 2.23\(b\)](#)). They found that under the ETM mode, the advance rates could be increased by 2.5 fold, cutter wear reduced by 2.5 fold. Please note that point attack picks and roller cutters rather than disc cutters were used on the two machines. More technical details can be found in [Table 2.7](#).

(2) Laboratory studies

Researches were also undertaken using open-ended microwave to break rock blocks. [Koiwa et al. \(1975\)](#) used a 30 kW microwave system to treat granite (80cm cubes) at 27 kW for 12 mins and at 19 kW for 30 mins and found spalling craters and that cracks as deep as 20cm can be observed. [Takahashi et al. \(1979\)](#) used a 200 kW microwave and an open-ended antenna to treat 1 meter sized granite and andesite cubes at a power of 34-60 kW for up to 34 mins and measured the UCS and ultrasonic wave velocities of the cored specimens at different locations. They found that the cracks are in the radial pattern and that the both UCS and wave velocity reduced significantly after microwave treatment. [Lindroth et al. \(1993\)](#) studied the change of the drilling rates of basalt and granodiorite after microwave treatment using a 15.6 kW magnetron and open-ended antenna and found the drillings rates can be doubled and tripled.

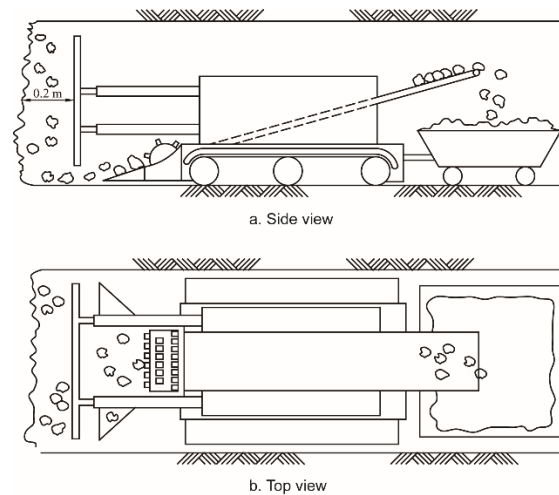


Fig. 2.21 The eletromagnetic machine used in a USSR hard rock mine (Hoekstra, 1976).

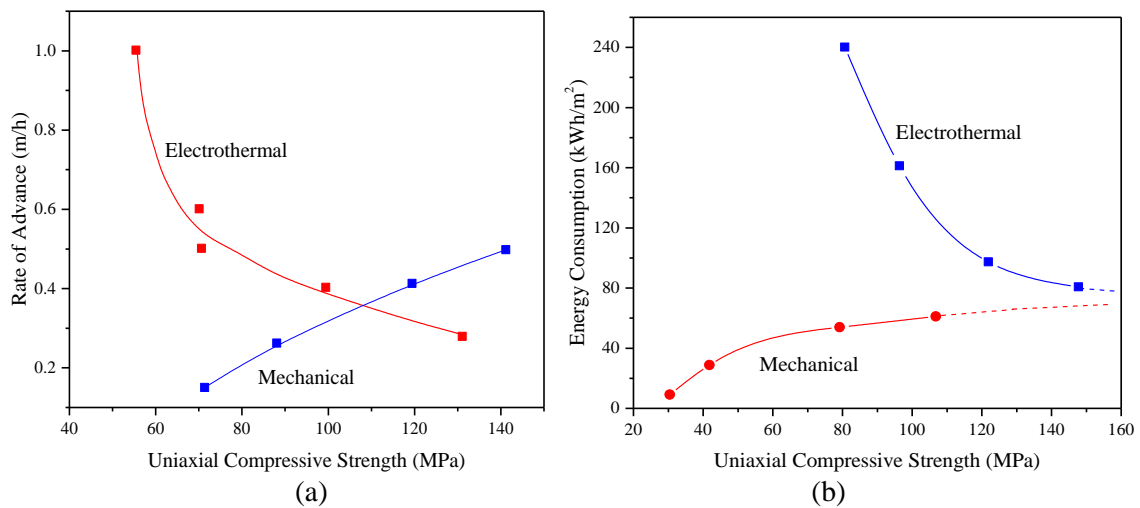


Fig. 2.22 Performance comparison between an electrothermal excavator and a mechanical excavator. (a) Advance rates vs rock strength; (b) Energy consumption vs rock strength (Gushchin et al., 1973).

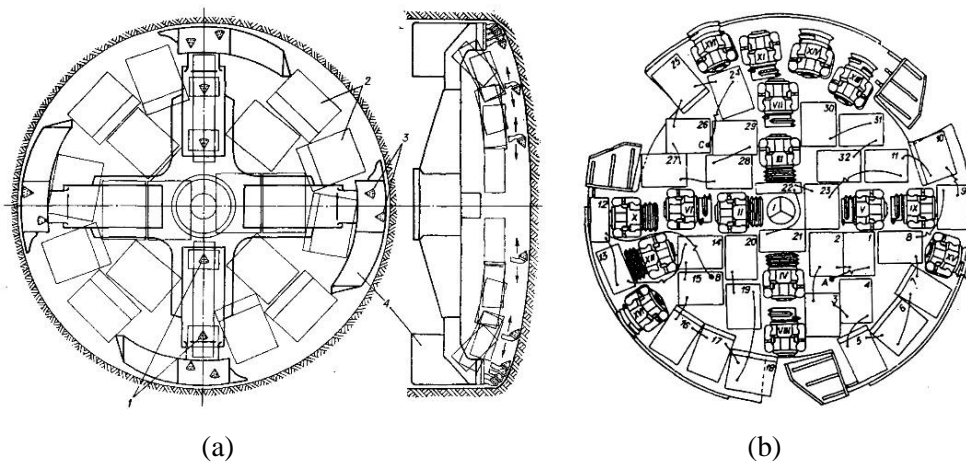


Fig. 2.23 Two designs of TBMs assisted with infrared generators in the Soviet Union. (a) The 450 kW PK-8ETM tunnelling machine (Gushchin et al., 1979); (b) The 380 kW Yasinovatets-2ETM tunnelling machine (Protasov et al., 1984).

Table 2.7 Field experiments using electrothermal and electrothermomechanical rock destruction.

Rock types	Rock properties	Applicator types	Power level (kW)	Exposure time	Findings	E_0 (kJ/cm ²)	Reference
Apatite, nepheline, urtite, etc	P-hardness 8-10 σ_t 4-9MPa E 40-90GPa	Rectangular antenna (5-7 m ²)	136	N/A	Rock breakage began at a distance of 0.8-1 m. Advance rate is 0.3 m/h using solely EM energy.	N/A	Gushchin et al. (1973)
	P-hardness 10-12 σ_t 4-9MPa E 40-90GPa	Rotating circular cutter head (5 m ²) with rectangular antenna	200	10-15 min	Working distance is 0.2-0.3 m. Fracture begins after 30-60 sec radiation. Broken rocks 7 × 5 × 1 cm in size. Advance rate 0.3-0.35 m/h. M mode: AR 0.2 m/h, E 290 kWh/m ³	1.2-1.8	
Apatite with calcite and natrilite	P-hardness 8-14	circular cutter head (10 m ²) with 16 rectangular antenna (45 cm × 60cm)	450	3-5 min	ET mode: AR 0.15 m/h, E 160kWh/m ³ TEM mode: AR 0.7-0.8 m/h, E 60-75 kWh/m ³	1.08-1.35	Gushchin et al. (1979)
Apatite	σ_t - 16-24 mN/cm ²	circular cutter head (10 m ²) with 32 rectangular antenna (45 cm × 60 cm)	380	N/A	M mode: AR 2.8 m/h TEM mode: 7 m/h Cutter wear reduced by 2.5 fold	N/A	Protasov et al. (1984)
Sandstone	Water content 0.1-2 %	3.5 mm wave	50	Pulsed radiation (30 ms)	Explosive fracture occurred	N/A	Krasnovskij and Uvarov (1991)

Note: E_0 is computed by total power level times exposure time divided by the cutterhead area.

In the literature most researchers used multi-mode industrial or domestic microwave ovens to treat rocks. [Znamenácková et al. \(2003\)](#) used a 3 kW domestic microwave oven to heat andesite. [Satish \(2005\)](#) used a 750W multi-mode microwave to treat basalt and found that the point load strength reduced as exposure time increases. [Sikong and Bunsin \(2009\)](#) used a 1 kW microwave to treat a granite for up to 30 mins and found that the compressive strength can be reduced by up to 40 %. [Peinsitt et al. \(2010\)](#) studied the heating rates, UCS and ultrasonic wave velocity of dried and saturated granite and basalt treated by a 3 kW multi-mode microwave. [Nejati \(2014\)](#) used a 6 kW industrial microwave oven to heat basalt specimens and found that the fracture toughness decreased linearly with respect to microwave power energy. [Nekoovaght \(2015\)](#) used a one commercial oven (up to 3 kW) and one industrial microwave oven (up to 15 kW) to treat basalt and norite cylinders and measured changes in UCS, BTS and Cerchar abrasivity index. In terms of microwave direct drilling, [Jerby et al. \(2002\); \(2017\)](#), [Oglesby et al. \(2014\)](#) and [Woskov \(2017\)](#) have attempted to use coaxial cables as a drilling tool in granite and basalt and found the technique to be technically feasible. A brief summary of the laboratory tests on the microwave treatment of rocks is presented in [Table 2.8](#).

(4) Research directions

(a) Laboratory studies vs field applications

The results from the field tests in the former Soviet Union are encouraging. However, the tests were conducted in an apatite mine (probably with high EM waves absorbing capacities) and the geological conditions are not described in a detailed manner. There have been no field tests of microwave/infrared assisted tunnelling in non-ore hard rock masses. Most of the lab studies used multi-mode cavity in which the samples are placed right in the centre. The results from this type of setups could not be extended to the field where only one face could be irradiated. It is essential to conduct more tests that involve surface microwave irradiation followed by linear cutting tests on different rock types.

(b) Rock weakening mechanisms

The response of rocks to microwave irradiation varies significantly. They are weakened in different manners: melting, cracking and spalling. For rocks composed of well-disseminated fine grains with close dielectric properties, they are most likely to be melted, as there will be little stress build-up for spalling to happen. For heterogeneous rocks like granite, they would spall under microwave irradiation. It is desired that rocks fail in the spalling mode as it is the most energy efficient. It is imperative to study the extent to which commonly found hard rocks could be weakened under microwave treatment. The finding will help to determine the applicability of microwave in assisting rock breakage and to select the right equipment if it is applicable. Works also include the measurement of the dielectric properties of the low loss minerals at the microwave frequency and at elevated temperatures to better understand the physical and mechanical behaviours of rocks.

Table 2.8 Review of microwave treatment of hard rocks in the laboratory (modified after [Zheng et al. \(2017\)](#)).

Microwave applicator	Power (kW) ^a	Heating time (s) ^b	Rock types	Specimen geometry	Temperature measurement	Parameters studied	Findings	References
Open ended waveguide	15.6	780	basalt, granodiorite	slab	Thermocouple	DR of tungsten drill bits	DRs can be doubled and tripled in the two rocks respectively.	Lindroth et al. (1993)
	24	30	granite	block	N/A	Linear cutting forces	Cutting forces can be reduced by 10 %.	Hartlieb and Grafe (2017)
Open ended coaxial antenna	1	120	glass, alumina, concrete	slab	N/A	Drill-ability	Temperature can up to 2000 °C, able to melt materials.	Jerby et al. (2002)
	10	180	granite, basalt, limestone	slab	N/A	Rock melt-ability	Temperature up to 2000 - 4000 °C, able to melting and vaporizing rocks.	Woskov et al. (2014)
Open ended horn antenna and multimode cavity	3	120	Basalt, granite, norite	cylinder	IR gun	UCS, BTS	Higher power levels at shorter duration yield better results.	Hassani et al. (2016)
	0.75	240	basalt	cylinder	IR camera	I _{s50}	I _{s50} can be reduced by up to 33 %.	Satish (2005)
Multimode cavity	3	300	basalt, granite, sandstone	cylinder	IR camera	UCS, V _p	V _p reduces as heating time increases whereas UCS fluctuated.	Peinsitt et al. (2008)
	3	240	basalt	cylinder	IR gun	UCS, CAI	CAI and UCS decrease by 30 %. BTS can be reduced by up to 80 %.	Nekoovaght (2009)
	4	30	basalt	disc	IR gun	K _{IC}	K _{IC} decreases linearly with energy output.	Nejati (2014)

Note: ^a- up to the power listed; ^b- up to the time listed; DR-drilling rate; I_{s50}- Point load index; V_p- P-wave velocity; BTS-Brazilian tensile strength; CAI-CERCHAR Abrasivity Index; K_{IC} -Fracture toughness.

(c) Energy consumption

The specific energy from the previous research are still high when compared to mechanical excavation. It is known that heating rocks at high power levels for shorter durations provides a thermal shock and has a lower energy requirement. More tests using microwave pulses at high power levels should be conducted.

2.5 Technical and economical comparison

As TBM performance has stagnated in extremely hard rocks, the interests in developing assisting rock breakage methods have been revitalised. However, there have been dissenting and contradictory views towards their use in assisting hard rock breakage as people's conclusions are made on works conducted three decades ago when those technologies are in their infancy of development. Below efforts are made to compare those methods from both technical and economic points of view.

(1) Technical comparison

Waterjet, laser and microwave are all technically viable for kerfing purposes. Microwave (infrared) can also be used to spall some rock types. The advantage of laser and high pressure waterjet over microwave is that they can keep the energy intensity over the short distance of transmission. Microwave, which has a longer wavelength, is more sensitive to the standoff distance. For microwave to be used, there must be an automatic tuning mechanism to match the EM impedance. Attention should be paid to the reflection of microwave energy. The disadvantage of waterjet and laser is that they are much more energy intensive in kerfing. The technical challenges have been discussed in the previous sections. It is believed that there are no technical barriers in using those technologies on TBMs. The main considerations would be the economy.

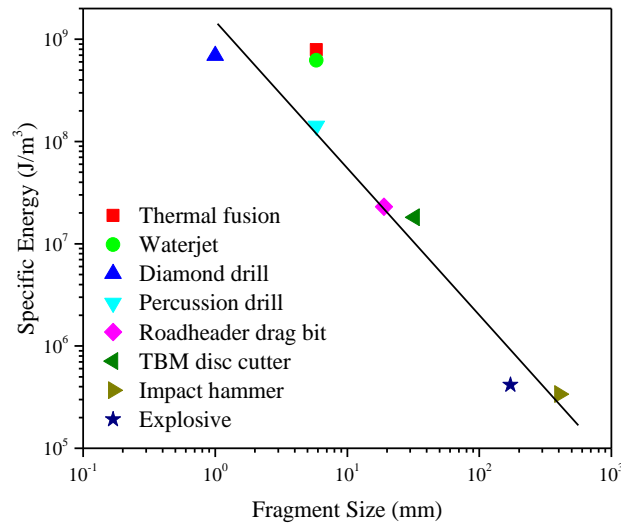
(2) Economic comparison

This chapter does not aim to compare the initial capital costs of the equipment used in those methods. Readers interested in equipment cost are referred to [Pierce et al. \(1996\)](#). In this chapter, only energy consumptions will be compared from the viewpoint of specific energy. Depending on the purpose of kerfing, two types of specific energy can be defined ([Maurer, 1980](#)). The specific energy (SE) is defined as the energy consumption divided by the volume of rock excavated. In the definition, the novel methods are regarded as excavation tools. Normally, there can be several orders of magnitude difference in it. The specific kerfing energy (SKE) is defined as the energy consumption divided by the kerf area. In this definition, the kerf width is not taken into account. Those methods are taken as assisting methods to generate new surfaces for easy mechanical rock breakage. The definitions are shown below.

$$SE = \frac{\text{Energy consumption}}{\text{volume excavated}} = \frac{\text{Energy consumption}}{\text{Kerf depth} \times \text{Kerf width} \times \text{Traverse speed}}$$

$$SKE = \frac{\text{Energy consumption}}{\text{Kerf area}} = \frac{\text{Energy consumption}}{\text{Kerf depth} \times \text{Traverse speed}}$$

The specific energy of different rock breakage methods is compared by [Cook and Joughin \(1979\)](#) and [Bieniawski et al. \(2012\)](#). [Figure 2.24](#) shows the correlation between the specific energy of various excavation methods and the size of rock fragments. Tests are conducted on quartzitic rock masses with a UCS of over 200 MPa. It is clear that laser and waterjet are the most energy intensive methods in rock breakage. They are 50-100 times higher than that of the TBM disc cutters.



[Fig. 2.24](#) Specific energy of different excavation methods ([Bieniawski et al., 2012](#)).

Test data of those methods on hard rock kerfing are also collected from the literature and are shown in [Table 2.9](#). It is not hard to observe the same conclusion. Plasma fracturing is the most energy intensive rock breaking methods, then the electron beam and waterjet. However, the specific energy is greatly influenced by the operating parameters. As shown by the results from [Mellor \(1972\)](#) and [Carstens et al. \(1970\)](#), the SE can vary by a factor of 4, even the same kerfing system is used.

It is obvious that except infrared (microwave) none of the novel methods could be used alone to break hard rocks. They must be used accompanied by mechanical excavators to amortise the high energy consumption. Unfortunately, there are very few data available in the literature to compare the SE of combined assisting methods and mechanical excavators. More linear cutting tests on rock blocks kerfed by novel/mechanical methods need to be conducted for a more comprehensive comparison.

Table 2.9 Comparison of SE in the Barre Granite using different methods (modified after [Graves et al. \(2002\)](#)).

Method	Traverse speed (cm/s)		Kerf depth (cm)		Kerf width (cm)		Power (kW)		SE (kJ/cm ³)		SKE (kJ/cm ³)		Reference
	Case 1	Case 2	Case 1	Case 2	Case 1	Case 2	Case 1	Case 2	Case 1	Case 2	Case 1	Case 2	
Electron beam	25.40	25.40	0.25	0.13	0.25	2.54	25	25	2.98	15.7	3.94	7.57	Carstens et al. (1970)
High pressure waterjet	5.94	0.64	0.2	0.46	0.03	0.03	4.4	4.3	110.3	454.6	3.64	15.0	Mellor (1972)
	17.0	2.12	0.55	0.98	0.11	0.12	23.3	23.3	22.7	93.5	2.49	11.2	Chadwick (1973)
	6.35	6.35	0.26	0.81	0.27	0.12	7.3	10.4	16.3	37.7	44.1	4.53	
	6.35	6.35	0.16	0.38	0.24	0.23	3.2	2.5	13.2	18.7	3.18	4.31	
Laser (CO ₂)	4.06	0.93	0.41	0.89			4.0	4.0			2.4	4.82	Carstens and Brown (1971)
Plasma	0.09	0.23	7.62	7.62			90	318			133	182	Poole and Thorpe (1973)
	0.11	0.13	28.6	15.2	1.9	1.9	270	182	46.9	49.63	89.1	94.3	
Infrared* (microwave)									0.58				Gushchin et al. (1979)
TBM**									0.04-				Rostami (2011)
									0.06				

Note: *Infrared rock breakage is conducted in an apatite mine in Russia. **Hard rocks (UCS > 200 MPa), not necessarily the Barre Granite.

2.6 Concluding remarks

This chapter presents an extensive review of the development of TBM technologies and the possible methods to assist TBMs in cutting hard and abrasive rocks. The following conclusions can be drawn from this chapter.

- Although modern TBMs have undergone tremendous technological innovations than their predecessors in terms of loading capacities and versatilities, they still have problems in digging through extremely hard and abrasive rocks. Assisting technologies must be developed to make it possible to dig through such rocks efficiently. The assistance of other methods can also profoundly reduce the construction time of long tunnels in hard to extremely hard rock masses.
- High pressure waterjet is successfully used in the field to assist TBM rock breakage. However, the energy consumption is deemed to be very high, which prevents it from commercialisation. This also applies to laser cutting, which can only be used to kerf between adjacent cutters. The future research should focus on the overall energy consumption of the rock breakage using an assisting method and the mechanical excavator. The overall energy consumption may fall into acceptable ranges. Research should also be conducted in developing pulsed technologies to reduce the energy consumption.
- Microwave and infrared irradiation was demonstrated in the Former Soviet Union to be cost effective. Therefore, more research should be conducted to study the weakening of rocks using industrial microwave systems. Another advantage of microwave rock tests is that the system is simple and that the test is relatively easy to conduct.

Reference

- Baumann, L., Henneke, J., 1980. Attempt of technical-economical optimization of high pressure jet assistance for tunneling machines, Fifth International Symposium on Jet Cutting Technology, Hanover, Germany, pp. 119-140.
- Bieniawski, R.Z.T., Celada, B., Tardaguila, I., Rodrigues, A., 2012. Specific energy of excavation in detecting tunnelling conditions ahead of TBMs. *Tunnels & Tunnelling International* February, 65-68.
- Bilgin, N., Copur, H., Balci, C., 2013. Mechanical excavation in mining and civil industries. Taylor & Francis.
- Bilgin, N., Copur, H., Balci, C., Tumac, D., 2017. TBM performance prediction using laboratory cutting tests in very hard and abrasive rock formations, TBM in Difficult Grounds, Wuhan, China.
- Carstens, J.P., Brown, C.O., 1971. Rock cutting by laser, Fall Meeting of the Society of Petroleum Engineers of AIME. Society of Petroleum Engineers, New Orleans, Louisiana, USA, p. 10.
- Carstens, J.P., Davison, W.R., BROWN, C.A., McGarry, F.J., Smith, A.R., 1970. Heat-assisted tunnel boring machines. United Aircraft Corporation Research Laboratories, p. 335.
- Chabay, R.W., Sherwood, B.A., 2015. Matter and interactions. Wiley.
- Chadwick, R.F., 1973. Continuous high-velocity jet excavation - Phase II. Bendix Research Lab.
- Chadwick, R.F., Kurko, M.C., 1972. Continuous high-velocity jet excavation - Phase I. Bendix Research Lab.
- Ciccu, R., Grosso, B., 2010. Improvement of the excavation performance of PCD drag tools by water jet assistance. *Rock Mech Rock Eng* 43, 465-474.
- Ciccu, R., Grosso, B., 2014. Improvement of disc cutter performance by water jet assistance. *Rock Mech Rock Eng* 47, 733-744.
- Cook, N.G.W., Joughin, N.C., 1979. Rock fragmentation by mechanical, chemical and thermal methods, The 6th International Mining Conference, Madrid, Spain, pp. 223-228.
- Deering, K., Dollinger, G.L., Krauter, D., Roby, J.A., 1991. Development and performance of large diameter cutters for use on high performance TBM's, 1991 Rapid Excavations and Tunnelling Conference, Seattle.
- Dehkhoda, S., 2011. Experimental and numerical study of rock breakage by pulsed water jets. University of Queensland, Brisbane.

- Dehkhoda, S., Fairhurst, C., 2017. Rapid excavation and tunneling techniques. *Hydraulic Fracturing Journal* 4, 101-108.
- Dubungnon, O., 1981. An experimental study of water jet assisted drag bit cutting of rocks, First US Water Jet Conference, Golden, Colorado, USA, pp. II-4.1-4.11.
- Fenn, O., Protheroe, B., Joughin, N.C., 1985. Enhancement of roller cutting by means of water jets, in: Mann, C.D., Kelley, M.N. (Eds.), 1985 Rapid Excavation and Tunnelling Conference. AIME, New York, USA, pp. 341-356.
- Graves, R.M., Araya, A., Gahan, B.C., Parker, R.A., 2002. Comparison of specific energy between drilling with high power lasers and other drilling methods, SPE Annual Technical Conference. Society of Petroleum Engineers, San Antonio, Texas, U.S., pp. 1-7.
- Graves, R.M., Bailo, E.T., 2004. Porosity and permeability changes in lased rocks calculated using fractal fragmentation theory, Canadian International Petroleum Conference. Petroleum Society of Canada, Calgary, Alberta, Canada.
- Graves, R.M., Bailo, E.T., 2005. Analysis of thermally altered rock properties using high-power laser technology, Canadian International Petroleum Conference. Petroleum Society of Canada, Calgary, Alberta, Canada.
- Gushchin, V.V., Kuznetsov, V.V., Chernikov, V.A., Merzon, A.G., Protasov, Y.I., Vartanov, G.A., 1979. Driving horizontal workings by means of an entry drifting machine with electrothermomechanical cutting. *Soviet Mining* 15, 133-137.
- Gushchin, V.V., Rzhetskii, V.V., Kuznetsov, V.V., Protasov, Y.I., Yurchenko, N.N., 1973. Driving of workings by a cutter-loader with electrothermal rock breaking. *Soviet Mining* 9, 618-622.
- Hamelin, M., Kitzinger, F., Pronko, S., Schofield, G., 1993. Hard rock fragmentation with pulsed power, Ninth IEEE International Pulsed Power Conference, Albuquerque, NM, USA.
- Hartlieb, P., Grafe, B., 2017. Experimental study on microwave assisted hard rock cutting of granite. *BHM Berg- und Hüttenmännische Monatshefte*, 1-5.
- Hassani, F., Nekoovaght, P.M., Gharib, N., 2016. The influence of microwave irradiation on rocks for microwave-assisted underground excavation. *Journal of Rock Mechanics and Geotechnical Engineering* 8, 1-15.
- Henneke, J., Baumann, L., 1978. Jet assisted tunnel boring in coal measure strata, 4th International Symposium on Jet Cutting Technology, Canterbury, UK, pp. J1-1-12.
- Hoekstra, P., 1976. Rock, frozen soil and ice breakage by high-frequency electromagnetic radiation: A review. Department of Defense, Department of the Army, Corps of Engineers, Cold Regions Research and Engineering Laboratory, p. 17.
- Hood, M., 1985. Waterjet-assisted rock cutting systems - the present state of the art. *International Journal of Mining Engineering* 3, 91-111.
- Hood, M., 1993. The use of water jets for rock excavation, in: Hudson, J.A. (Ed.), *Comprehensive rock engineering: principles, practice and projects*, pp. 229-260.
- Hood, M., Knight, G.C., Thimons, E.D., 1992. A Review of Jet Assisted Rock Cutting. *Journal of Engineering for Industry* 114, 196-206.
- Hustrulid, W., 1976. A technical and economic evaluation of water jet assisted tunnel boring. University of Utah, p. 152.
- Jerby, E., Dikhtyar, V., Aktushev, O., Groszlick, U., 2002. The microwave drill. *Science* 298, 587-589.
- Jerby, E., Nerovny, Y., Meir, Y., Korin, O., Peleg, R., Shamir, Y., 2017. A silent microwave drill for deep holes in concrete. *IEEE Transactions on Microwave Theory and Techniques* PP, 1-8.
- Jurewicz, B.R., 1976. Rock excavation with laser assistance. *International Journal of Rock Mechanics and Mining Sciences & Geomechanics Abstracts* 13, 207-219.
- Kitzinger, F., Nantel, J., 1992. Plasma blasting method. Google Patents.
- Knickmeyer, W., Baumann, L., 1983. High-pressure water jet-assisted tunneling techniques, Second U.S. Water Jet Conference, Rolla, Missouri, USA, pp. 346-356.
- Koiwa, T., Shiratori, Y., Takahashi, H., Matsumoto, S., 1975. Rock breaking by microwave radiation-effects of local heating and thermal fracture. Ministry of Transport, Nagase, Yokosuka, Japan, pp. 181-209.
- Kouzovich, I.A., Merzlyakov, V.G., 1983. Schemes of coal massif breakage by disc cutter and high-velocity water jet, Second U.S. Water Jet Conference, Rolla, Missouri, USA, pp. 381-400.
- Krasnovskij, S.S., Uvarov, A.P., 1991. Examination of possibility of lowering of power consumption of rocks fracture at affecting of thick streams of microwave energy of millimeter wave, 6 Russian scientific

- conference. "Microwave energy application in processes and scientific examinations, Saratov, Russia, pp. 139-140.
- Lauriello, P.J., Chen, Y., 1973. Thermal fracturing of hard rock. *Journal of Applied Mechanics* 40, 909-914.
- Lindroth, D.P., Berglund, W.R., Morrell, R.J., Blair, J.R., 1993. Microwave-assisted drilling in hard rock. *Tunnels and Tunnelling* 25, 24-27.
- Maurer, W.C., 1980. Advanced drilling techniques. Petroleum Pub. Co.
- McGarry, F.J., Moavenzadeh, F., 1970. Laser heating effects on rock samples, The 12th U.S. Symposium on Rock Mechanics (USRMS), . American Rock Mechanics Association, Rolla, Missouri, USA.
- Mellor, M., 1972. Normalization of specific energy values. *International Journal of Rock Mechanics and Mining Sciences & Geomechanics Abstracts* 9, 661-663.
- Metaxas, A.C., Meredith, R.J., 1983. Industrial microwave heating. IET.
- Misnik, Y.M., Nekrasov, L.B., 1969. Breaking frozen loose rocks by means of a combination of high-frequency and mechanical fields. *Soviet Mining* 5, 646-650.
- Misnik, Y.M., Nekrasov, L.B., 1973. Electrothermal breaking of frozen rocks (Principal problems and research results). *Soviet Mining* 9, 487-491.
- Moavenzadeh, F., McGarry, F.J., Williamson, R.B., 1968. Use of Laser and Surface Active Agents for Excavation in Hard Rocks, Fall Meeting of the Society of Petroleum Engineers of AIME. Society of Petroleum Engineers, Houston, Texas.
- Montross, C.S., Florea, V., Bolger, J.A., 1999. Laser-induced shock wave generation and shock wave enhancement in basalt. *International Journal of Rock Mechanics and Mining Sciences* 36, 849-855.
- Mosavat, K., 2017. A smart disc cutter monitoring system using cutter instrumentation technology, RETC 2017, San Diego, USA, pp. 109-118.
- Murray, C., Courtley, S., Howlett, P.F., 1994. Developments in rock-breaking techniques. *Tunnelling and Underground Space Technology* 9, 225-231.
- Nejati, H., 2014. Analysis of physical properties and thermo – mechanical induced fractures of rocks subjected to microwave radiation, Department of Mining and Materials. McGill.
- Nekoovaght, P.M., 2009. An investigation on the influence of microwave energy on basic mechanical properties of hard rocks. Concordia University.
- Nekoovaght, P.M., 2015. Physical and mechanical properties of rocks exposed to microwave irradiation: Potential application to tunnel boring, Department of Mining and Materials. McGill University.
- Nelson, P.P., 1993. TBM performance analysis with reference to rock properties in: Hudson, J.A. (Ed.), *Excavation, support and monitoring*. Pergamon, Oxford, pp. 261-291.
- NRC, 1994. Microwave processing of materials. The National Academies Press, Ishington, DC.
- O'Brien, D.G., Graves, R.M., O'Brien, E.A., 1999. Laser-rock-fluid interaction: application of free-electron laser (FEL) in petroleum well drilling and completions, *Optoelectronics '99 - Integrated Optoelectronic Devices*. SPIE, San Jose, CA, United States, pp. 168-176.
- Oglesby, K.D., Woskov, P., Einstein, H., Livesay, B., 2014. Deep geothermal drilling using millimeter wave technology, p. 206.
- Ozdemir, L., 2002. The cutting edge. *World Tunnelling*, 86-88.
- Ozdemir, L., Dollinger, G.L., 1984. Recent developments in mechanical and water jet assisted tunnel boring technology for civil and mining engineering applications, *ISRM Symposium: Design and Performance of Underground Excavations*., Cambridge, U.K. , pp. 295-303.
- Ozdemir, L., Evans, R.J., 1983. Development of waterjet assisted drag bit cutting head for coal measure rock, in: Sutcliffe, H., Wilson, J.W. (Eds.), *1983 Rapid Excavation and Tunnelling Conference*, Chicago, Illinois.
- Peinsitt, T., Kuchar, F., Hartlieb, P., Moser, P., Kargl, H., Restner, U., Sifferlinger, N., 2010. Microwave heating of dry and water saturated basalt, granite and sandstone. *International Journal of Mining and Mineral Engineering* 2, 18-29.
- Peinsitt, T., Kuchar, F., Kargl, H., Restner, U., Sifferlinger, N., Moser, P., 2008. Microwave heating of rocks with different water content, *Proceedings of Microwave Technology '08*, pp. 1-9.
- Pierce, K.G., Livesay, B.J., Finger, J.T., 1996. Advanced drilling systems study. Sandia National Laboratories.
- Poole, J.W., Thorpe, M.L., 1973. Study of high power plasma for in situ hard rock disintegration, p. 85.
- Pooniwal, S.A., 2006. Lasers: The next bit, SPE Eastern Regional Meeting. Society of Petroleum Engineers, Canton, Ohio, USA.
- Protasov, Y.I., Kuznetsov, V.V., Merzon, A.G., Chernikov, V.A., Retinskii, V.S., 1984. A study of electrothermomechanical destruction of hard rocks with a rotary heading machine. *Soviet Mining* 20, 462-467.

- Rad, P.F., McGarry, F.J., 1970. Thermally assisted cutting of granite, The 12th U.S. Symposium on Rock Mechanics (USRMS). American Rock Mechanics Association, Rolla, Missouri, USA.
- Ramezanzadeh, A., Hood, M., 2010. A state-of-the-art review of mechanical rock excavation technologies. *Journal of Mining and Environment* Volume 1, 29-39.
- Rauer, M., 2014. Tunnel boring machines in mines – A brief review of past use with a status report on use today in Australia, 15th Australasian Tunnelling Conference 2014, Sydney, Australia, pp. 663-669.
- Res, J., Wladzielczyk, K., Ghose, A.K., 2003. Environment-friendly techniques of rock breaking. Taylor & Francis.
- Robbins, R.J., 1987. Machine tunnelling in the twenty-first century. *Tunnelling and Underground Space Technology* 2, 147-154.
- Roby, J., Sandell, T., Kocab, J., Lindbergh, L., 2008. The current state of disc cutter design and development direction, in: Roach, M.F., Kritzer, M.R., Ofiara, D., Townsend, B.F. (Eds.), *North American Tunnelling 2008*. SME, San Francisco, USA, pp. 36-45.
- Ropchan, D., Wang, F.-D., Wolgamott, J., 1980. Application of water jet assisted drag bit and pick cutter for the cutting of coal measure rocks. Final Technical Report.
- Rostami, J., 2011. Mechanical rock breaking, in: Darling, P. (Ed.), *SME Mining Engineering Handbook*, Third Edition, 4 ed. SME, USA, pp. 417-434.
- Rostami, J., Ozdemir, L., 1993. A new model for performance prediction of hard rock TBM, in: Bowerman, L.D. (Ed.), *Rapid Excavation and Tunnelling Conference 1993*, Boston, MA, pp. 793-809.
- Satish, H., 2005. Exploring microwave assisted rock breakage for possible space mining applications, Department of Mechanical Engineering, McGill University.
- Segsworth, R.S., Kuhn, K., 1977. Electrical rock breaking. *IEEE Transactions on Industry Applications* IA-13, 53-57.
- Siegman, A.E., 1986. *Lasers*. University Science Books.
- Sikong, L., Bunsin, T., 2009. Mechanical property and cutting rate of microwave treated granite rock. *Songklanakarin Journal of Science and Technology* 31, 447-452.
- Smading, S., 2017a. Large-diameter 20-inch disc cutters: A comparison of tool life and performance on hard rock TBMs, RETC 2017, San Diego, USA, pp. 254-260.
- Smading, S., 2017b. TBM disc cutters in the field: Extreme tunnel conditions inform the latest cutting tool advancements, 3rd International Conference on Tunnel Boring Machines in Difficult Grounds, Wuhan, China.
- Summers, D.A., 1995. *Waterjetting Technology*. CRC Press.
- Summers, D.A., Henry, R.L., 1972. Water jet cutting of sedimentary rock. *Society of Petroleum Engineers*, New Orleans, LA, pp. 797-802.
- Takahashi, H., Koiwa, T., Miyazaki, S., Kihara, S., Matsumoto, S., 1979. Rock excavation by microwave - Capability of high power microwave rock breaker (100kW, 200kW) for rock excavation. Port and Airport Research Institute.
- Tecen, O., Fowell, R.J., 1983. Hybrid rock cutting: Fundamental investigations and practical applications, in: Summers, D.A., Haston, F.F. (Eds.), *2nd U.S. Waterjet Conference*, Rolla, Missouri, USA, pp. 347-357.
- Vogt, D., 2016. A review of rock cutting for underground mining: past, present, and future. *Journal of the Southern African Institute of Mining and Metallurgy* 116, 1011.
- von Hippel, A., 1954. *Dielectrics and waves*. John Wiley & Sons, Inc., New York.
- Wang, F.-D., Miller, R., 1976. High pressure water jet assisted tunneling, *Rapid Excavation and Tunnelling Conference*, Las Vegas, USA, pp. 649-676.
- Weber, M.J., 1998. *Handbook of laser wavelengths*. CRC Press.
- Williamson, R.B., F., M., McGarry, F.J., 1968. Some relationships between power level, exposure time, sample size and weakening in laser-assisted rock fracture. MIT Department of Civil Engineering.
- Wilson, J.W., Summers, D.A., Gertsch, R.E., 1997. The development of waterjets for rock excavation, 4th International Symposium on Mine Mechanisation and Automation, Brisbane, Australia.
- Woskov, P., 2017. Millimeter-wave directed energy deep boreholes, *Drilling for Geology II Conference 2017*. Australian Institute of Geoscientists, Brisbane.
- Woskov, P.P., Einstein, H.H., Oglesby, K.D., 2014. Penetrating rock with intense millimeter-waves, 39th International Conference on Infrared, Millimeter, and Terahertz waves (IRMMW-THz), pp. 1-2.
- Zheng, Y.L., Zhang, Q.B., Zhao, J., 2016. Challenges and opportunities of using tunnel boring machines in mining. *Tunnelling and Underground Space Technology* 57, 287-299.

- Zheng, Y.L., Zhang, Q.B., Zhao, J., 2017. Effect of microwave treatment on thermal and ultrasonic properties of gabbro. *Applied Thermal Engineering*.
- Znamenácková, I., Lovás*, M., Hájek, M., Jakabský, Š., 2003. Melting of andesite in a microwave oven. *Journal of Mining and Metallurgy* 39, 549-557.

CHAPTER 3

Fundamentals of Microwave Interactions with Minerals and Rocks

3.1 Introduction

Microwave heating has been the common practice in the food industry for thawing, heating, baking and sterilization (Chandrasekaran et al., 2013; Datta, 2001; Venkatesh and Raghavan, 2004), in microwave chemistry (Lidström et al., 2001; Mingos and Baghurst, 1991), in rubber vulcanization (Clark and Sutton, 1996; Sombatsompop and Kumnuantip, 2006), and in ceramic sintering (Bengisu, 2013; Katz, 1992; Sebastian et al., 2017). Through the history, research have also been conducted on microwave assisted wood drying and modification (Torgovnikov, 1993), coal drying and desulphurisation (Binner et al., 2014; Standish et al., 1988), microwave assisted leaching (Pickles, 2009a, b), microwave assisted mineral processing (Haque, 1999; Kingman, 2006), treatment of contaminated soil (Jones et al., 2002), microwave assisted concrete curing and aggregate recycling (Makul et al., 2014; Ong and Akbarnezhad, 2014), weeding and insect killing (Brodie et al., 2015b; Brodie et al., 2012), pyrolysis of sewage sludge (Menéndez et al., 2002; Zhai et al., 2012), and rock breakage and drilling (Hoekstra, 1976; Santamarina, 1989), among others. However, the mechanisms how microwave heats materials and the applicators used can be significantly different.

This chapter presents the scientific fundamentals of microwave-material interactions to elucidate the governing physics of dielectric heating. Different polarisation mechanisms of materials are first introduced, with an emphasis on the electronic and atomic polarisations for rock forming minerals. The factors that have an influence on the dielectric properties (DPs) of minerals and rocks, such as temperature, frequency, grain size and dissemination, are discussed. The chapter then briefly reviews the commonly used techniques to measure the DPs of materials. It provides a state-of-the-art review on the microwave assisted ore mineral processing and rock treatment and serves as a background of this research.

3.2 What is microwave?

Microwave is the collective name of the electromagnetic (EM) waves with a frequency ranging from 300 MHz to 300 GHz and a corresponding wavelength ranging from 1 m to 1 mm. Its frequency band and wavelength on the EM spectrum is shown in Figure 3.1. EM waves are self-propagating waves characterised by electric (E) and magnetic (H) field components oscillating in phase and perpendicular with each other and also perpendicular to the direction of propagation (Metaxas and Meredith, 1983). As shown in Figure 3.2, EM waves are generated by the acceleration of a charge (Chabay and Sherwood, 2015). If the charge moves sinusoidally, the EM radiation will be sinusoidal as well.

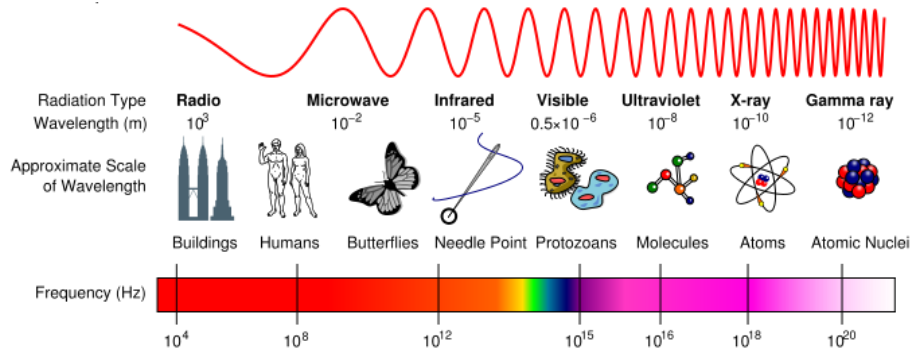


Fig. 3.1 Wavelength and frequency spectrum of electromagnetic waves.

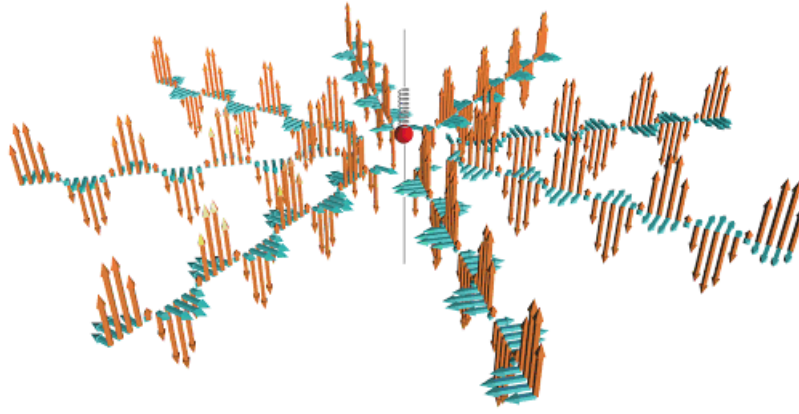


Fig. 3.2 Generation of electromagnetic waves by the acceleration of a charge (Chabay and Sherwood, 2015).

EM waves can propagate in free space (vacuum), a physical medium, and waveguides of certain dimensions. The following Maxwell's Equations must be met for the propagation to happen (Chabay and Sherwood, 2015).

$$\text{Gauss's Law} \quad \nabla \cdot E = \frac{\rho}{\epsilon_0} \quad (3.1)$$

$$\text{Gauss's law for magnetism} \quad \nabla \cdot B = 0 \quad (3.2)$$

$$\text{Faraday's law} \quad \nabla \times E = -\frac{\partial B}{\partial t} \quad (3.3)$$

$$\text{Ampère's circuital law} \quad \nabla \times B = \mu_0 \frac{\partial D}{\partial t} \quad (3.4)$$

Where E is the electric field strength, B is the magnetic flux, D is the electrical displacement, ϵ_0 and μ_0 are the permittivity and permeability of the free space.

To avoid the possible interference with communications, only a handful of EM wave frequencies are allocated for industrial, scientific and medical (ISM) purposes. The frequencies often used for

microwave processing of materials are 915 MHz, 2.45 GHz and 5.8 GHz, among which the 2.45 GHz is the most commonly used.

3.3 Polarisation mechanisms

Essentially, any material can be heated using high frequency EM waves provided that the material is neither a perfect electrical conductor nor a perfect insulator (Kobusheshe, 2010; Metaxas and Meredith, 1983). EM heating of materials (termed as dielectrics) originates from the ability of the electric field to polarise charges in the material and the inability of this polarisation to follow extremely rapid reversals of the electric field or through direct conduction effects (Metaxas and Meredith, 1983). The interaction of an electric field with a dielectric has its origin in the response of charge particles to the applied field. The displacement of these charge particles from their equilibrium positions gives rise to induced dipoles which respond to the applied field. Such induced polarisation arises mainly from the displacement of electrons around the nuclei (electronic polarisation) or due to the relative displacement of atomic nuclei because of the unequal distribution of charge in molecule formation (atomic polarisation) (von Hippel, 1954). In addition to the induced dipoles, dielectrics, known as polar dielectrics, contain permanent dipoles due to the asymmetric charge distribution of unlike charge partners in a molecule which tend to reorientate under the influence of a changing electric field, thus giving rise to orientation polarisation. Finally, another source of polarisation arises from charge build-up in interfaces between components in heterogeneous systems, termed interfacial, space charge or Maxwell—Wagner polarisation (von Hippel, 1954). As shown in Figure 3.3, dielectric polarisation mechanism can be divided into ionic, dipolar, atomic and electronic polarisation at different scales (von Hippel, 1954).

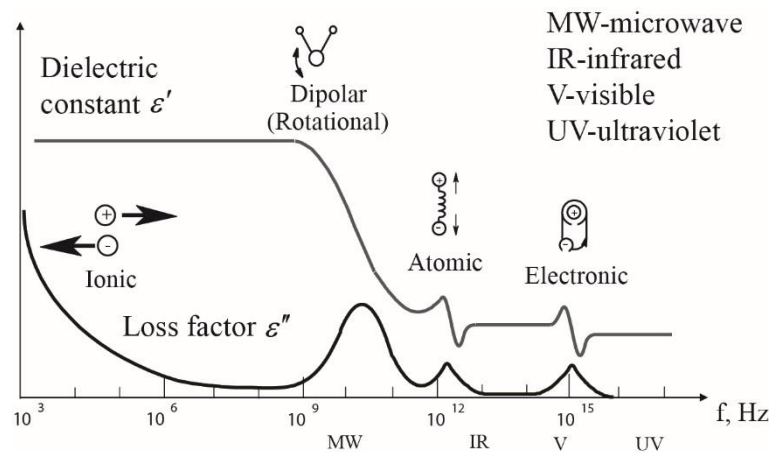


Fig. 3.3 Four basic polarisation mechanisms of dielectric heating (Agilent, 2004).

3.3.1 Electronic polarisation

Materials consist of positively charged atomic nuclei surrounded by negatively charged electron clouds. Upon an external electric field the electrons are displaced slightly with respect to the nuclei, inducing dipole moments and causing the so-called electronic polarisation of materials (von Hippel, 1954). This type of polarisation takes a very short time to happen (10^{-15} s), indicating that it exists, regardless of the

materials, at a frequency band from radio frequency up to visible light (optical) and ultraviolet frequency of 10^{15} Hz (Carter and Norton, 2007). For frequency higher than this, radiative reactions happen. At the microwave frequency, the oscillation of the induced dipoles will be able to generate a very weak electric current and heat.

3.3.2 Atomic polarisation

When atoms of different types form molecules or crystals, they will normally not share their electrons symmetrically, as the electron clouds will be displaced eccentrically toward the stronger binding atoms. Thus atoms acquire charges of opposite polarity and the external field acting on these of net charges will tend to change the equilibrium positions of the atoms themselves. By this displacement of charged atoms or groups of atoms with respect to each other, a second type of induced dipole moment is created. Such moments experience a torque in an applied field that tends to orient them in the field direction. Consequently an orientation polarisation can arise (von Hippel, 1954). Figure 3.4 compares the polarisation of quartz and perovskite unit cells when subjected to an external electric field. For quartz crystals, the silicon atoms are tightly bound in a tetrahedron of oxygen atoms. When subjected to an external field, the electrons around the oxygen and silicon atoms will be slightly displaced. However, the tetrahedron structure itself is so rigid that the silicon atom will not be able to move. By contrast, the Barium titanate (BaTiO_3) has relatively free oxygen and titanium atoms, which will be easily displaced upon an external electric field. With varying degrees of polarisation, the amount of heat generated also differs. At the microwave frequency, the atomic polarisation may be the dominating mechanism for dielectric heating.

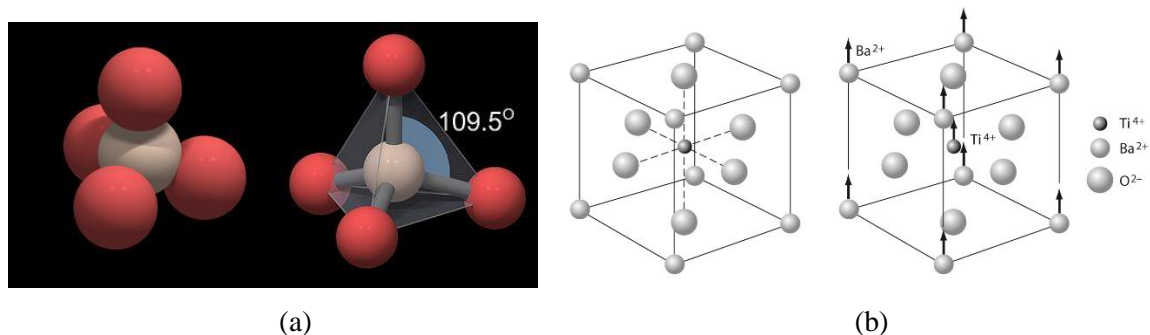


Fig. 3.4 Polarisation of mineral crystals under an external electric field: (a) Polarisation of the quartz crystal; (b) Displacement of atoms in a barium titanate unit cell.

3.3.3 Dipolar (orientation) polarisation

Dipolar polarisation, also referred to as orientation polarisation, occurs in dielectrics containing permanent dipoles which are present even in the absence of an external electric field (von Hippel, 1954). Permanent dipoles arise from an imbalance in charge distribution in molecules such as water. The dipole moments are oriented in a random manner in the absence of an electric field so that no polarisation exists. When an external field is applied, a torque is induced on the dipoles and they rotate to align with the electric field causing polarisation. At low frequencies, the molecules will be polarised

uniformly but at higher frequencies, molecules cannot cope with phase change and the alternating motion generates heat due to frictional losses (Meredith, 1998). The dipolar polarization happens at a frequency up to 10^{10} Hz. This type of polarisation is the dominant mechanisms in heating water-bearing materials, for example, food and sedimentary rocks. However, the natural igneous hard rocks contain very little moisture content, thus the role this mechanism plays in microwave heating igneous rocks could be neglected.

3.3.4 Ionic polarisation

This mechanism applies to materials that contain free charge carriers which may migrate freely under an electric field. One of the representative materials is NaCl which has free-moving Na^+ and Cl^- ions in an electric field. The free movement of ions induces current and heating due to electrical resistance (von Hippel, 1954). The ionic polarization takes longer to happen due to the large size of particles involved. It typically occurs at frequencies between 10^9 - 10^{13} Hz. As for the basic rock forming minerals and natural hard rocks, the contribution of this mechanism to heating is expected to be small.

3.3.5 Interfacial polarisation

The last polarisation mechanism that does not appear in Figure 3.3 is the interfacial polarisation (also referred to as Maxwell-Wagner polarization). Unlike the previous four mechanisms which are due to charges that are locally bound in atoms, in molecules, or in the structures of solids and liquids, in interfacial polarisation carriers that can migrate for some distance through the dielectric usually exist. When such carriers are impeded in their motion, either because they become trapped in the material or on interfaces, or because they cannot be freely discharged or replaced at the electrodes, space charges and a macroscopic field distortion result (von Hippel, 1954). This mechanism could significantly influence the polarisation of heterogeneous mixtures with constituents having different permittivity (microwave absorption capabilities) and electrical conductivity or solid materials with charged particles mobile in an enclosed region, at the lowest frequency band used for industrial heating. At the microwave frequency, it could also be neglected.

The total polarizability of a dielectric material is the sum of the five terms.

$$\alpha = \alpha_e + \alpha_a + \alpha_d + \alpha_i + \alpha_s \quad (3.5)$$

The Clausius-Mosotti-Lorentz-Lorenz calculated the polarizability as:

$$\alpha = \frac{\epsilon' - 1}{\epsilon' + 2} \frac{3M\epsilon_0}{\rho N_0} = \frac{n^{*2} - 1}{n^{*2} + 2} \frac{3M\epsilon_0}{\rho N_0} \quad (3.6)$$

Where M designates the molecular weight in kg, ρ is the density of the dielectric, n is the Complex Refractive Index, N_0 is the number of molecules per mole (which is the Avogadro's number of 6.023×10^{23}).

$$n^* = n - ik \quad (3.7)$$

Where n is the refractive index and k is the absorption coefficient.

$$n = \frac{0.5 \times (N_{oil}^2 - 1)}{N_{oil} \frac{1 + R_{oil}}{1 - R_{oil}} - \frac{1 + R_{air}}{1 - R_{oil}}} \quad (3.8)$$

$$k = \sqrt{\frac{(n-1) \times R_{air}^2 - (n-1)^2}{\sqrt{1 - R_{air}}}} \quad (3.9)$$

Where R_{air} and R_{oil} are the reflectivity of the mineral in air and in oil, N_{oil} is the refractive index of the Cargille oil.

3.4 Dielectric properties of minerals

3.4.1 Definitions of dielectric properties

A dielectric material has the ability to absorb and store energy through polarisation when an external electric field is applied. The extent to which energy may be absorbed and dissipated in a material depends on its DPs which include permittivity, permeability, conductivity and resistivity. Permittivity is the most important property that defines the interaction of EM waves with materials. The permittivity of a material is composed of a real part and an imaginary part. The real part is known as the dielectric constant (ϵ') and is a measure of the ability of a material to be polarised and store energy. The imaginary part (ϵ'') is a measure of the ability of the material to dissipate stored energy into heat (Metaxas and Meredith, 1983). The two are related by the expression:

$$\epsilon = \epsilon' - j\epsilon'' \quad (3.10)$$

The ratio of effective loss factor to dielectric constant is called loss tangent ($\tan \delta$) which measures the capability of the dielectric to store energy and convert it into heat.

$$\tan \delta = \frac{\epsilon''}{\epsilon'} \quad (3.11)$$

The DPs of a material are frequency and temperature dependent and also vary considerably with density and moisture content (Meredith, 1998).

Power absorption by a dielectric material is often expressed as a power density (W/m^3) and is given by the equation below (Meredith, 1998).

$$P_d = 2\pi f \epsilon_0 \epsilon'' E^2 \quad (3.12)$$

Where f is the microwave frequency (2.45 GHz), ϵ_0 is the permittivity of the free space ($8.85 \times 10^{-12} \text{ F/m}$), E is the electric field strength in the mineral (V/m).

When microwave energy is absorbed by materials, the amplitude of the wave decreases gradually as the wave propagates into the material. If any internally reflected waves are neglected, the power density (and therefore power absorbed) falls exponentially with depth. The microwave penetration depth, D_p is defined as the distance into the material at which the power flux falls to $1/e = 0.368$ of its surface

value (Metaxas and Meredith, 1983). D_p can be calculated by the following equation, in which λ is the wavelength of the incident wave.

$$D_p = \frac{\lambda_0}{2\pi\sqrt{2\varepsilon'}} \times \frac{1}{\sqrt{[(1 + (\frac{\varepsilon''}{\varepsilon'})^2)^{0.5} - 1]}} \quad (3.13)$$

When $\varepsilon'' < \varepsilon'$, the above equation can be reduced to the following equation, with an error up to 10%.

$$D_p = \frac{\lambda\sqrt{2\varepsilon'}}{2\pi f \varepsilon''} \quad (3.14)$$

It should be mentioned that there is no direct correlations between the dielectric constant and the loss factor. There are special ceramics that have very high dielectric constants but very low loss factors. However, materials that have a low dielectric constant normally also have a low dielectric loss factor, for example, fused quartz and alumina. Although the dielectric constant could be theoretically determined by the density functional theory which is based on computational quantum mechanics (Dal Corso et al., 1994; Jones and Gunnarsson, 1989), the loss factors must be measured experimentally.

3.4.2 Microwave heating and weakening mechanisms

The absorption of microwave energy will result in the temperature increase.

$$Q = C_p m \Delta T \quad (3.15)$$

Where C_p is the specific heat capacity (J/kg/K), m is the mass (g), ΔT is the temperature increase after microwave heating (°C). By combining Equations 3.12 and 3.15, we get

$$C_p m \Delta T = P_d V t = 2\pi f \varepsilon_0 \varepsilon'' E^2 V t \quad (3.16)$$

Where V is the volume of the rock/mineral, t is the heating time. Rearranging Equation 3.16 we get the heating rates as

$$\frac{\Delta T}{t} = \frac{2\pi f \varepsilon_0 \varepsilon'' V E^2}{C_p m} = \frac{2\pi f \varepsilon_0}{C_p \rho} \varepsilon'' E^2 \quad (3.17)$$

Equation 3.17 indicates that the heating rate of a material under microwave irradiation is governed by the dielectric loss factor, the electric field strength, the specific heat capacity and the density.

3.4.3 Factors influencing the dielectric properties of minerals and rocks

(a) Frequency

The dependence of DPs of materials on frequency has been explored by Campbell and Ulrichs (1969), Khalafalla (1973), Kaatze and Giese (1980), Nelson et al. (1989), Ulaby et al. (1990), Atwater and Wheeler (2004), and Sengwa and Soni (2008). It is generally believed that the dielectric constant decreases with an increasing microwave frequency, while the dielectric loss factor varies depending on the polarisation mechanisms and the relaxation time. The relaxation time is defined as the time it takes for the original and induced dipoles to restore to the random state and represents how fast the dipoles

can act on the alternating electric field. For water-rich materials, the dipolar (orientation) polarisation plays the dominant roles. As shown in [Figure 3.5](#), at room temperature (25°C) the dielectric constant begins to decrease at around 5 GHz. By comparison, the loss factor increases with the microwave frequency until it peaks at around 19.5 GHz which is the relaxation frequency of water dipoles at 25 °C ([Barba and d'Amore, 2012](#)). [Atwater and Wheeler \(2004\)](#) observed similar trends for the DPs on carbon.

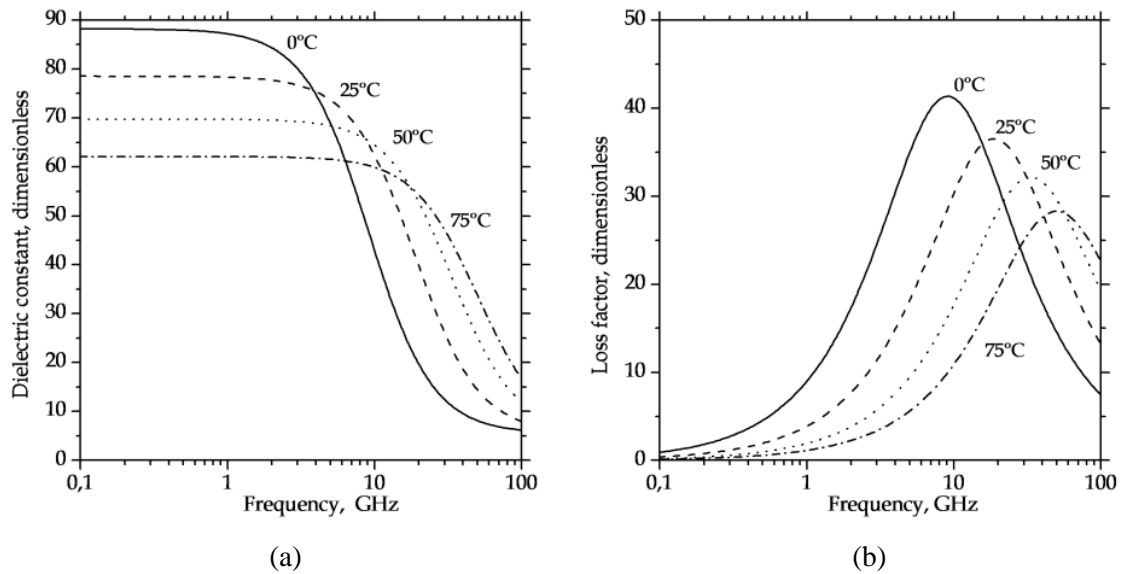


Fig. 3.5 Dielectric properties of water as a function of microwave frequency at different temperatures. (a) Dielectric constant; (b) loss factor ([Barba and d'Amore, 2012](#)).

For dried materials or materials with very little moisture content (such as igneous rocks), the electronic and atomic polarisation mechanisms dominate. [Nelson et al. \(1989\)](#) measured the DPs of some low loss rock forming minerals using the short circuited waveguide method proposed by [Roberts and Von Hippel \(1946\)](#). Their results, shown in [Figure 3.6](#), indicate that the dielectric constants decrease as microwave frequency increases, however, the relationship between the loss factors and the frequency differs from mineral to mineral. The loss factors of diopside (a type of pyroxene) and labradorite (a type of plagioclase) decreases with frequency and then slightly increases, while the loss factors of other minerals keep relatively unchanged.

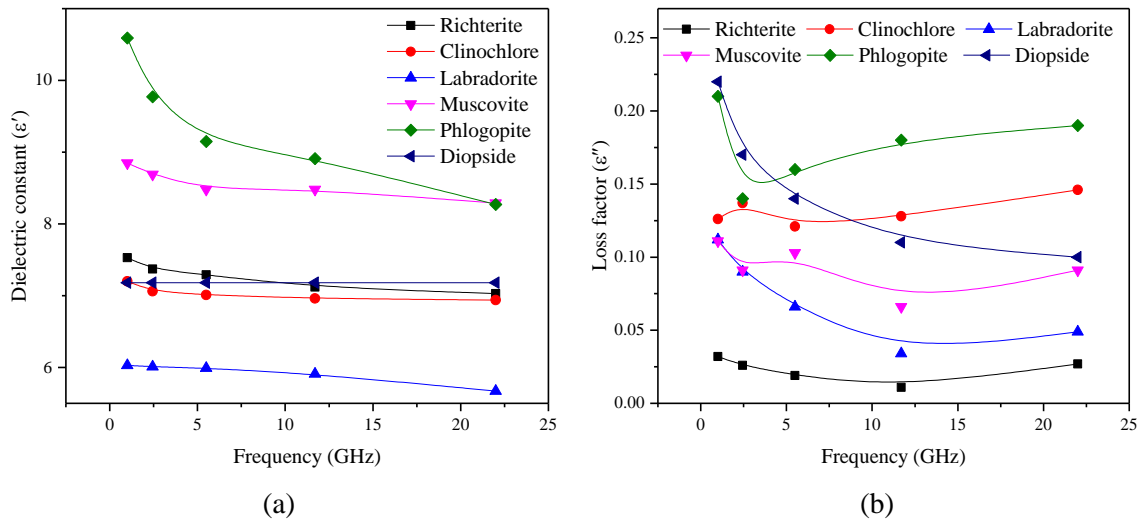


Fig. 3.6 Dielectric properties of low loss minerals as a function of microwave frequency. (a) Dielectric constant, (b) loss factor (Data from Nelson et al. (1989)).

Ulaby et al. (1988) and Ulaby et al. (1990) measured the dielectric constants of 80 rock samples from 0.5 GHz to 18 GHz using two coaxial probes and their loss factors using five resonant cavities from 1.6 GHz to 16 GHz. They found that the dielectric constant is frequency-independent while the loss factor decreases with increasing frequency between 1.6 GHz and 5 GHz and then it levels off at higher frequencies (Figure 3.7). Among the rock groups shown, the carbonates exhibit the lowest loss and the igneous volcanics exhibit the highest loss. They also managed to correlate the DPs with the density and chemical compositions. They also found that the dielectric constant is highly density dependent while loss factor is not.

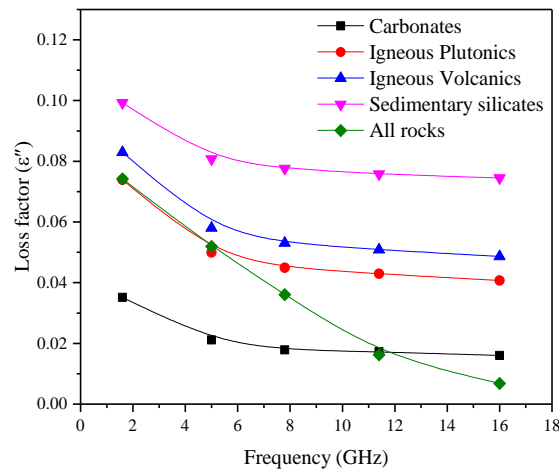


Fig. 3.7 Variation of loss factor of different rock types from 1.6 GHz to 16 GHz (reproduced from Ulaby et al. (1988)).

It should be mentioned that the broadband measuring techniques such as coaxial probes are not suitable for low loss minerals and that the resonant cavity techniques can only measure DPs at discrete frequencies. That said, the influence of frequency on the DPs of low loss minerals and rocks are not well understood. Another reason is that the allocated microwave frequencies are very limited, meaning

studying the frequency-dependence of mineral DPs is less crucial when compared to the temperature-dependence (Folorunso, 2015).

(b) Temperature

Temperature may have a significant impact on the DPs by influencing the relaxation time (Komarov et al., 2005). As temperature increases, the relaxation time decreases. With a higher polarizability comes a higher dielectric constant and usually, but not necessarily, a higher dielectric loss factor. Campbell and Ulrichs (1969) measured the DPs of solid and powdered rocks at frequencies of 450 MHz and 35 GHz from 20 °C to 600 °C. Their results, as shown in Figure 3.8, indicate that temperature has no impact on the DPs of quartz, aplite granite and dunite (olivine peridotite), however, the DPs of the two basalts, especially the loss factor, increases as temperature increases.

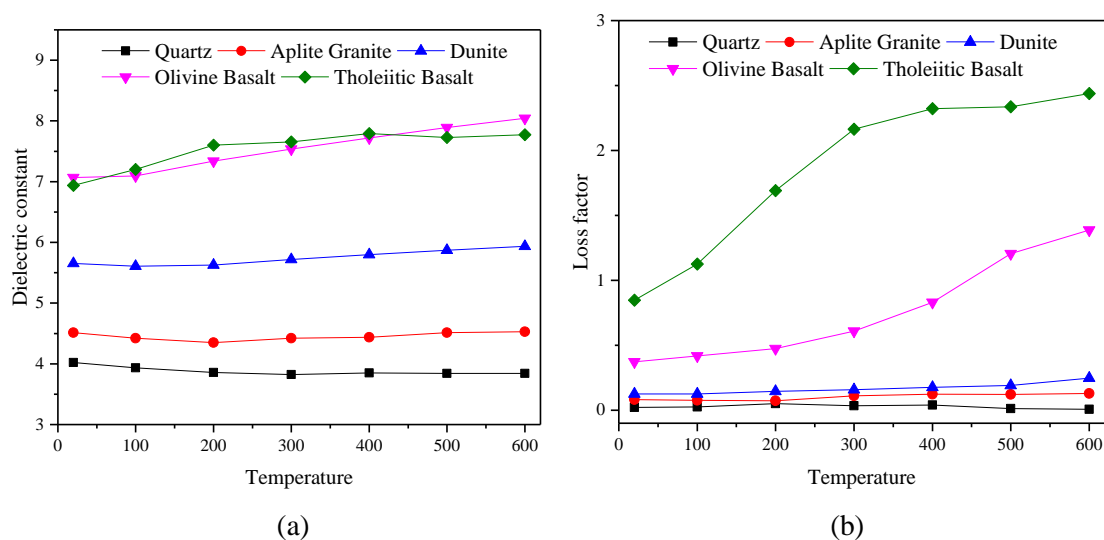


Fig. 3.8 Dielectric properties of some rock types as a function of temperature at 35 GHz. (a) Dielectric constant, (b) loss factor (reproduced from Campbell and Ulrichs (1969)).

Cumbane (2003) measured the DPs of some gangue minerals and ore minerals from room temperature to up to 600 °C using the resonant cavity techniques. As shown in Figure 3.9, he found that in the temperature range the DPs of quartz and orthoclase are not affected by temperature increase. The DPs of sphalerite and galena begin to increase at 400 °C. By contrast, the DPs of ore minerals of chalcopyrite, pyrite and chalcocite vary considerably with temperature. The dielectric constant of chalcopyrite and pyrite increases significantly at 375 °C while this happens to chalcocite at a temperature of 200 °C. The loss factors of the three ore minerals fluctuate in the temperature range, resulting in great uncertainties in the temperature increase while microwave heating. For instance, for chalcocite, the temperature can increase without control at 350 °C, leading to the thermal runaway.

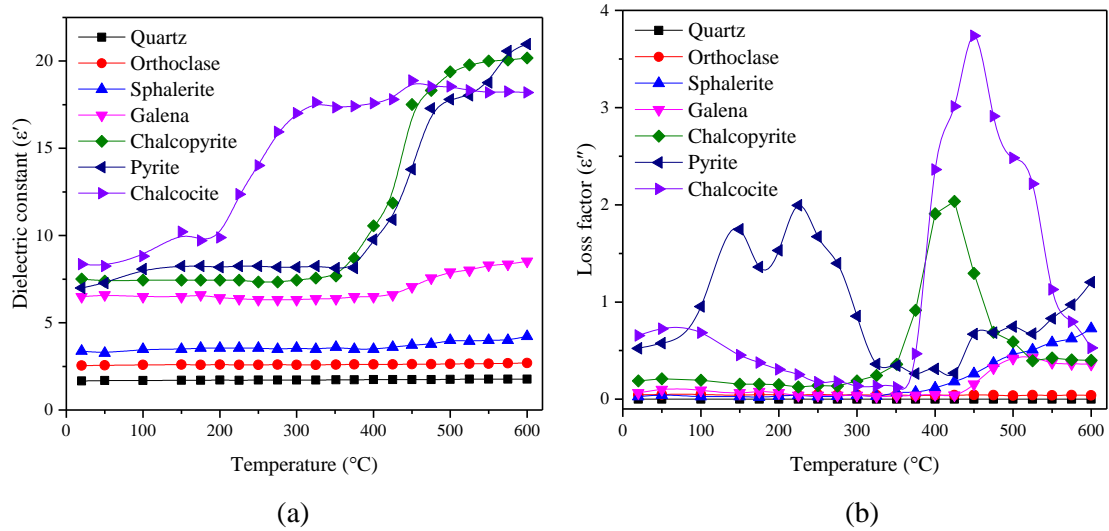


Fig. 3.9 Dielectric properties of some minerals as a function of temperature at the frequency of 2.216 GHz. (a) Dielectric constant, (b) loss factor (Data from [Cumbane \(2003\)](#)).

(c) Crystallography

The crystallography of materials can have a great, if not dominant, impact on their DPs at the microwave frequencies. One of the argument is that the DPs of water and ice are significantly different although their chemical compositions are exactly the same ([Matzler and Wegmuller, 1987](#)). In ice, the water molecules are bound together and the dipolar polarisation loses its dominant role in in heating. Another argument is that gold and copper are microwave isolators in the solid state, however, they can be good microwave absorbers when pulverised ([Roy et al., 1999](#)). The crystallography directly governs the degree of atomic polarisation of the crystals.

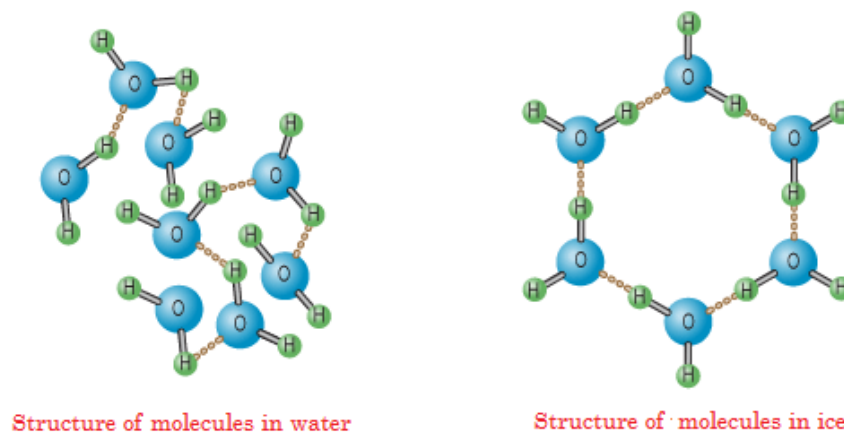


Fig. 3.10 Structures of molecules of water and ice.

(d) Other parameters

Some minerals can only be measured in the form of powder (inevitable due to the need for purification). The density then directly determines how much material is interacting with the EM field. Under this circumstance, the results are highly independent on the bulk density. The effective medium theories can

be used to obtain the DPs of the solids (Nelson, 2015a; Nelson, 2001; Nelson et al., 1989; Nelson and Trabelsi, 2012).

The grain size of minerals and their dissemination in the rock matrix also have an impact on the DPs of the rocks (Harrison, 1997; Standish, 1989). Microstructure affects the dispersion of EM waves in the materials. Generally it is believed that the DPs increase with a decreasing grain size density. The inclusion of defects such as weak planes and cracks also contributes to higher dielectric properties.

The DPs of materials, in this case minerals and rocks, are of fundamental importance to the understanding of the microwave-material interactions and the consequent heating and weakening of hard rocks. Those data are critically essential in explaining the thermal cracking process of rocks and in supporting numerical simulations. Depending on the frequency and temperature of interest, the form of the materials (solid, powder, liquid), and how lossy they are, there are different techniques to choose from. The techniques include the resonant cavity perturbation techniques, transmission line techniques, free space techniques, coaxial probe techniques, and stripline and microstrip methods. Each method has its inherent advantages and disadvantages and corresponding applicability. Excellent reviews on those methods could be found in books written by Metaxas and Meredith (1983), Meredith (1998), NRC (1994), Komarov et al. (2005) and Nelson (2015a). In this section, only the most commonly used techniques at the microwave frequency are briefly presented.

3.5 Dielectric properties measurement techniques

3.5.1 Resonant cavity technique

The resonant cavity perturbation technique is the best method to measure the complex permittivity of low loss materials and of materials at high temperature (Chen et al., 1999; Kraszewski and Nelson, 1994; Sheen, 2005; Ulaby et al., 1990). The measurement setup usually consists of a vector network analyser and a resonant cavity, connected by a coaxial cable (Figure 3.11(a)). The cavity can have either one-port (Figure 3.11(a)) or two ports (Figure 3.11(b)). As shown in Figure 3.11 and 3.12, the insertion of a small sample right in the middle of the initially empty cavity (where the electric field is the maximum) will slightly shift the resonant frequency and the quality factor (Q) of the cavity. To use this technique, the sample to be tested must be very small compared to the cavity such that the EM fields in the cavity will only be slightly disturbed and there will still be a resonance near the initial resonant frequency.

Based on the shift in the resonant frequency and Q and the relationship between bandwidth and quality factor, the complex permittivity can be calculated using the equations below (ASTM, 2013).

$$Q = \frac{f_c}{f_h - f_l} \quad (3.18)$$

$$\varepsilon' = 1 + \frac{V_c(f_c - f_s)}{2V_s f_s} \quad (3.19)$$

$$\varepsilon'' = \frac{V_c}{4V_s} \left(\frac{1}{Q_s} - \frac{1}{Q_c} \right) \quad (3.20)$$

Where f_c and f_s are the resonant frequencies of the empty cavity and the filled cavity; Q_c and Q_s are the quality factors of the empty cavity and the filled cavity; V_c and V_s are the volumes of the cavity and the samples; f_l and f_h are the 3dB frequency from the resonant frequency.

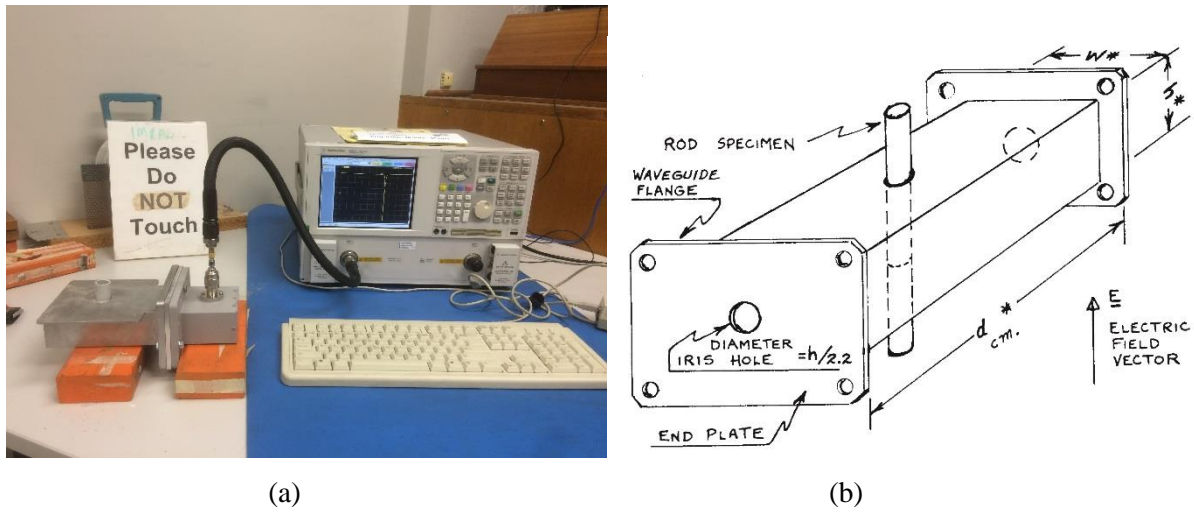


Fig. 3.11 Dielectric properties measurement using the resonant cavity perturbation technique. (a) Measurement setup using the short-circuited method, (b) methods recommended by the ASTM-D2520 (ASTM, 2013).

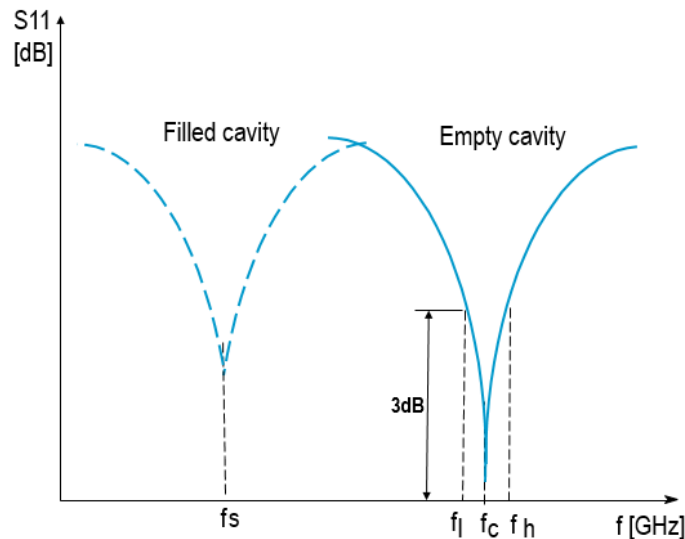


Fig. 3.12 Shift of resonant frequency and quality factor after insertion of a dielectric.

Although the accuracy of resonant cavity perturbation technique is very high and the resolution can be up to 10^{-4} , a cavity with a fixed dimension can only measure the DPs of a material at a specific frequency. To measure the DPs at other frequencies, one must resort to other techniques. In the thesis, this technique is used for dielectric properties measurement of powder minerals. However, the quality factor of the cavity used is not high enough, which yields unsatisfactory results.

3.5.2 Coaxial probe technique

This technique is the most popular technique for medium to high loss materials at the microwave frequency (Agilent, 2004; Marsland and Evans, 1987). As shown in Figure 3.13, the system setup consisting of a network analyser and a coaxial probe is very simple and straightforward. The measurement process involves touching the probe tip with a polished surface of a material or immersing the probe in the powder or liquid. By sending a signal from the probe to the material under test and analysing the reflected signal (phase and amplitude), the DPs can be computed. This method makes it possible to measure the DPs of materials over a wide frequency range from 500 MHz to 110 GHz (Brodie et al., 2015b).

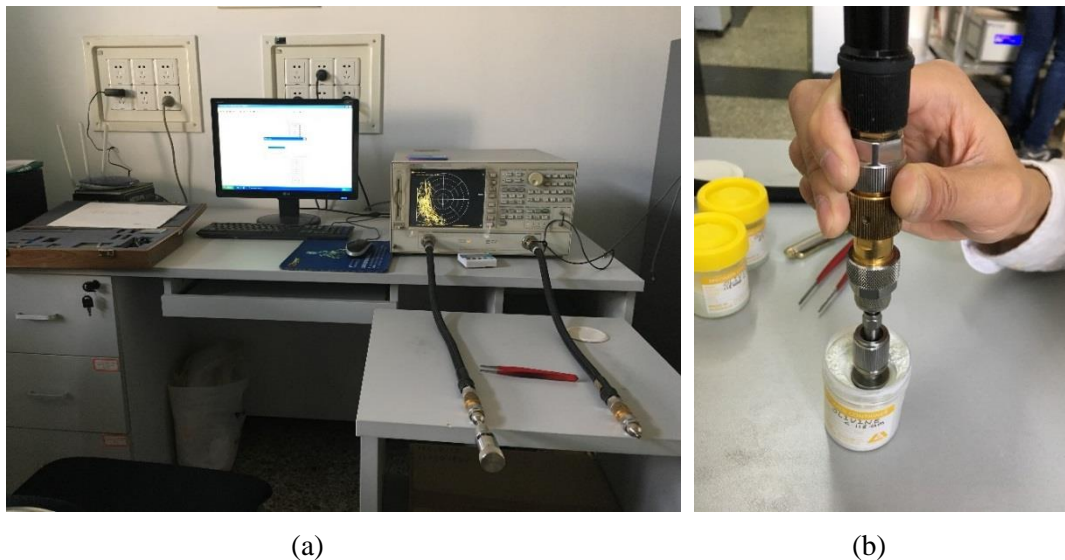


Fig. 3.13 The coaxial probe technique for dielectric properties measurement. (a) Measurement setup composing a coaxial probe, a network analyser and a computer; (b) Immersion of the probe into the materials under test.

The coaxial probe technique requires less material manipulation except that the surface must be very flat. However, one of its biggest drawback is that for low loss materials it requires the material under test to be infinitely large, which is sometimes very difficult to achieve (Nelson and Bartley, 1998). In other words, it is not suitable for low loss rock forming minerals. Attempts are made to measure the DPs of minerals and rocks from 1 GHz to 20 GHz using this technique (Figure 3.13). However, the results are far from satisfactory as the assumptions are no longer valid.

3.5.3 Free space technique

The free space technique is suitable for non-contact, broadband measurement of solid materials (Kraszewski and Nelson, 1990; Trabelsi and Nelson, 2003). A typical free-space system consists of a vector network analyzer, two antennae facing each other with a sample holder in between, as is shown in **Figure 3.14**. One antenna works as the transmitter and the other works as a receiver. The VNA is able to measure the attenuation and phase shift after inserting the sheet material and then compute the DPs. The sample must be far enough away from the antennae to be out of the reactive region, greater than wavelength λ , ideally in far field or $2d^2/\lambda$, where d is the largest dimension of the antenna. Samples must be large enough to contain the 3 dB beam spot. The sample must be thick enough to contain ideally 20 degrees of the wavelength of interest (Agilent, 2004). This technique is best for thin flat parallel faced materials, or other materials that can be formed into this shape.

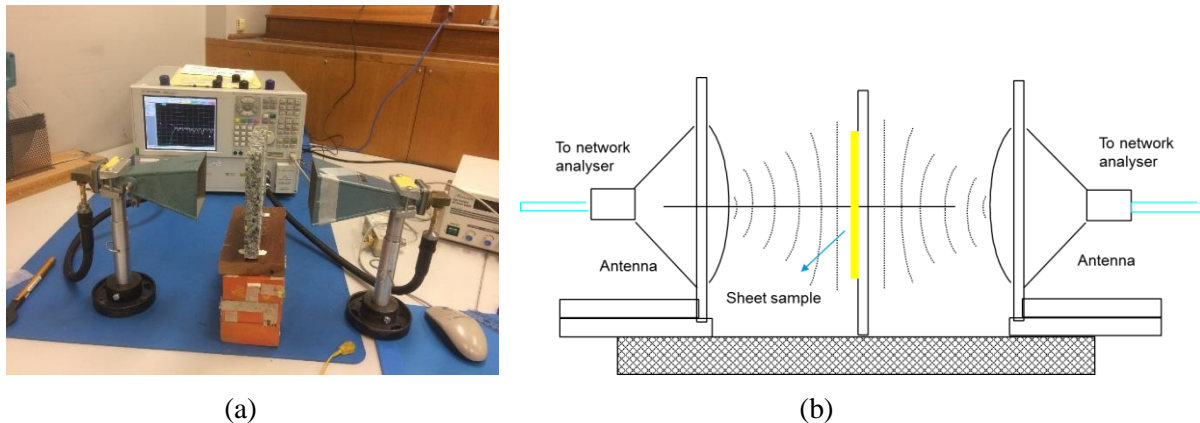


Fig. 3.14 Measurement of the dielectric properties using the free space technique. (a) Setup at Monash University, (b) Schematic of the technique (Agilent, 2004).

3.5.4 Parallel plate technique

The parallel plate technique is one of the most widely used method for measuring the DPs of solid materials or liquids (Agilent, 2004; ASTM, 2011). As shown in **Figure 3.15**, it involves the inserting of a very thin sheet in between a two parallel plate capacitor and measuring its capacitance, impedance and dissipation by an impedance measuring instrument (usually a passive/ active network analyser or an impedance analyser). The DPs are then computed by software. This method is mostly suitable for low frequency measurements of thin sheets or liquids. Since the results are quite sensitive to pores and air gaps, it is not recommended to be used to measure the DPs of powdered materials. The frequency range from as low as 1 Hz to up to several GHz. If enclosed in a temperature control system, this technique is also suitable to study the effect the DPs of materials at different temperatures.

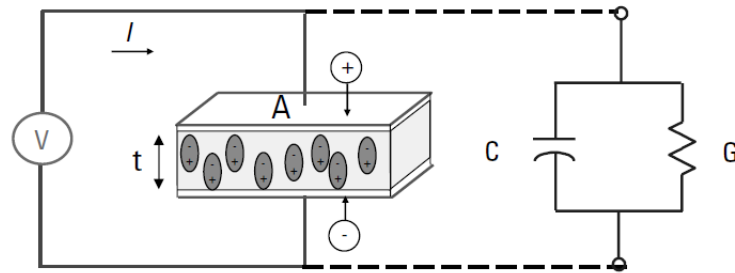


Fig. 3.15 Graphical representation and its equivalent circuit model of parallel plate methods (Agilent, 2004).

3.5.5 Dielectric properties of minerals and rocks

The DPs of minerals and rocks must be characterised to understand their interactions with microwave. The principle techniques used to characterise the DPs of materials rely on sending an EM wave to a material and analysing the reflected or transmitted signals. The most widely used methods are the cavity perturbation technique, coaxial transmission method, the free space methods and the parallel plate methods. Their strengths and applicability can be seen in Table 3.1.

Table 3.1 Common dielectric properties measurement techniques (After Agilent (2004)).

Measurement technique	Schematic	Strength and applicability
Parallel Plate		Low Frequency Best for thin flat sheets
Coaxial Probe		Broadband, Best for liquids, semi-solids
Transmission Line		Broadband Best for machine-able solids
Free Space		Broadband, mm-wave Non-contacting
Resonant Cavity		Single frequency, High accuracy, Best for low loss, or very thin samples

Table 3.2 summarises the DPs of most common rock-forming minerals. It shows that the silicates and carbonates have low loss factors, while metal oxide and most of the sulphides are more microwave sensitive. It should be noted that there is a great discrepancy in the magnitudes of loss factors of some minerals as different measurement techniques are used.

Table 3.2 Dielectric properties of minerals at 2.45GHz and room temperature.

Groups	Mineral	Chemical composition	Dielectric constant	Loss factor
Silicates	Feldspar	$\text{KAlSi}_3\text{O}_8 - \text{NaAlSi}_3\text{O}_8 - \text{CaAl}_2\text{Si}_2\text{O}_8$	6.01 ⁽ⁱ⁾	0.090 ⁽ⁱ⁾
	Quartz	SiO_2	2.82 ⁽ⁱⁱⁱ⁾	0.02 ⁽ⁱⁱⁱ⁾
			2.26 ^(v)	0.01 ^(v)
			3.89 ⁽ⁱⁱ⁾	5.4×10^{-4} ⁽ⁱⁱ⁾
	Biotite	$\text{K}(\text{Mg,Fe})_{2-3}\text{Al}_{1-2}\text{Si}_{2-3}\text{O}_{10}(\text{OH,F})_2$	5.9 ⁽ⁱⁱ⁾	2.04×10^{-4} ⁽ⁱⁱ⁾
	pyroxene	$\text{XY}(\text{Si,Al})_2\text{O}_6$	7.18 ⁽ⁱ⁾	0.17 ⁽ⁱ⁾
	Amphibole	$(\text{Mg, Fe, Ca})\text{-Si}_8\text{O}_{22}(\text{OH})_2$	7.37 ⁽ⁱ⁾	0.026 ⁽ⁱ⁾
	Muscovite	$\text{KAl}_2(\text{AlSi}_3\text{O}_{10})(\text{F,OH})_2$	8.69 ⁽ⁱ⁾	0.091 ⁽ⁱ⁾
	Phlogopite	$\text{KMg}_3(\text{AlSi}_3\text{O}_{10})(\text{F,OH})_2$	5.40 ^(iv)	1.6×10^{-3} ^(iv)
			9.77 ⁽ⁱ⁾	0.14 ⁽ⁱ⁾
Carbonates	Calcite	CaCO_3	8.87 ⁽ⁱⁱ⁾	4.93×10^{-4} ⁽ⁱⁱ⁾
	Hematite	Fe_2O_3	18.3 ⁽ⁱ⁾	2.23 ⁽ⁱ⁾
			4.90 ^(v)	0.40 ^(v)
Metal Oxides	Magnetite	Fe_3O_4	61.9 ⁽ⁱ⁾	10.7 ⁽ⁱ⁾
	Ilmenite	FeTiO_3	23.6 ⁽ⁱ⁾	11.2 ⁽ⁱ⁾
			3.75 ^(v)	2.26 ^(v)
	Geothite	$\text{FeO}(\text{OH})$	13.6 ^(v)	0.24 ^(v)
Sulphides	Galena	PbS	11.10	1.41
			6.75 ^(v)	0.12 ^(v)
			10.30 ⁽ⁱⁱⁱ⁾	2.28 ⁽ⁱⁱⁱ⁾
	Chalcopyrite	CuFeS_2	4.75 ^(v)	0.26 ^(v)
			11.01 ^(vi)	8.02 ^(vi)
			8.25 ^(v)	1.00 ^(v)
	Pyrite	FeS_2	8.25 ^(v)	1.00 ^(v)
	Water	H_2O	80	26

Sources: (i) Nelson et al (1989); (ii) Church et al. (1988); (iii) Walkiewicz et al. (1988); (iv) Santamarina (1989); (v) Harrison (1997).

3.6 Common microwave systems

3.6.1 Microwave basic components

Generally an industrial microwave heating system consists of a high voltage power supply, a microwave generator (also called a magnetron head for lower power systems), a circulator/isolator to ensure one-way microwave flow, a tuner to match the impedances of the generator and the load, an applicator to hold the sample, water load, and other measurement and protection devices (Meredith, 1998; Ong and Akbarnezhad, 2014). Figure 3.16 illustrates the basic components of an industrial microwave system. Depending on the EM field distribution in the applicator, the applicators could be divided into single-mode applicator, multi-mode applicator and travelling wave/open ended applicator.

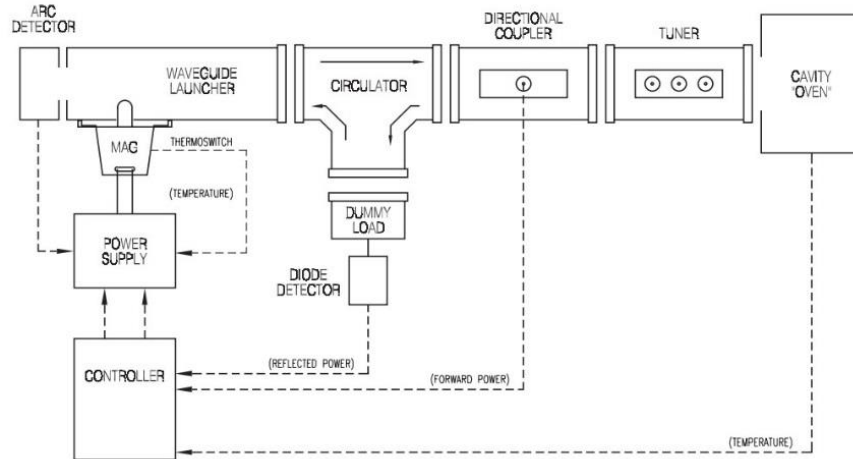


Fig. 3.16 Key components of an industrial microwave system (Courtesy of Richardson Electronics).

3.6.2 Industrial multimode microwave

This type of cavities is most commonly used for heating food (Mehdizadeh, 2015). It takes the simplest form of a large metallic box. One of its main features is that it could accommodate more than one mode in the cavity, thus has a good adaptability (NRC, 1994). The electric and magnetic field distribution in the cavity is more complicated. Figure 3.17 shows the scenario of a cavity operated in the TE_{324} mode. This means that in the X, Y and Z dimensions there are 3, 2 and 4 half wavelengths, respectively. Even though the EM fields are more evenly distributed, the field intensities are significantly lower when compared to that of a single-mode cavity. Moreover, when introducing a load in the cavity, the EM fields are not readily obtainable and the heating results could be unpredictable.

3.6.3 Industrial single mode microwave

For the single-mode applicators, the electric and magnetic field in the applicators have closed-form analytical solutions and are simple and straightforward (Metaxas and Meredith, 1983). Figure 3.18(a) shows the schematic of a single mode cavity adapted from a WR340 waveguide (Mehdizadeh, 2015). Normally on one side of the cavity is an iris (a metallic plate with a circular hole in the centre) for microwave to enter the applicator and on the other side is a metallic plate. The length of the waveguide is controlled to be an integral number of half wavelengths by moving the plunger. Due to reflections on the cavity walls there will be standing waves in the cavity. Figure 3.18(b) shows the electric field distribution in the TE_{103} mode in the applicator. For the microwave processing of materials, a small sized sample is placed at the crest where the electric field strength is the highest. If the dimension of a sample is the same as the interior dimension of the waveguide, the theoretical electric field distribution can be also easily obtained by solving the Maxwell's Equations with known boundary conditions. Since the size of the cavity is much smaller than that of a multi-mode cavity, at the same output power the electric field intensity in the single mode applicator would be several orders higher in magnitude. This

is the main reason why single mode microwave systems are more often used for laboratory research in the ISM sectors.

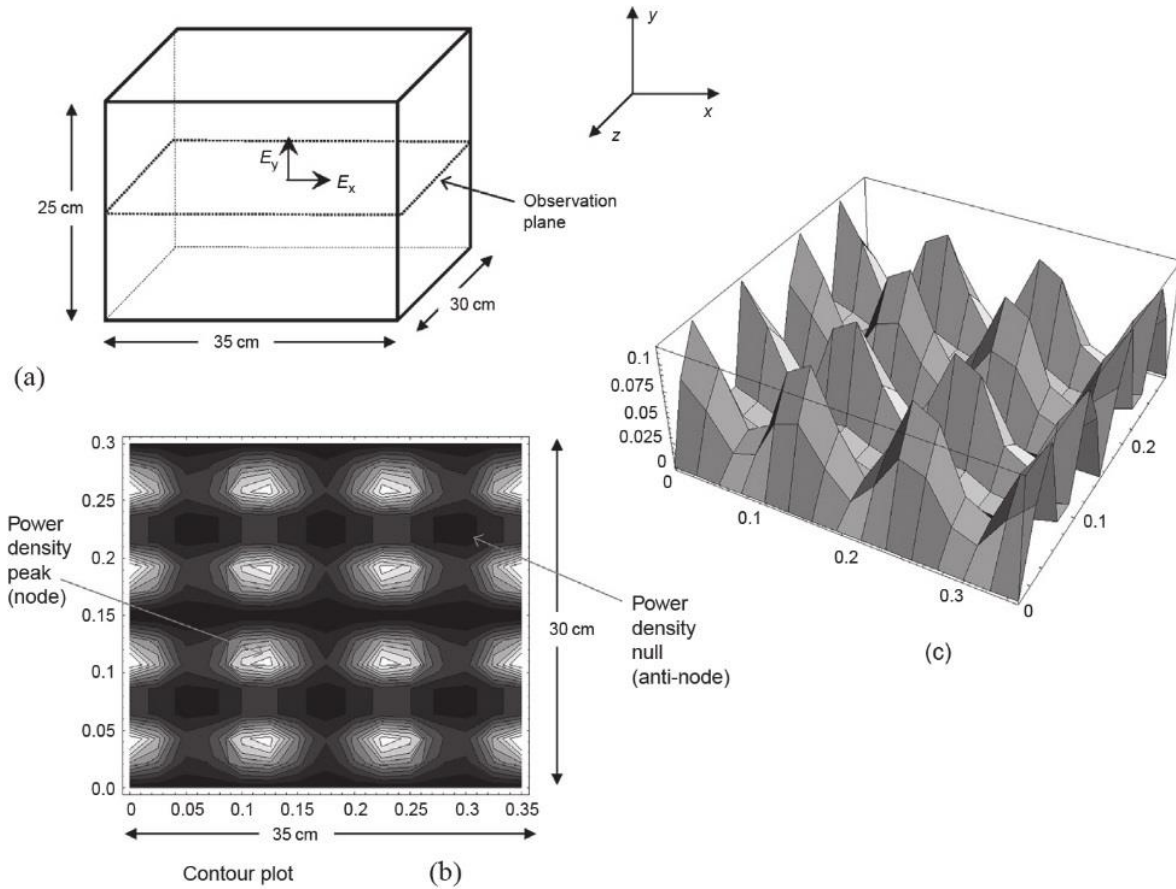


Fig. 3.17 Power density (E^2) distribution in a TE_{324} mode in a 35 cm × 30 cm × 25 cm cavity at 2.45 GHz. (a) Cavity and plane of observation in the middle of the height; (b) Contour plot of the electric field strength; (c) Three-dimensional plot (Mehdizadeh, 2015).

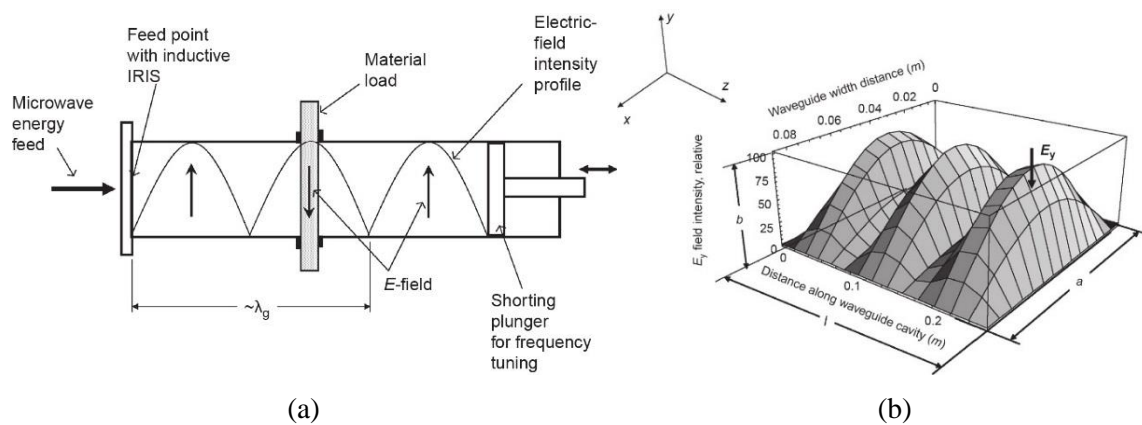


Fig. 3.18 Schematic of a single mode cavity. (a) Cavity adapted from a WR340 waveguide in the TE_{103} mode, (b) electric field distribution (Mehdizadeh, 2015).

3.6.4 Other applicators

The abovementioned single mode and multi-mode applicators could not be used in some cases, for instance, when microwave is used for assisted rock breakage on site or when conveyor belts are used for continuous processing. The open-ended applicators (antennas) could apply energy directly to the surface of the materials to be treated. The applicator types will be presented in Chapter 6.

3.7 Measurement of the dielectric properties of gabbro and granite

3.7.1 Sample preparation

The dielectric properties of two rock types (gabbro and granite) are measured in this thesis. Their petrographic properties can be found in Chapter 5. As the parallel plate technique is very sensitive to air gaps, special attentions should be paid to the sample preparation. A Buehler IsoMet 4000 Precision Saw is used to cut the 13 mm diameter cylinders into 1 mm thick sheet samples (Figure 3.19). The saw cuts materials with minimal specimen deformation and low kerf loss. It features a manual blade positioning knob that accelerates set-up while clamping a specimen in a large unrestricted workspace.

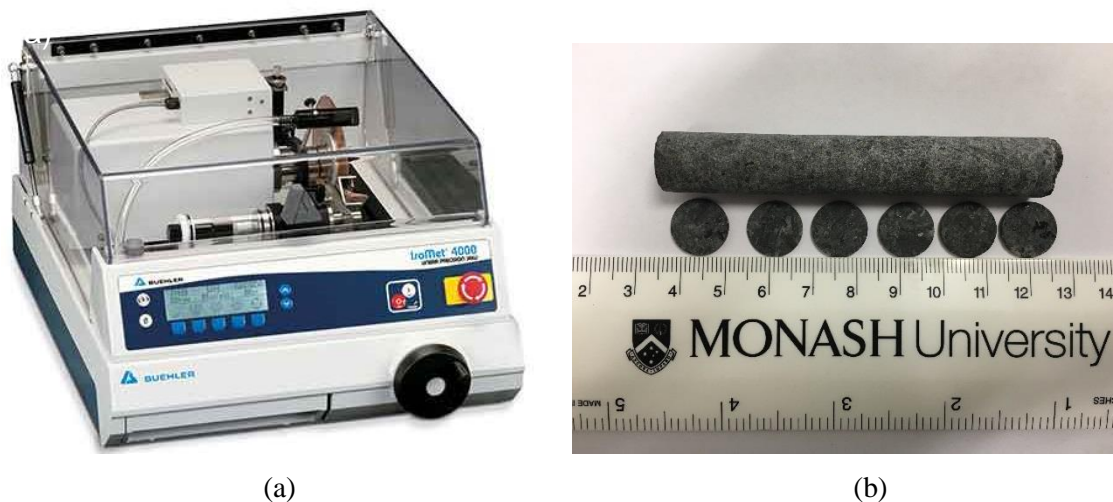


Fig. 3.19 Preparation of sheet samples. (a) IsoMet 4000 precision saw; (b) A 13mm drill core and 1 mm thick sheet samples.

3.7.2 Parallel plate measurement system

The parallel plate system used is shown in Figure 3.20. It consists of a radio frequency (RF) sample cell Broadband spectroscopy (BDS) 2200, a Quatro Cryosystem for temperature control and an RF impedance analyser Keysight E4991B, connected by the RF extension line and the BDS 2300 mounting rack. Ideally the system is able to measure the DPs of sheet materials in the frequency from 1 MHz to 3 GHz, however, experiences imply that beyond 2 GHz the accuracy of the test results will be compromised. This is a very common problem for the parallel plate techniques. The temperature control and data acquisition and processing is achieved on the computer with the help of the software package WinDeta.

The main parts of the Quatro Cryosystem **Figure 3.20(b)** are the cryostat BDS 1100, gas heating module BDS 1310, pressurizer module BDS 1320, vacuum system with BDS 1350, liquid nitrogen dewar, Quatro controller BDS 1330 and power supply BDS 1340. It is designed for easy, safe and fully automatic operations enabling computer controlled experiments. Ideally the temperature range is -160 °C to 400 °C, however, the maximum temperature achieved during the tests is 300 °C due to a bad sealing of the system. The BDS 2200 RF sample cell, as shown in **Figure 3.20(c)** has an inner diameter of 14 mm. The loss factor accuracy could be as low as 3×10^{-3} .

3.7.3 Test procedures

During the test, the procedures below are followed. The system is first calibrated using a 50 Ohms capacitor, a low loss capacitor and a short circuited end (**Figure 3.21**), then the DPs are measured automatically by the E4991B analyser from 1 MHz to 2 GHz and from 25 °C to 300 °C. The temperature increase rate is 5 °C/min.



(a)

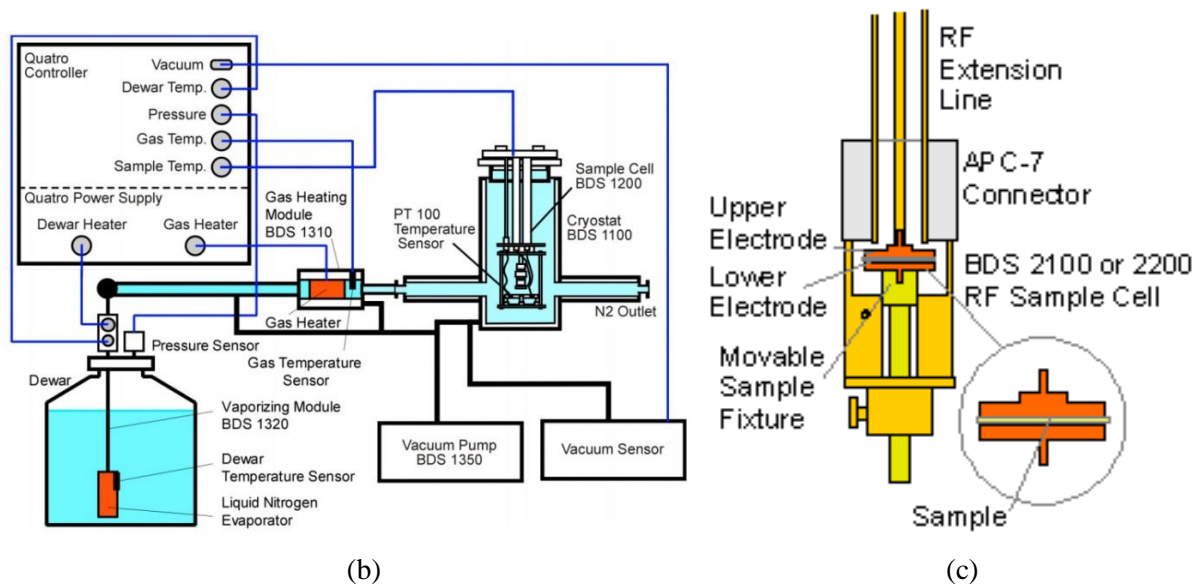


Fig. 3.20 Measurement of the dielectric properties using the parallel plate technique. (a) Photo of the measurement setup; (b) Schematic of the Quatro Cryosystem; (c) Schematic of the RF sample cell BDS 2200 (Courtesy of Novocontrol Technologies).



Fig. 3.21 Calibration sets for the Novocontrol RF cell (from left to right: 50 Ohms capacitor, low loss capacitor, short circuited ends).

3.7.4 Measurement results and discussion

(a) Gabbro

Figures 3.22 to 3.24 show the dielectric constant and loss factor of gabbro as a function of the frequency and temperature of three samples. Figures 3.25 and 3.26 show the arithmetic means of the three samples. It could be observed that for the Austral Black Gabbro the dielectric constant decreases as the frequency increases and that the loss factor fluctuates over the frequency range. The fluctuations come from the heterogeneity of the rock samples. At lower temperatures and MHz frequencies (Figure 3.22(a), Figure 3.23(a), Figure 3.24(a), Figure 3.25(a)), the dielectric constant decreases almost linearly as frequency increases. This is in good agreement with Nejadi (2014)'s measurement results of a Chinese basalt and

Wang (2016)'s measurement of sandstone. It is because at low frequencies all the polarisation mechanisms have enough time to follow the changing electric field and contribute to a larger dielectric constant. At higher frequencies (hundreds of MHz to GHz), the dielectric constant slightly increases or keeps almost unchanged. This is due to the fact that the ionic and interfacial polarisation mechanisms can no longer follow the fast changing electric field. As for the temperature dependence, the test results indicate that the dielectric constant (Figure 3.22(c), Figure 3.23(c), Figure 3.24(c), Figure 3.25(c)) increases at a very slow rate first and then decreases after reaching about 125 °C.

The dependence of loss factor on frequency and temperature is shown in Figures 3.22(b)-3.25(b) and 3.22(d)-3.25(d) and Figure 3.26(d), it is clear that it is hugely fluctuating rather than monotonic as either temperature or frequency increases. The fluctuations come from the inhomogeneity of the specimens which are composed of minerals of different types and grain sizes.

Figure 3.27 singles out the dielectric properties of the Austral Black Gabbro as a function of temperature at 2 GHz, which is close to the frequency of the industrial microwave to be used. It can be found that the dielectric constant decreases as temperature increases. The dielectric constant changes from 6.84 to 4.93 while the loss factor peaks at 0.95 with a minimum value of 0.48. The maximum value of loss factor appears at the temperature of 125 °C. According to Santamarina (1989), the dielectric constant and loss factor of gabbro at 3 GHz are 7 and 0.91, respectively. Zheng et al. (2005) found the dielectric constant and loss factor of gabbro at 9.75 GHz to be 7.95 and 0.4. It should be noted that the mineralogical compositions of the gabbro could be significantly different, therefore, it is necessary to characterise the dielectric properties of pure minerals, or the sub-group minerals if possible. This will help to understand the microwave weakening mechanisms and derive the dielectric properties of rocks.

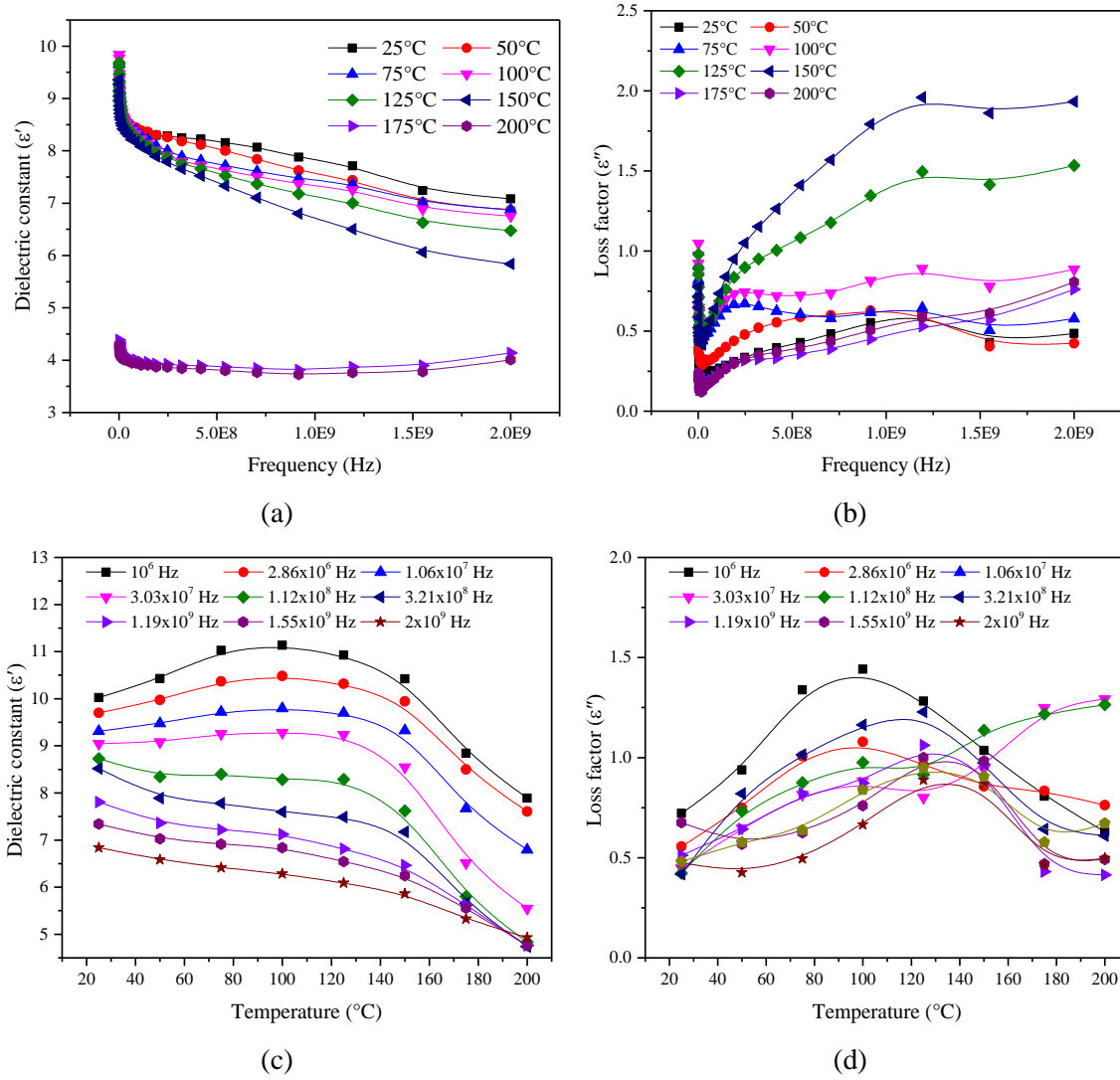


Fig. 3.22 Dielectric properties of the Austral Black Gabbro Sample No.4 as a function of frequency and temperature. (a) Dielectric constant vs frequency; (b) loss factor vs frequency; (c) dielectric constant vs temperature; (d) loss factor vs temperature.

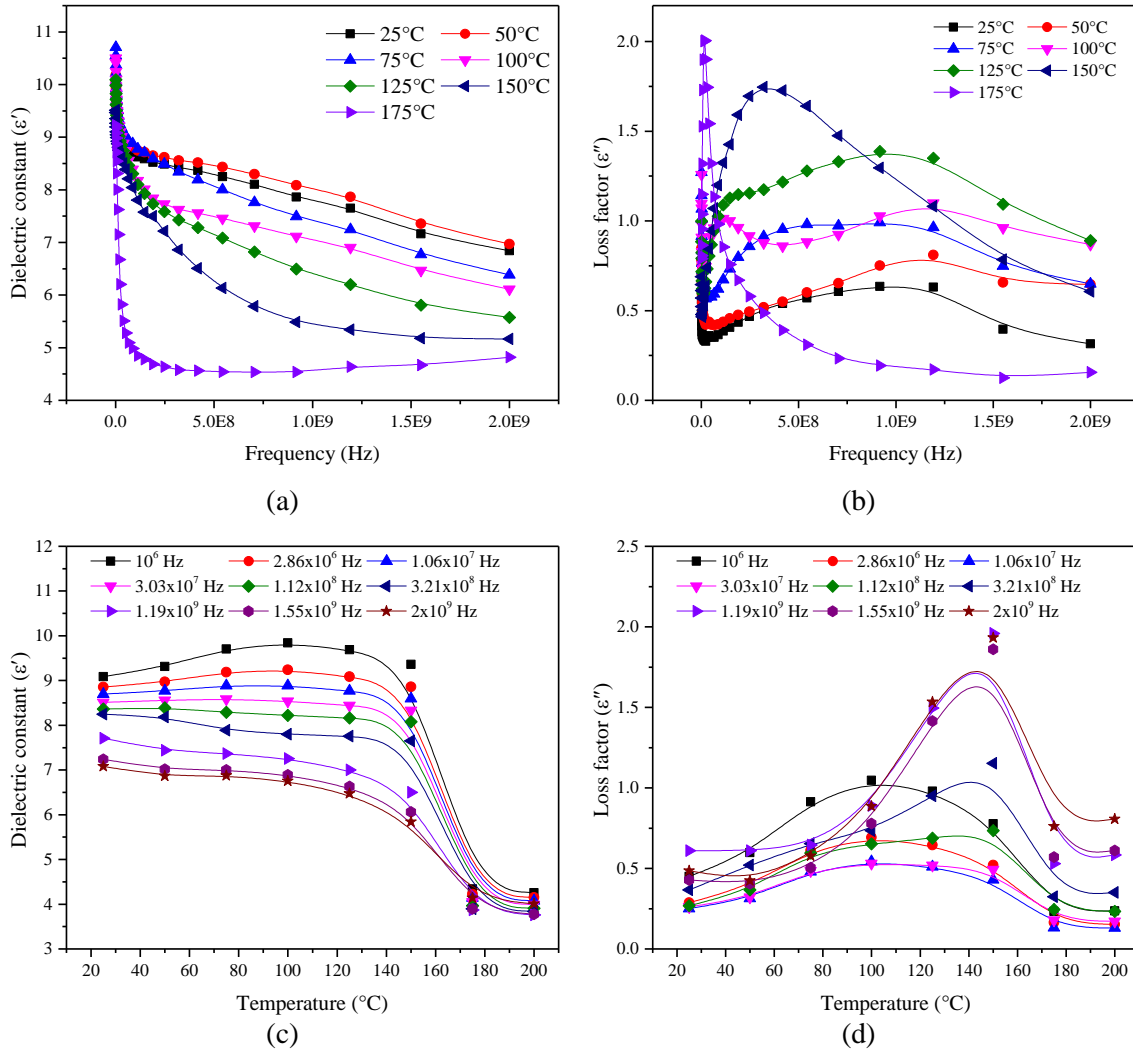


Fig. 3.23 Dielectric properties of the Austral Black Gabbro Sample No.5 as a function of frequency and temperature. (a) Dielectric constant vs frequency; (b) loss factor vs frequency; (c) dielectric constant vs temperature; (d) loss factor vs temperature.

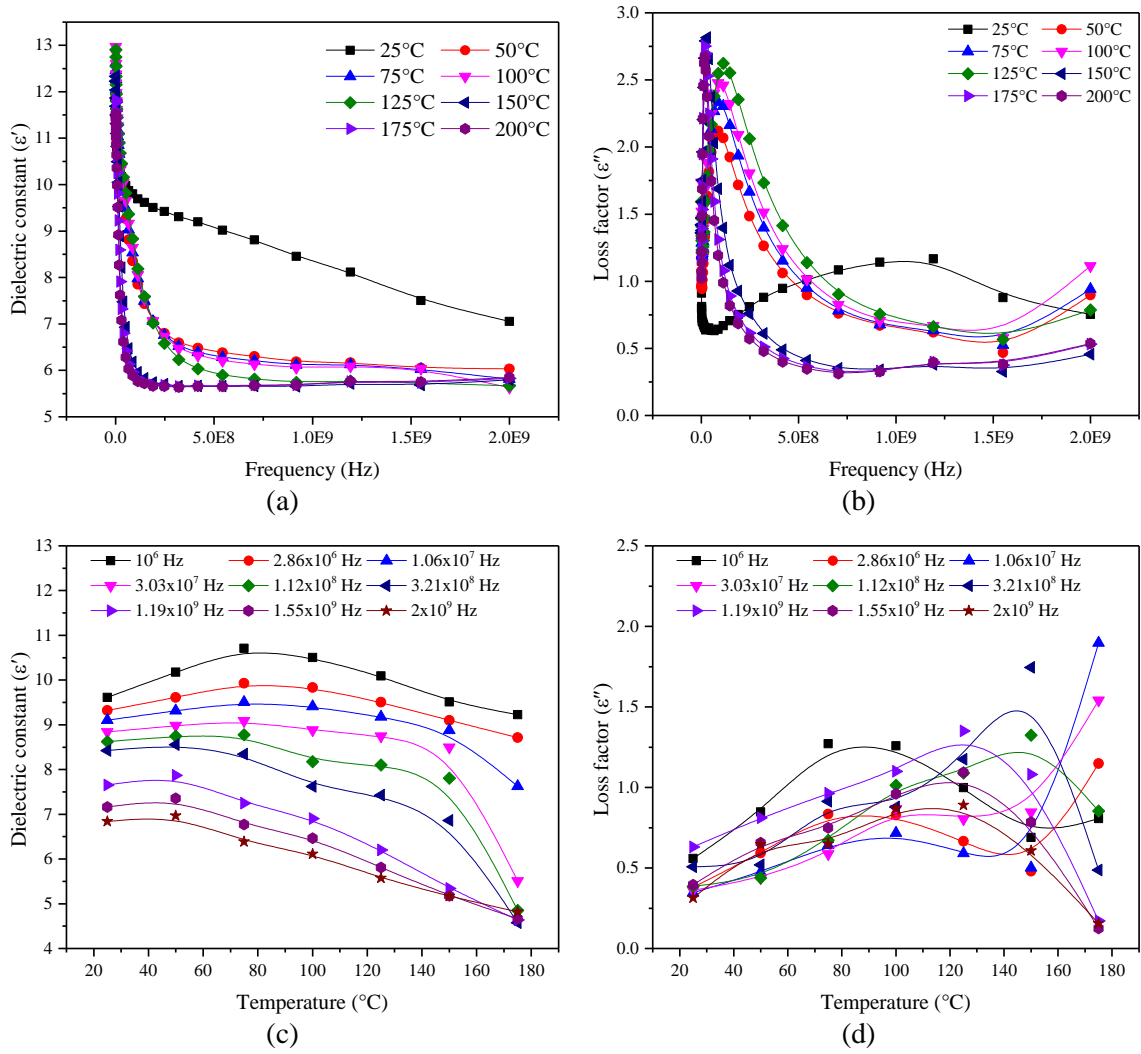


Fig. 3.24 Dielectric properties of the Austral Black Gabbro Sample No.6 as a function of frequency and temperature. (a) Dielectric constant vs frequency; (b) loss factor vs frequency; (c) dielectric constant vs temperature; (d) loss factor vs temperature.

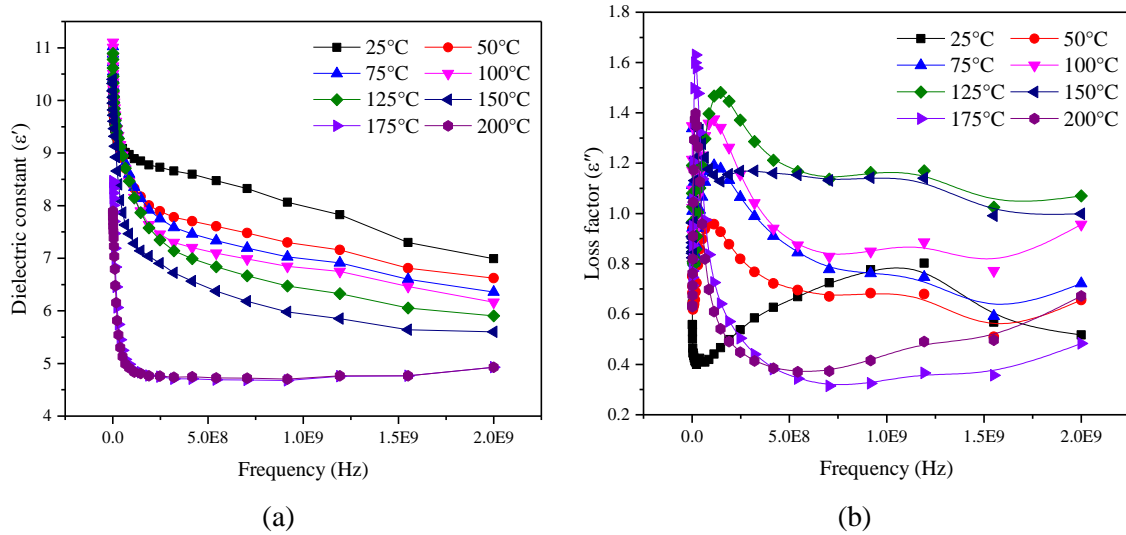


Fig. 3.25 Average dielectric properties of the Austral Black Gabbro as a function of frequency (samples 4-6). (a) Dielectric constant; (b) Loss factor.

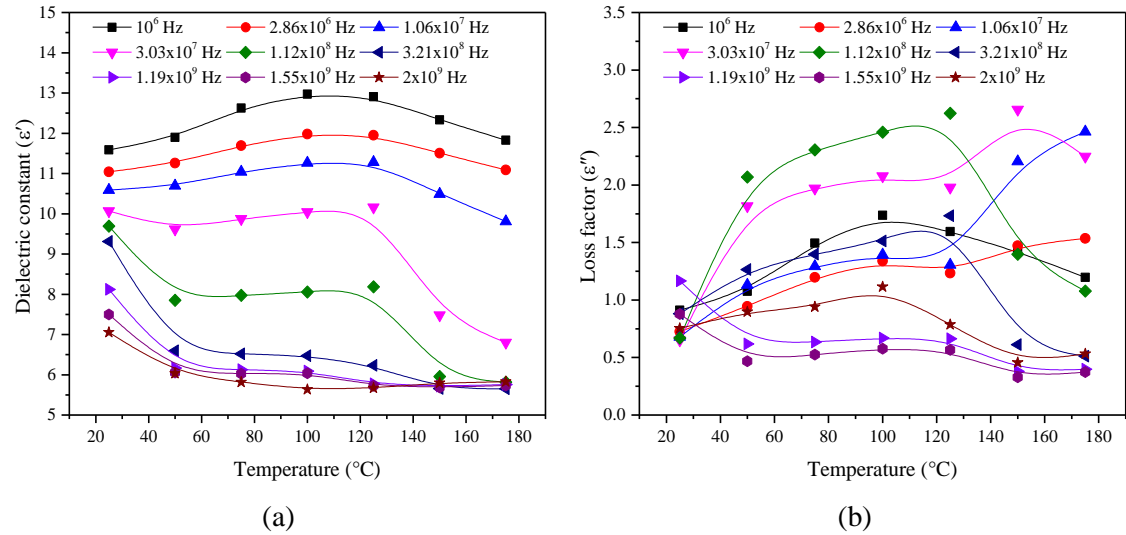


Fig. 3.26 Average dielectric properties of the Austral Black Gabbro as a function of temperature at selected frequencies. (a) Dielectric constant; (b) Loss factor.

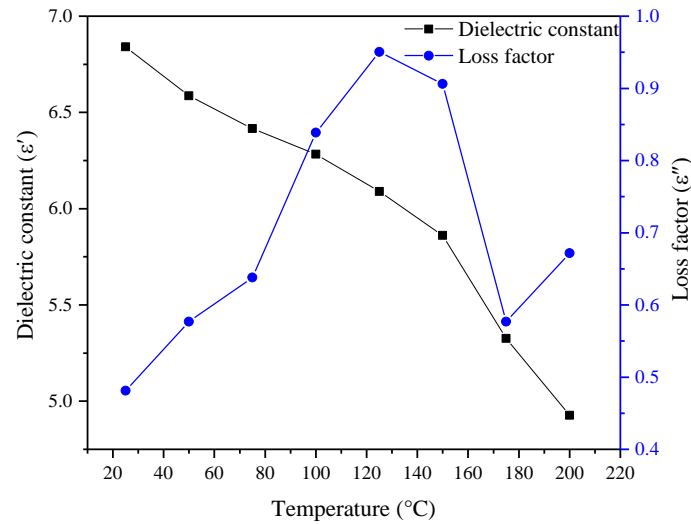


Fig. 3.27 Dielectric properties of the Austral Black Gabbro as a function of temperature at 2 GHz.

(b) Granite

Figures 3.28 to 3.30 show the dielectric constant and loss factor of the granite specimens as a function of frequency and temperature. For granite specimen No. 2, the loss factor is not affected by frequency, however, it increases as temperature increases. For specimen No. 3 the loss factor decreases as frequency increases. The difference may come from the heterogeneity of the rock samples. For specimen No. 5 the dielectric constant keeps unchanged while the loss factor increases as frequency increases.

Figure 3.31 shows the arithmetic means of the three samples. Unlike the gabbro specimens, whose dielectric constant decreases as the frequency increases, the dielectric constant of the granite specimens tested increase slightly as frequency and temperature increase. Figure 3.32 singles out the dielectric properties of the granite as a function of temperature at 1.43 GHz. It can be said that at a frequency of 1.43 GHz, the dielectric constant varies from 4.5 to 5.5 while the loss factor varies from 0.1 to 0.4. According to Santamarina (1989), the dielectric constant and loss factors of granite at 3 GHz fall into the range of 5-5.8 and 0.03-0.2, respectively. Campbell and Ulrichs (1969) measured the dielectric properties of alkali granite at 450 MHz and 35 GHz at room temperature. The dielectric constants are 5.3 and 5.2, the loss factor 0.2 and 0.12. The measurement results of the thesis are in good agreement of the literature.

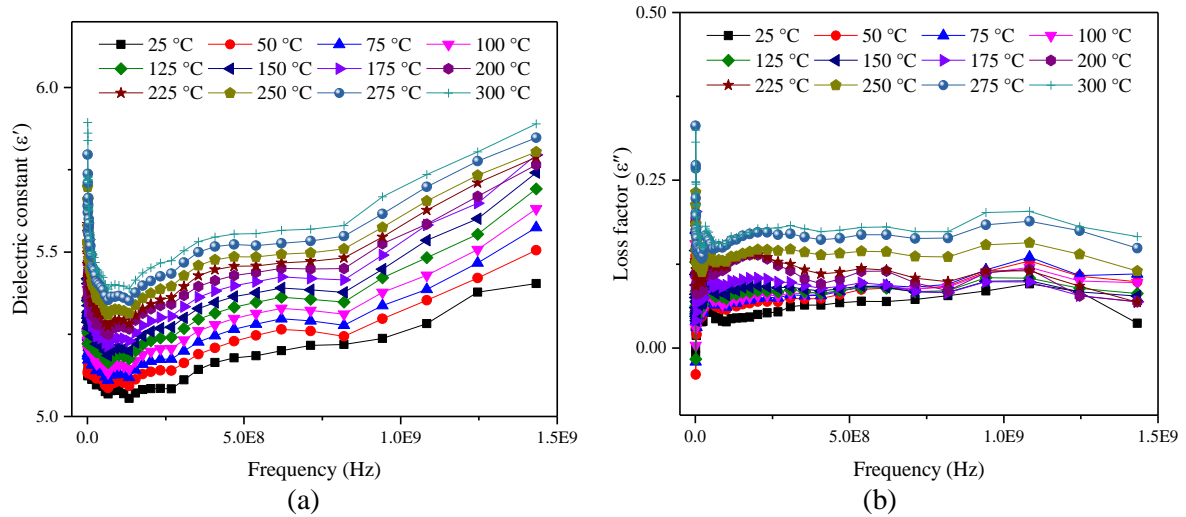


Fig. 3.28 Dielectric properties of the granite sample No.2 as a function of frequency and temperature. (a) Dielectric constant vs frequency; (b) loss factor vs frequency.

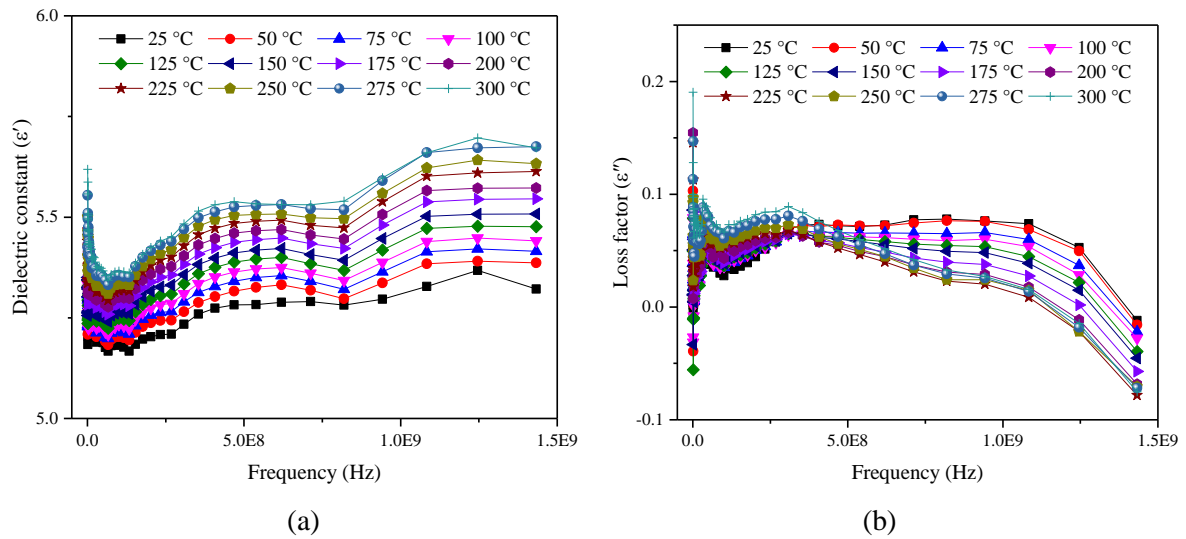


Fig. 3.29 Dielectric properties of the granite sample No.3 as a function of frequency and temperature. (a) Dielectric constant vs frequency; (b) loss factor vs frequency.

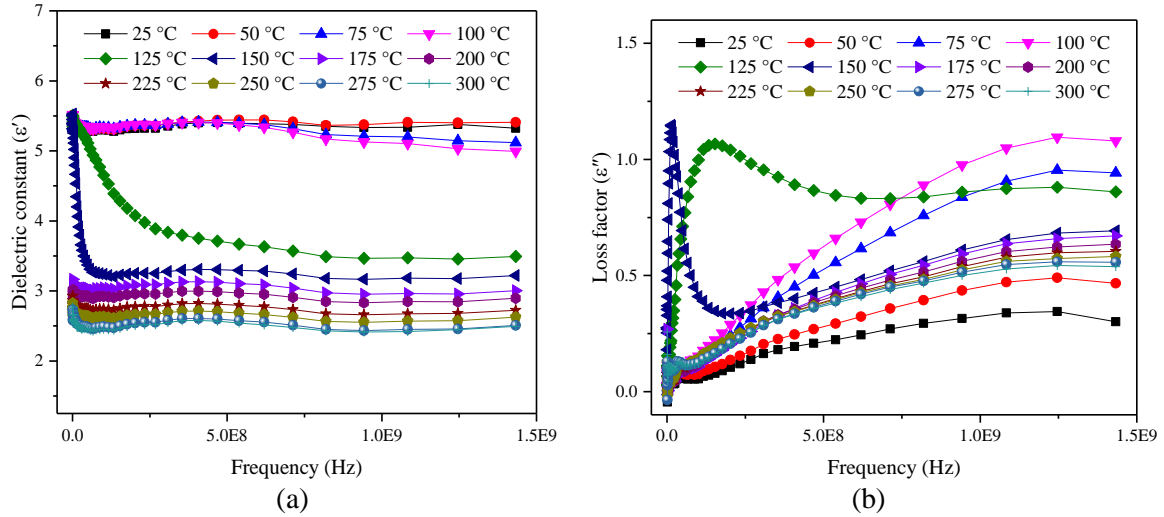


Fig. 3.30 Dielectric properties of the granite sample No.5 as a function of frequency and temperature.

(a) Dielectric constant vs frequency; (b) loss factor vs frequency.

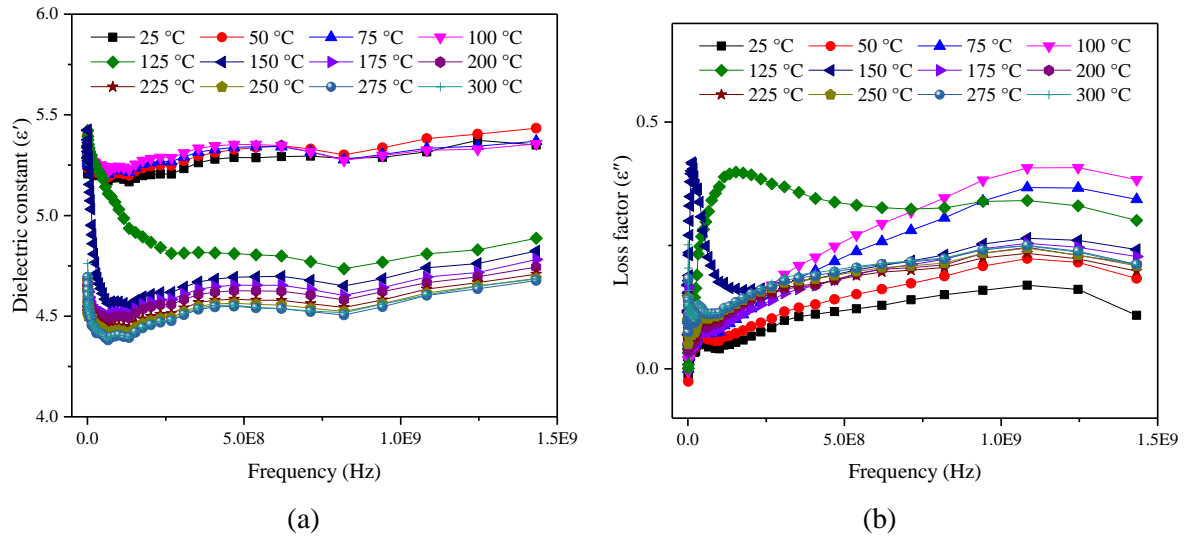


Fig. 3.31 Average dielectric properties of granite as a function of frequency and temperature. (a)

Dielectric constant vs frequency; (b) loss factor vs frequency.

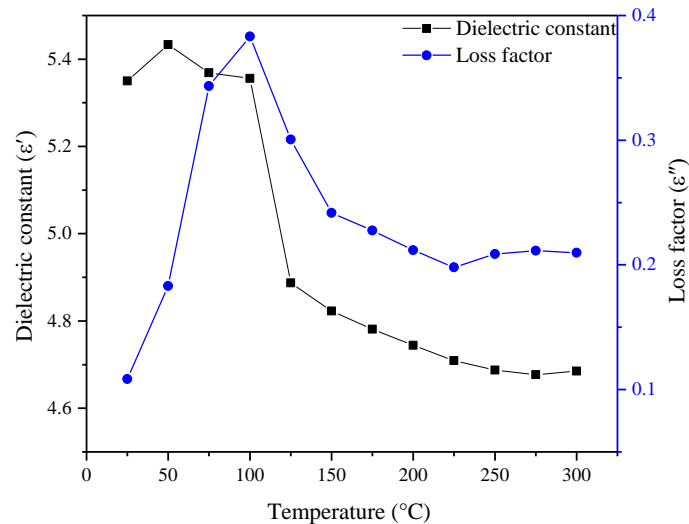


Fig. 3.32 Dielectric properties of the granite as a function of temperature at 1.43 GHz.

3.8 Research gaps

From reviewing the previous studies, the following research gaps are identified:

- Previous research focused on the microwave assisted ore comminution which involves high lossy ore minerals. The basic rock forming minerals are regarded as microwave transparent. Their dielectric properties and temperature and frequency dependency have not been systematically studied. In order to use microwave in TBM tunnelling, the dielectric properties of non-ore rocks and the rock forming minerals must be characterised.
- All existing researches concerning the effect of microwave radiation on the physical and mechanical properties of non-ore rocks used multimode cavity applicators, in which the samples are placed right in the centre of the cavities. This could not simulate the field application scenario where only one face of the rock can be exposed to microwave irradiation. Moreover the multimode microwave is large in cavity size and normally does not have an impedance tuning mechanism, resulting in a poor heating and weakening effect. Open-ended single-mode microwave applicators which involve intensified electric fields and travelling waves should be used in the tests.
- A comparative study on the microwave treatment of commonly encountered hard and abrasive rocks has not been conducted. The effect of microwave power level and exposure time on the physical and mechanical properties (heating rates, thermal gradient, ultrasonic wave velocities, Young's modulus, loading capacity, crack pattern and density, etc.) should be investigated. Special attention should be paid to study the crack patterns (trans-granular or intergranular) in different rock types.
- Although the feasibility of using microwave has been explored by [Nekoovaght \(2015\)](#), very little technical details in field application have been considered.

3.9 Concluding remarks

In this chapter, the polarisation mechanisms that govern the microwave-mineral/rock interactions are presented. Emphases are placed on the electronic and atomic polarisations which dominate in dielectric heating of hard and igneous rocks and the rock-forming minerals. The commonly used measurement techniques for DPs of materials are discussed and compared. The chapter also presented the common microwave applicators and their applicability in different industries. It summarises the research gaps for microwave to be used in TBM tunnelling.

The dielectric properties of gabbro and granite are measured using the parallel plate technique at a frequency from 1 MHz to 2 GHz and from room temperature to 300 °C. The test results show that the dielectric properties have a large fluctuation due to the heterogeneity of the natural rocks. The dielectric constant of the rocks at low frequencies decreases as frequency increases and then stabilise at high frequency, while the loss factor experience fluctuations and exhibits an unpredictability. At 2 GHz and from room temperature to 200 °C the dielectric constant of gabbro changes from 6.84 to 4.93 while the loss factor peaks at 0.95 with a minimum value of 0.48. At 1.43 GHz and from room temperature to 300 °C, the dielectric constant of granite varies from 4.5 to 5.5 while the loss factor varies from 0.1 to 0.4.

Reference

- Agilent, 2004. Basics of measuring the dielectric properties of materials - Application note, p. 34.
- Al-Harashsheh, M., 2005. A fundamental investigation into the microwave assisted leaching of sulphide minerals, Department of Chemical and Environmental Engineering, Faculty of Engineering University of Nottingham.
- Andriese, M.D., 2015. Microwave assisted comminution of sulfide ore. Michigan Technological University.
- ASTM, 2011. Standard test methods for AC loss characteristics and permittivity (dielectric constant) of solid electrical insulation. ASTM International, West Conshohocken, PA, USA.
- ASTM, 2013. Standard test methods for complex permittivity (dielectric constant) of solid electrical insulating materials at microwave frequencies and temperatures to 1650 oC. ASTM International, West Conshohocken, PA, USA.
- Atwater, J.E., Wheeler, J., R.R., 2004. Microwave permittivity and dielectric relaxation of a high surface area activated carbon. *Applied Physics A* 79, 125-129.
- Barba, A.A., d'Amore, M., 2012. Relevance of dielectric properties in microwave assisted processes, in: Costanzo, S. (Ed.), *Microwave materials characterization*. InTech, Rijeka, p. Ch. 06.
- Bengisu, M., 2013. *Engineering ceramics*. Springer Berlin Heidelberg.
- Binner, E., Lester, E., Kingman, S., Dodds, C., Robinson, J., Wu, T., Wardle, P., Mathews, J.P., 2014. A review of microwave coal processing. *Journal of Microwave Power and Electromagnetic Energy* 48, 35-60.
- Brodie, G., Jacob, M.V., Farrell, P., 2015. Techniques for measuring dielectric properties, *Microwave and radio-frequency technologies in agriculture: An introduction for agriculturalists and engineers*. De Gruyter Open, pp. 52-77.
- Brodie, G., Ryan, C., Lancaster, C., 2012. Microwave technologies as part of an integrated weed management strategy: A review. *International Journal of Agronomy* 2012, 14.
- Campbell, M.J., Ulrichs, J., 1969. Electrical properties of rocks and their significance for lunar radar observations. *Journal of Geophysical Research* 74, 5867-5881.

- Carter, C.B., Norton, M.G., 2007. Locally redistributing charge, *Ceramic materials: Science and engineering*. Springer New York, New York, NY, pp. 556-574.
- Chabay, R.W., Sherwood, B.A., 2015. *Matter and interactions*. Wiley.
- Chandrasekaran, S., Ramanathan, S., Basak, T., 2013. Microwave food processing—A review. *Food Research International* 52, 243-261.
- Chen, L., Ong, C.K., Tan, B.T.G., 1999. Amendment of cavity perturbation method for permittivity measurement of extremely low-loss dielectrics. *IEEE Transactions on Instrumentation and Measurement* 48, 1031-1037.
- Church, R.H., Webb, W.E., Salsman, J.B., 1988. *Dielectric properties of low-loss minerals*. United-States Department of the Interior and The Bureau of Mines.
- Clark, D.E., Sutton, W.H., 1996. Microwave processing of materials. *Annual Review of Materials Science* 26, 299-331.
- Cumbane, A., 2003. *Microwave treatment of minerals and ores: Dielectric properties of minerals-The Effect of microwave radiation on the grindability and mineral liberation*. University of Nottingham.
- Dal Corso, A., Baroni, S., Resta, R., 1994. Density-functional theory of the dielectric constant: Gradient-corrected calculation for silicon. *Physical Review B* 49, 5323-5328.
- Datta, A.K., 2001. *Handbook of microwave technology for food application*. Taylor & Francis.
- Folorunso, O., 2015. *Microwave processing of vermiculite*, Energy and Sustainability Research Division, Faculty of Engineering. University of Nottingham.
- Haque, K.E., 1999. Microwave energy for mineral treatment processes—a brief review. *International Journal of Mineral Processing* 57, 1-24.
- Harrison, P.C., 1997. *A fundamental study of the heating effect of 2.45GHz microwave radiation on minerals*. University of Birmingham.
- Hartlieb, P., Leindl, M., Kuchar, F., Antretter, T., Moser, P., 2012. Damage of basalt induced by microwave irradiation. *Minerals Engineering* 31, 82-89.
- Hoekstra, P., 1976. *Rock, frozen soil and ice breakage by high-frequency electromagnetic radiation: A review*. Department of Defense, Department of the Army, Corps of Engineers, Cold Regions Research and Engineering Laboratory, p. 17.
- Jin, L., 2015. *The impact of water on heat distribution and mechanical properties of basalt after microwave treatment*, Department of Mining and Materials. McGill University.
- Jokovic, V., 2012. *Microwave processing of minerals*.
- Jones, D.A., Lelyveld, T.P., Mavrofidis, S.D., Kingman, S.W., Miles, N.J., 2002. Microwave heating applications in environmental engineering—a review. *Resources, Conservation and Recycling* 34, 75-90.
- Jones, R.O., Gunnarsson, O., 1989. The density functional formalism, its applications and prospects. *Reviews of Modern Physics* 61, 689-746.
- Kaatze, U., Giese, K., 1980. Dielectric relaxation spectroscopy of liquids: frequency domain and time domain experimental methods. *Journal of Physics E: Scientific Instruments* 13, 133.
- Katz, J.D., 1992. Microwave sintering of ceramics. *Annual Review of Materials Science* 22, 153-170.
- Khalafalla, A.S., 1973. *Effect of frequency and temperature on rock dielectric properties*. Honeywell Incorporated.
- Kingman, S.W., 2006. Recent developments in microwave processing of minerals. *International Materials Reviews* 51, 1-12.
- Kingman, S.W., Rowson, N.A., 1998. Microwave treatment of minerals—a review. *Minerals Engineering* 11, 1081-1087.
- Kobusheshe, J., 2010. *Microwave enhanced processing of ores*, Department of Chemical and Environmental Engineering, Faculty of Engineering. University of Nottingham.
- Komarov, V., Wang, S., Tang, J., 2005. Permittivity and measurement, in: Chang, K. (Ed.), *Encyclopedia of RF and microwave engineering*, pp. 3693-3711.
- Kraszewski, A., Nelson, S., 1990. Study on grain permittivity measurements in free space. *Journal of Microwave Power and Electromagnetic Energy* 25, 202-210.
- Kraszewski, A.W., Nelson, S.O., 1994. Resonant-cavity perturbation measurement for mass determination of the perturbing object, *Conference Proceedings. 10th Anniversary. IMTC/94. Advanced Technologies in I & M. 1994 IEEE Instrumentation and Measurement Technology Conference (Cat. No.94CH3424-9)*, pp. 1261-1264 vol.1263.

- Lidström, P., Tierney, J., Wathey, B., Westman, J., 2001. Microwave assisted organic synthesis—a review. *Tetrahedron* 57, 9225-9283.
- Liu, F., 2015. Exploration of microwave-assisted breakage of rocks: The effect of size, shape, and internal discontinuity of rock on microwave distribution, Department of Mining and Materials.
- Makul, N., Rattanadecho, P., Agrawal, D.K., 2014. Applications of microwave energy in cement and concrete – A review. *Renewable and Sustainable Energy Reviews* 37, 715-733.
- Marsland, T.P., Evans, S., 1987. Dielectric measurements with an open-ended coaxial probe. *IEE Proceedings H - Microwaves, Antennas and Propagation* 134, 341-349.
- Matzler, C., Wegmuller, U., 1987. Dielectric properties of freshwater ice at microwave frequencies. *Journal of Physics D: Applied Physics* 20, 1623.
- Mehdizadeh, M., 2015. Chapter 6 - Applicators and probes based on the open end of microwave transmission lines, *Microwave/RF Applicators and Probes (Second Edition)*. William Andrew Publishing, Boston, pp. 184-218.
- Menéndez, J.A., Inganzo, M., Pis, J.J., 2002. Microwave-induced pyrolysis of sewage sludge. *Water Research* 36, 3261-3264.
- Meredith, R.J., 1998. *Engineers' handbook of industrial microwave heating*. Institution of Electrical Engineers, London, UK.
- Metaxas, A.C., Meredith, R.J., 1983. *Industrial microwave heating*. IET.
- Mingos, D.M.P., Baghurst, D.R., 1991. Applications of microwave dielectric heating effects to synthetic problems in chemistry. *Chemical Society Reviews* 20, 1-47.
- Nejati, H., 2014. Analysis of physical properties and thermo – mechanical induced fractures of rocks subjected to microwave radiation, Department of Mining and Materials. McGill.
- Nekoovaght, P.M., 2009. An investigation on the influence of microwave energy on basic mechanical properties of hard rocks. Concordia University.
- Nekoovaght, P.M., 2015. Physical and mechanical properties of rocks exposed to microwave irradiation: Potential application to tunnel boring, Department of Mining and Materials. McGill University.
- Nelson, S., 2015. *Dielectric properties of agricultural materials and their applications*. Elsevier Science.
- Nelson, S.O., 2001. Measurement and calculation of powdered mixture permittivities. *IEEE Transactions on Instrumentation and Measurement* 50, 1066-1070.
- Nelson, S.O., Bartley, P.G., 1998. Open-ended coaxial-line permittivity measurements on pulverized materials. *IEEE Transactions on Instrumentation and Measurement* 47, 133-137.
- Nelson, S.O., Lindroth, D.P., Blake, R.L., 1989. Dielectric properties of selected and purified minerals at 1 to 22 GHz. *Journal of Microwave Power and Electromagnetic Energy* 24, 213-220.
- Nelson, S.O., Trabelsi, S., 2012. Factors influencing the dielectric properties of agricultural and food products. *Journal of Microwave Power and Electromagnetic Energy* 46, 93-107.
- NRC, 1994. *Microwave processing of materials*. The National Academies Press, Washington, DC.
- Ong, K.C.G., Akbarnezhad, A., 2014. *Microwave-assisted concrete technology: Production, demolition and recycling*. CRC Press.
- Peinsitt, T., Kuchar, F., Kargl, H., Restner, U., Sifferlinger, N., Moser, P., 2008. Microwave heating of rocks with different water content, *Proceedings of Microwave Technology '08*, pp. 1-9.
- Pickles, C.A., 2009a. Microwaves in extractive metallurgy: Part 1 – Review of fundamentals. *Minerals Engineering* 22, 1102-1111.
- Pickles, C.A., 2009b. Microwaves in extractive metallurgy: Part 2 – A review of applications. *Minerals Engineering* 22, 1112-1118.
- Roberts, S., Von Hippel, A., 1946. A new method for measuring dielectric constant and loss in the range of centimeter waves. *Journal of Applied Physics* 17, 610-616.
- Roy, R., Agrawal, D., Cheng, J., Gedevanishvili, S., 1999. Full sintering of powdered-metal bodies in a microwave field. *Nature* 399, 668.
- Santamarina, J.C., 1989. Rock excavation with microwaves: A literature review, in: Kulhawy, F.H. (Ed.), 1989 Foundation Engineering Conference. ASCE, Evanston, Illinois, United States, pp. 459-473.
- Satish, H., 2005. Exploring microwave assisted rock breakage for possible space mining applications, Department of Mechanical Engineering. McGill University.
- Sebastian, M.T., Uvic, R., Jantunen, H., 2017. *Microwave materials and applications*. Wiley.

- Sengwa, R.J., Soni, A., 2008. Dielectric properties of some minerals of western Rajasthan. *Indian Journal of Radio and Space Physics* 37, 57-63.
- Sheen, J., 2005. Study of microwave dielectric properties measurements by various resonance techniques. *Measurement* 37, 123-130.
- Sombatsompop, N., Kumnuantip, C., 2006. Comparison of physical and mechanical properties of NR/carbon black/reclaimed rubber blends vulcanized by conventional thermal and microwave irradiation methods. *Journal of Applied Polymer Science* 100, 5039-5048.
- Standish, N., 1989. Unusual effects of microwave irradiation in granular materials, First Australian Symposium on Microwave Power. University of Wollongong. Microwave Applications Research Centre.
- Standish, N., Worner, H., Kaul, H., 1988. Microwave drying of brown coal agglomerates. *Journal of Microwave Power and Electromagnetic Energy* 23, 171-175.
- Torgovnikov, G.I., 1993. Dielectric properties of wood and wood-based materials. Springer-Verlag.
- Trabelsi, S., Nelson, S.O., 2003. Free-space measurement of dielectric properties of cereal grain and oilseed at microwave frequencies. *Measurement Science and Technology* 14, 589.
- Ulaby, F.T., Bengail, T., Eastl, J., Dobson, M.C., Garvin, J., Evans, D., 1988. Microwave dielectric spectrum of rocks, NASA TM ; 89719.
- Ulaby, F.T., Bengal, T.H., Dobson, M.C., East, J.R., Garvin, J.B., Evans, D.L., 1990. Microwave dielectric properties of dry rocks. *IEEE Transactions on Geoscience and Remote Sensing* 28, 325-336.
- Venkatesh, M.S., Raghavan, G.S.V., 2004. An overview of microwave processing and dielectric properties of agri-food materials. *Biosystems Engineering* 88, 1-18.
- von Hippel, A., 1954. Dielectrics and waves. John Wiley & Sons, Inc., New York.
- Wang, H., 2016. Microwave heating effects on formation damages in tight gas sands, Department of Petroleum Engineering, Faculty of Science and Engineering. Curtin University, Curtin.
- Walkiewicz, J.W., Kazonich, G., McGill, S.L., 1988. Microwave heating characteristics of selected minerals and compounds. *Minerals and Metallurgical Processing* 5, 39-42.
- Zhai, X., Zhang, P., Liu, C., Bai, T., Li, W., Dai, L., Liu, W., 2012. Highly luminescent carbon nanodots by microwave-assisted pyrolysis. *Chemical Communications* 48, 7955-7957.

CHAPTER 4

Heating Rates and Dielectric Properties of Low Loss Rock Forming Minerals

4.1 Introduction

Rock breakage and fracturing using microwave makes use of the differences in dielectric properties and thermal expansion rates of rock forming minerals. Although ore minerals have been extensively studied in the mineral processing sector, low loss (weak microwave absorbing) rock forming minerals have been seldom touched, or they are categorised as poor microwave absorbers or even deemed as transparent to microwave. To determine the heating rates of minerals and rocks, the knowledge of the dielectric properties of the composing minerals are of paramount importance (Nelson, 2015b). This is very essential to understand the thermal damage of rocks from the fundamental physics. However, the characterisation of dielectric properties of low loss minerals is very technically challenging, especially when they are in the form of powder. This chapter investigates the heating rates of 8 basic rock forming minerals at different power levels. It then presents the derivations of the loss factors of those minerals at the microwave frequency of 2.45 GHz using a new method which combines the microwave heating tests, the effective medium theory and numerical simulations. The method is then used to predict the heating rates of mineral mixtures (simulated rocks) and compared with the values from experiments. The results indicate that using the effective medium theories the heating rates could be predicted at a high confident level.

4.2 Literature review on heating rates of minerals

4.2.1 Literature review on mineral heating rates

The research of microwave treatment of materials started with the heating rate tests of minerals and chemical compounds. In those research, different minerals, most of the time in the form of powder, sometimes solids, are placed in either a domestic microwave oven or an industrial microwave cavity. The temperature of the minerals subjected to microwave exposure is measured simultaneously or at the end of the test. Heating rates are then determined and compared. Based on the heating rates, minerals are classified into different categories, usually as high loss, medium loss and low loss materials.

The first ever recorded heating rate tests by microwave are reported by Ford and Pei (1967) who used a 1.6 kW Raytheon oven at 2.45 GHz to heat 17 metal (calcium, iron, magnesium, manganese, lead and zinc, etc.) oxides and sulphides and one charcoal. They found that the dark coloured materials may be rapidly heated to about 1000 °C where a cut-off occurs and that the light coloured materials require longer times for heating, but in certain cases reached higher temperatures. They proposed uses for this phenomenon, including reacting metal sulphides with hydrogen to produce metal and hydrogen sulphide and reacting ammonia and carbon to produce hydrogen cyanide. Mention should be made that no low loss minerals are heated in their research.

Chen et al. (1984) treated 40 minerals in an industrial microwave with a maximum output power of 800 watts for up to 5 mins. The purified minerals with a mass of 0.5-1 gram were placed in a closed cavity (See Figure 4.1). Difficulties were reported in making accurate temperature measurements within the microwave cavity using an infrared camera. They found that most silicates, carbonates and sulfates, some oxides and some sulfides are transparent to microwave energy but other oxides are readily heated. Both natural and synthetic jarosite-type compounds (a hydrous sulfate of potassium and iron) are unaffected by microwave irradiation. Most sulfides, arsenides, sulfosalts and sulfarsenides are readily heated and consequently, fuse or dissociate prior to eventual oxidation. Microwave effects are compositionally dependent, and elemental substitutions affect the mineral behaviour. For instance, the high-Fe sphalerite ((Fe,Zn)S) is more microwave sensitive than the high-Zn sphalerite. Table 4.1 shows the minerals they asserted are transparent to microwave irradiation, which include muscovite, potassium feldspar (orthoclase) and quartz. This pioneering work has far reaching negative impacts as following researchers believe that microwave could not heat those low loss minerals.

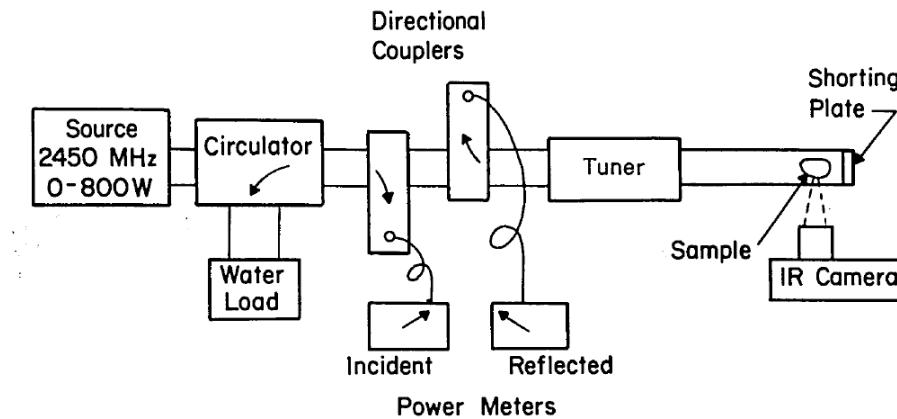


Fig. 4.1 Schematic of the microwave system used for heating rate tests by Chen et al. (1984).

Table 4.1 Minerals transparent to microwave irradiation (Chen et al., 1984).

Mineral Class	Minerals/Compounds
Carbonates	Aragonite, calcite, dolomite, siderite
Jarosite-type compounds	Argentojarosite, synthetic natrojarosite, synthetic plumbogjarosite
Silicates	Almandine, allanite, anorthite, gadolinite, muscovite, potassium feldspar, quartz, titanite, zircon
Sulphates	Barite, gypsum
Others	Fergusonite, monazite, sphalerite (low-Fe), stibnite

Walkiewicz et al. (1988) furthered the study on microwave heating of minerals and reagent grade inorganic compounds at 2.45 GHz. As shown in Figure 4.2(a), they used a domestic microwave oven with a 1 litre water load in it as well. Samples of 25 g or a constant volume of 18 mL for low-density

materials were placed in a 20-mL alumina cylindrical crucible and enclosed in a 250-mL beaker in an inert environment. Their test results (Table 4.2) revealed that the highest temperatures are obtained with carbon and most of the metal oxides: NiO, MnO₂, Fe₃O₄, Co₂O₃, CuO and WO₃. Most metal sulphides heat well but without any consistent pattern. Gangue minerals such as quartz, calcite and feldspar (albite and orthoclase) do not heat.

McGill et al. (1988) continued to examine the effect of microwave power level (500 W to 2000 W) on the heating rates of minerals using a WR975 waveguide applicator (Figure 4.2(b)). They found that quartz (SiO₂) and calcite (CaCO₃), which are common gangue constituents, are not microwave receptive. They argued that the slight increase in temperature observed as power increase is due to oven heating effects from a lack of an absorbing load. In these situations the percentage for error in the sample temperature measurements increases and they believed that there is no true increase in heating rates with increasing input power levels for these non-absorbing samples (McGill et al., 1988).

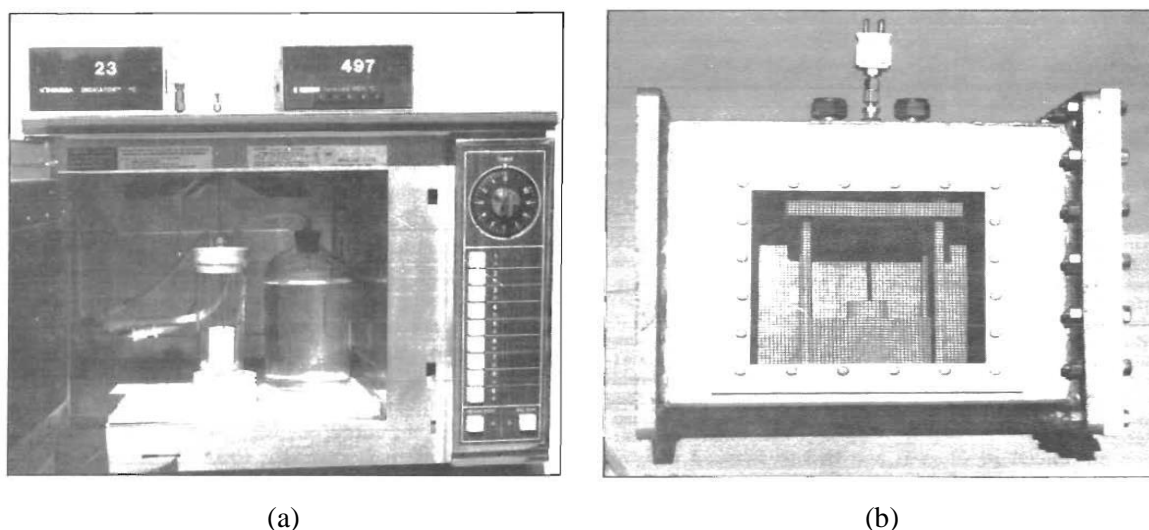


Fig. 4.2 Microwave system used for heating rates measurement by McGill et al. (1995). (a) Domestic microwave oven with a 1 litre water load at 1 kW. (b) Waveguide applicator for varying power levels from 0.5 kW to 2 kW.

Tinga (1989) reported the microwave heating behaviour of several metal oxides. The metal oxides are classified based on the heating rates into hyperactive, active, difficult-to-heat and inactive. He also demonstrated that microwave energy could be effective in the heating of minerals and inorganic compounds. The heating rates of ore minerals are also examined by Wong (1975), Liu et al. (1990), and Barani et al. (2012). As can be seen in Table 4.2, ore minerals have much better microwave absorbing capacities than the commonly found rock forming minerals. In the context of microwave assisted TBM tunnelling, only the low loss (gangue) minerals are often encountered and of interest. Therefore, this thesis will not elaborate on the testing results of ore minerals.

Table 4.2 Heating of natural minerals at 1 kW using a domestic oven (Walkiewicz et al., 1988).

Mineral	Chemical composition	Temperature after 1 min (°C)	Maximum temperature (°C)	Time (min)
Albite (plagioclase)	NaAlSi₃O₈	53	69	7
Arizonite	Fe ₂ O ₃ - 3TiO ₂	84	290	10
Chalcocite	Cu ₂ S	506	746	7
Chalcopyrite	CuFeS ₂	920	920	1
Chromite	FeCr ₂ O ₄	89	155	7
Cinnabar	HgS	83	144	8.5
Galena	PbS	755	956	7
Hematite	Fe ₂ O ₃	102	182	7
Magnetite	Fe ₃ O ₄	861	1258	2.75
Marble	CaCO₃	50	74	4.25
Molybdenite	MoS ₂	108	192	7
Orpiment	As ₂ S ₃	71	92	4.5
Orthoclase	KAlSi₃O₈	49	67	7
Pyrite	FeS ₂	816	1019	6.75
Pyrrhotite	Fe _{1-x} S	730	886	1.75
Quartz	SiO₂	52	79	7
Sphalerite	ZnS	65	88	7
Tetrahedrite	Cu ₁₂ Sb ₄ S ₁₃	64	151	7
Zircon	ZrSiO ₄	41	52	7

Harrison (1997) irradiated 25 minerals with a 650 W domestic microwave oven for 180 s and classified minerals into three groups, according to their thermal responses (peak temperature and heating rates) to microwave.

- Group I-high heating rate minerals (temperature over 175 °C), such as pyrites, galena, magnetite, pyrrhotite, bornite, and chalcopyrite.
- Group II-medium heating rate minerals (temperature between 68 and 110 °C), such as ilmenite, hematite, cassiteite and bauxite;
- Group III-Low heating rate minerals (temperature below 50 °C), such as **quartz**, **feldspar**, calcite, **mica**, barites, sphalerite and rutile.

Lu et al. (2017) used a 2 kW multimode cavity to treat eleven basic rock-forming minerals for up to 3 minutes. It is not clear whether the microwave is equipped with an impedance matching tuner. As shown in Figure 4.3, it is observed that rock-forming minerals exhibits different responses to microwave treatment. Enstatite presents the strongest microwave absorption capacity by a large margin and most of the rock-forming minerals are weak microwave absorbers. Through SEM-EDX analysis, they asserted that the heating rates of minerals are governed by the iron abundance in the minerals.

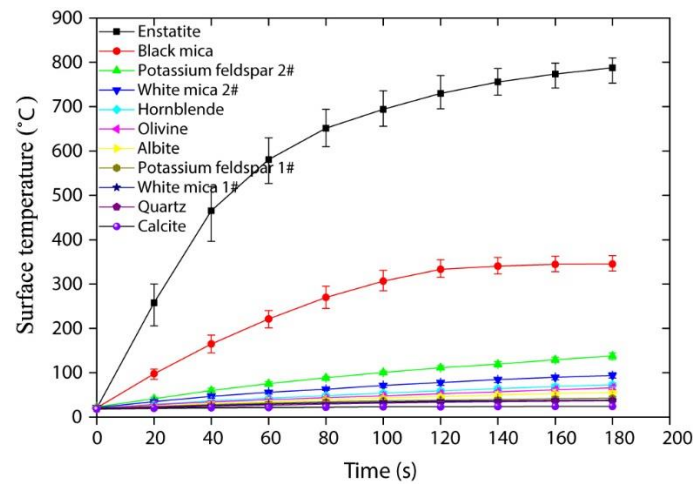


Fig. 4.3 Surface temperature of 11 rock-forming minerals after microwave treatment for 3 mins at 2 kW (Lu et al., 2017).

4.2.2 Problems of existing research

The pioneering studies on the heating rates of minerals provide good insights into the capabilities of minerals in absorbing microwave energy. However, those research concentrated on the ore minerals for potential application in microwave assisted comminution or in-situ leaching. The heating rates and dielectric properties of low loss rock forming minerals have not been systematically investigated. The non-ore low loss minerals have been misjudged to be either transparent or less responsive to microwave irradiation. This misjudgement has cast a miserable pall on the microwave assisted hard rock breakage and hindered research in this field.

Moreover, those research are exploratory and descriptive in nature and test results could vary from, or even contradict with, each other due to the facts that different microwave systems are used and that minerals of different weight are heated. The measured temperature can also be greatly influenced by the power supplied, the exposure time, the size of the cavity and the matching of the electromagnetic impedance of the system. Even the location where the minerals are placed could affect the consequent temperature and heating rates. Their effects on the heating rates will be discussed in a more detailed manner in later sections. Thus, the heating rates of minerals are not an intrinsic parameter such as density, but influenced by lots of other parameters. Methods should be proposed to derive the dielectric properties from the heating rate tests.

Another problem associated with using published data is that minerals are not pure compounds, but are usually mixtures whose composition can vary. The molecular composition of most minerals varies significantly. Some minerals are composed of various mixtures of different molecules each of which can and often do form different elemental compositions for the same mineral (Church et al., 1988). The many variations in one mineral group make the characterisation of minerals very challenging. Efforts should be made to collect different sub-minerals in one mineral group for a more comprehensive study.

4.3 Materials and methodologies

As one of the objective of the study is to understand the interactions between commonly encountered igneous rocks and microwave, the basic rock forming minerals (shown in [Figure 4.4](#)) rather than ore minerals are collected. They are quartz, plagioclase, orthoclase, biotite, muscovite, hornblende, diopside and olivine. Of the minerals, biotite and muscovite are the most widely seen micas and plagioclase and orthoclase are the most common feldspars. Hornblende is one of the amphiboles found in igneous and metamorphic rocks. Diopside collected from a gem store is one of the most common pyroxenes. According to the literature ([Campbell and Ulrichs, 1969](#); [Chen et al., 1984](#); [Church et al., 1988](#); [Harrison, 1997](#); [Nelson et al., 1989b](#); [Shannon et al., 1992](#); [Shannon et al., 1991](#)), all those minerals are low loss minerals compared to ore minerals such as hematite, pyrite, magnetite and galena. As a rule of thumb, the heating rates and loss factor of the minerals can be judged by their optical appearances ([Harrison, 1997](#)). The darker the minerals in colour, the higher the capacities in absorbing microwave. This means that the sequence of the minerals in microwave absorption capacity from low to high is quartz, muscovite, plagioclase, orthoclase, olivine, diopside, biotite and hornblende. However, the dielectric properties of minerals are also affected by the particle size, bulk density, and a lot other factors such as the heating conditions (power level) and the impedance matching during the heating process. The above postulation is yet to be examined via heating rate tests. Understanding the dielectric properties of pure minerals is the very first step of investigating the microwave-rock interactions. By mixing minerals at different percentages and with different combinations, artificial igneous rocks (similar in mineral compositions rather than mechanical properties) could be made to validate the effective medium theories. Those rocks that can be produced from the eight minerals include granite, andesite, gabbro, diorite, basalt and monzonite, etc.

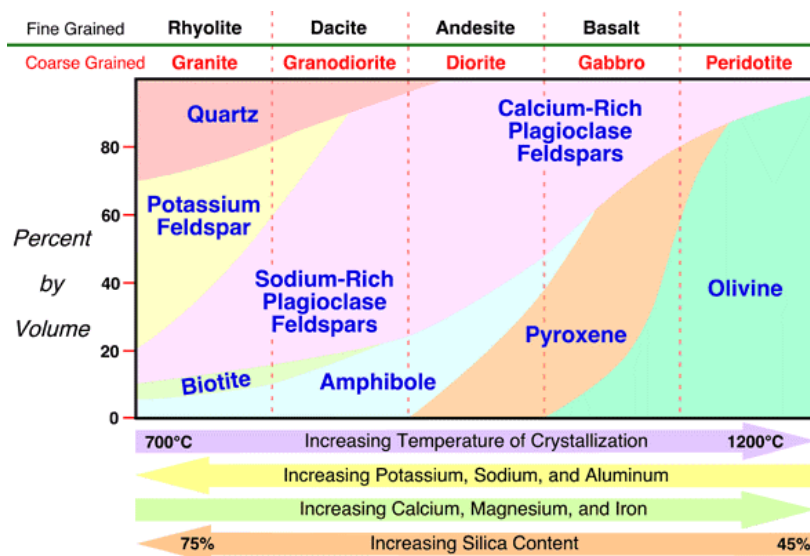


Fig. 4.4 The classification of igneous rocks and the rock forming minerals ([Tarbuck et al., 2016](#)). Fine grained rocks are volcanic and coarse grained rocks are intrusive.

Table 4.3 Physical and dielectric properties of the selected minerals (specific heat capacity data from Waples and Waples (2004) and Krupka et al. (1985); reference in the table are for the dielectric properties of minerals).

Minerals	Mineral group	Source	Chemical formula	Crystallography	Colour	Rocks	C_p (J/kg/K)	f (GHz)	ε'	ε''	Reference
Quartz	Quartz	Lianyungang, China	SiO ₂	Hexagonal	Transparent	Granite, granodiorite	740	2.45	2.82 2.26	0.02 0.01	Walkiewicz et al. (1988) Harrison (1997)
Muscovite	Mica	Lingshou County, China	KAl ₂ (Si ₃ AlO ₁₀)(OH) ₂	Monoclinic	Greyish white	Granite	760	2.45 N/A	8.69 5.40	0.091 0.0016	Nelson et al. (1989b) Santamarina (1989)
Diopside	Pyroxene	Heilongjiang, China	MgCaSi ₂ O ₆	Monoclinic	Dark green	Basalt, gabbro	800	2.45	7.18	0.17	Nelson et al. (1989b)
Orthoclase	Feldspar	Lingshou County, China	KAlSi ₃ O ₈	Monoclinic	Reddish	Granite, monzonite	628	9.37 2.45	4.75 1.86	0.044 0.01	Zheng et al. (2005) Cumbane (2003)
Plagioclase	Feldspar	Lingshou County, China	NaAlSi ₃ O ₈ – CaAl ₂ Si ₂ O ₈	Triclinic	White	Basalt, gabbro, andesite	540	2.45	6.01	0.090	Nelson et al. (1989b)
Olivine	Olivine	Heilongjiang, China	(Mg, Fe) ₂ SiO ₄	Orthorhombic	Light green	Basalt, gabbro	576	9.37	8.05	0.058	Zheng et al. (2005)
Biotite	Mica	Lingshou County, China	K(Mg,Fe) ₂₋₃ Al ₁₋₂ Si ₂₋₃ O ₁₀ (OH,F) ₂	Monoclinic	Black	Granite, granodiorite	770	2.45	5.9	0.0002	Church et al. (1988)
Hornblende	Amphibole	Lingshou County, China	(Ca,Na) ₂₋₃ (Mg,Fe,Al) ₅ (Si,Al) ₈ O ₂₂ (OH,F) ₂	Monoclinic	Black	Granite, granodiorite, andesite	840	N/A	5	0.01	Prokopenko (2011)

Note: C_p -Specific heat energy; f -frequency of microwave.

4.3.1 Minerals

Research quality minerals are purchased from different suppliers in China. The raw minerals before crushing and grinding are shown in [Figure 4.5](#). Quartz, olivine and hornblende are free from impurities and are crushed directly. All other minerals are carefully crushed by a jaw crusher first and then the impurities are removed before they are ground by an agate mill. The basic physical and dielectric properties of those minerals obtained from the literature are shown in [Table 4.3](#). It is worth mentioning that the chemical compositions of a mineral can vary significantly and that there are lots of sub-category minerals in one mineral group. It is expected that the dielectric properties and heating results from different researchers may vary. For instance, the general formula of pyroxene is $XY(\text{Si},\text{Al})_2\text{O}_6$, where X can be calcium, sodium, iron₊₂ and magnesium and Y represents chromium, aluminium, iron₊₃, magnesium, cobalt, manganese, scandium, titanium, vanadium. As a result, there are more than 20 minerals in the pyroxene group with different compositions and varying dielectric properties. Another example is biotite, whose composition can vary from 0 to 17 % Mg and 0 to 33 % Fe. If sourced from different locations, the measurement results could be different from each other, let alone different measurement facilities are used ([Church et al., 1988](#)). In this study the chemical compositions of minerals are determined by the energy dispersive analysis (EDS).



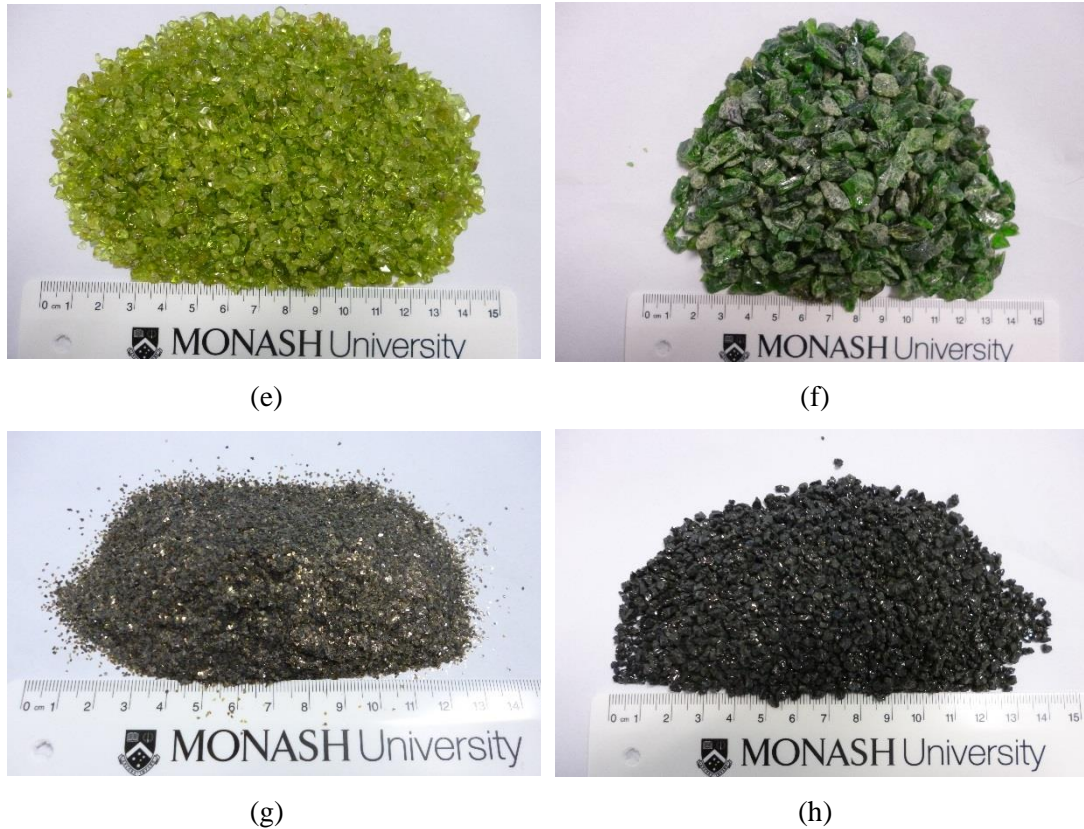


Fig. 4.5 Optical images of the 8 rock forming minerals before crushing and milling. (a) quartz, (b) muscovite, (c) plagioclase, (d) orthoclase, (e) olivine, (f) diopside, (g) biotite and (h) hornblende.

4.3.2 Crushing and grinding facility

To avoid the possible impact of the grain size on the measured heating rates and derived dielectric properties, the minerals are crushed and milled into similar grain sizes using the facilities (shown in [Figure 4.6](#)) at the Rock Crushing Laboratory, School of Earth, Atmosphere and Environment, Monash University. In the crushing process, the mineral contaminants, middling and tailing are hand removed from plagioclase, orthoclase and diopside using a tweezer. The crushed minerals are then milled by the agate mill assisted with a vibrator. After that the milled minerals go through two different mesh sizes, i.e. 125 μm and 75 μm . In total there are three particle size ranges: smaller than 75 μm , 75-125 μm , over 125 μm . In the crushing and grinding process, a procedure is followed to avoid possible cross contamination. To standardise the tests, the smallest particle size range is used in the heating tests for comparisons between minerals. To study the grain size on the heating rates of minerals, all the ranges of olivine and plagioclase are used. The minerals after crushing and milling (grain size smaller than 75 μm) are shown in [Figure 4.7](#).

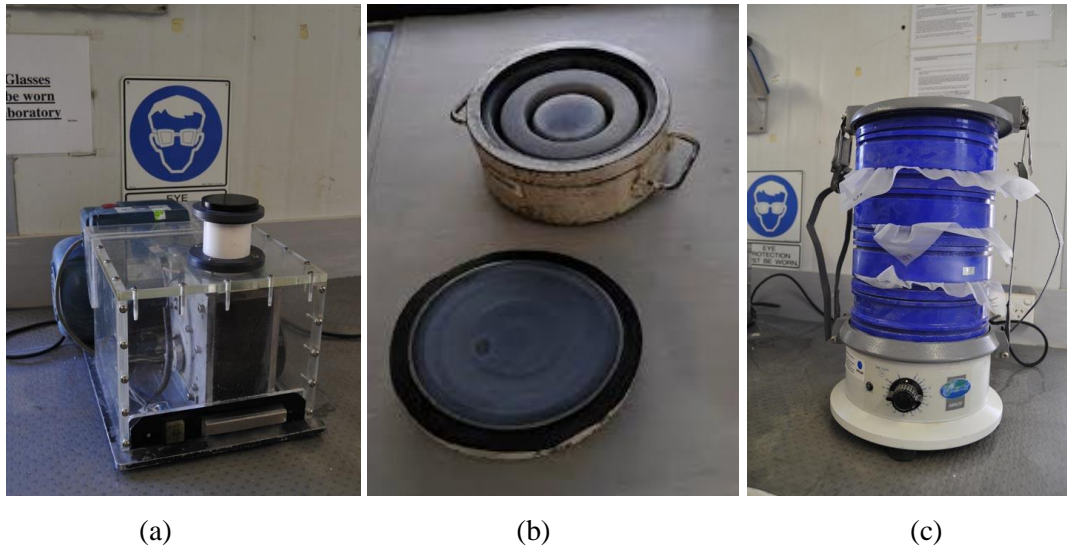


Fig. 4.6 Equipment used for crushing and grinding. (a) Jaw crusher, (b) Agate mill, (c) Sieve shaker.



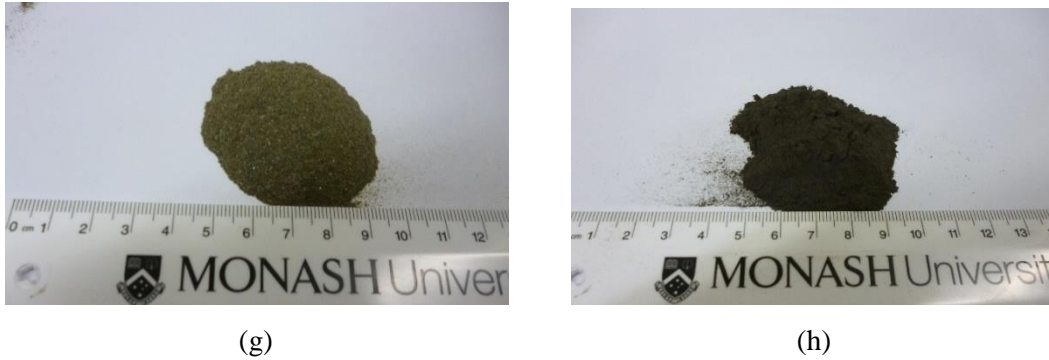


Fig. 4.7 Minerals after crushing and milling crushing and grinding (grain size smaller than 75 μ m). (a) quartz, (b) muscovite, (c) plagioclase, (d) orthoclase, (e) olivine, (f) diopside, (g) biotite and (h) hornblende.

4.3.3 Energy-dispersive X-ray spectroscopy

To study the effect of chemical elements on the heating rates and DPs of the minerals, a FEI Quanta SEM (3D GEGSEM) with a function of energy-dispersive X-ray (EDS) feature is used. The microscope, as shown in **Figure 4.8(a)**, is fitted with a large area SDD x-ray detector and EBSD system allowing for fast x-ray mapping and crystallographic scans. The mineral powders are mounted on stubs using carbon tapes and are then carbon coated, following a standard procedure (**Figure 4.8(b)**). The machine are operated at an accelerating voltage of 15 kV, a probe current of 0.11 nA, a spot size of 5 and a working distance of 10 mm. At least 3 spots are measured to assure a good consistency.

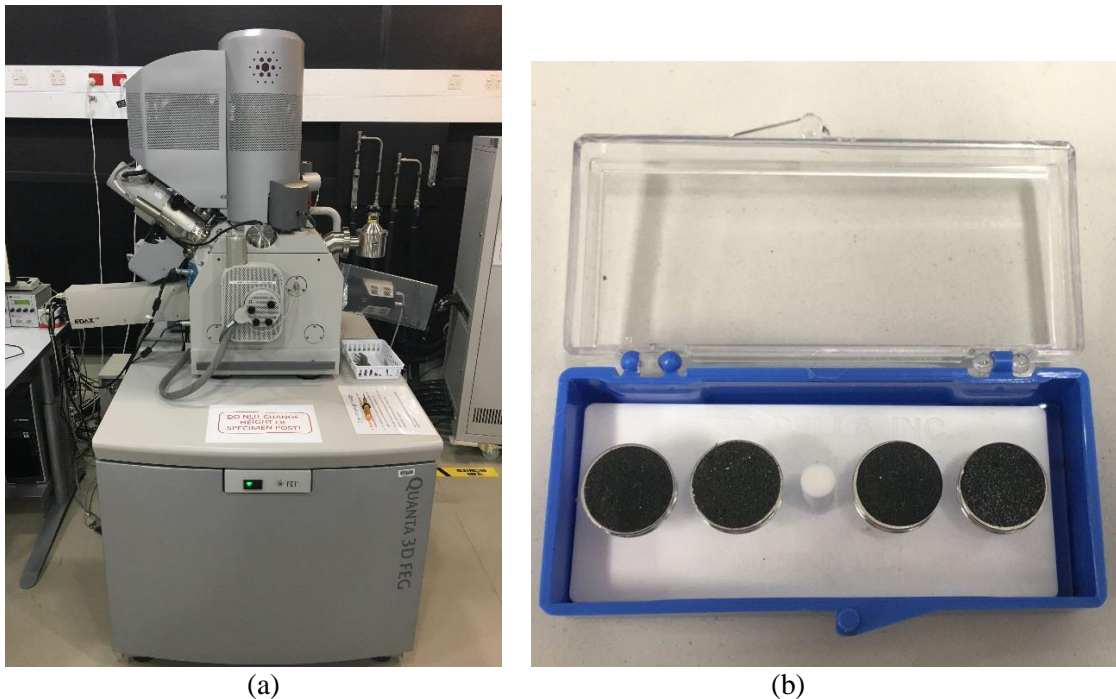


Fig. 4.8 EDS analysis of minerals. (a) The FEI Quanta scanning electron microscope (SEM), (b) Carbon coated specimens on stubs.

4.3.4 Industrial microwave system

For laboratory study of the effect of heating rates of minerals and rocks subjected to microwave irradiation, a single mode industrial microwave system should be selected. The reasons are twofold. First, a domestic oven has a relatively lower output power (normally around 1 kW) and a larger cavity (400mm by 400mm by 250mm), resulting in a relatively low electric field strength and less heat generation within the rock. They are designed for heating water-contained food only. Due to a lack of an impedance matching mechanism, low loss hard rocks and minerals will not heat up easily if placed in a domestic microwave. This has been proved by previous research (Peinsitt et al., 2010; Sikong and Bunsin, 2009; Walkiewicz et al., 1988). By contrast, the industrial microwaves have an impedance tuner which is able to provide a controlled electric field in the cavity for different tests. Moreover, they usually have higher output powers (up to 100 kW) and smaller cavities (cross-section 86mm by 43mm at a frequency of 2.45 GHz), thus the electric field strength can be significantly intensified. The second reason is that the engineering scenario, for instance, mechanised tunnelling and deep drilling, involves only one surface of rock exposed to microwave irradiation. This can only be simulated using an industrial microwave with an open ended single-mode applicator rather than a closed cavity.

In this study, a single mode industrial microwave heating system with a maximum output power of 2 kW is used. As can be seen in **Figure 4.9**, the MUEGGE system consists of a high power supply and control, a magnetron head, an isolator, an impedance matching tuner, an applicator/sample holder and a water/dummy load. The power supply and magnetron head can work together to generate microwave at 2.45 GHz. The power can be adjusted from 1 % to 100 % on the control panel. The microwave can then propagate in the WR340 waveguide and reach the load in the sample holder. In between the magnetron and applicator are the adjustable tuner and isolator. The isolator protects the magnetron head by redirecting the excess microwave energy reflected back from the load. The excess microwave energy is redirected to a water load and can be measured by a power meter and be displayed on the control panel of the power supply. The function of the tuner is to match the electromagnetic impedance of the microwave source and the transmission line to that of the load, therefore maximising the microwave absorbed by the workload in the applicator and minimising the power reflection. The impedance matching is achieved by manually adjusting the stubs of the tuner at a very low microwave power before heating at a higher power. For the mineral heating tests, the reflection coefficient can be controlled as 20-30 %. Aluminium foil tape is used to seal connections to prevent possible microwave leakage. A microwave leakage meter is used during the test to make sure that the microwave level is below 5 mW/cm² at any point.

In the tests, the quartz beakers are placed along the geometric centreline of the waveguide where the electric field strength is the highest.

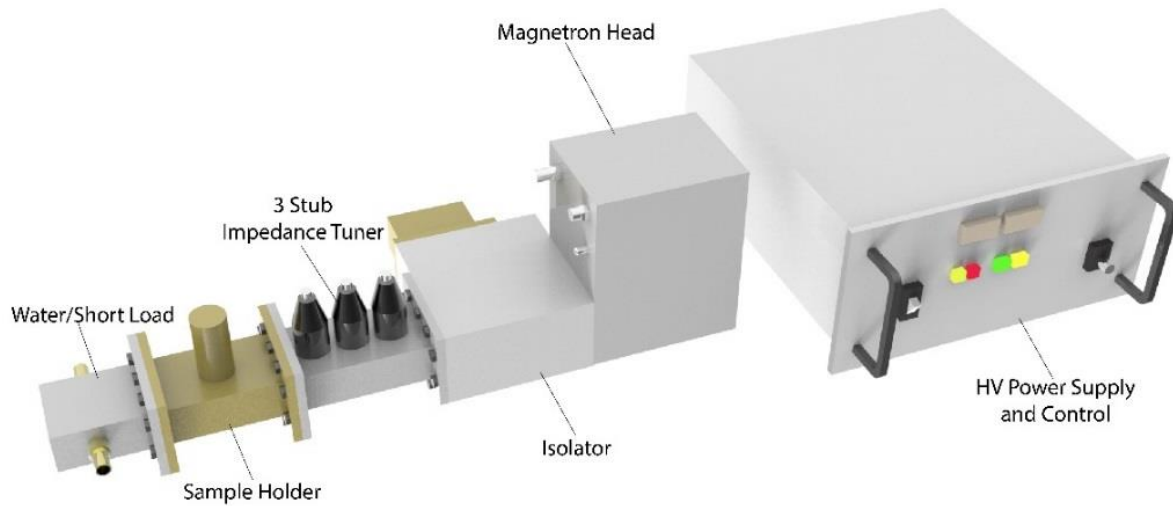


Fig. 4.9 Schematic of the experimental setup of microwave treatment of rocks.

4.3.5 Temperature measurement

Continuous temperature measurement of the specimen during microwave irradiation is crucial but can also be technically challenging if not impossible. Because of an intensified electric field strength, no metallic thermocouple probes can be placed in the applicator or in the specimen itself to prevent arcing from happening. Accufibre can be employed to measure temperature up to 400 °C but are too fragile for most industrial applications. The common practice is to use an infrared camera/gun to measure the surface temperature or to insert a thermocouple into the specimen with previous bored holes.

In this research, one infrared camera (ULIRVision TI160) and one infrared gun (INTH-2013) is used for quick temperature measurement (**Figure 4.10**). Specifications of the two thermometers can be found in **Table 4.4**. The software of IRSee is used to analyse the thermal images to get the temperature at a particular point, along a line or over an area. It should be noted that the temperature range of the camera is relatively and the maximum temperature can be up to 709 °C, however the average temperatures obtained are still indicative. For temperature above the range of the camera, the infrared gun is used to get the maximum temperature of the rock surface. The measurement is done 3-5 seconds after the tests are finished. Optical images are also taken for comparative studies.



Fig. 4.10 Thermometers used for temperature measurement. (a) ULIRVision TI160 IR camera; (b) INTHT-2013IR shotgun.

Table 4.4 Specifications of infrared camera and gun.

Parameters	TI160 IR camera	INTHT-2013 IR Gun
Temperature Range	-20-220 °C 180-600 °C	-50-1350 °C
Accuracy	±2 °C ±2 %	±1.5 °C ±1.5 %
Sensitivity	0.1 °C	0.1 °C
Resolution	160 × 120 pixels	N/A
Response Time	0.5s	0.2s

4.3.6 Solid density measurement

The density of the mineral solids are measured by a Quantachrome multi-pycnometer (Figure 4.11) which is based on the Archimedes principle of fluid displacement to determine the volume. The pycnometer determines the true density of solid or powdered samples by measuring the pressure difference when a known quantity of helium under pressure is allowed to flow from a precisely known reference volume into a sample cell containing the solid or powdered material (Quantachrome, 2017). Before measuring the density of minerals, the pycnometer is calibrated based on the guideline provided by the manufacturer. Table 4.5 illustrates the results of the measurement. From the table we can know that the density of mineral solid measured has a very little variation.



Fig. 4.11 Quantachrome multipycnometer for the measurement of solid density.

Table 4.5 Solid density of the powdered minerals (grain size smaller than 75 μ m).

Minerals	Test 1	Test 2	Test 3	Average
Biotite	2.93	2.93	2.93	2.93
Hornblende	3.21	3.25	3.25	3.24
Muscovite	2.85	2.82	2.87	2.85
Diopside	3.31	3.28	3.29	3.29
Orthoclase	2.64	2.58	2.62	2.61
Olivine	3.41	3.42	3.40	3.41
Quartz	2.68	2.66	2.67	2.67
Plagioclase	2.59	2.58	2.57	2.58

4.3.7 Design of experiment

(1) Heating rates of pure minerals

The pure minerals are filled in 10 ml fused quartz beakers and heated at four power levels (0.5-2 kW) for four durations (1-4 mins). They are placed in the same location in the cavity to minimise the effect of location on the results. The minerals are compacted to the maximum possible bulk densities. Given the difference in the bulk densities of minerals, different weights of minerals are heated. However, whenever possible the weight is close to 18 gram. The 10 ml beakers are made of fused quartz (over 99 % pure) and do not heat up when subjected to microwave irradiation. After the heating tests stop, the infrared thermal camera is used to capture the temperature. It should be noted that the surface temperature from the infrared camera, although measured in an instant manner, is lower than the interior

temperature. This is evidenced by the fact that when melting and plasma take place from the core the surface temperature is only 400-500 °C. Due to the limitation of the tests (no thermocouples could be placed in the cavity and temperature drops very quickly after test stops), no other methods of temperature measurement is undertaken.

(2) Grain size effect

The grain size effect on the heating rates is examined by heating olivine and diopside at different grain sizes. **Figure 4.12** shows the olivine of different grain sizes in beakers. As described in Section 4.3.2, the grain sizes are 10mm, over 125µm, 75-125µm and smaller than 75µm, respectively.



Fig. 4.12 Olivine of different grain sizes in the 10 ml quartz beakers.

(3) Mineral mixtures

To study the contribution of individual minerals in the overall heating rates and to validate the effective medium theories, different minerals are mixed at a half/half ratio. They are plagioclase and orthoclase mixture to simulate monzonite, plagioclase and diopside mixture to simulate gabbro and basalt. Quartz are mixed with orthoclase first and then 20 % biotite is added to simulate granite. Those mixtures are heated at 1 kW and 2 kW. The heating rates of mixtures are then compared to that of the pure minerals.

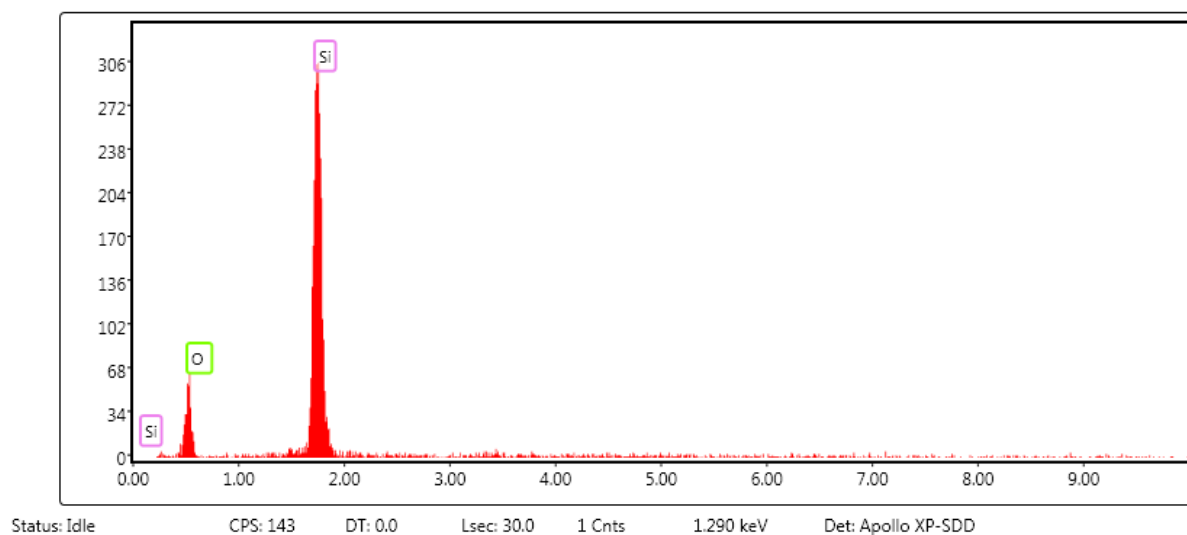
(4) Environment temperature

The environment temperature keeps at about 22 °C. During the tests, the cavity could be heated up at high power levels. Under this circumstance, next tests only start when the cavity cools off.

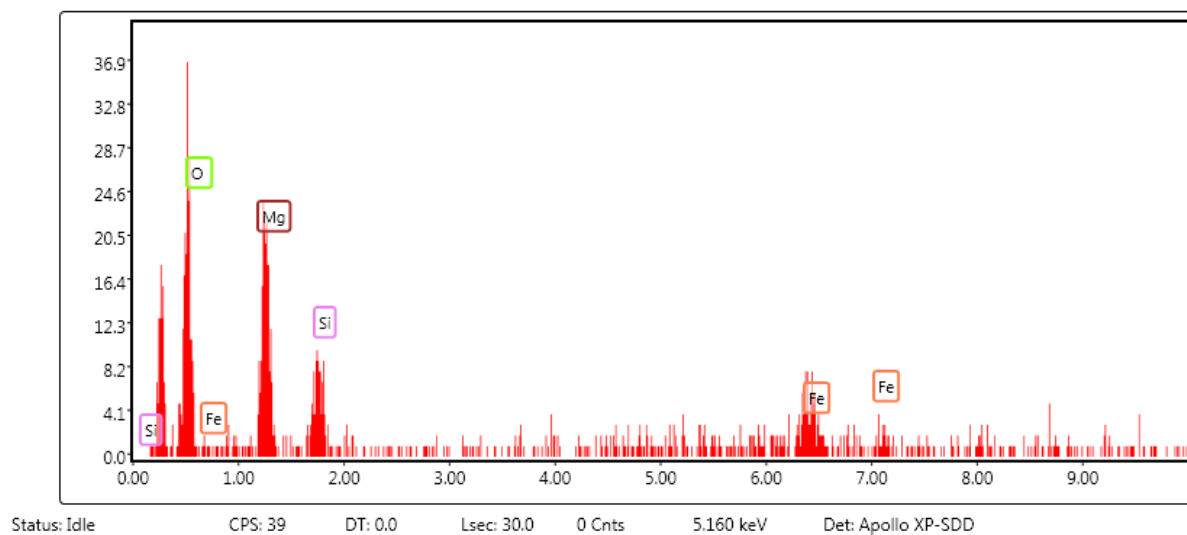
4.4 Test results and discussions

4.4.1 Element compositions of minerals

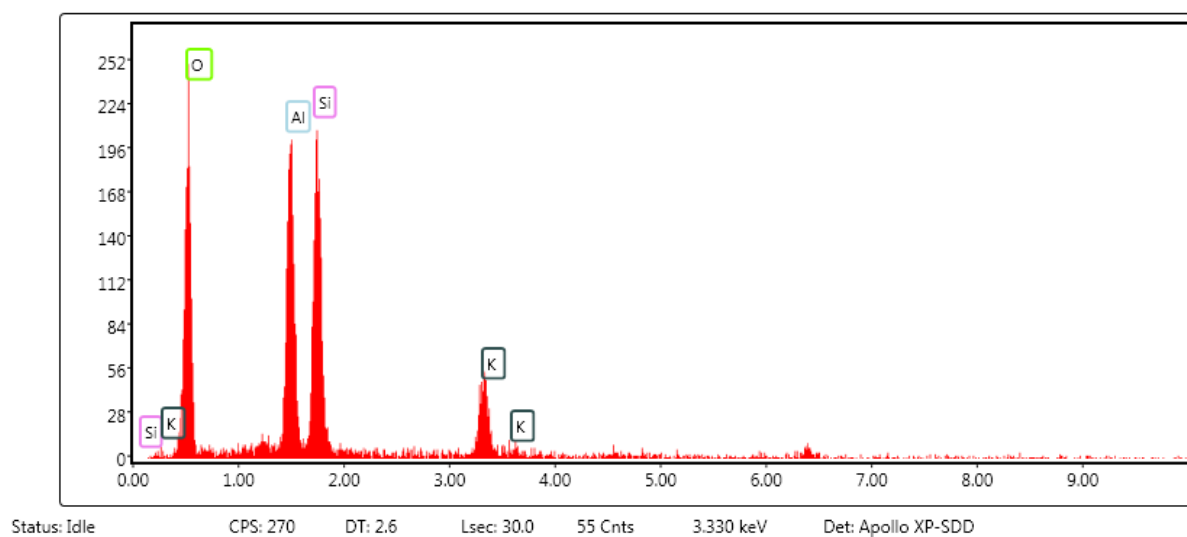
The EDS spectrums of the minerals are shown in **Figure 4.13**. The software TEAM™ is used to determine the element types and their percentage. It can be found that the types of elements are in well consistency with the chemical formula in **Table 4.3**. The percentages of the chemical elements are summarised in **Table 4.6**. It should be mentioned here that hydrogen cannot be detected from the spectrum and that the results are qualitative only.



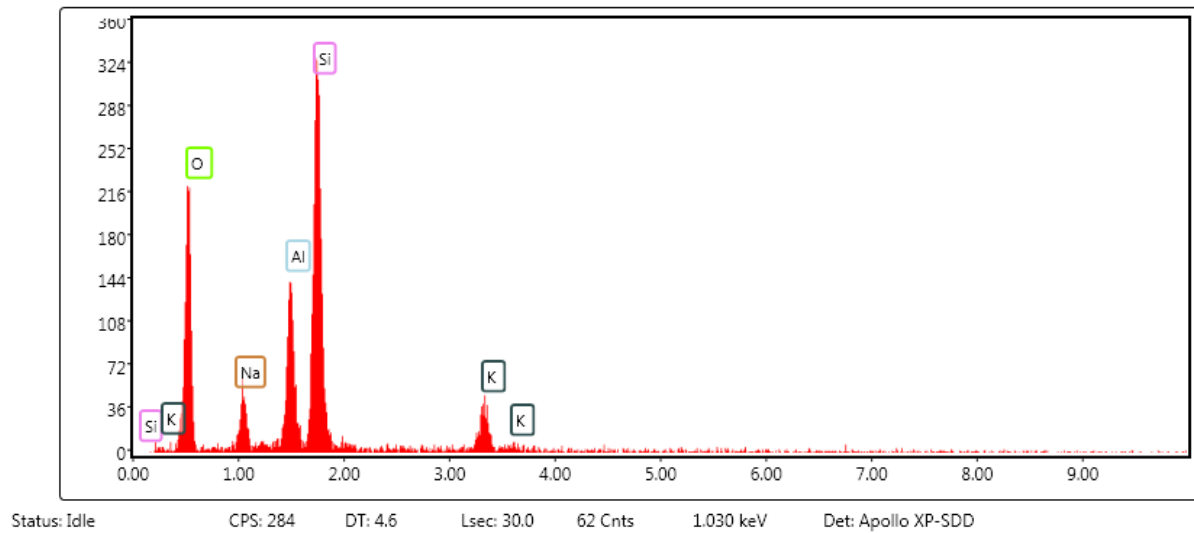
(a) Quartz



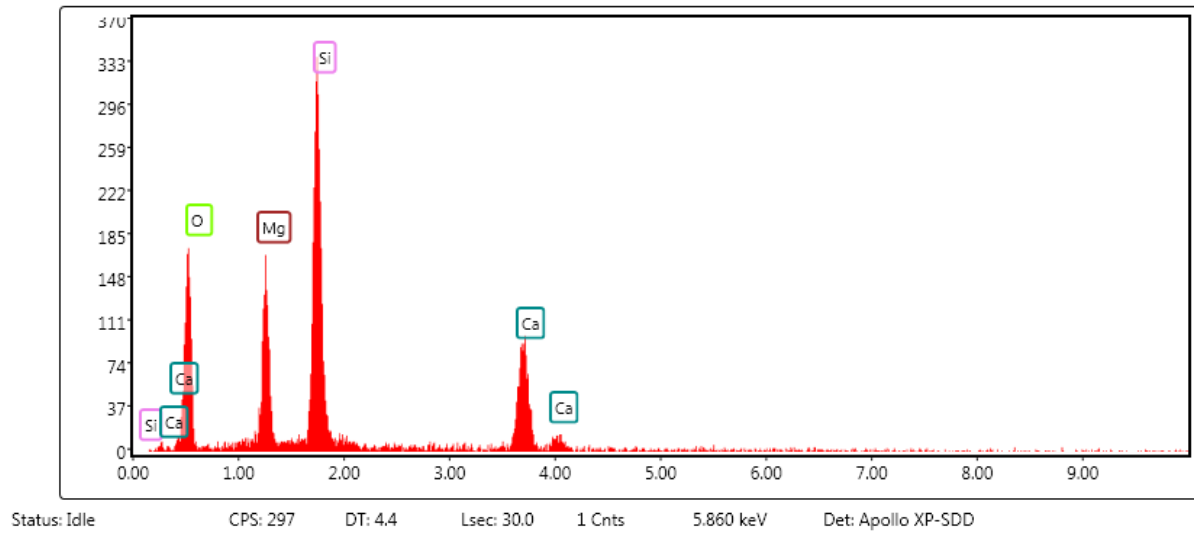
(b) Olivine



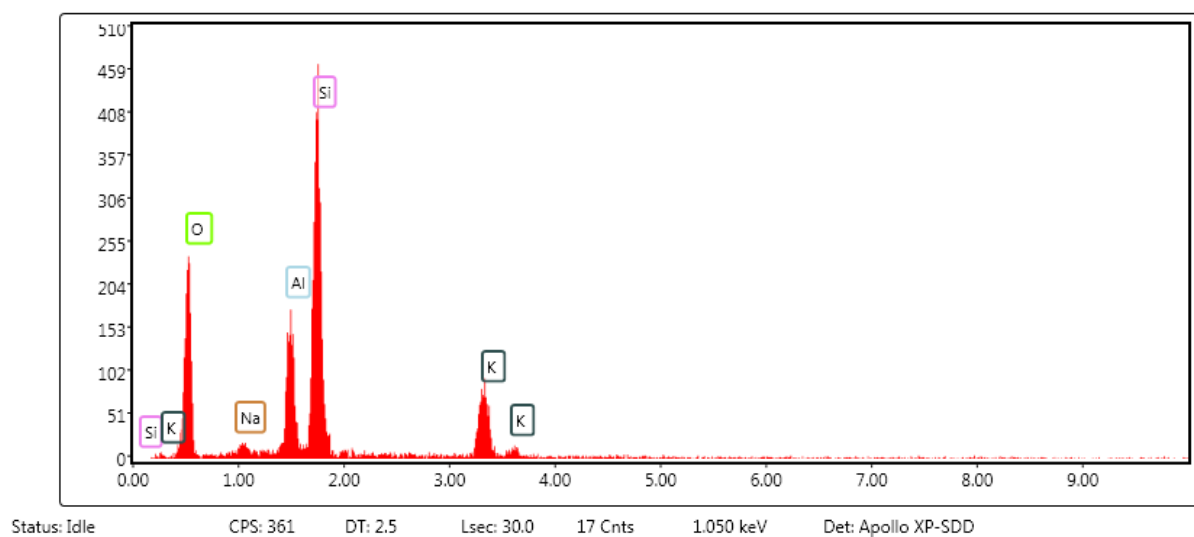
(c) Plagioclase



(d) Muscovite



(e) Diopside



(f) Orthoclase

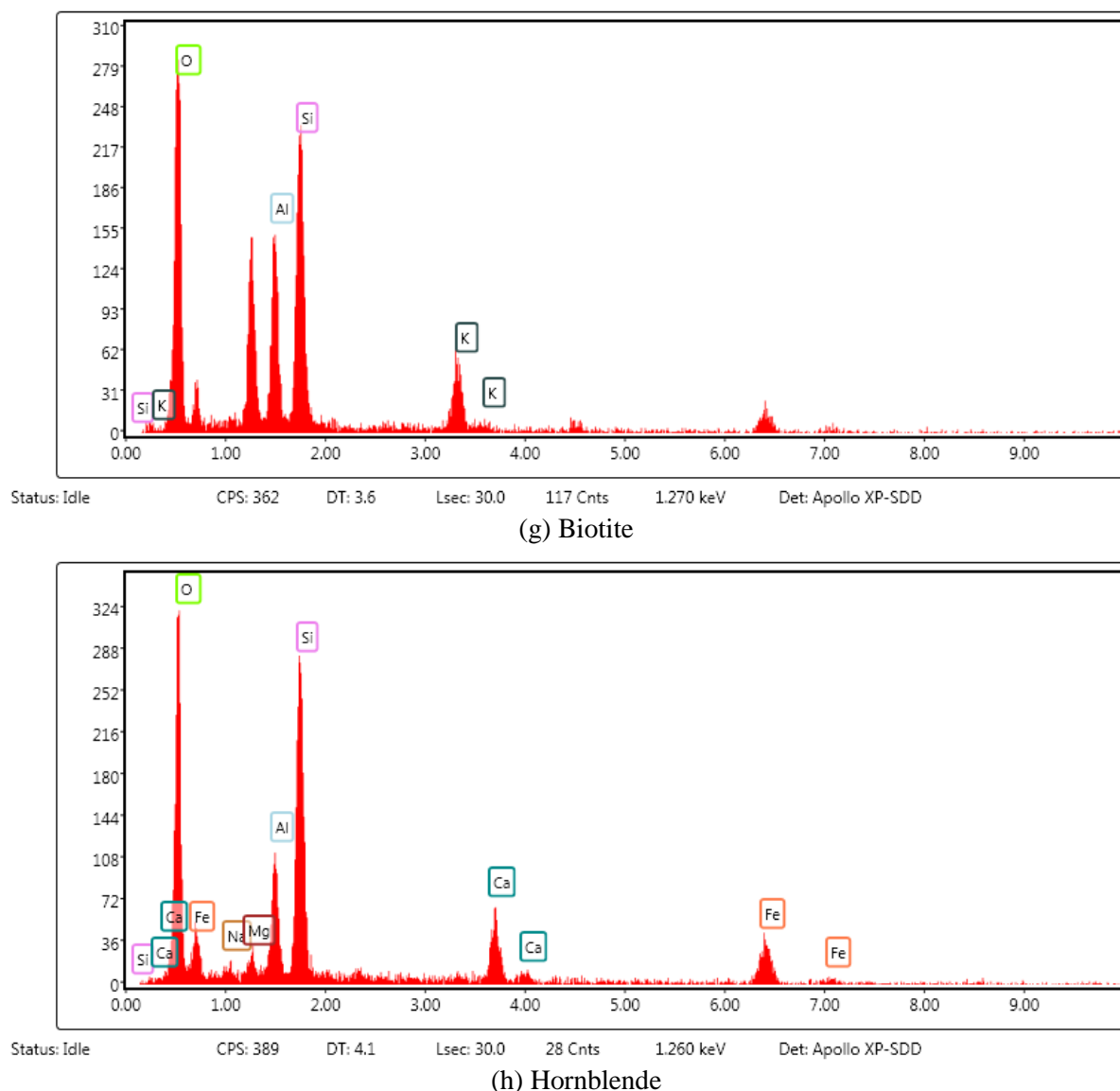


Fig. 4.13 EDS spectrums of the 8 rock forming minerals. (a) quartz, (b) olivine, (c) muscovite, (d) plagioclase, (e) diopside, (f) orthoclase, (g) biotite and (h) hornblende.

Table 4.6 Elemental compositions of the minerals from the EDS analysis.

Minerals	Element percentage by weight (%)								
	O	F	Na	Mg	Al	Si	K	Ca	Fe
Quartz	40.5					59.5			
Olivine	28.18			20.84		5.86			45.13
Muscovite	49.49				18.93	21.36	10.22		
Plagioclase	43.89		5.98		12.14	31	6.98		
Diopside	42.48			11.66		25.64		20.22	
Orthoclase	42.19		1.47		10.91	31.59	13.84		
Biotite	42.74	1.49		10.49	10.76	17.54	7.51		9.47
Hornblende	42.91		0.61	1.19	7.09	19.99		8.55	19.66

4.4.2 Heating rates of pure minerals

During the tests, minerals including quartz, diopside, olivine, muscovite and plagioclase stay relatively cool. However, biotite and hornblende heat up quickly even at low power levels and plasma is frequently observed leading to a vibrant impedance mismatch between the load and the microwave source. The mismatch attributes to either the change of the dielectric properties of minerals at high temperatures (hornblende) or the change of volume size because of heat swelling (biotite). Thus no test data are available for hornblende at over 1 kW and for biotite at over 1.5 kW. **Figure 4.14** shows the melting of hornblende (melting point about 800 °C) in the cavity when heated at 1 kW for 20s (planned time is 60s). Of the 8 minerals heated, hornblende is the most microwave absorptive. Biotite also starts to melt from the core in the beakers at high power levels. When test ends, sintered cores can be observed in the beakers.



Fig. 4.14 Melting of hornblende when heated at 1 kW for 20s.

Figure 4.15 shows the heating rates (slopes of the temperature curves) of the pure minerals at the power of 1 kW except hornblende. It is clear that the minerals could be classified into three categories based on the heating rates.

- Category 1: Good microwave absorbers including hornblende and biotite. These are the dark coloured minerals rich in iron and magnesium.
- Category 2: Intermediate microwave absorber including orthoclase. Note that orthoclase is reddish.
- Category 3: Poor microwave absorbers including quartz, diopside, olivine, muscovite and plagioclase. These are the light-coloured minerals that are either white or transparent/opaque. Those minerals are silicate based and the percentages of iron and magnesium are low.

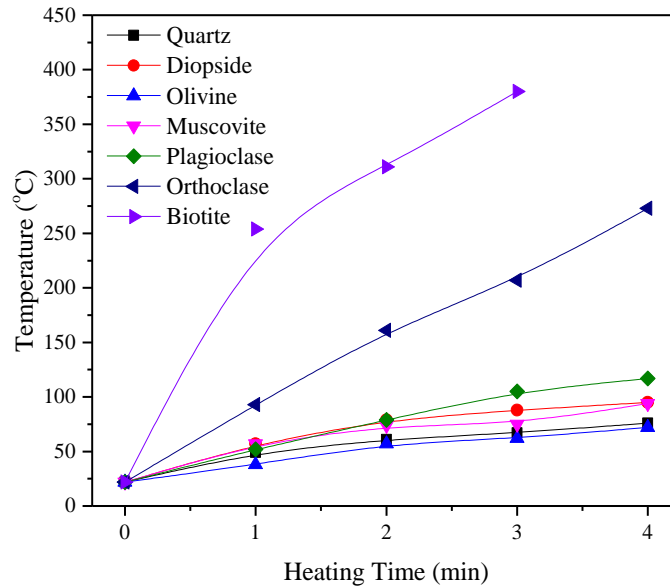


Fig. 4.15 Heating rates of seven rock forming minerals at 1 kW.

Figure 4.16 shows the heating rates of the Category 3 minerals at the power of 1 kW and 2 kW. The test results are in good agreement with those of Lu et al. (2017) except diopside and hornblende (Figure 4.3). In Lu et al. (2017)'s research, the enstatite has 18 % of iron, which is presumably to be ferrosilite ($\text{Fe}_2\text{Si}_2\text{O}_6$)-enstatite ($\text{Mg}_2\text{Si}_2\text{O}_6$) mixture rather than pure enstatite (Figure 4.17). The higher proportions of magnesium and iron could have possibly explained why the higher temperatures were recorded in their tests. The diopside ($\text{MgCaSi}_2\text{O}_6$) used in the tests is less magnesium rich and contains no iron, thus the low temperatures measured is reasonable. From the viewpoint of appearance, ferrosilite and enstatite are also darker than diopside. In their tests minerals in the natural state were heated. The characteristics of bulkiness and impurity inclusions could also have resulted in higher temperatures. As for hornblende, its dielectric properties at the microwave frequency have not been found in the literature. Prokopenko (2011) reported that at the radio frequency the dielectric constant and loss factor of hornblende are 5 and 0.01, respectively, making it a relatively good absorber. Nelson et al. (1989b) measured the dielectric properties of richterite (another amphibole in the monoclinic series), labradorite (plagioclase), muscovite and diopside employing the short-circuited waveguide method. Their results show that the dielectric properties of diopside at 2.45 GHz are the highest. As the heating rates are a results of energy absorption and temperature increase, they cannot be used directly to compare the dielectric properties of minerals.

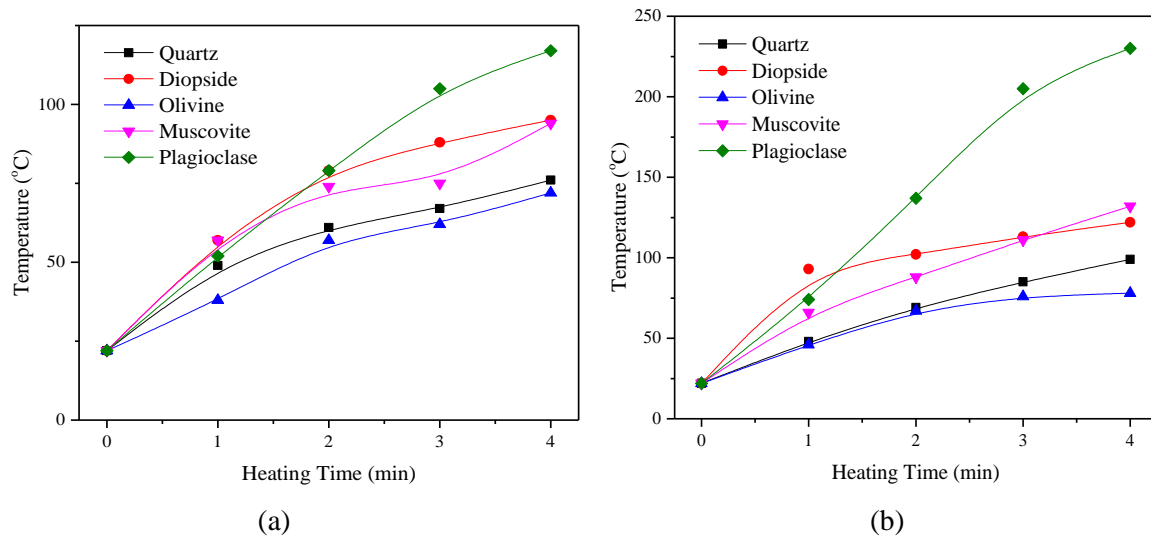


Fig. 4.16 Heating rates of Category 3 minerals at (a) 1 kW and (b) 2 kW.

Another reason of the test result difference may attribute to the setup of the microwave cavity and the matching of the electromagnetic impedance. As shown in Figure 4.1, if there is tuner, being it automatic or manual, microwave reflection from the cavity to the microwave source could be controlled. If the cavity is short circuited, the microwave energy will be channelled into the minerals. Under this circumstance, although the natural dielectric properties of minerals are different, the minerals are going to absorb more or less the same amount of energy. The consequent temperature will depend primarily on the specific heat of the minerals, rather than their dielectric properties. Measurement from this setup could be inaccurate and misleading.

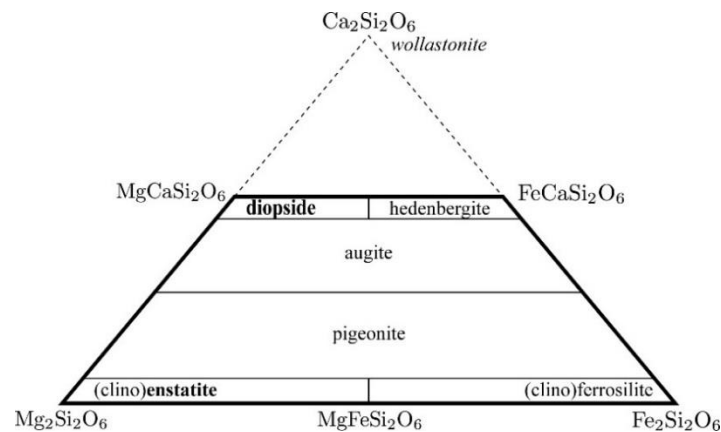


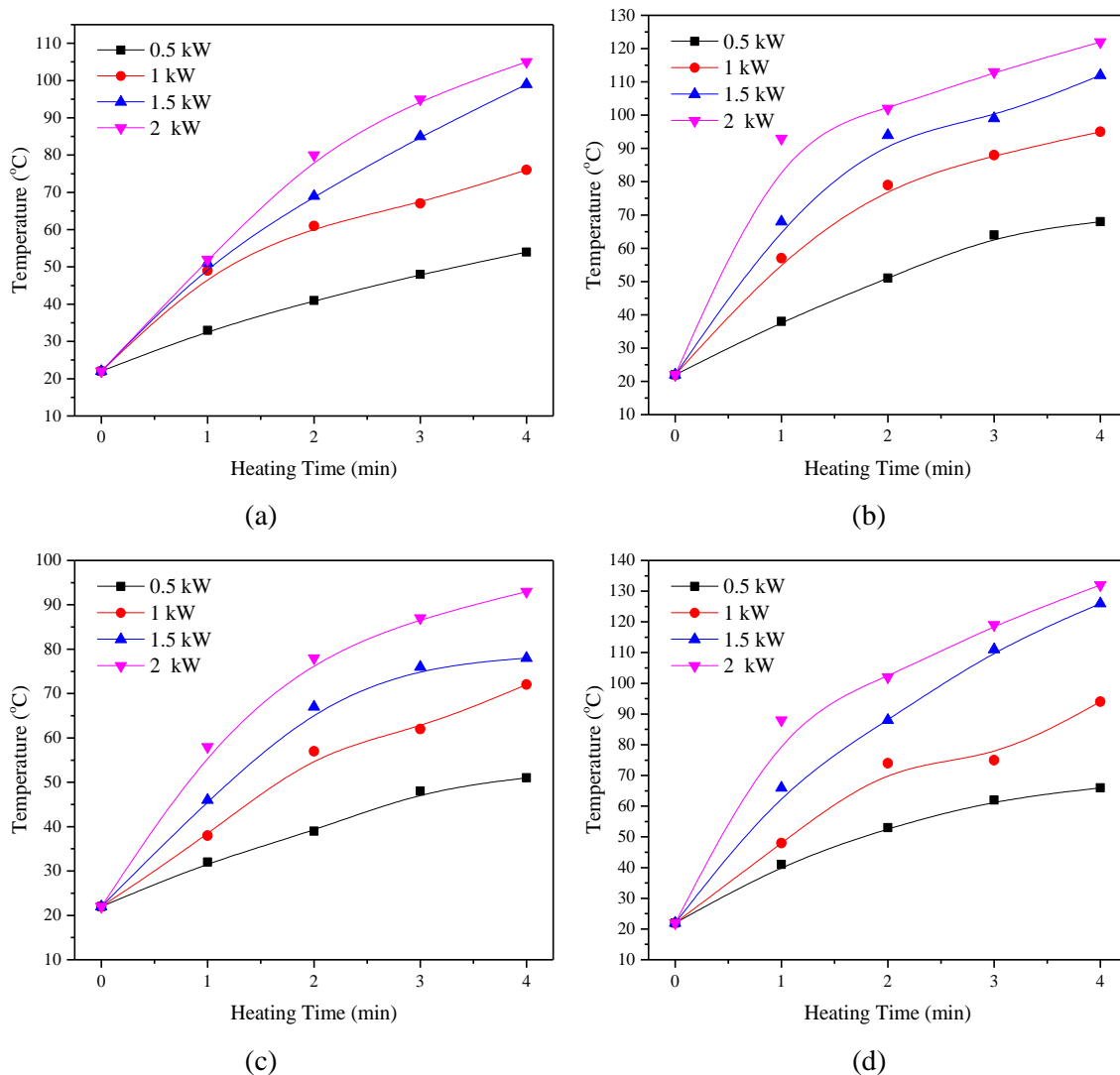
Fig. 4.17 Difference in chemical compositions of pyroxenes.

On the other hand, if there is no automatic/manual impedance tuner in between the cavity and the microwave source, there will be an even greater problem. Without impedance matching, the microwave energy stored in the cavity will be uncertain, even though the samples are placed in the same position. To be more precise, the low temperature of minerals after microwave heating may be the result of the fact that more energy is reflected back due to the mismatch between the load and the microwave source. Results using this setup are also unreliable if not totally wrong.

In this test, the reflection coefficient is controlled at around 20 % and the water load is used at the end of the circuit rather than a short load. This kind of setup solves both the abovementioned problems and provides a relatively controllable environment for the measurement of heating rates of minerals.

4.4.3 Effect of power level on heating rates

Figure 4.18 shows the heating rates of the individual pure minerals at the four different power levels. It can be observed that for all the minerals, the heating rates increase as the power level increases. The heating rates of plagioclase and orthoclase are highly linear at the four power levels. However, for other minerals, linearity can only be observed at low power levels (0.5 kW and 1 kW). This could possibly be explained by the losses due to radiation and convection. Linear correlations of the heating rates of the minerals ($^{\circ}\text{C}/\text{min}$) at different power levels are performed and are shown in Table 4.7. The slowing down of heating may be explained by the higher energy convention to the environment at high temperatures. It can be said from Table 4.7 that the order of the heating rates, regardless of the mass of the minerals, is olivine, quartz, muscovite, diopside, plagioclase, orthoclase, biotite and hornblende. This almost supports the postulation in Section 4.3.1 except diopside.



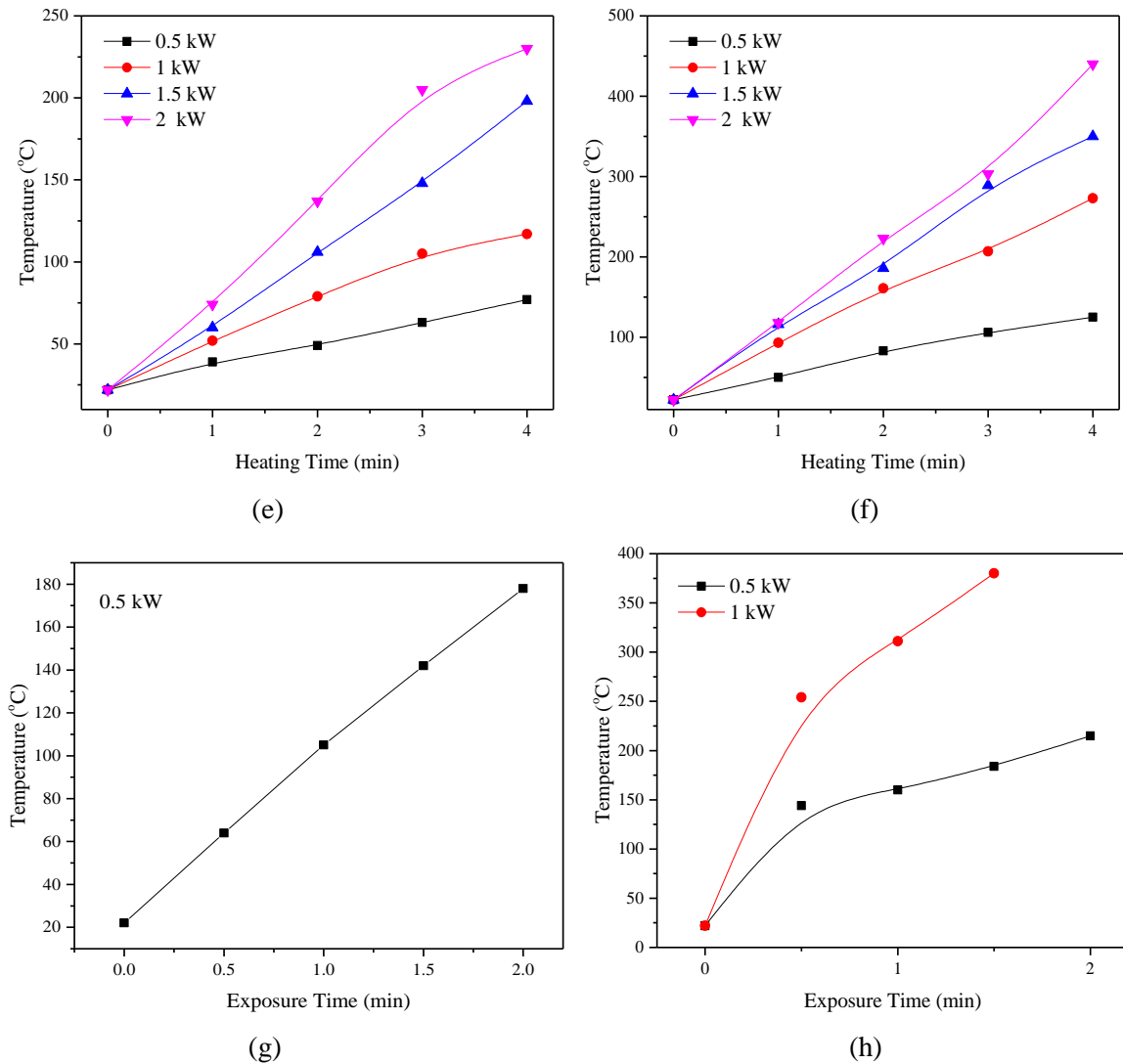


Fig. 4.18 Heating rates of (a) quartz, (b) diopside, (c) olivine, (d) muscovite, (e) plagioclase, (f) orthoclase, (g) biotite and (h) hornblende at different power levels.

Table 4.7 Heating rates ($^{\circ}\text{C}/\text{min}$) of pure minerals at four power levels.

Minerals	0.5 kW	1 kW	1.5 kW	2 kW
Quartz	7.9	12.6	18.8	20.9
Olivine	7.4	12.4	14.2	17.1
Muscovite	10.9	17.1	25.3	25.1
Plagioclase	13.4	24.3	44	54.7
Diopside	11.8	17.7	21.1	22
Orthoclase	26.2	61.6	82.9	102.1
Biotite	42.6	113.1	N/A	N/A
Hornblende	75.8	N/A	N/A	N/A

It compels mentioning that in the heating rate tests, different mass of minerals are used. To study the possible impact of mass, the heating rates in terms of °C/min/g are computed and presented in [Table 4.8](#). When comparing to [Table 4.7](#), it can be found that the order can be significantly affected, mainly due to the change in the electric field strength resulting from a mass difference. Heating rate is not regarded as an intrinsic physical parameter of minerals. Moreover, the heating rates of solid minerals which are different from the powdered minerals are still unknown. The heating rates of rocks composed of different minerals still could not be determined from the heating rate data of bulk minerals. Therefore, a new method that can derive the dielectric properties should be developed.

Table 4.8 Heating rates (°C/min/g) of pure minerals at four power levels.

Minerals	Mass (g)	0.5 kW	1 kW	1.5 kW	2 kW
Quartz	18.55	0.426	0.679	1.013	1.127
Olivine	21.36	0.346	0.581	0.665	0.801
Muscovite	7.22	1.510	2.368	3.504	3.476
Plagioclase	18.32	0.731	1.326	2.402	2.986
Diopside	22.57	0.523	0.784	0.935	0.975
Orthoclase	18.09	1.448	3.405	4.583	5.644
Biotite	11.28	3.777	10.027	N/A	N/A
Hornblende	19.2	3.948	N/A	N/A	N/A

4.4.4 Effect of grain size on heating rates

The effect of the grain size on the heating rates of minerals is also examined. [Figures 4.19](#) and [4.20](#) shows the test results of olivine and diopside. It can be said that as the grain size increases, the heating rate decreases. This is in agreement with observations of granular materials by previous researchers such as [Walkiewicz et al. \(1988\)](#), [Standish \(1989\)](#) and [Florek and Lovás \(1995\)](#).

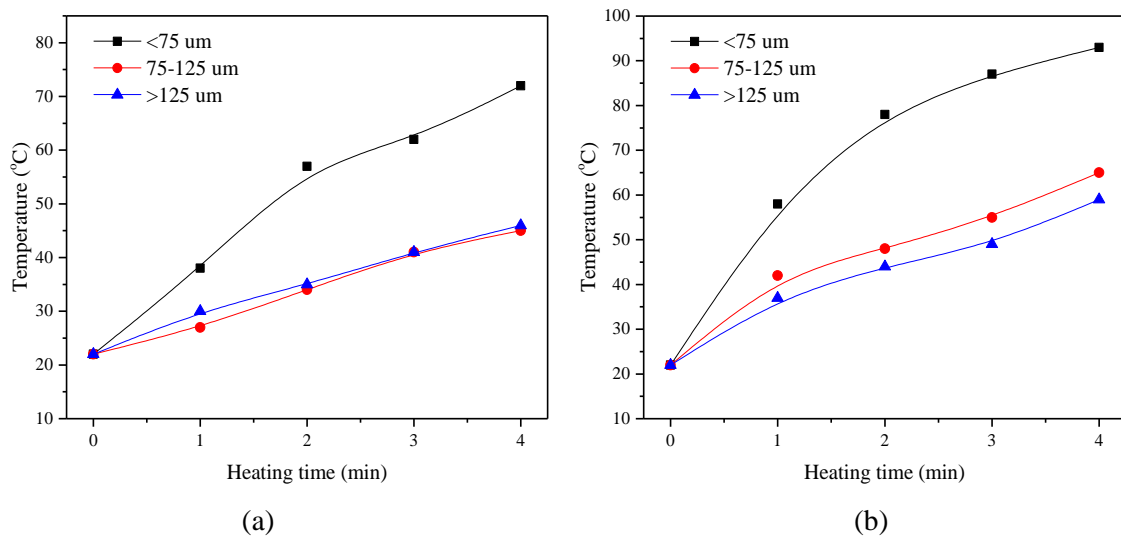


Fig. 4.19 Heating rates of olivine of different grain sizes at (a) 1 kW and (b) 2 kW.

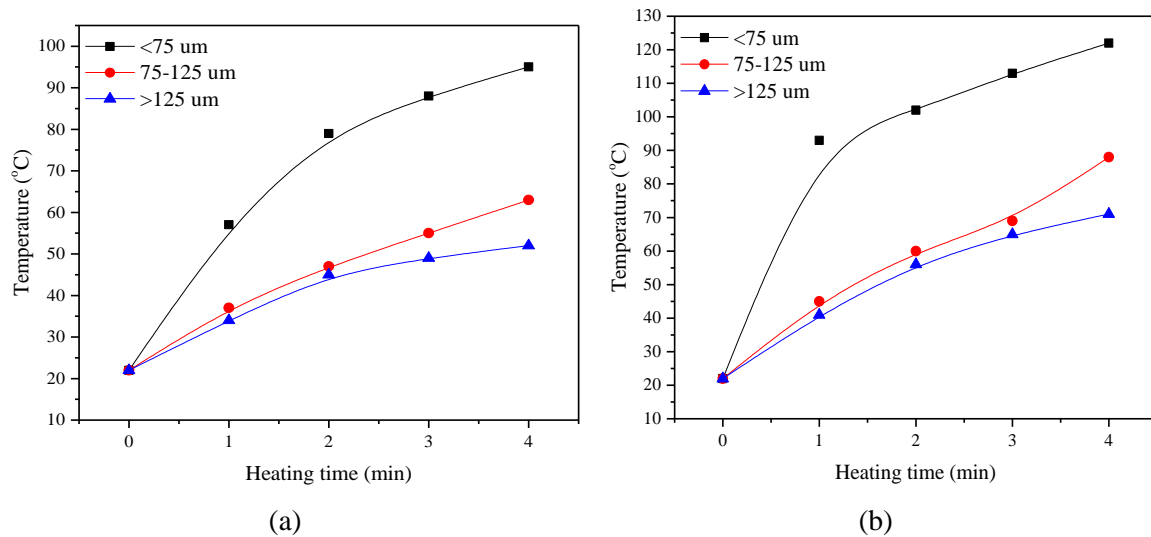


Fig. 4.20 Heating rates of diopside of different grain sizes at (a) 1 kW and (b) 2 kW.

In the literature, the mechanism of the grain size effect on heating rates has not been well explained. Wang and Forssberg (2000) and Kumar et al. (2010) think that by increasing the surface area, there is a higher loss of heat due to conduction. To the understanding of the candidate, this could possibly be explained by the increase of surface areas when the grain size is smaller, which translates as more reflections and scattering at the interfaces. Take a quartz crystal or glass as an example, in the natural state it is transparent to light and to microwave as well, however, when crushed it turns to be white and translucent. As illustrated in Figure 4.21, more interfaces result in a higher degree of mineral-microwave interactions and more heat generation. This applies to all the light coloured minerals such as quartz, muscovite, plagioclase, olivine and diopside. To further extend this hypothesis, for igneous rocks, the finer the grain size, the more microwave absorptive.

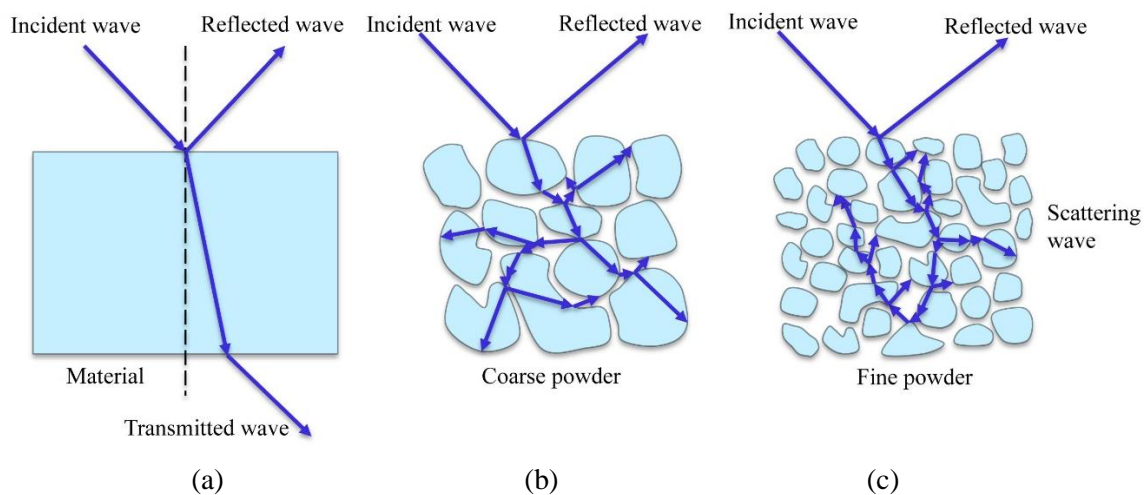


Fig. 4.21 Light (microwave) transmission and scattering in (a) glass, (b) coarse powder, (c) fine powder. Wave reflection, scattering and transmission are illustrative only.

4.4.5 Derivations of loss factors of minerals

(a) Effective medium theory

Based on the effective medium theories, the dielectric properties of a two-phase mixture could be calculated using either the Complex Refractive Index (CRI) Equation or the Landau, Lifshitz and Looyenga (LLL) Equation as shown Equations 4.1 and 4.2 (Nelson and Trabelsi, 2012).

$$(\varepsilon_m)^{1/2} = v_1 (\varepsilon_1)^{1/2} + v_2 (\varepsilon_2)^{1/2} \quad (4.1)$$

$$(\varepsilon_m)^{1/3} = v_1 (\varepsilon_1)^{1/3} + v_2 (\varepsilon_2)^{1/3} \quad (4.2)$$

Where ε_m represents the dielectric properties of the mixture, ε_1 and ε_2 are the dielectric properties of the two components of the mixture, v_1 and v_2 are the volume fractions of the corresponding component ($v_1 + v_2 = 1$). For the case of pure pulverised minerals, they are in fact air-mineral mixtures. In this thesis, only the CRI Equation is adopted as the two equations yield close results. Since air has a dielectric constant of 1 and a loss factor of 0, the CRI equation can be converted into:

$$(\varepsilon'_m)^{1/2} = \left((\varepsilon'_2)^{1/2} - 1 \right) \frac{\rho_b}{\rho_s} + 1 \quad (4.3)$$

$$(\varepsilon''_m)^{1/2} = \frac{\rho_b}{\rho_s} (\varepsilon''_2)^{1/2} \quad (4.4)$$

Where ρ_m and ρ_s are the densities of the bulk mineral (air-mineral mixture) and solid mineral respectively. The density of the solids has been presented previously in Table 4.5.

From Equation 3.17, the heating rates are governed by the density ρ , specific heat capacity C_p , the dielectric loss factor ε'' and the electric field strength E . Of those variables, only ε'' and E are unknown. However, E in a mineral is dependent on its dielectric constant ε' and the overall configurations of the transmission network (Metaxas and Meredith, 1983), which cannot be regarded as unchanged when different materials are heated. Harrison (1997) adopted the method proposed by Florek and Lovás (1995) which involves derivation of the electric field strength by measuring the temperature change of a water load (with a known loss factor of 80) in the cavity. An inappropriate assumption that the electric field strength is unchanged for different minerals was made. As shown in Table 4.9, Harrison (1997) found that the measured heating rates are over 10 times higher than predicted ones. This is because that the dielectric properties of water ($\varepsilon = 80 - 20j$) are fundamentally different from those of low lossy minerals or rocks ($\varepsilon = (5 \square 8) - (0.001 \square 0.2)j$) and the electric field strength in water can be one order of magnitude lower than that in the minerals. If the electric field strength is

assumed unchanged, the electric field and heating rates will be significantly underestimated. To reduce this discrepancy, other methods much be adopted.

Table 4.9 Predicted and measured heating rates of minerals by [Harrison \(1997\)](#).

Mineral	Loss factor	Specific heat capacity (J/kg/K)	Density (kg/m ³)	Predicted heating rate (°C/s)	Measured heating rate (°C/s)
Quartz	0.01	750	2650	0.002	0.083
Feldspar	0.09	600	2600	0.031	0.111
Ilmenite	0.24	800	4700	0.035	0.500
Hematite	0.40	900	5200	0.047	0.472
Chalcopyrite	2.28	1000	4200	0.295	1.000
Pyrite	.00	650	5000	0.168	1.000
Magnetite	2.50	800	5200	0.327	2.111
Galena	1.41	200	7500	0.464	2.388
Water	4.1	4200	1000	0.520	0.520

[Bleaney and Bleaney \(1976\)](#) proposed that when the volume of the dielectric is small, the electric field strength in it could be calculated based on the perturbation theory as:

$$E = \frac{3}{\epsilon' + 2} E_0 \quad (4.5)$$

Although this makes it possible to compare the dielectric properties of different minerals, the exact values of E_0 and loss factors are still undetermined. This method could also be problematic because the volume of the mineral samples in this thesis is not small enough so the perturbation theory is no longer valid, meaning that after the insertion of samples into the cavity, the original electromagnetic fields will be significantly disturbed.

The dielectric constants of minerals are relatively easy to measure and existing data from the literature are collected. In this research, the numerical simulation method is adopted to determine E in the minerals at different power levels. ϵ'' can then be determined using [Equation 4.4](#). Using numerical simulation, ϵ'' can be computed and compared with values in [Table 4.3](#).

(b) Modelling strategy

The modelling strategy are described as below. Using the effective medium theory in [Equation 4.3](#), the dielectric constant of mineral-air mixture is first derived. The dielectric constant will then be used as an input in the numerical simulation to obtain the electric field strength in the mixture at a certain power level. In [Equation 3.17](#), once the heating rate and the electric field strength are known, the loss factor

of the mineral-air mixture can be determined. By using the effective medium theory (Equation 4.4) again, the dielectric loss of mineral solids could be determined.

(c) Modelling setup

A multiphysics software is adopted in this section to study the electric field strength in the dielectric. As shown in **Figure 4.22**, a WR340 waveguide with a cross section of 86.36 mm by 43.18 mm and a length of 249 mm is built. This is the same dimension of the waveguide cavity used in the test. On the left end is the energy source Port operating at 2.45 GHz in the TE₁₀ mode. The waveguide is made of aluminium and its interior is coated with copper to minimise the wall loss. A dielectric (2.2 cm in diameter and 3 cm in height) is placed in the cavity where the electric field strength is the largest. Its thermal and dielectric properties could be predefined. Also in the waveguide is a water load which is to absorb most of the energy from the Port. As the copper coating can be considered as a perfect electric conductor, the Maxwell's equations, i.e. the temporal and spatial electric and magnetic fields, only need to be solved in the air domain and the dielectric domain. Different power levels as in the experiments with a consideration of a reflection coefficient of 20 % are adopted in the simulation.

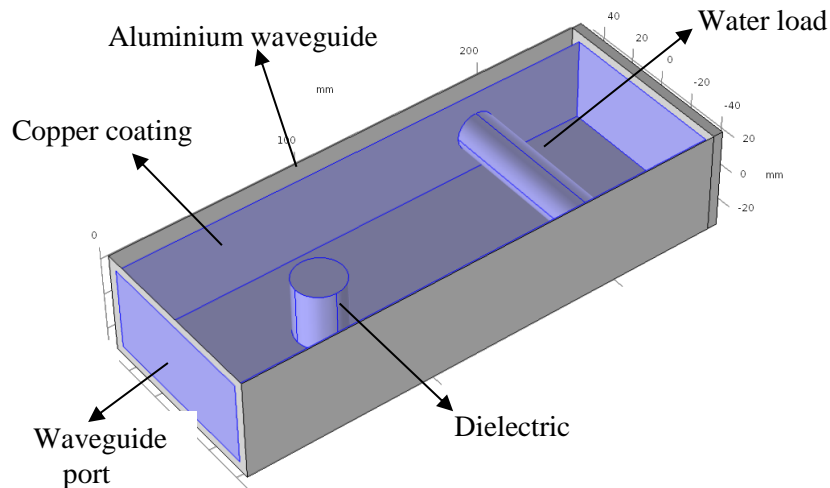


Fig. 4.22 Numerical simulation setup with geometries and boundary conditions.

Figure 4.23 shows the change in electric field strength after the insertion of minerals in the cavity. It can be noticed that by inserting the mineral sample, the electric field distribution is changed. There is a concentration of electric field above the samples, however, the electric strength in the sample is much lower than before the insertion. Using the default function of the software, the average electric field strength in the mineral sample could be computed. It should be noted that for different minerals the electric field strength and distributions are significantly different, primarily depending on the dielectric constants.

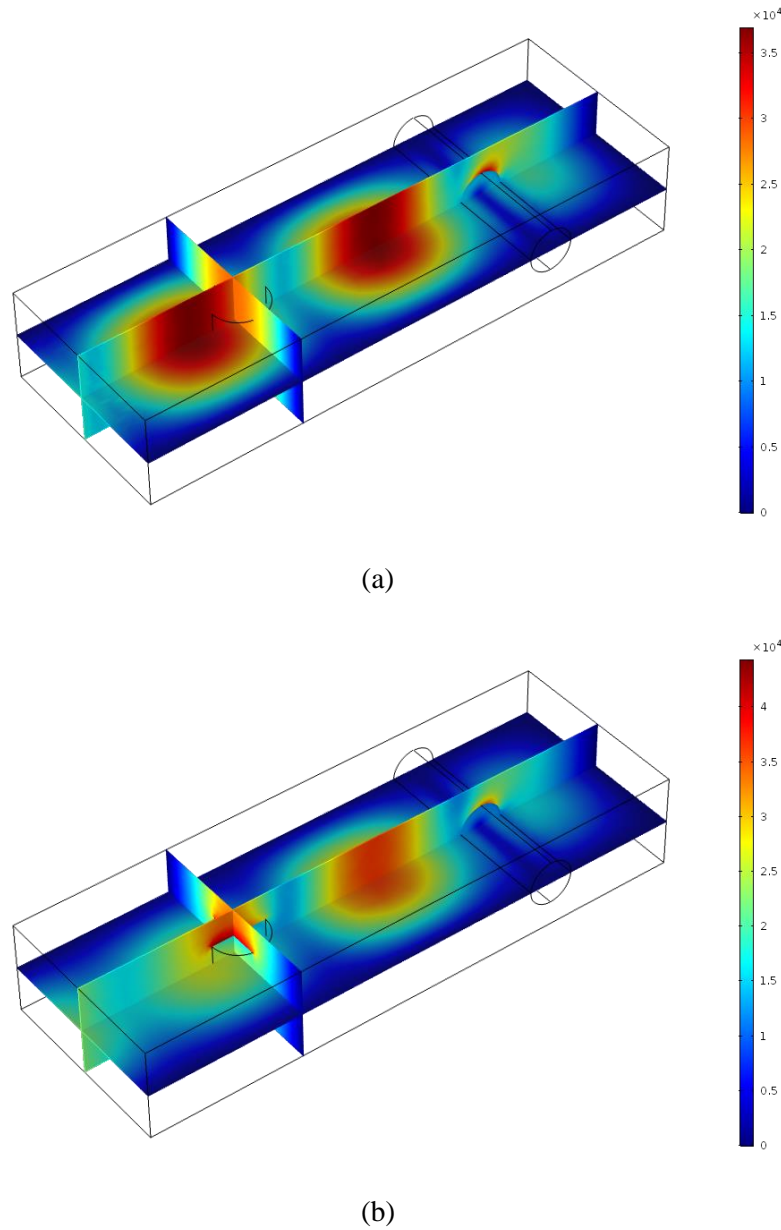


Fig. 4.23 Electric field strength (V/m) in the cavity (a) before and (b) after the insertion of samples.

(d) Modelling results

Table 4.10 shows the calculated electric field strengths at different power levels in minerals. The dielectric constants of minerals of the particulate minerals are derived from Equation 4.3 knowing the dielectric constant of solid minerals, the solid density and bulk density. Results show that the influence of dielectric loss factors on the electric field distribution can be neglected. From **Table 4.10**, it is clear that the electric field strength is negatively correlated to the dielectric constant of minerals. Attempts is made to compare the simulated electric field strength with that computed from Equation 4.5. It shows that Equation 4.5 either overestimate or underestimate the value by about 10 %.

Table 4.10 Calculated electric field strength at different power levels using numerical simulations.

Minerals	m (g)	ρ_m (g/cm ³)	C_{pm} (J/kg/K)	ϵ'_s	ϵ'_m	$E (\times 10^4)$ (0.5 kW)	$E (\times 10^4)$ (1 kW)	$E (\times 10^4)$ (1.5 kW)	$E (\times 10^4)$ (2 kW)
Biotite	11.29	1.13	297	5.9	2.40	1.59	2.25	N/A	N/A
Hornblende	19.20	1.92	498	5	3.00	1.52	2.15	N/A	N/A
Muscovite	7.22	0.72	193	8.69	2.23	1.60	2.27	2.78	3.21
Diopside	22.57	2.26	549	7.18	4.63	1.28	1.81	2.21	2.56
Orthoclase	18.09	1.81	435	5.42	3.69	1.46	2.06	2.52	2.91
Olivine	21.36	2.14	361	7.27	4.25	1.41	1.99	2.44	2.82
Quartz	18.85	1.89	522	2.26	1.84	1.66	2.34	2.88	3.31
Plagioclase	18.32	1.83	383	6.01	4.12	1.36	1.92	2.36	2.72

Using Equations 3.17 and 4.4, the dielectric properties of those minerals could be determined. The results are shown in **Table 4.11**. The order of the loss factors from low to high are quartz, olivine, muscovite, diopside, plagioclase, orthoclase, biotite and hornblende.

Table 4.11 Derivations of loss factors using Equations 3.17 and 4.4.

Minerals	ϵ''_m (0.5 kW)	ϵ''_m (1 kW)	ϵ''_m (1.5 kW)	ϵ''_m (2 kW)	ϵ''_s (0.5 kW)	ϵ''_s (1 kW)	ϵ''_s (1.5 kW)	ϵ''_s (2 kW)
Biotite	0.0069	0.0092	N/A	N/A	0.0466	0.0618	N/A	N/A
Hornblende	0.0384	N/A	N/A	N/A	0.1094	N/A	N/A	N/A
Muscovite	0.0007	0.0006	0.0006	0.0004	0.0112	0.0088	0.0087	0.0065
Diopside	0.0109	0.0082	0.0065	0.0051	0.0233	0.0174	0.0139	0.0109
Orthoclase	0.0119	0.0140	0.0126	0.0116	0.0248	0.0292	0.0262	0.0242
Olivine	0.0035	0.0030	0.0023	0.0020	0.0090	0.0075	0.0057	0.0052
Quartz	0.0035	0.0028	0.0027	0.0023	0.0070	0.0055	0.0055	0.0046
Plagioclase	0.0062	0.0056	0.0068	0.0064	0.0123	0.0112	0.0135	0.0126

The heating rates and dielectric loss factors of the 8 minerals are shown in **Figures 4.24** and **4.25**. It can be found that the heating rates can be used as an indicator to determine the microwave receptiveness of minerals. However, to accurately compare the receptiveness of two very low lossy minerals, the dielectric loss factor should be used. For example, the heating rates of pulverised quartz are higher than that of olivine at the same power level. This does not mean that its dielectric loss factor is also higher.

As shown in Table 4.9 and Figure 4.25, olivine has a relatively higher loss factor. The higher heating rates of olivine may result from its smaller specific heat capacity.

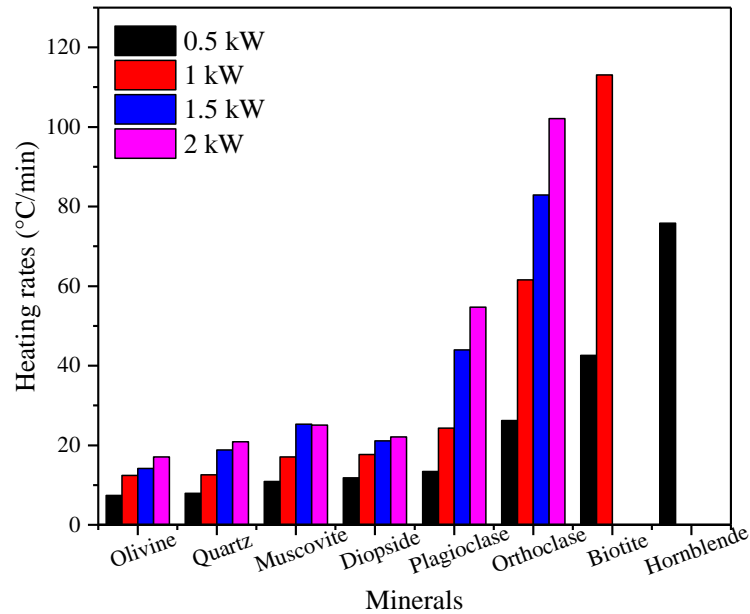


Fig. 4.24 Heating rates of minerals at different power levels.

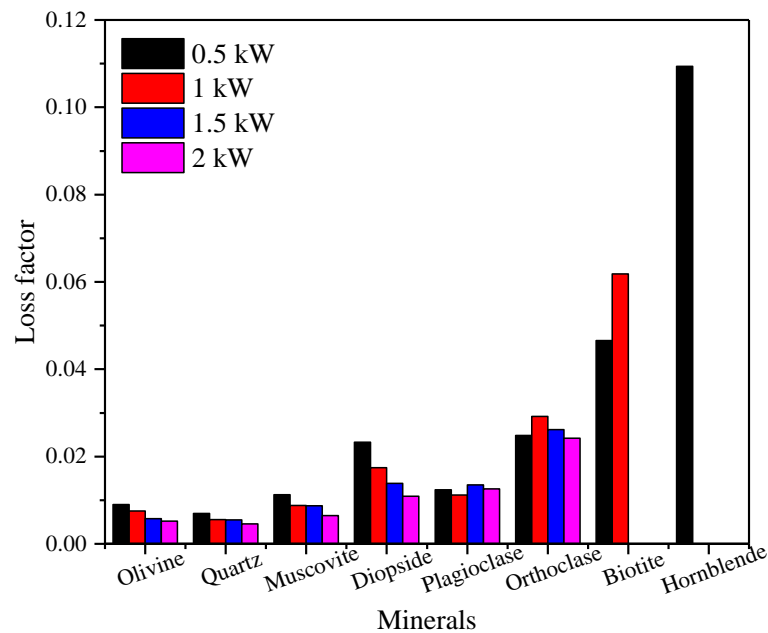


Fig. 4.25 Calculated loss factors of minerals at different power levels.

4.4.6 Heating rates of mineral mixtures (comparing with the pure ones)

Knowing the dielectric properties of pure minerals, the dielectric properties and heating rates of more complex rocks when subjected to microwave irradiation could be predicted. As stated in 4.3.1, minerals are mixed at a half/half ratio for simplicity considerations. For granite, it is composed of 40 % of orthoclase, 40 % of quartz and 20 % of biotite by weight percentage. This section tries to compare the measured temperature (heating rates) with that of the predicted values using Equations 4.3, 4.4 and 3.17. The heating rates of the artificial monzonite, gabbro and granite at 1 kW and 2 kW are shown in

Figures 4.26 to 4.29. From these figures it can be found that the temperature and heating rates of the mineral mixtures fall in between those of the pure minerals. This is more obvious for the case of granite (Figure 4.29). The temperatures of orthoclase and quartz are relatively low, however when 20 % biotite is added to the mixture, the temperatures at the same heating conditions are considerably increased. Those observations well supports the effective medium theories.

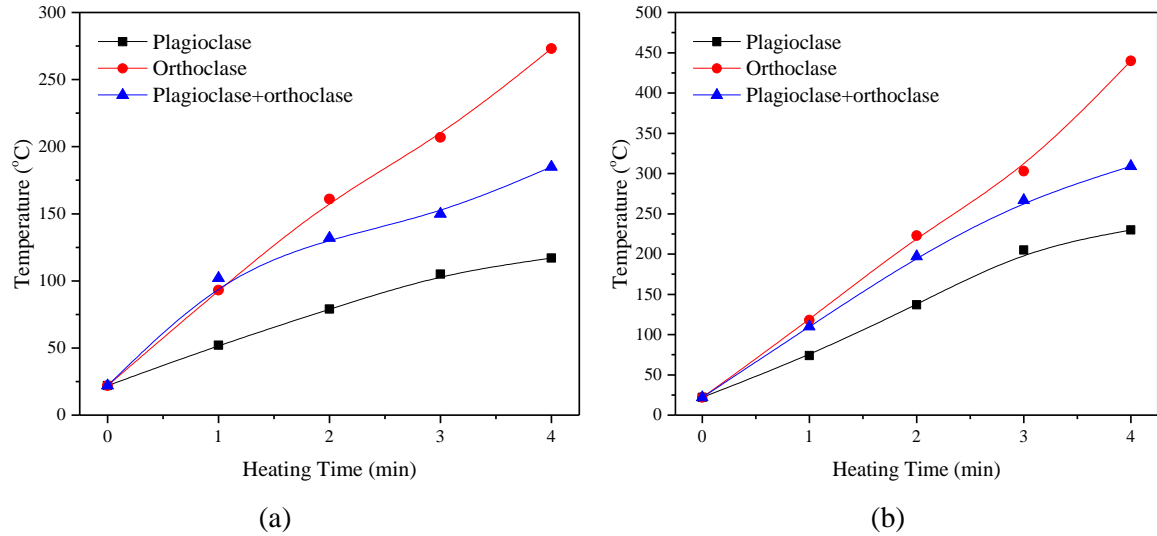


Fig. 4.26 Heating rates of plagioclase-orthoclase mixture (simulated monzonite) at (a) 1 kW and (b) 2 kW.

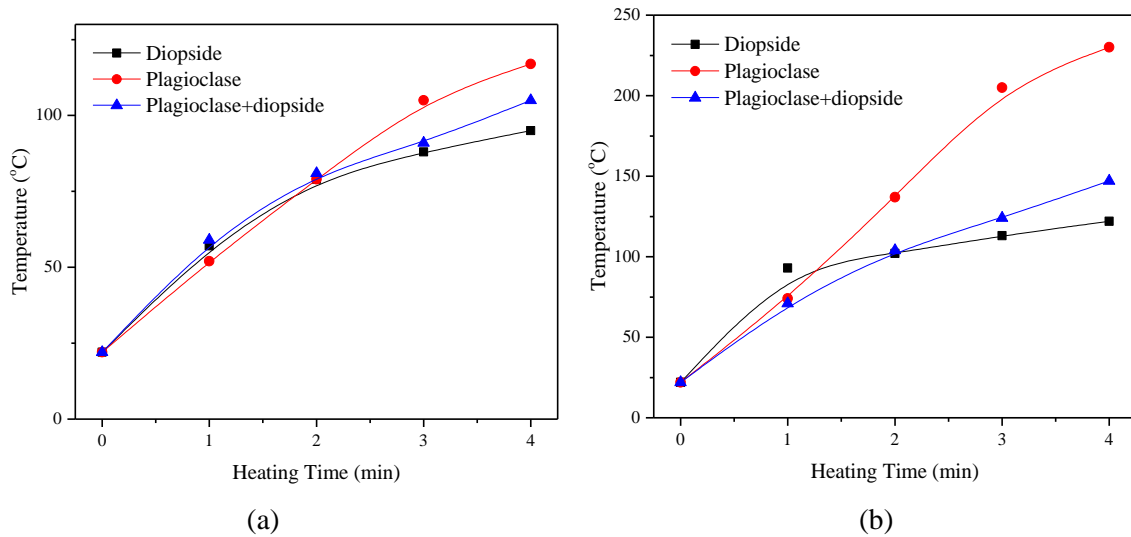


Fig. 4.27 Heating rates of plagioclase-diopside mixture (simulated gabbro) at (a) 1 kW and (b) 2 kW.

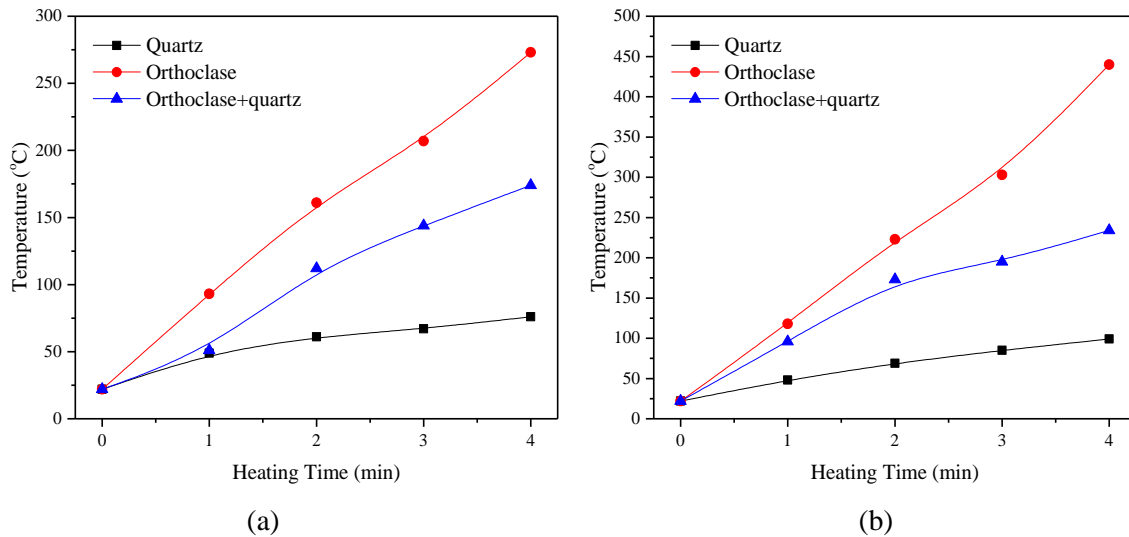


Fig. 4.28 Heating rates of orthoclase and quartz mixture at (a) 1 kW and (b) 2 kW.

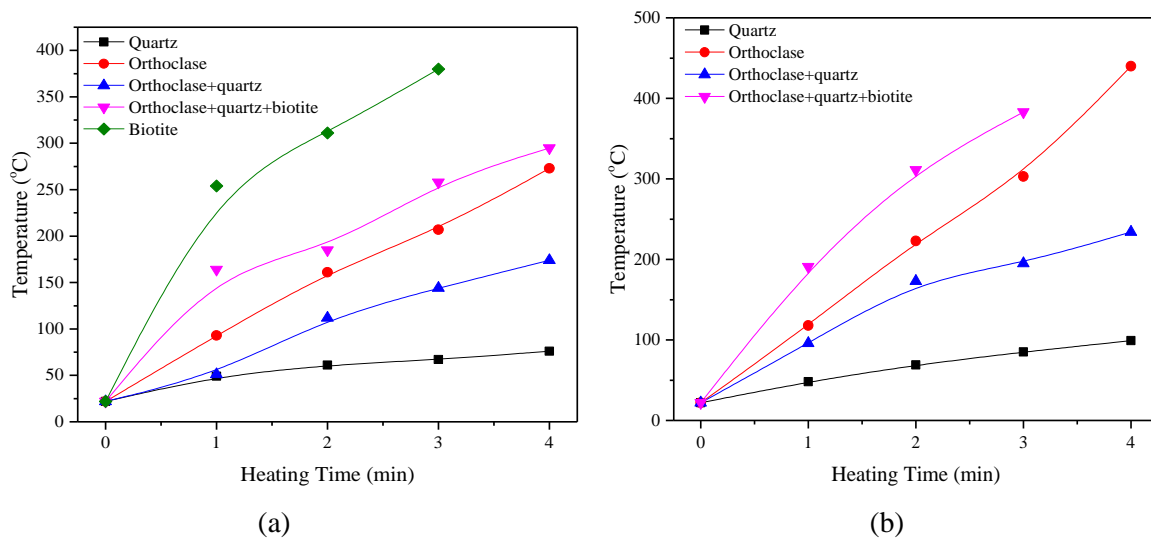


Fig. 4.29 Heating rates of orthoclase, quartz and biotite mixture (simulated granite) at (a) 1 kW and (b) 2 kW.

Table 4.12 shows a comparison between the measured and predicted heating rates of those mineral mixtures at 1 kW and 2 kW. The results at 1 kW indicate that although the measured values are about 10 % less than the predicted values, the prediction is quite satisfactory. The margin between predicted and measured heating rates becomes larger at 2 kW, which might be because of the high heat loss at high temperature due to conventional conduction, irradiation and convection ($P = aT^4$, where a is the Stefan-Boltzmann Constant of $5.67 \times 10^{-8} \text{ W}/(\text{m}^2\text{K}^4)$).

Table 4.12 Comparison between measured and predicted heating rates ($^{\circ}\text{C}/\text{min}$) of mineral mixtures at 1 kW and 2 kW

Minerals	Loss factor	Measured Heating rates (1 kW)	Predicted Heating rates (1 kW)	Measured Heating rates (2 kW)	Predicted Heating rates (2 kW)
Plagioclase-orthoclase (monzonite)	0.0091	37.40	40.04	66.70	80.07
Plagioclase-diopside (gabbro)	0.0077	14.78	19.73	24.80	39.46
Orthoclase-quartz	0.0067	40.10	44.67	80.60	89.34
Orthoclase-quartz-biotite (granite)	0.0113	46.60	49.85	66.70	99.69

4.4.7 Further discussions

Attempts are made to find the dependence of loss factors on the chemical compositions. As shown in [Figure 4.30](#), no significant dependence of loss factors on chemical elements has been found, although [Lu et al. \(2017\)](#) claims that the ferrum content has a significant impact. This holds true for biotite and hornblende, but not for olivine which has the highest ferrum content. Thus no such conclusions can be made soundly in the thesis. Generally the loss factor increases as the complexity (types of elements) of the minerals increases.

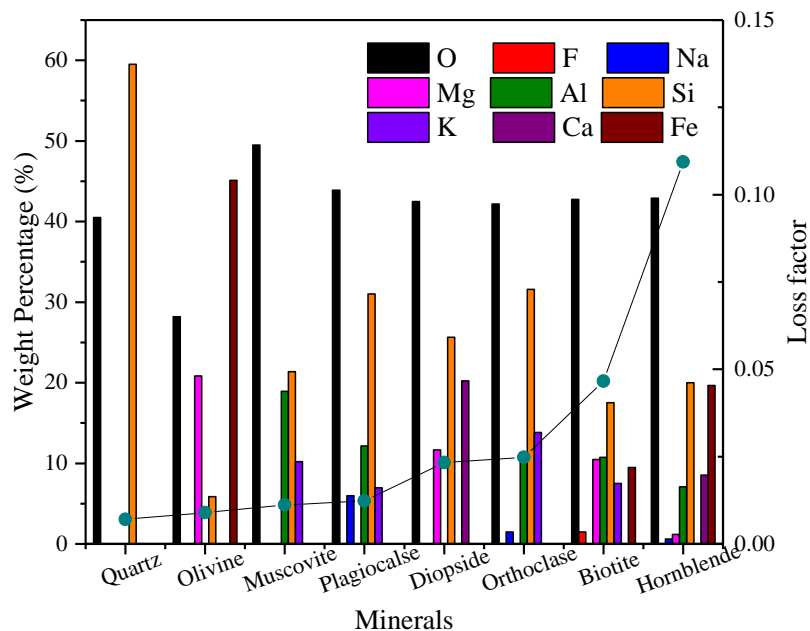


Fig. 4.30 Dependence of loss factor on chemical compositions.

In [McGill et al. \(1988\)](#)'s research, it is found that quartz and orthoclase (25g - 50g) did not heat up effectively from a power range of 500 W to 2000 W. The highest temperature after 7 minutes microwave

treatment are 76 and 67 °C, respectively. In contrast, highest temperatures measured in this research are 105 °C and 440 °C, indicating that even the low loss minerals could be efficiently heated up if the setup of treatment is correct. Arguments based on previous tests using large cavities that microwave is not effective in weakening non-ore normal hard rocks are in a great degree inaccurate, if not wrong.

In the experiment, an infrared thermal camera is used to get the surface temperature of mineral samples. This may lead to a certain underestimation of the heating rates and the dielectric loss factors of the minerals.

4.5 Conclusions

This chapter presents the heating rate tests of 8 basic rock forming minerals of igneous rocks. They are subjected to microwave irradiation at four power levels (0.5 kW to 2 kW) for up to 4 mins. Minerals are classified into categories based on their heating rates. Using a new method combining the heating rates, the effective medium theory and numerical simulations, the dielectric loss factors are computed and compared. The following conclusions can be drawn from this chapter.

- The experimental setup used in the past for the heating rate tests of low loss rock forming minerals are inappropriate. In those tests, they either used closed microwave cavities with no water loads (Chen et al., 1984), or domestic microwave oven with no impedance matching mechanisms (McGill et al., 1995; McGill et al., 1988; Walkiewicz et al., 1988). Those setups could not obtain the heating rates in a realistic manner and could either overestimate or underestimate the heating rates and dielectric properties to a great extent. The setup used in this thesis provides a controlled electromagnetic field for heating rate measurement. The reflection coefficient is controlled by the three-stub impedance tuner and the water load at the end of the circuit makes the waveguide applicator work like open-ended. The results are more close to the field scenario.
- The order of the heating rates from low to high, regardless of the mass of the minerals, is olivine, quartz, muscovite, diopside, plagioclase, orthoclase, biotite and hornblende. They are classified into three categories: good microwave absorbers including hornblende and biotite, intermediate microwave absorber including orthoclase and poor microwave absorbers including quartz, diopside, olivine, muscovite and plagioclase. The results indicate that all the minerals are microwavable at relative high electric field strength. Due to the significant difference in heating rates, it is believed that for rocks in nature minerals will be selectively heated which can be favourable from the viewpoint of energy saving.
- The order of the dielectric loss factors from low to high is quartz, olivine, muscovite, diopside, plagioclase, orthoclase, biotite and hornblende. The relatively low loss factor may attribute to the fact that by crushing and milling those minerals, the crystal structures and the optical properties change. The colours of minerals change from dark green or light green to white.

- The effect of grain size on the heating rates and dielectric properties of minerals indicate that as grain size decreases, heating rates and dielectric properties increase.
- The method combining the heating rates tests, effective medium theories and numerical simulations to derive the dielectric loss factors is demonstrated to be reliable. It can be used to predict the heating rate of more complex rocks subjected microwave irradiation.
- No significant dependence of loss factors on the chemical elements of the minerals has been found.

Reference

- Barani, K., Koleini, S.M.J., Rezai, B., Khodadadi, A., 2012. The effect of sample geometry and placement of sample on microwave processing of iron ore. *International Journal of Applied Physics and Mathematics* 2, 131-134.
- Bleaney, B.I., Bleaney, B., 1976. *Electricity and magnetism*. Oxford University Press, London.
- Campbell, M.J., Ulrichs, J., 1969. Electrical properties of rocks and their significance for lunar radar observations. *Journal of Geophysical Research* 74, 5867-5881.
- Chen, T.T., Dutrizac, J.E., Haque, K.E., Wyslouzil, W., Kashyap, S., 1984. The relative transparency of minerals to microwave radiation. *Canadian Metallurgical Quarterly* 23, 349-351.
- Church, R.H., Webb, W.E., Salsman, J.B., 1988. *Dielectric properties of low-loss minerals*. United-States Department of the Interior and The Bureau of Mines.
- Cumbane, A., 2003. *Microwave treatment of minerals and ores: Dielectric properties of minerals-The Effect of microwave radiation on the grindability and mineral liberation*. University of Nottingham.
- Florek, I., Lovás, M., 1995. The influence of the complex electric permittivity and grain size on microwave drying of the grained minerals. *Fizykochemiczne Problemy Mineralurgii* 29, 127-133.
- Ford, J.D., Pei, D.C.T., 1967. High Temperature Chemical Processing via Microwave Absorption. *Journal of Microwave Power and Electromagnetic Energy* 2, 61-64.
- Harrison, P.C., 1997. *A fundamental study of the heating effect of 2.45GHz microwave radiation on minerals*. University of Birmingham.
- Krupka, K.M., Robie, R.A., Hemingway, B.S., Kerrick, D.M., Ito, J., 1985. Low-temperature heat capacities and derived thermodynamic properties of anthophyllite, diopside, enstatite, bronzite, and wollastonite. *American Mineralogist* 70, 249-260.
- Kumar, P., Sahoo, B.K., De, S., Kar, D.D., Chakraborty, S., Meikap, B.C., 2010. Iron ore grindability improvement by microwave pre-treatment. *Journal of Industrial and Engineering Chemistry* 16, 805-812.
- Liu, C., Xu, Y., Yang, Y., 1990. Applications of microwave energy in extractive metallurgy. *Chinese Journal of Metal Science and Technology* 6.
- Lu, G.-m., Li, Y.-h., Hassani, F., Zhang, X., 2017. The influence of microwave irradiation on thermal properties of main rock-forming minerals. *Applied Thermal Engineering* 112, 1523-1532.
- McGill, S.L., Walkiewicz, J.W., Clark, A.E., 1995. *Microwave heating of chemicals and minerals*. United States Department of the Interior, p. 34.
- McGill, S.L., Walkiewicz, J.W., Smyres, G.A., 1988. The effects of power level on the microwave heating of selected chemicals and minerals. *MRS Proceedings* 124, 247-252.
- Metaxas, A.C., Meredith, R.J., 1983. *Industrial microwave heating*. IET.
- Nelson, S., 2015. *Mining application, Dielectric properties of agricultural materials and their applications*. Elsevier Science, pp. 131-146.
- Nelson, S.O., Lindroth, D.P., Blake, R.L., 1989. Dielectric properties of selected minerals at 1 to 22 GHz. *Geophysics* 54, 1344-1349.
- Nelson, S.O., Trabelsi, S., 2012. Factors influencing the dielectric properties of agricultural and food products. *Journal of Microwave Power and Electromagnetic Energy* 46, 93-107.
- Peinsitt, T., Kuchar, F., Hartlieb, P., Moser, P., Kargl, H., Restner, U., Sifferlinger, N., 2010. Microwave heating of dry and water saturated basalt, granite and sandstone. *International Journal of Mining and Mineral Engineering* 2, 18-29.

- Prokopenko, A., 2011. Microwave heating for emolliating and fracture of rocks, in: Grundas, S.a. (Ed.), *Advances in induction and microwave heating of mineral and organic materials*. InTech.
- Quantachrome, 2017. Gas pycnometers-True density analysis of powders, foams and bulk solids.
- Santamarina, J.C., 1989. Rock excavation with microwaves: A literature review, in: Kulhawy, F.H. (Ed.), 1989 Foundation Engineering Conference. ASCE, Evanston, Illinois, United States, pp. 459-473.
- Shannon, R.D., Oswald, R.A., Rossman, G.R., 1992. Dielectric constants of topaz, orthoclase and scapolite and the oxide additivity rule. *Physics and Chemistry of Minerals* 19, 166-170.
- Shannon, R.D., Subramanian, M.A., Hosoya, S., Rossman, G.R., 1991. Dielectric constants of tephroite, fayalite and olivine and the oxide additivity rule. *Physics and Chemistry of Minerals* 18, 1-6.
- Sikong, L., Bunsin, T., 2009. Mechanical property and cutting rate of microwave treated granite rock. *Songklanakarin Journal of Science and Technology* 31, 447-452.
- Standish, N., 1989. Unusual effects of microwave irradiation in granular materials, First Australian Symposium on Microwave Power. University of Wollongong. Microwave Applications Research Centre.
- Tarbut, E.J., Lutgens, F.K., Tasa, D., 2016. *Earth: An introduction to physical geology*, Global edition. Pearson Education.
- Tinga, W.R., 1989. Microwave dielectric constants of metal oxides at high-temperature. *Electromagnetic Energy Reviews* 2, 349-351.
- Walkiewicz, J.W., Kazonich, G., McGill, S.L., 1988. Microwave heating characteristics of selected minerals and compounds. *Minerals and Metallurgical Processing* 5, 39-42.
- Wang, Y., Forssberg, E., 2000. Microwave-assisted comminution and liberation of minerals, in: Hicilymaz, C., Hosten, C., Arol, A.I., Ozbayoglu, G., Atalay, M.U. (Eds.), 8th international mineral processing symposium, Antalya, Turkey.
- Waples, D.W., Waples, J.S., 2004. A review and evaluation of specific heat capacities of rocks, minerals, and subsurface fluids. Part 1: minerals and nonporous Rocks. *Natural Resources Research* 13, 97-122.
- Wong, D., 1975. Microwave dielectric constants of metal oxides at high temperature. University of Alberta, Canada.
- Zheng, Y., Wang, S., Feng, J., Ouyang, Z., Li, X., 2005. Measurement of the complex permittivity of dry rocks and minerals: application of polythene dilution method and Lichtenecker's mixture formulae. *Geophysical Journal International* 163, 1195-1202.

CHAPTER 5

Experimental Study of Microwave Treatment of Igneous Hard Rocks

5.1 Introduction

This chapter presents in a detailed manner the experimental investigation into the microwave treatment of three representative igneous rocks (gabbro, quartz monzonite and alkali feldspar granite) using a 2 kW single mode microwave system. The selection of the rock types is first justified. The dielectric properties of the rocks and minerals have been characterised in **Chapters 3** and **4**. Their petrographic, physical and mechanical properties are examined following ISRM suggested methods. Then the study methodology, experimental techniques and test procedure are described. This chapter assesses the influence of microwave power level and exposure time on the heating rates, spatial temperature distributions, ultrasonic wave velocities, mechanical strength reductions and crack generation of the three rocks.

5.2 Materials and sample preparation

5.2.1 Rock type selection

As reviewed in **Chapter 3**, the dielectric properties of rocks and minerals in the igneous rock group, which are usually hard and abrasive, vary significantly depending primarily on the mineralogical compositions. The minerals that play a critical role in microwave absorption and rock weakening are very lossy ore minerals (pyrite, hematite, ilmenite, magnetite etc.), relative lossy minerals (feldspar, pyroxene, olivine, mica, etc.) and the low lossy minerals (quartz and calcite). For common igneous rocks, the latter two types of minerals are dominant. Other mineral parameters that influence the weakening of rocks are the difference in dielectric and thermodynamic properties, grain size and microstructure. The most ideal case for microwave to work efficiently is to enclose a good microwave absorber in a microwave transparent mineral to exaggerate the thermal mismatch between grains to the greatest possible extent. Given that the most common igneous rocks encountered in the mining and tunnelling engineering are mafic rocks (basalt, diabase and gabbro which have a silicate content between 45 % and 52 %), intermediate rocks (andesite, micro-diorite and diorite which have a silicate content between 52 % and 63 %) and felsic rocks (granite and granodiorite which have a silicate content over 63 %), one rock type in each class is selected for a comparative study in this PhD research. The selected rocks are gabbro, quartz monzonite (hereafter referred to as monzonite) and alkali feldspar granite (hereafter referred to as granite). The rocks in the QAPF diagram are presented in **Figure 5.1**. The monzonite is fine grained, while the granite and gabbro are medium grained. The dominant minerals in these three rocks are plagioclase, alkali feldspar (mainly K-feldspar), pyroxene and quartz. Each rock has a certain proportion of plagioclase feldspars and varying proportions of pyroxene, orthoclase and quartz. Detailed mineralogical compositions of each rock will be presented in the following sections.

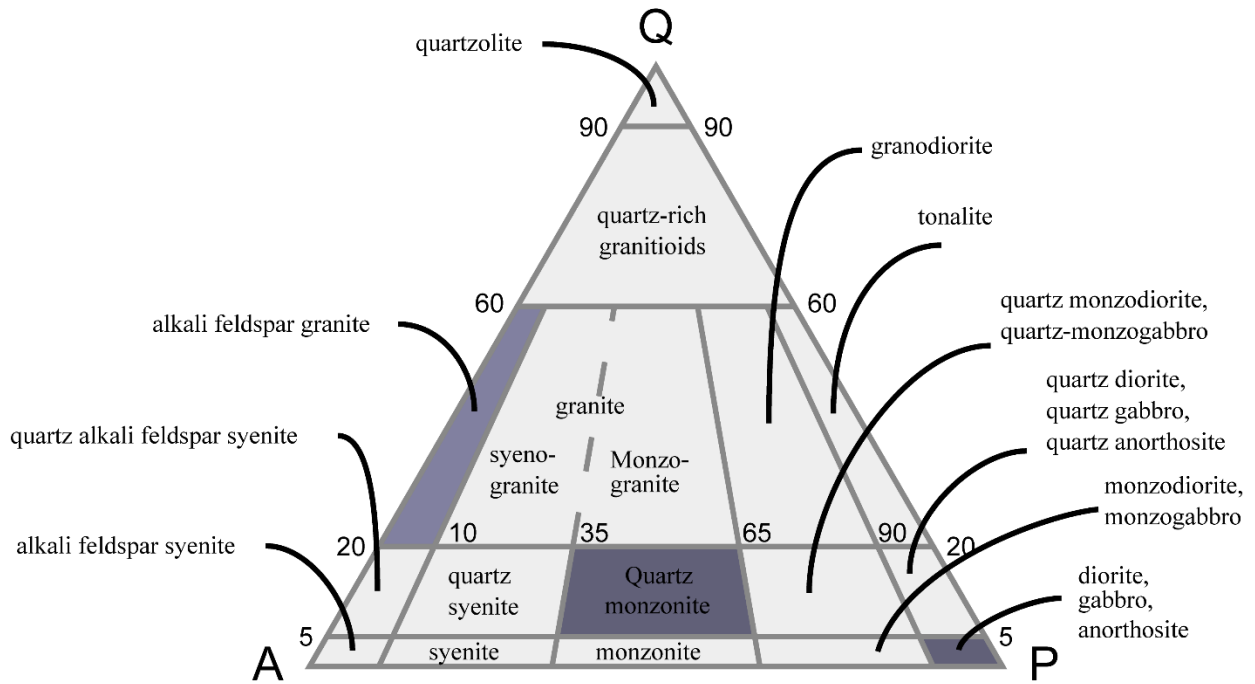


Fig. 5.1 Selected rock types in the QAPF diagram for plutonic rocks (highlighted in dark blue).

5.2.2 Rock descriptions

(a) Gabbro

The Austral Black Gabbro is from the Black Hill Quarry in Adelaide, South Australia. The X-ray diffraction (XRD) analysis is performed using a PANalytical X'Pert powder diffractometer. The XRD spectrum (Figure 5.2) shows that the gabbro is composed of 72 % of feldspar (plagioclase 67 % and orthoclase 5 %), 25 % of pyroxene (clinopyroxene 15 % and orthopyroxene 10 %), and 3 % of biotite, ilmenite and other accessory minerals. Petrographic thin sections are prepared and observed under plane polarised light (PPL) and cross polarised light (XPL) using a Zeiss microscope, as shown in Figure 5.3. The gabbro is fine to medium grained and dark black in colour. Grain sizes range from 100 μm to 3 mm, with some large plagioclase intrusions up to 7 mm in length. The dry density is measured as 2.98 g/cm^3 . Uniaxial compression and tensile tests following the ISRM suggested method show a uniaxial compressive strength (UCS) of 199 MPa, a Brazilian tensile strength of 23.4 MPa, a Young's Modulus of 85 GPa and a Poisson's ratio of 0.24. P-wave velocity is measured as 5858 m/s.

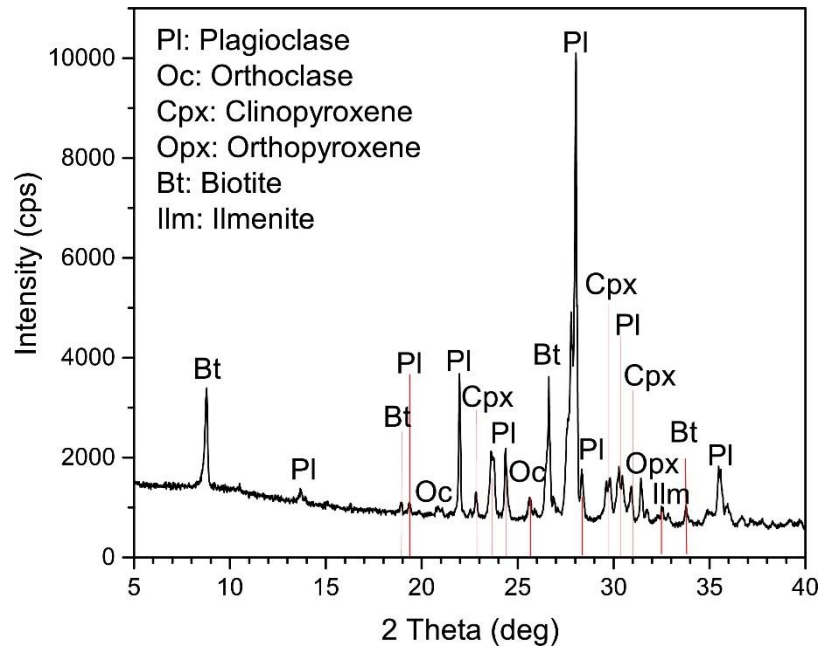


Fig. 5.2 X-ray diffraction (XRD) pattern of the Austral Black Gabbro

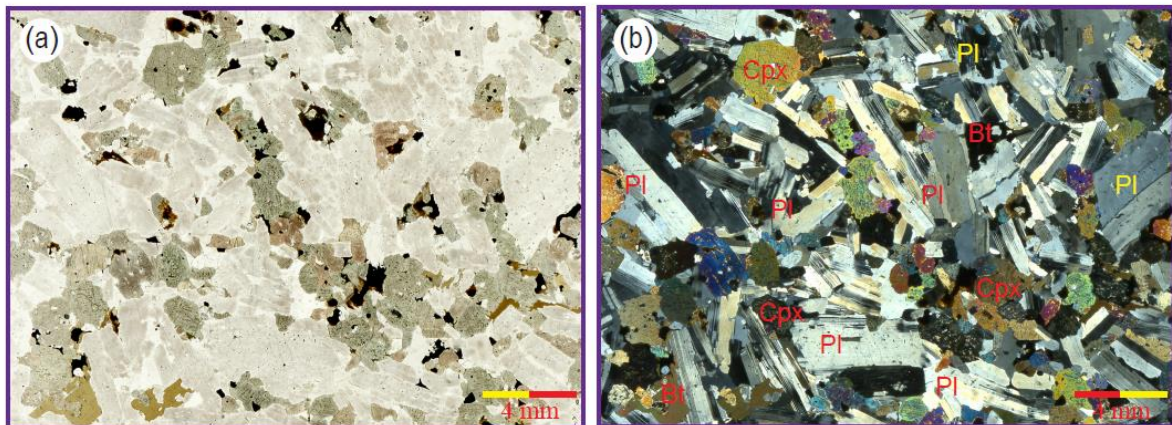


Fig. 5.3 Petrographic microscopy images of the Austral Black Gabbro under (a) PPL and (b) XPL. Pl-plagioclase; Cpx - clinopyroxene; Opx – orthopyroxene; Bt-biotite.

(b) Monzonite

The monzonite is sourced from Fujian Province, China. It is fine grained and grey dark to dark in colour. The petrographic images are shown in Figure 5.4. Mineralogical compositions and contents are estimated based on the PPL and XPL images. The estimate shows that the monzonite consists of 38 % of alkali feldspar, 30 % of plagioclase, 10 % of quartz, 10 % of biotite, 7 % of pyroxene and 5 % of other accessory minerals. Grain sizes range from 100 μm to 1 mm. The dry density is measured as 2.87 g/cm^3 . Uniaxial compression tests following the ISRM suggested method show a uniaxial compressive strength (UCS) of 210 MPa, a Brazilian tensile strength of 14.1 MPa, Young's Modulus of 90 GPa and Poisson's ratio of 0.22.

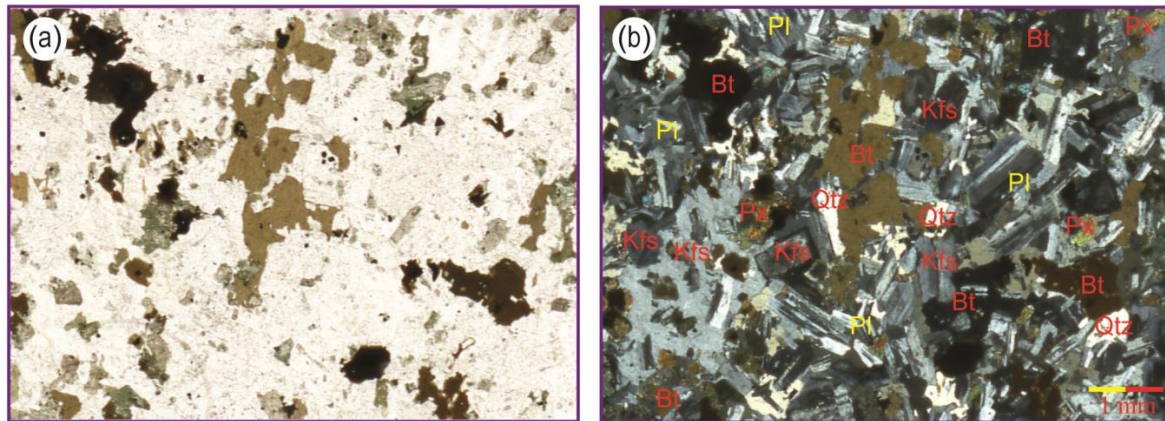


Fig. 5.4 Petrographic microscopy images of the monzonite under (a) PPL and (b) XPL. Bt-biotite; Kfs-k feldspar; Pl-plagioclase; Qtz-quartz.

(c) Granite

The granite is sourced from Hubei province, China. It is medium grained and light grey in colour. The petrographic images are shown in **Figure 5.5**. Estimates from the PPL and XPL images show that the granite consists of 55 % of alkali feldspar, 5 % of plagioclase, 30 % of quartz, 5 % of biotite and 5 % of accessory minerals. The rock is equigranular with a grain size of about 2 mm. The dry density is measured as 2.70 g/cm³. Compression tests show the uniaxial compressive strength (UCS) of 170 MPa, Young's Modulus of 74 GPa and Poisson's ratio of 0.21.

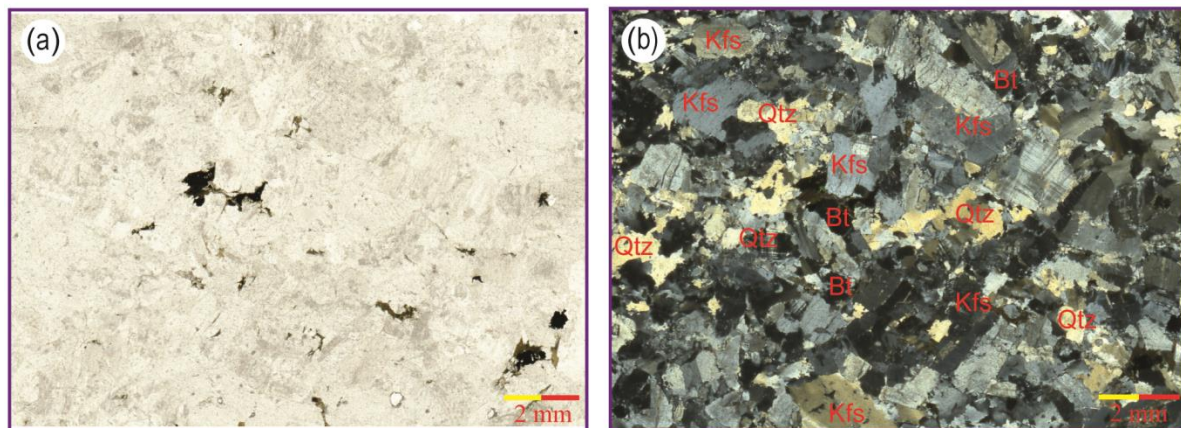


Fig. 5.5 Petrographic microscopy images of the granite under (a) PPL and (b) XPL.

5.2.3 Sample preparation

Gabbro rock slabs with a dimension of 1000 mm long, 600 mm wide and 30 mm thick are sliced from a large rock block. Since the interior cross section of the waveguide applicator is 86 mm wide by 43 mm high, the dimension of specimens is prepared at a size of 84 mm by 41 mm using a diamond saw and a grinding wheel. The cutting accuracy is ± 1 mm. Granite and monzonite specimens are ordered from China. The specimens are free from visible cracks and are consistent in ultrasonic wave velocities.

Specimens are dried in an oven at 60 °C for 48 hours before microwave treatment to mitigate the possible influence of moisture content on the test results.

5.3 Experimental facilities and procedures

5.3.1 Microwave system setup and temperature measurement

For laboratory study of the effect of microwave treatment on the physical and mechanical properties of hard rocks, a single mode industrial microwave system should be selected. The system has been introduced in Section 4.3.3. A schematic of the system is shown. Some features and advantages of the microwave system include: (1) it is single-mode and is able to provide a much higher electric field (which converts to a high power density); (2) it has an electromagnetic impedance tuner to maximise the microwave power transmission; (3) it has a water load at the end to simulate the field scenario where rock to be treated is infinite; (4) it is able to exaggerate the heating non-uniformity using a relatively low power. The power levels used in this study are 0.5 kW, 1 kW, 1.5 kW and 2 kW. The exposure times are 30 s, 60 s, 90 s and 120 s. In total there are 16 testing conditions. Three to four heating tests were performed for one condition to obtain statistic results.

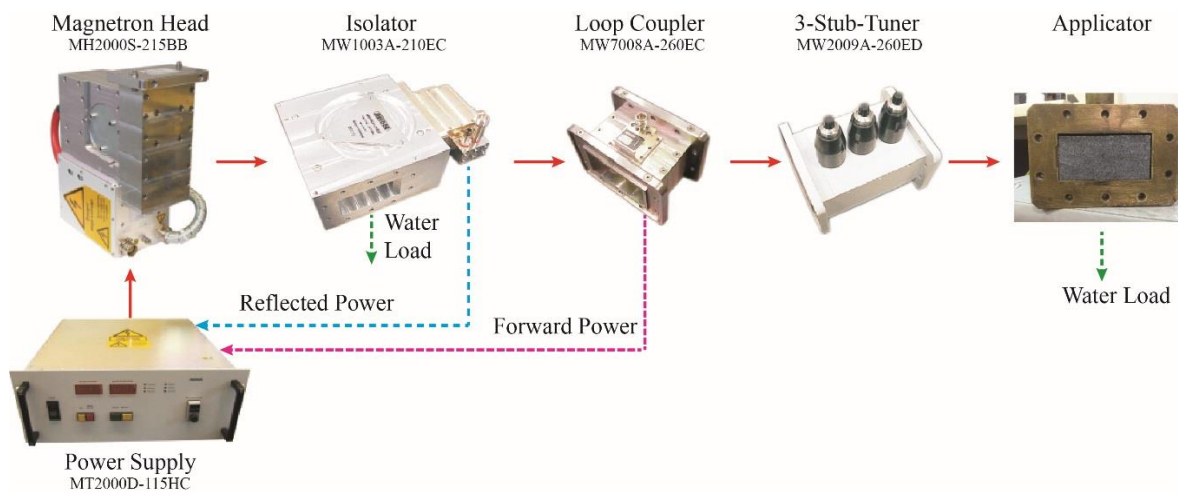


Fig. 5.6 Schematic of the experimental setup of microwave treatment of rocks.

5.3.2 Crack extraction techniques

The fluorescent approach proposed by Nishiyama and Kusuda (1994) is adopted to extract the crack patterns. The methodology is briefly described below. Fluorescent dye mixed with Araldite two-part epoxy is used to impregnate the microwave treated specimens in a vacuum desiccator. After the epoxy is hardened specimens are polished on a grinder to remove the excess fluorescent and then observed under the ultraviolet (UV) light to reveal the crack information. Thin sections are then made and observed using the ZEISS petrographic microscope. By comparing the UV light images and the microscopic images, the crack patterns are identified.

A Zeiss Xradia 520 Versa X-ray Microscopy with a submicron precision is used to extract the internal cracks in the microwave treated specimens. The process involves placing the specimens in between an

X-ray source and aperture and a detector and rotating the specimens on the stage by 360° around its vertical axis. The 2D projections are then reconstructed to 3D volumes and further analysed using XRM Reconstructor software image processing software Avizo.

5.3.3 Thin section preparation

Petrographic studies based on thin section microscopic observations provide insights into the mineral compositions and the rock textures. In this study, petrographic thin sections with a cross section of 60 mm by 40 mm and a thickness of 30 micron are made and observed at the School of Earth, Atmosphere and Environment, Monash University. The mineral composition of the three rocks, intergranular and trans-granular macro/microcrack are distinguished and characterised. The equipment used in preparing thin sections are presented in Figure 5.7. The procedures taken by the author in this study include the following steps.

- (1) Impregnation of microwave treated friable gabbro with epoxy resin. This is to protect the existing texture as good as possible and reduce generation of new cracks during the later cutting, grinding and polishing steps. The epoxy resin used is Araldite 3600 which is a two part epoxy mixing at a precise ratio of 3:1. In the impregnation step, a vacuum desiccator (Figure 5.7(a)) is used to ensure penetration of epoxy resin into the cracks. The impregnated specimen is then placed on a hot plate (Figure 5.7(b)) at 90 degree for about 90 mins to fast harden the epoxy.
- (2) Trimming and lapping of specimens into glass slide-size blocks. Trim saw diamond wheel grinder and flat glass (Figures 5.7(e)-(e)) are used. A very good flatness should be observed by the reflection test.
- (3) Mounting the rock block on a glass slide. One side of glass slides is frosted on the flat glass and the rock block is then mounted on the slide with the Araldite epoxy. Air bubbles in the epoxy should be avoided and eliminated. The bonded blocks is then placed on the bonding/mounting jig (Figure 5.7(f)) to minimise epoxy wedging between block and glass slide. The hardening of epoxy in room temperature takes about 12 hours.
- (4) Thinning bonded blocks. The bonded block is cut by the saw on the left side of Figure 5.7(g) to a thickness of 2 mm and then grinded to a thickness between 100 micro to 200 micro by the grinder on the right. This is to reduce the cracks induced by grinding and to reduce the time on final lapping to 30 microns.
- (5) Final lapping of thin sections. The section is then grinded on the flat glass with silicon carbide to a thickness of 30 micron. At the last stage of this step, frequent checks should be done with the help of a microscopy and the Michel-Levy chart (Figure 5.7(h)) and the micrometre.
- (6) Covering of thin sections. Sections are then carefully cleaned and covered with a slide cover using a UV glue.
- (7) A general description of mineral distribution and crack can be obtained by using a geological scanner with polarising films placed above and/or below a thin section. The scanner is a very

efficient and time saving tool to map the petrology and fabric information on the thin sections. However, the resolution is not high enough for identifying microcracks due to a limited focus adjustment capability of the scanner. To be able to distinguish the microcracks and count/calculate the crack density, one needs to use the petrographic microscopies which have larger magnifications and higher focusing capabilities.



(a)



(b)



(c)



(d)



(e)



(f)



(g)

(h)

Fig. 5.7 Thin section preparation facilities. (a) Vacuum desiccator; (b) Hot plates; (c) Trim saw; (d) Diamond grinder; (e) Flat glass; (f) Slide mounting jig; (g) Thin section saw and grinder; (h) Microscopy and ultrasonic cleaner.

5.3.4 Petrographic microscopy observation

Observations of the thin section are carried out at the Microscopy Laboratory, School of Earth, Atmosphere and Environment, Monash University. The two polarising microscopies used are Nikon Optiphot2 and Zeiss Axio (**Figure 5.8**). The magnifications of the two microscopies are X5, X10, X20 and X40. Both microscopies can work in plane-polarised and cross polarised light modes and are equipped with real time cameras. The observation normally starts with X5 magnification and then tune in higher magnification to observing more details such as microcracks. A coordinates adjusting system can be mounted on the rotating stage for a precision control of the section position. This is crucial for mapping the whole thin section.



(a)



(b)

Fig. 5.8 Petrographic microscopies utilised. (a) Nikon Optiphot2 microscopy; (b) Zeiss Axio microscopy.

5.3.5 P-wave velocity measurement

The ultrasonic compressive wave (P wave) velocities of the specimens are measured before and after microwave treatment using the ultrasonic pulse transmission method to quantify the thermal damages induced. The P-wave transducers used are Olympus Model V103 with a working frequency of 1 MHz. A spike-shaped excitation pulse for a duration of 200ns is generated using the PXI-5412 waveform generator. The emitter is driven by a Trek piezo driver (Model 2100HF) while the signal of the receiver is amplified by an Olympus preamplifier (Model 5660B). The sampling rate of the system is 10MHz to achieve a high enough accuracy. Olympus Couplant B-Glycerin is used to keep the transducers and

rock in good contact for efficient sound transmission. The layout of the basic components is shown in **Figure 5.9(a)**. The P-wave velocity before microwave treatment is denoted as V_0 . Considering the variation of the degradation at different locations, P-wave velocity at three locations (left, middle and right) are measured, as shown in **Figure 5.9(b)**. The P wave velocities are named as V_l , V_m , V_r accordingly. The overall p-wave velocity of the specimen after microwave treatment is measured from the left end to the right end and is termed as V_0' .

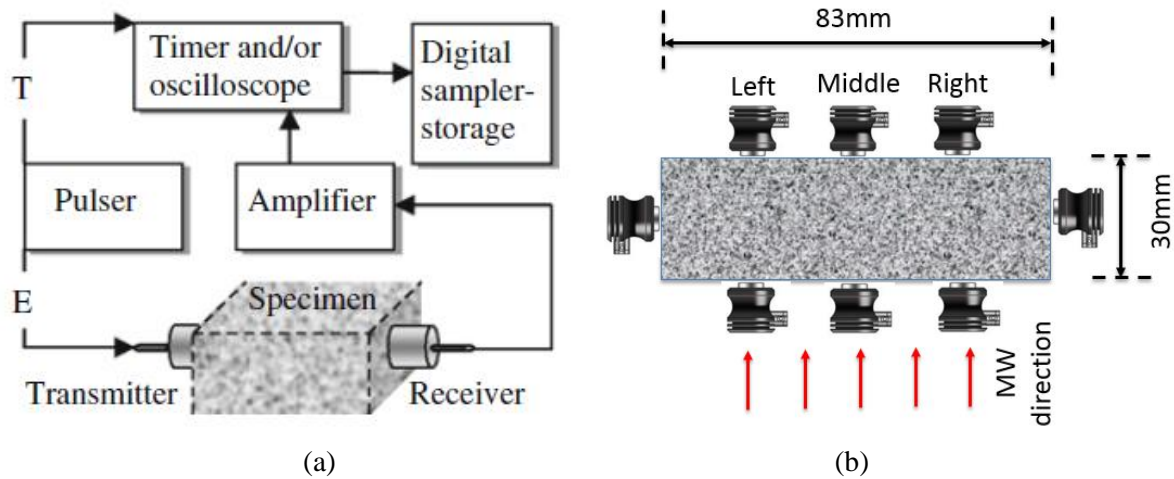


Fig. 5.9 Measurement of P-wave velocity. (a) Measurement setup (ISRM); (b) Measurement locations.

5.3.6 Compression testing machine

Compression tests along the long dimension are performed using a 300 kN Shimadzu AGS-X Series testing machine (**Figure 5.10**) to quantitatively evaluate the reduction in destructive energy after microwave treatment. The loading rate is set at 0.2 mm/min for all the tests. By integrating the area under the load-displacement envelope, the destruction work proposed by [Thuro and Spaun \(1996\)](#) can be calculated and compared. It is worth mentioning here the strength cannot be called as the UCS as those rock specimens are damaged to different degrees at different locations and the dimension doesn't conform to the standards for mechanical strength testing.



Fig. 5.10 300 kN Shimadzu AGS-X Series testing machine

5.3.7 Test procedures

The experimental tests are carried out following four steps. The P-wave velocity of the specimen before microwave treatment is measured to make sure it is consistent at different locations. Then, the specimens are treated by the microwave system at four power levels (0.5, 1, 1.5 and 2 kW) for four exposure times (30, 60, 90 and 120 seconds). Three tests are performed for one testing condition. Once the heating is finished, the temperature of the specimen surface is taken using two thermometers within 5 seconds. Ordinary optical images are also taken simultaneously for comparative studies. The P-wave velocities of microwave-treated specimens are measured to quantify the thermal damage. Finally, thin sections of specimens treated by the fluorescent technique are prepared and observed under the ZEISS petrographic microscope and under the UV light to extract crack patterns. The room temperature varies between 15 and 21 °C during tests. Below is a description of the microwave testing procedure:

- (1) Connect water circulation and preheat the microwave system for about 3 minutes at 2 kW.
- (2) Place a dried specimen in the sample holder and seal the flange connection with aluminium tape and a pair of strong clamps
- (3) Set a low output power on the panel (3 %) and switch MW-On
- (4) Adjust the stubs of the impedance tuner to achieve the minimum possible power reflection, then press MW-Off
- (5) Set the desired power level on the panel and press MW-On and start the stopwatch or timer
- (6) Manually adjust the stubs to maintain the lowest possible reflection coefficient

- (7) Record the reflection power and keep vigilant. Turn off the microwave when plasma is observed or cracking is heard.
- (8) When time is up, press MW-Off.
- (9) Quickly remove the clamps and tape and take the thermal/optical images of the rock surface and use the shot gun when necessary
- (10) After the sample cools off, remove it from the applicator Record the crack patterns on a notebook and take photos if necessary
- (11) Repeat (1)-(13) for other tests

5.4 Test results and discussions


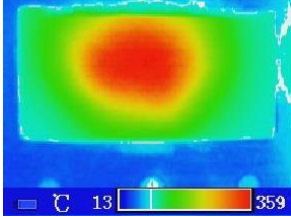

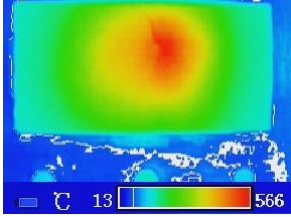

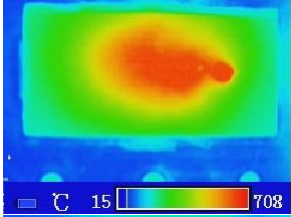

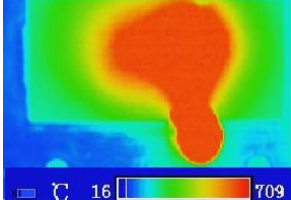
5.4.1 General observations

(a) Gabbro specimens

For the gabbro tested, the reflection coefficients at the four levels are controlled at around 16 %. Depending on the power level and exposure time, different phenomena after microwave treatment are observed. **Table 5.1** summarises the observations of one set of the gabbro specimens heated at 2 kW for up to 120 seconds to elucidate the possible outcomes. Basically there are three expected results, namely no visible cracks, cracks, and crack and melting. For specimens heated at low power levels or at high power levels for short durations, for example, when heated at 0.5 kW for 60 seconds, or at 2 kW for 30 seconds, no visible cracks can be observed by naked eyes. However, when using the fluorescent resin technique, cracks at the top or bottom middle of the specimens can be identified.

Table 5.2 shows the cracks in the gabbro specimens after microwave treatment at different power levels for different durations. As either power level or exposure time increases, visible cracks are observed starting from the top or bottom middle of specimens (as shown in the optical and thermal images in **Table 5.2**). This is due to the stronger electromagnetic field and higher thermal gradients in the middle part of the specimens. When the specimens are heated at even higher power levels, not only cracks but also melting are observed. For microwave assisted rock breakage and fracturing, melting should be avoided as a lot of energy will be wasted. From **Table 5.2** it is clear that as either power level or exposure time increases, the crack number and density increase.

Table 5.1 Observations of gabbro specimens heated at 2 kW for different durations

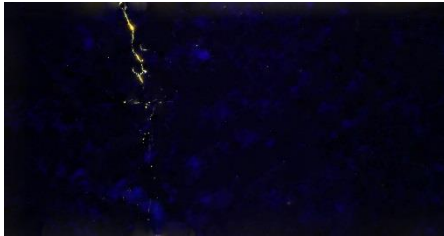

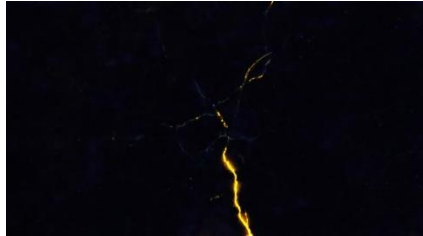
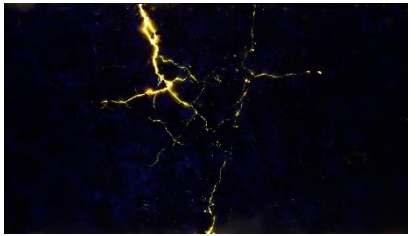


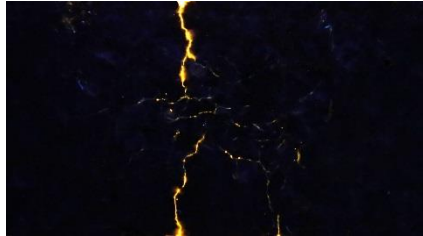


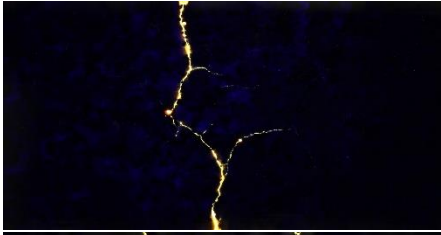
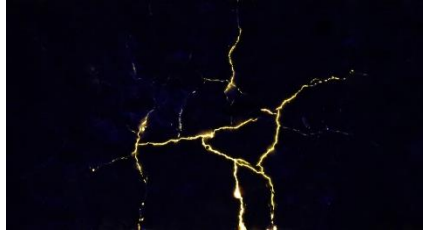



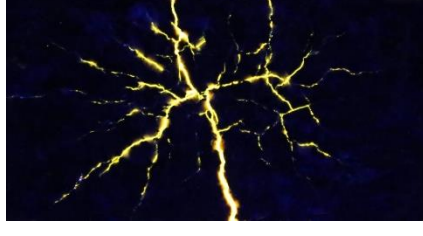

Time (s)	Optical images	IR images	Temp (°C)	Crack/melt	Comments
30			359 ^a	Cracked Not melted	Maximum temperature appears in the centre. Most typical for specimens heated at lower power levels.
60			566 ^a	Cracked	Crack appear from the upper/lower middle. Temperature not high enough to melt the rock. Typical for specimens heated at low powers or for short durations.
90			750 ^b	Cracked and melted	Crack appears in the centreline. Lava-like melting takes place in the centre. Temperature measured is 50 to 100 °C lower than that at the core.
120			900 ^b	Cracked and melted	Large area in the centre of the specimen is melted. Highest temperature is expected to be over 1400 °C (melting point of plagioclase).

Note: a- temperature measured using the thermal camera; b- temperature measured using the IR gun.

(b) Monzonite specimens

For monzonite specimens, similar phenomena as gabbro specimens are observed. Table 5.3 shows the optical and IR images of one set of monzonite specimens heated at 2 kW. Due to the difficulties in manually matching the electromagnetic impedance of the transmission line and the load, the reflection coefficients of tests are about 32 %, meaning the microwave heating is 16 % less efficient than heating the gabbro specimens. To compensate the power loss due to reflection, estimate of maximum temperature is performed by multiplying the measured values by 1.24. This higher temperature may have been achieved if an automatic tuner is used. Another reason for the low temperature is due to the low dielectric properties of monzonite than that of gabbro. Those two factors combined contribute to the low temperatures and a possible lower rock weakening effect. For all the heating conditions, the monzonite specimens only melt when heated at 2 kW for 120 seconds. During the tests very few acoustic emissions took place. The cracks in the specimens after microwave treatment are shown in Table 5.4. It can be found that after microwave treatment much fewer cracks can be identified in the monzonite specimens than in the gabbro specimens under the same heating condition. This might be attributed to the fact that the grain size is smaller translating as a smaller stress build-up.


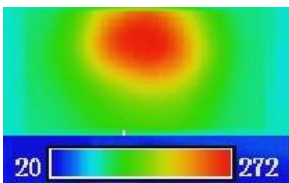

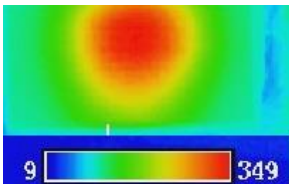

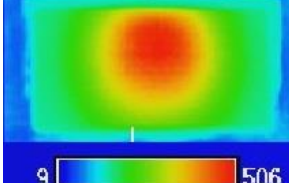

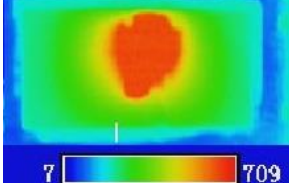
Table 5.2 Microcrack extraction in gabbro specimens after microwave treatment using the fluorescent resin technique.

	0.5 kW	1 kW	1.5 kW	2 kW
30 s				
60 s				
90 s				
120 s				

Note: Sample size: 80mm by 40mm.

The software Photoshop is used to remove the speckles on the surface.

Table 5.3 Observations of monzonite specimens heated at 2 kW for different durations

Time (s)	Optical images	IR images	Max. temp. (°C)	Max temp. if well-tuned	Crack/ melt
30			272 ^c	337	Cracked Not melted
60			349 ^c	434	Cracked Not melted
90			506 ^c	627	Cracked Not melted
120			900 ^d	N/A	Cracked and melted

Note: c- temperature measured using the thermal camera; d- temperature measured using the IR gun.

(c) Granite specimens

The microwave treatment of granite specimens shows some substantially different features. When heated at power levels of 0.5 kW for 30 seconds and 60 seconds, the specimens stay relatively cool and no cracks can be observed by naked eyes and the fluorescent technique. As exposure time increases, acoustic emission activities begin to occur indicating cracking events. However, when heating at higher power levels, catastrophic failures took place. **Figure 5.11** shows some of the typical failure modes. **Figures 5.11(a)-(c)** show a specimen heated at 1 kW for 10 seconds when the maximum measured temperature is only 72 °C. It is not hard to find that microwave is selectively heating biotite. However, due to the quick dropping of temperature, the temperature of melted biotite could not be captured. **Figures 5.11(d)-(f)** show a specimen heated at 2 kW for 1 second only. **Figure 5.11(g)** shows a specimen heated at 1 kW for 50 seconds. **Figure 5.11(h)** shows a specimen heated at 1.5 kW for 90 seconds. It is not hard to tell from the photos that microwave is selectively heating the dark minerals (biotite and accessory minerals) in middle part of the granite specimens. The quick heating of those mineral will induce great thermal expansion in the granite. When the temperature is high enough those minerals may melt and the thermal stress is able to efficiently break the rocks. If the dark minerals are concentrated in geometry centres the phase change would shatter the rock piece into halves (**Figures 5.11 (a)-(g)**). If

the dark mineral is close to the free surface, the melt mineral will extrude to the surface and generate local cracks and/or spalling (Figures 5.11 (d), (g) and (i)). Under those circumstances, the dark mineral will experience thermal runaway and quicker temperature increase, resulting in generation of plasma (microwave induced electrical arcing), unmatched impedance and catastrophic rock failures. As a result at 2 kW the granite cannot be heated for over 60 seconds. Also no data are available for heating at 1.5 kW for 120 seconds, even though a couple of attempts are made. From Table 5.6, one can find that the crack numbers in granite specimens after microwave treatment are significantly less than in the gabbro and monzonite specimens. Those specimens fail in a brittle way before more complicated crack networks are developed. From a rock breakage point of view, granite is the most favourable rock type for microwave.

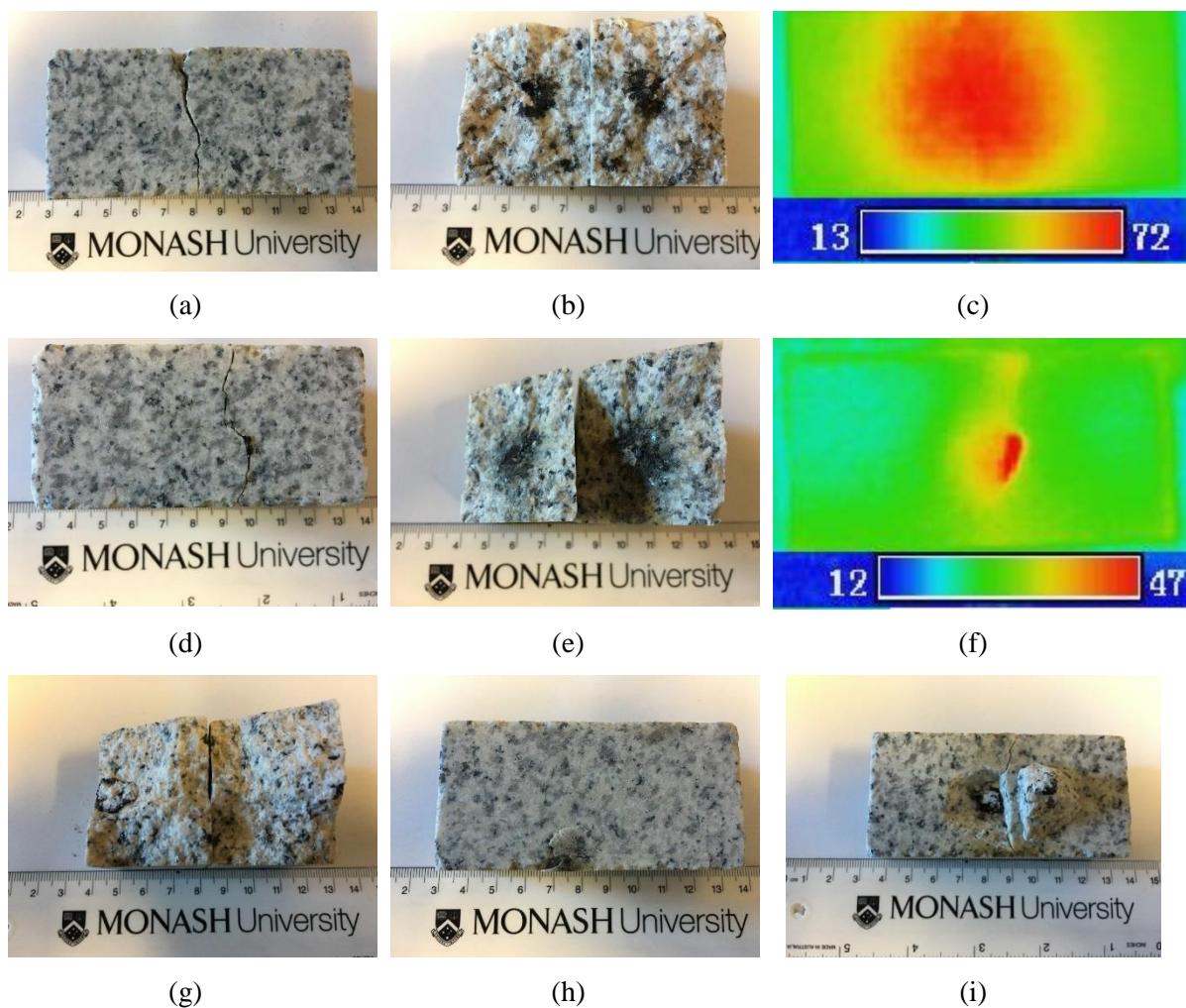
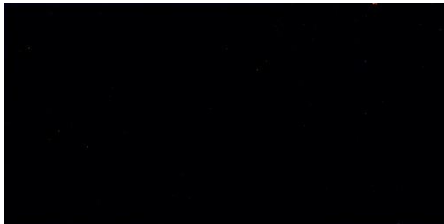

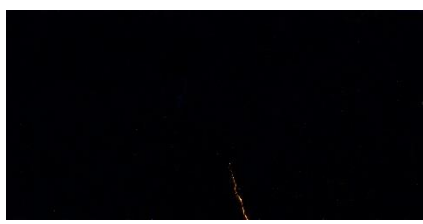
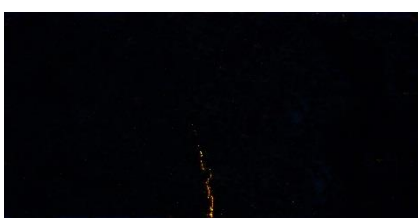
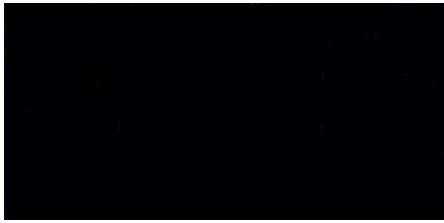
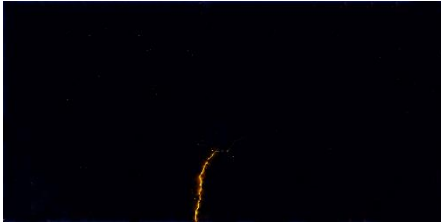
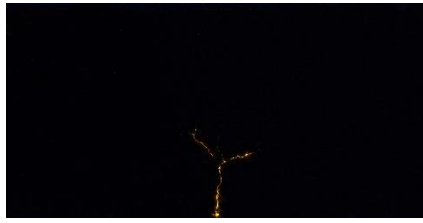


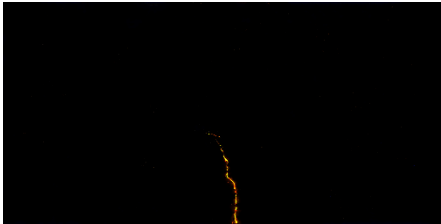

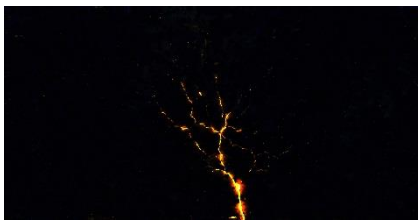
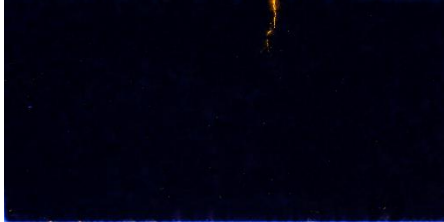

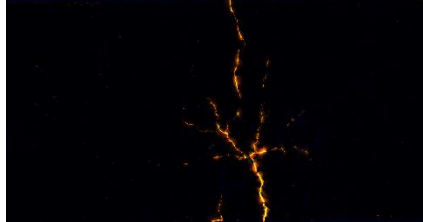
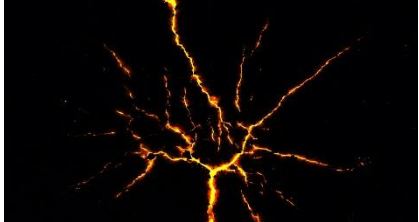


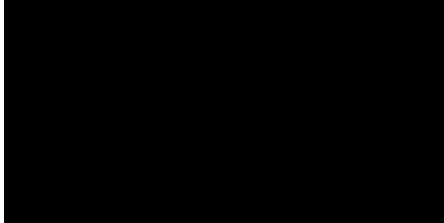



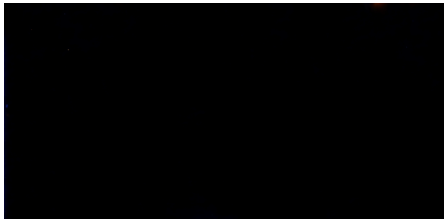
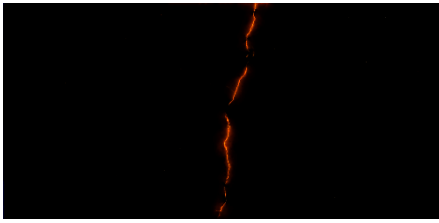
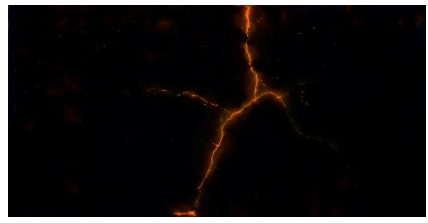





Fig. 5.11 Microwave treatment of granite specimens. (a)-(c) show a specimen heated at 1 kW for 10 seconds; (d)-(f) show a specimen heated at 2 kW for 1 second; (g) shows a specimen heated at 1 kW for 50 seconds; (h) shows a specimen heated at 2 kW for 3 seconds; (i) shows a specimen heated at 1.5 kW for 90 seconds.

Table 5.4 Crack extraction in monzonite specimens after microwave treatment using the fluorescent resin technique.

	0.5 kW	1 kW	1.5 kW	2 kW
30 s				
60 s				
90 s				
120 s				

Note: The software Photoshop is used to remove the speckles on the surface.

Table 5.5 Crack extraction in granite specimens after microwave treatment using the fluorescent resin technique.

	0.5 kW	1 kW	1.5 kW	2 kW
30 s				
60 s				N/A
90 s				N/A
120 s			N/A	N/A

Note: The software Photoshop is used to remove the speckles on the surface.

Data at high power levels are not available (N/A) because specimens failed in a vibrant way before the expected time is reached.

5.4.2 Temperature vs exposure time

(a) Gabbro specimens

Figure 5.12 shows the maximum temperature (T_M) and average temperature (T_A) of the gabbro specimen surfaces as a function of exposure time at the four power levels. The solid lines represent the correlation of the average temperatures of three tests under each heating condition. As stated before, the reflection coefficients during the tests are about 16 %. It can be found that the tests have a very good repeatability with small discretions. It should be noted that as exposure time increases both the maximum and average temperature curves tend to level off due to heat conduction between different mineral grains. From Figure 5.12(a), at 0.5 kW T_M is only up to 293 °C after 120 seconds, which is not high enough to induce a significant thermal damage. At the high powers of 1.5 kW and 2 kW, high temperatures (over 300 °C) can be easily achieved. At a given power level, both T_M and T_A increase linearly with the increase of exposure time. Linear correlations between T_M and T_A and the exposure time (t) in the expression of $T = kt + b$ are performed to obtain the heating rates (heating rate k , °C/s) at the four power levels, as summarised in Table 5.6. Heating rates in terms of T_M increase from 1.85 °C/s at 0.5 kW to 6.04 °C/s at 2 kW. Heating rates for T_A increase from 0.89 °C/s at 0.5 kW to 2.93 °C/s at 2 kW.

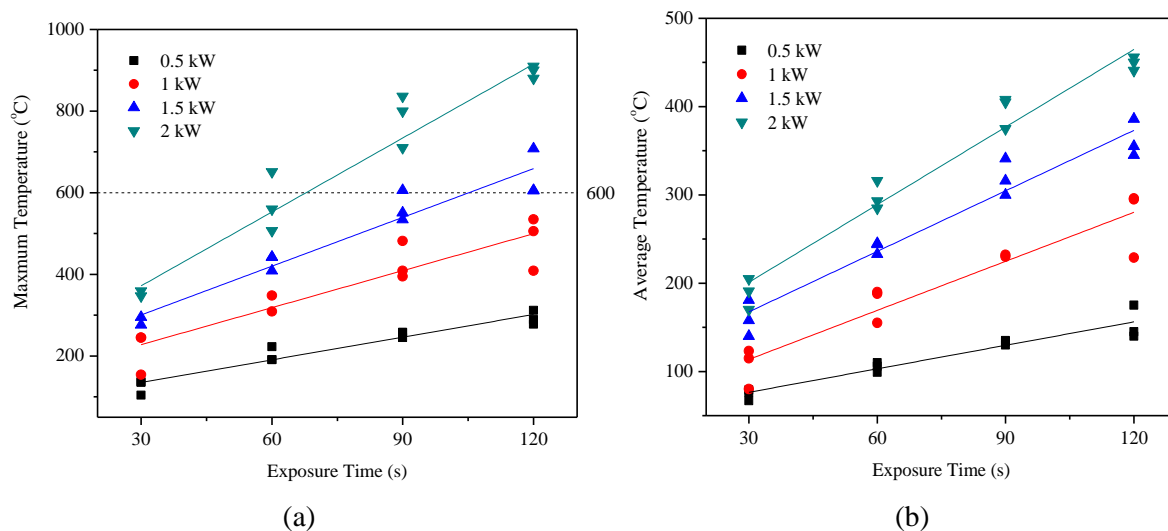


Fig. 5.12 Influence of exposure time on temperature of gabbro specimens at four power levels. (a) Maximum temperature (T_M); (b) Average temperature (T_A).

It should be noted that the heating rates of microwave (up to 360 °C/min) are 1-3 orders of magnitude higher than those adopted in conventional heating with a rate of 0.4-12.5 °C/min (Yong and Wang, 1980). The rapid heating is able to induce thermal shocks between different mineral grains and could possibly generate cracks at a relatively low temperature. This thermal shock might explain why heating at higher power levels for short durations (for example heated at 2 kW) could yield a better rock weakening effect than heat at lower power level.

Table 5.6 Linear regression of maximum and average temperature with exposure time ($T = kt + b$) at the four power levels for the gabbro specimens.

Power level (kW)	Maximum temperature (T_M)			Average temperature (T_A)		
	k	b	R ²	k	b	R ²
0.5	1.85	80	0.97	0.89	50	0.99
1	3.02	137	0.97	1.85	58	0.98
1.5	3.98	181	0.97	2.28	99	0.98
2	6.04	191	0.99	2.93	113	0.97

According to [Keshavarz et al. \(2010\)](#) and [Jones et al. \(1997\)](#), 600 °C is the critical temperature for the physical and mechanical properties of gabbro to change dramatically at a conventional heating rate (1-1.67 °C/min). From [Fig. 5.12\(a\)](#), it is known that most of the surface temperatures of the gabbro specimens heated at 0.5 kW and 1 kW are below the 600 °C temperature line. However, at higher power levels of 1.5 kW and 2 kW, the surface temperature is close to or over 600 °C. Considering the core temperatures are higher than the surface temperature, severe thermal damages must have been induced in the gabbro specimens.

(b) Monzonite specimens

[Figure 5.13](#) shows the temperature increase of the monzonite specimens as a function of the exposure time. One can see that this rock is less microwave receptive with the maximum temperature and average temperature about 100 °C lower than those of the gabbro specimens heated under the same condition. Also this type of rock has a relatively smaller dielectric heterogeneity. The heating rates at the four power levels are obtained based on the linear regression analysis ([Table 5.7](#)). Heating rates in terms of maximum temperature increase from 1.50 °C/s at 0.5 kW to 4.51 °C/s at 2 kW. Heating rates for T_A increase from 0.84 °C/s at 0.5 kW to 2.68 °C/s at 2 kW. Due to the difficulties in manually matching the impedance of the rock specimens with the transmission line, the reflection coefficient is around 36 %, implying that the heating process is 20 % less efficient than that of gabbro. If an automatic tuner is used the temperature is expected to increase by 20 %. In this case the heating rates of monzonite are comparable to those of the gabbro.

In the literature, no critical temperature for quartz monzonite has been reported. [Page and Heard \(1981\)](#) studied the effect of temperature (up to 500 °C) and confining pressure (up to 55 MPa) on the elastic modulus of the Climax quartz monzonite. They found that the elastic modulus decreases with increasing temperature and decreasing pressure. At a confining pressure of 6.9 MPa, the elastic modulus dropped to 20 % at a temperature of over 300 °C. In this test, though temperature over 300 °C could be easily achieved at power levels of 1.5 kW and 2 kW, not much cracks are observed ([Table 5.3](#)). The reduction in elastic modulus will be discussed in later sections.

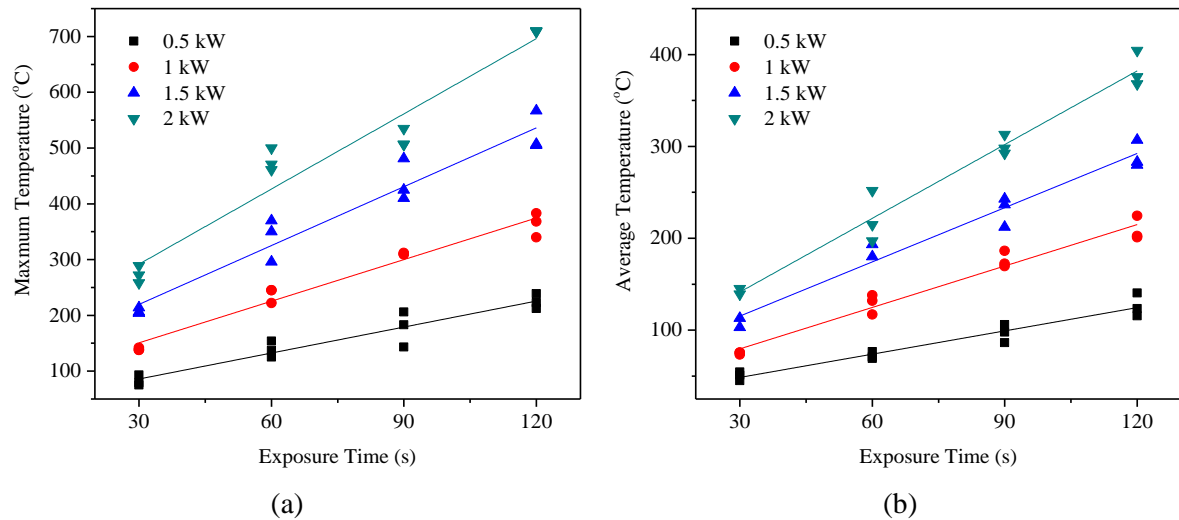


Fig. 5.13 Influence of exposure time on temperature of monzonite specimens. (a) Maximum temperature (T_M); (b) Average temperature (T_A).

Table 5.7 Linear regression of maximum and average temperature with exposure time ($T = kt + b$) for the monzonite specimens.

Power level (kW)	Maximum temperature (T_M)			Average temperature (T_A)		
	k	b	R ²	k	b	R ²
0.5	1.50	48	0.95	0.84	23	0.99
1	2.40	80	0.96	1.50	35	0.98
1.5	3.32	132	0.92	1.97	56	0.98
2	4.51	154	0.89	2.68	61	1

(c) Granite specimens

Figure 5.14 shows the maximum temperature (T_M) and average temperature (T_A) of the granite specimen surfaces as a function of exposure time at the four power levels. Due to abrupt shattering failures at 2 kW, the only available data at such a high power is from samples heated for 30 seconds. The reflection coefficient of the tests is about 16 %. Heating rates (Table 5.8) in terms of T_M increase from 1.10 °C/s at 0.5 kW to 3.49 °C/s at 1.5 kW. Heating rates for T_A increase from 0.81 °C/s at 0.5 kW to 1.89 °C/s at 1.5 kW. In comparison, at 0.5 kW and 1 kW the heating rates of granite specimens are about half of that of gabbro specimens.

Granites are the most extensively studied materials for geothermal energy utilisation and nuclear waste disposal (Chaki et al., 2008; Chen et al., 2012; David et al., 1999; Homand-Etienne and Houpert, 1989; Inserra et al., 2013; Reuschlé et al., 2006; Wang et al., 1989; Zhou et al., 2018). Most of the tests are conducted at a slow heating rate except Zhou et al. (2018). According to Fredrich and Wong (1986), the onset of thermal cracking of the Westerly granite occur within the 100-165 °C temperature interval, with a substantial proportion cracked by 250 °C. Chen et al. (2012) and Shao et al. (2015) demonstrated

that the largest property change of the Strathbogie granite occur in the temperature range of 400 to 600 °C, mostly likely due to the phase change of quartz at 573 °C. Zhou et al. (2018) conducted hydraulic fracturing experiment under triaxial stress at 20 °C, 100 °C, 200 °C, 300 °C and 400 °C, and found that crack initiation pressure decreased remarkably after 300 °C. For the microwave heating tests conducted in this thesis, it is obvious that the failure modes of granite are dramatically different from those observed by other researchers. Although the thermal damages of granite specimens at high power levels are apparent from the catastrophic failures, the damage at low temperatures still needs to be quantified.

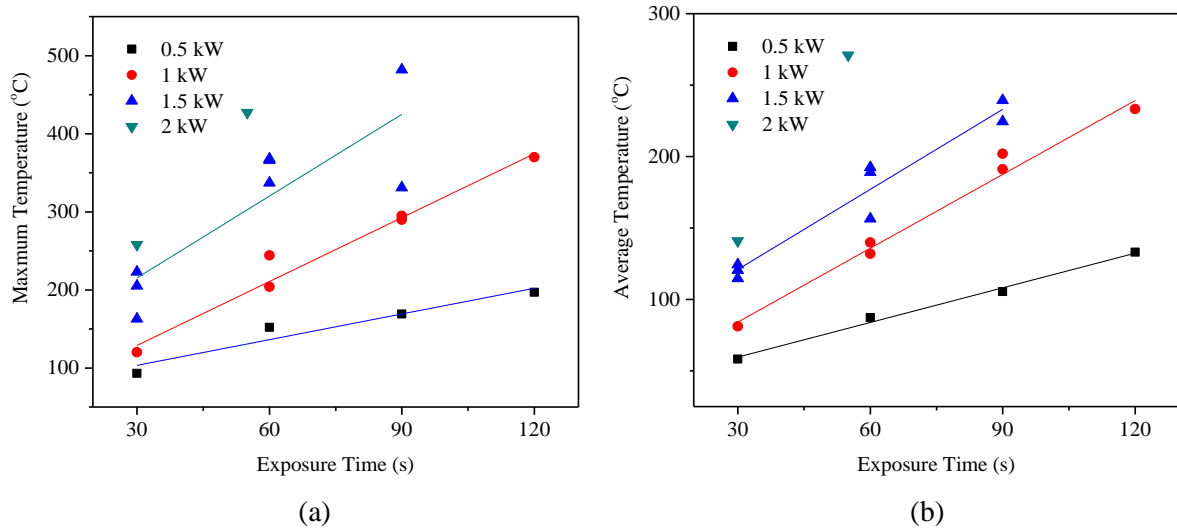


Fig. 5.14 Influence of exposure time on temperature of granite specimens. (a) Maximum temperature (T_M); (b) Average temperature (T_A).

Table 5.8 Linear regression of maximum and average temperature with exposure time ($T = kt + b$) for the granite specimens.

Power level (kW)	Maximum temperature (T_M)			Average temperature (T_A)		
	k	b	R ²	k	b	R ²
0.5	1.10	71	0.83	0.81	35	1.00
1	2.73	47	0.98	1.72	32	0.99
1.5	3.49	110	0.90	1.89	65	0.99

5.4.3 Temperature vs power level

Figure 5.15 shows the maximum and average temperature of the three rocks as a function of power level. It can be found that at the same exposure time, temperature increases linearly with an increasing power level.

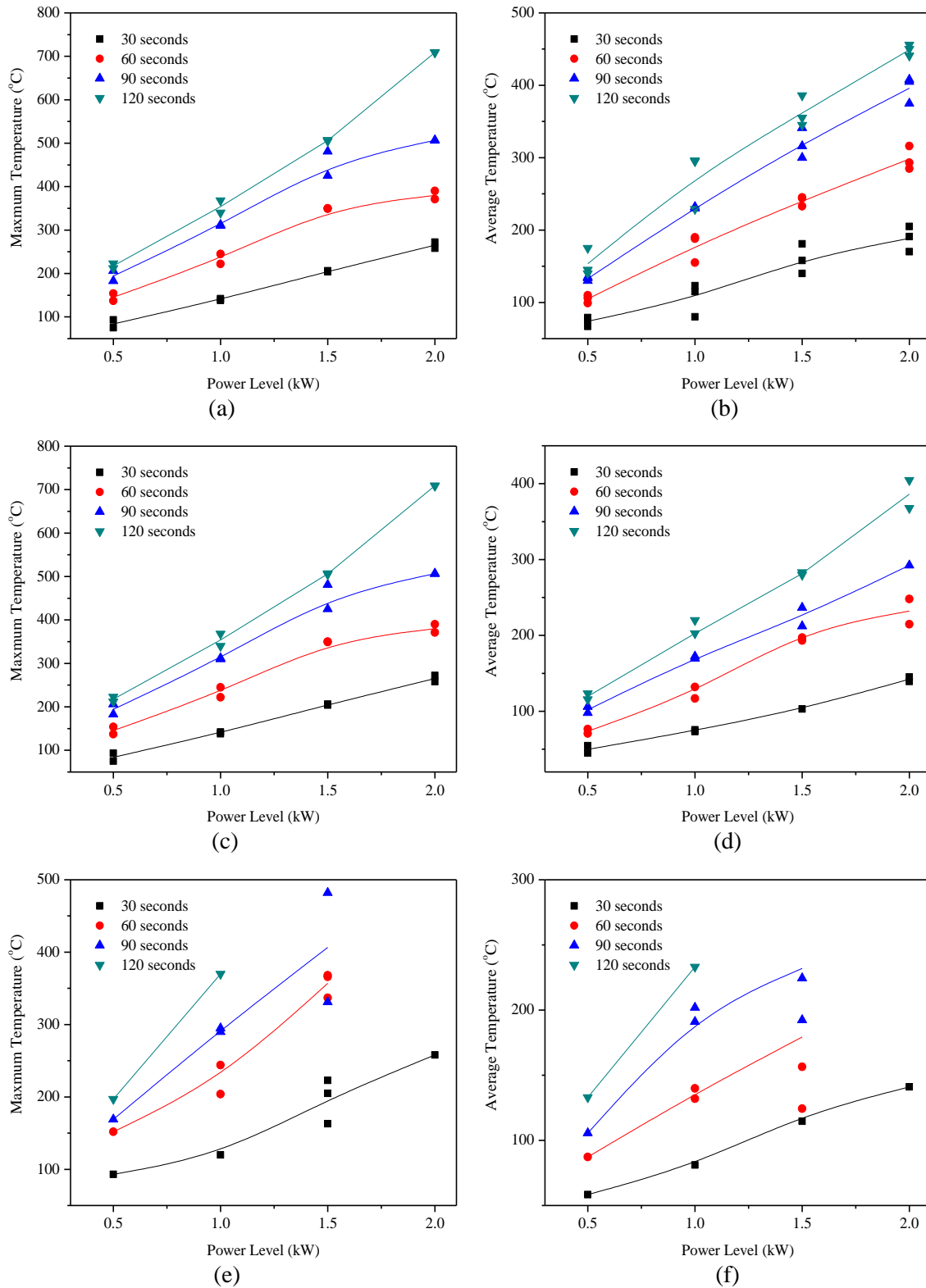


Fig. 5.15 Influence of power level on temperature. (a) Maximum temperature (T_M) of gabbro; (b) Average temperature (T_A) of gabbro; (c) Maximum temperature (T_M) of monzonite; (d) Average temperature (T_A) of monzonite; (e) Maximum temperature (T_M) of granite; (f) Average temperature (T_A) of granite.

5.4.4 Temperature distribution

To investigate the effect of exposure time and power level on the spatial temperature distribution, IR images of specimens heated at 1 kW and for the duration of 90 seconds are analysed given the availability of the temperature data. **Figure 5.16** shows the IR images of the gabbro specimens heated at 1 kW for four exposure times. IR images of monzonite and granite specimens are similar thus will not be presented in the thesis.

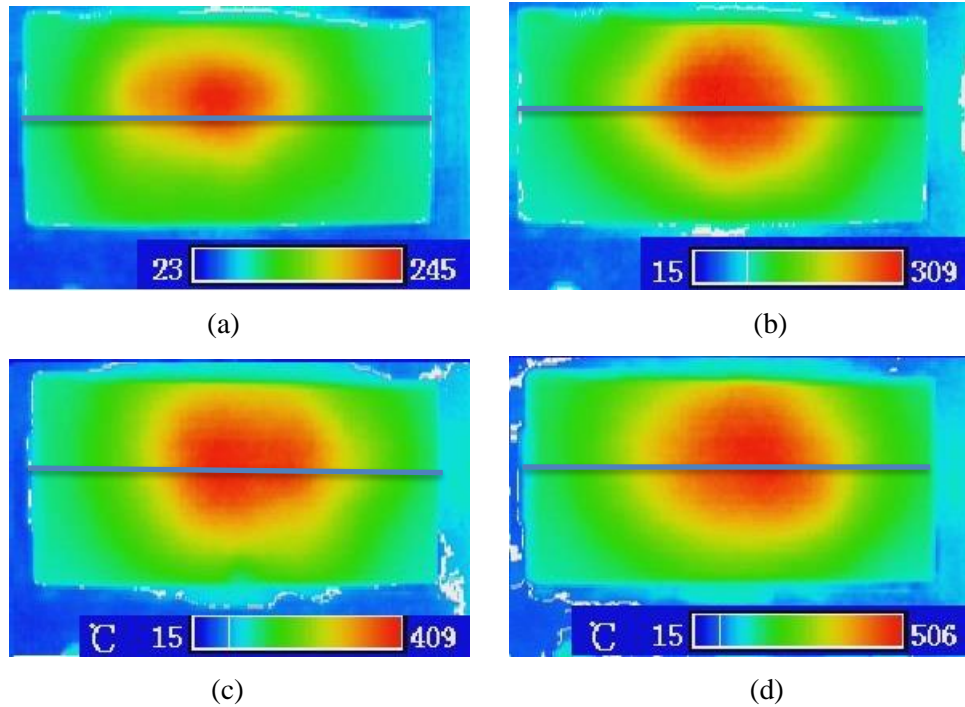


Fig. 5.16 Temperature distribution along the centreline of gabbro specimens at 1 kW: (a) 30 seconds; (b) 60 seconds; (c) 90 seconds; (d) 120 seconds.

Figure 5.17 shows the temperature distribution along the centrelines of specimens from left to right of the surface as indicated in **Figure 5.16**. One can find that the temperature is more or less symmetrically distributed. The highest temperatures appear to be in the middle of the specimens. Thermal gradients along the centrelines increase as either exposure time or power level increases. Given the availability of temperature data, thermal gradients between the maximum temperature measured and the temperatures at the points in the dashed box (about 18 mm from the left side) are calculated.

For the gabbro specimens, the thermal gradients are 3.42, 4.92, 7.33 and 8.46 °C/mm for the four exposure times at 1 kW, and 5.54, 7.33, 6.63 and 13.75 °C/mm for the four power levels after heating for 90 seconds. For the monzonite specimens, the thermal gradients are 2.71, 4.80, 5.95 and 7.71 °C/mm for the four exposure times at 1 kW, and 3.50, 5.95, 9.00 and 9.25 °C/mm for the four power levels after heating for 90 seconds. For the granite specimens, the thermal gradients are 3.79, 6.75, and 5.75 °C/mm for the three exposure times at 1 kW, and 6.27, 9.38 and 11.42 °C/mm for the three power levels after heating for 90 seconds. The results indicate an increase in the thermal mismatch and the non-uniformity of microwave heating, especially heating at high power levels.

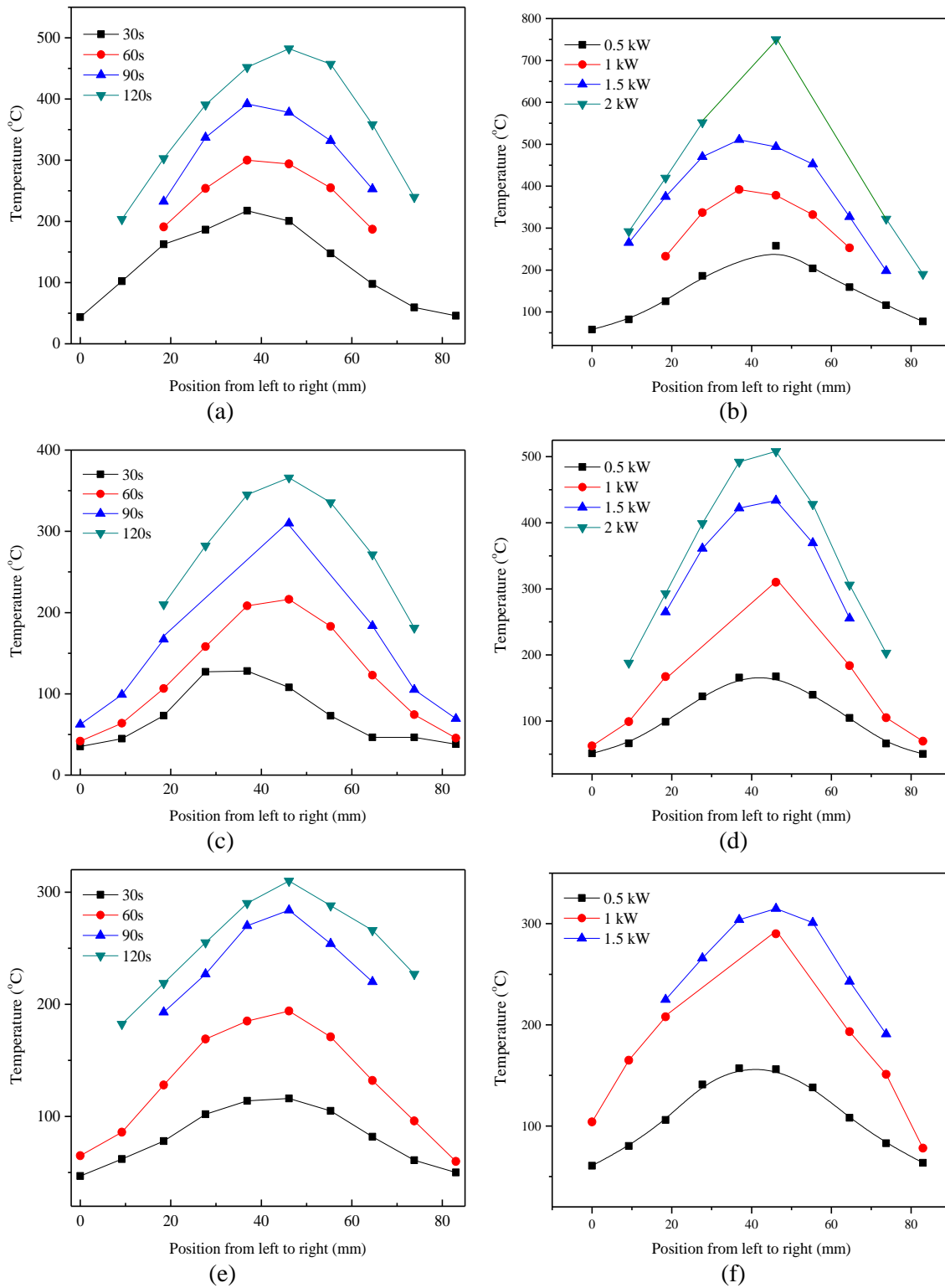


Fig. 5.17 Temperature distribution along the centrelines. (a) Gabbro specimens heated at 1 kW; (g) Gabbro specimens heated for 90 seconds; (a) Monzonite specimens heated at 1 kW; (g) Monzonite specimens heated for 90 seconds; (a) Granite specimens heated at 1 kW; (g) Granite specimens heated for 90 seconds.

It compels attention that among the three rock types, monzonite specimens have the smallest thermal gradients though its maximum temperature and average temperature are higher than that of granite. This

may due to the fact that it is fine grained and the possibility that it has a higher conductivity. Which one induces the larger thermal damage remains to be studied by measuring the ultrasonic wave velocities.

5.4.5 P-wave velocity reduction at different locations

Figure 5.18 shows the normalized P-wave velocities at the three locations of specimens treated at a power of 1 kW. The results are in good agreement with the temperature distribution shown in Figure 5.17. The higher the temperature, the lower the P-wave velocity. For the gabbro specimens, for an exposure time of 30 seconds, the ultrasonic velocity is 70 % of the intact rocks, indicating a 30 % P-wave velocity reduction. After 120 seconds of heating, the P-wave velocity in the middle can drop to 37 % (reduced by 63 % without visible cracks). For the monzonite specimens, the P-wave velocity after 30 seconds of microwave irradiation is reduced by 7 % only. After 120 seconds of heating, the P-wave velocity in the middle dropped to 71 %. In contrast, P-wave velocity of granite specimens after 120 seconds microwave heating dropped to 68 %, a slightly larger weakening effect.

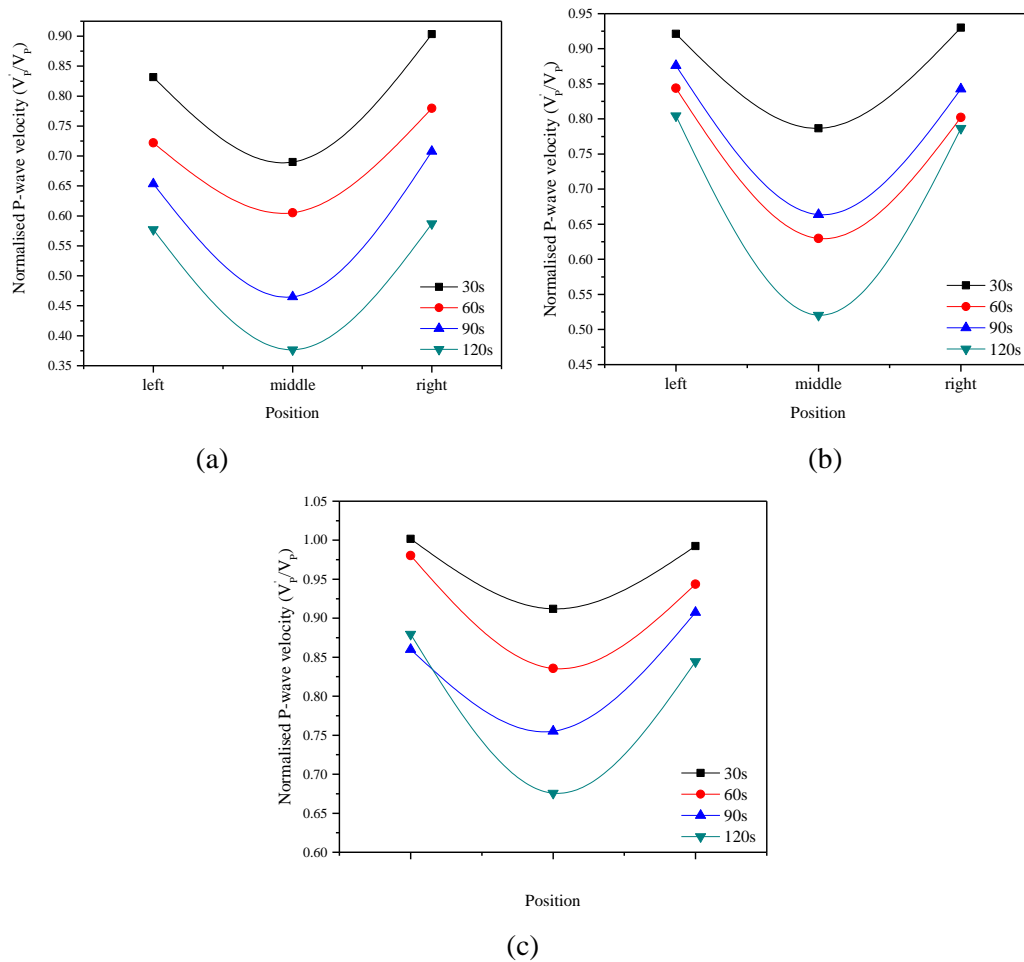


Fig. 5.18 Normalised P-wave velocities at three locations of the specimens heated at 1 kW. (a) Gabbro; (b) Monzonite; (c) Granite.

5.4.6 Local and overall P-wave velocity reduction

Figure 5.19 shows the normalised P-wave velocities in the middle (V'_{pm}/V_{pm}) of the specimens and from the left end to the right end (V'_p/V_p) of the specimens as a function of exposure time. The former indicates the extent to which the microwave treatment can weaken specimens while the latter is the evaluation of the overall damage of specimens. One can find from Figure 5.19(a) that with the increase of exposure time, V_{pm} of gabbro specimens decreases quickly at the beginning, then at a lower rate. For all specimens heated at 2 kW for 120 seconds, macrocracks and melting take place. In those cases, a normalized velocity of 0.2 in the middle is assumed. At 2 kW even only treated for 30 seconds, V_{pm} could be reduced by up to 40 %. In contrast, V_{pm} at 0.5 kW for 120 seconds is only reduced by 20%, though the same amount of energy is used in these two tests. This means that microwave is more efficient in reducing local P-wave velocities at higher power levels. Figure 5.19(b) indicates that V'_p of gabbro specimens reduces at a constant rate under the heating conditions. For the same exposure time, the higher the power, the greater the P-wave velocity (both V_{pm} and V'_p) reduction.

For the monzonite specimens, the P-wave velocity reduction follows the same trends as gabbro. The P-wave velocities after 120 seconds of microwave treatment a 2 kW are reduced to 35 % in the middle (Figure 5.19(c)) and to 61 % for the overall specimens (Figure 5.19(d)).

For the granite specimens, the P-wave velocity reductions at the two low power levels (0.5 kW and 1 kW) are not significant, with 32 % reduction in the middle and 16 % reduction for the overall specimens. However, the P-wave velocities experienced a sharp drop to zero due to the catastrophic shattering failures at higher power levels. This implies that for microwave to work efficiently higher power levels are preferred.

5.4.7 Overall S-wave velocity

Figure 5.20 shows the normalised overall S-wave velocities of the specimens after microwave treatment. Due to the small thickness of the specimens, measurement of the S-wave velocity in the middle is no longer reliable. It can be found that for the three rock types tested the reduction of S-wave velocities is not as pronounced as that of the P-wave velocities. At the power levels of 0.5 kW and 1 kW, the reduction of gabbro is the largest, granite the lowest. Again, S-wave velocities at 2 kW of granite dropped to zero due to brittle failures.

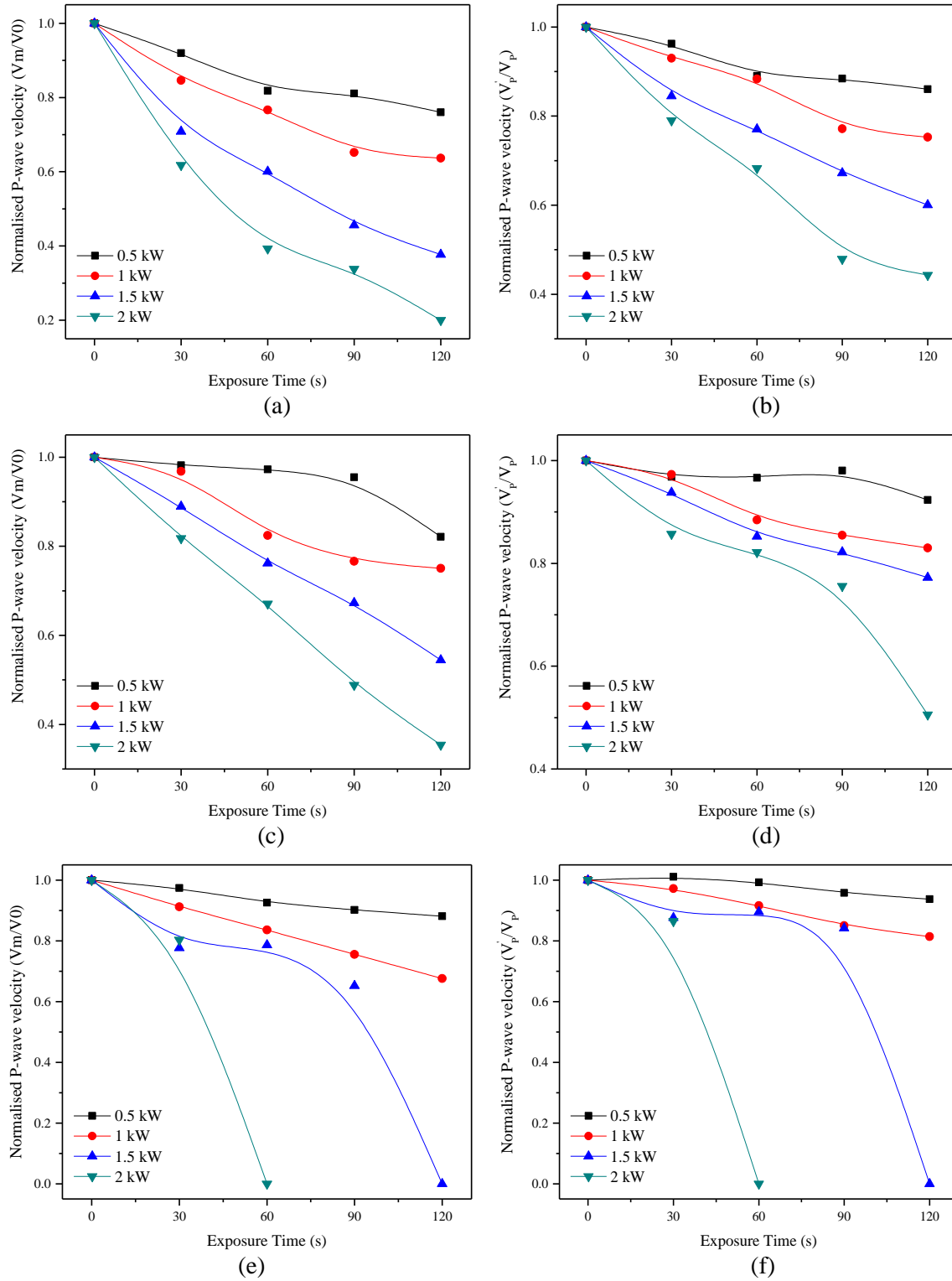


Fig. 5.19 Normalised P-wave velocities as a function of exposure time. (a) V'_{Pm}/V_{Pm} of gabbro; (b) V'_P/V_P of gabbro; (c) V'_{Pm}/V_{Pm} of monzonite; (d) V'_P/V_P of monzonite; (e) V'_{Pm}/V_{Pm} of granite; (f) V'_P/V_P of granite.

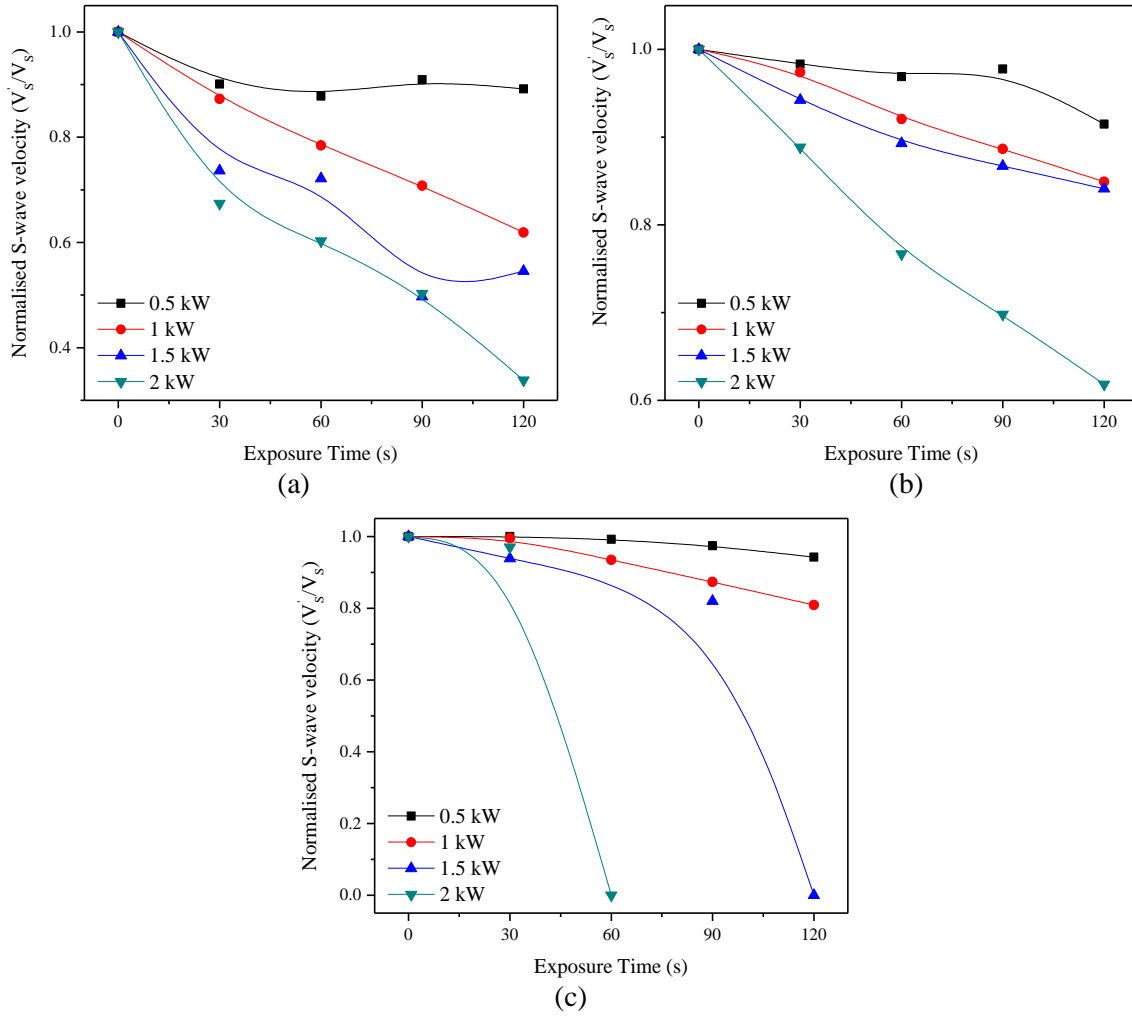


Fig. 5.20 Normalised S-wave velocities (V'_s/V_s) after microwave treatment of gabbro (a), monzonite (b) and granite (c).

5.4.8 Dynamic elastic modulus

Assuming the rocks are isotropic, the dynamic elastic moduli of the rocks can be derived from the measured ultrasonic wave velocities using the following equations:

$$\nu = \frac{V_p^2 - 2V_s^2}{2(V_p^2 - V_s^2)}$$

$$E = 2\rho V_s^2(1 + \nu)$$

Figure 5.21 shows the normalised dynamic elastic moduli (the ratio of the modulus after treatment to that before treatment) of the three rock types with respect to exposure time at the four power levels. It is clear that microwave is effective in reducing the elastic moduli and that the gabbro specimens experienced the highest degree of thermal damages. At 0.5 kW microwave reduced the elastic modulus by 20 % in gabbro but the reduction did not continue as exposure time increased. This also applies to monzonite specimens heated at 0.5 kW. It may be due to the fact that the heating rate and thermal gradients are both low, resulting in a relatively uniform temperature field and less crack generation. At

higher power levels, the elastic moduli decrease almost at a linear rate as exposure time increases. For gabbro specimens the elastic modulus after treated at 2 kW for 120 seconds is reduced to 12.37 GPa (13 %) from 96.52 GPa for the intact specimen (Note this is higher than the static elastic modulus of 85 GPa). For monzonite the elastic moduli are reduced from 64.18 GPa to 16.47 GPa (27 %).

For granite, a relatively higher reduction in elastic moduli is observed at lower power levels of 0.5 kW and 1 kW. This indicates that although heating rates of granite are low microwave is more efficient in weakening granite. Researchers (e.g. (Hughes and Maurette (1956); Hughes and Cross (1951))) have demonstrated that a temperature of 200 °C (confining pressure of 0.1-52 MPa) could lower the elastic moduli in seven granites by up to 50 % and that at 300 °C the moduli in three gabbros could be reduced by up to 13 %. In comparison, rock treated by microwave experienced more severe damage at the same temperature.

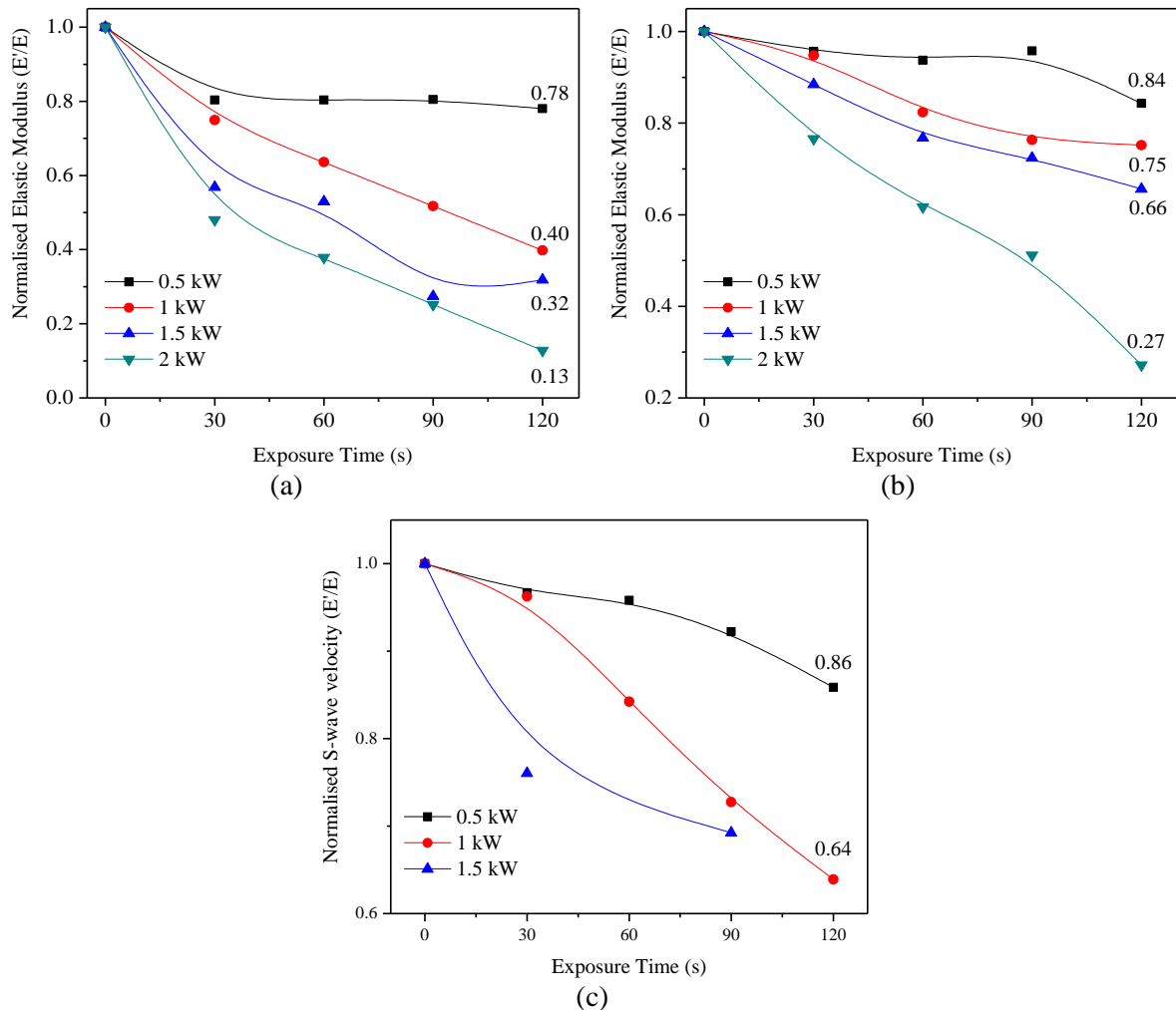


Fig. 5.21 Normalised elastic moduli of (a) gabbro specimens, (b) monzonite specimens and (c) granite specimens (data at 2 kW not available).

5.4.9 Reductions in loading capacity

Figure 5.22 shows the compression test results of gabbro and monzonite specimens heated at 2 kW for up to 120 seconds (Compression results at lower power levels exhibit large fluctuations thus will not be

shown here). As mentioned earlier the granite specimens would shatter into pieces when heated at 2 kW for long durations thus testing results for granite are also not available. Figure 22(a) and (b) show the load-displacement curves of the gabbro and monzonite specimens. It can be found that the loading capacity of the specimens decreases as the exposure time increases, especially when heated for long durations where melting took place. The specimens tended to experience ductile failure modes after microwave treatment. For the gabbro, the peak load reduced from 176 kN for the untreated specimen to 60 kN for the specimen treated at 2 kW for 120 seconds. For the monzonite, the peak load reduced from 215 kN to 92 kN. The peak loads of the two rocks are reduced by 66 % and 57 %, respectively, after microwave treatment for 120 seconds at 2 kW.

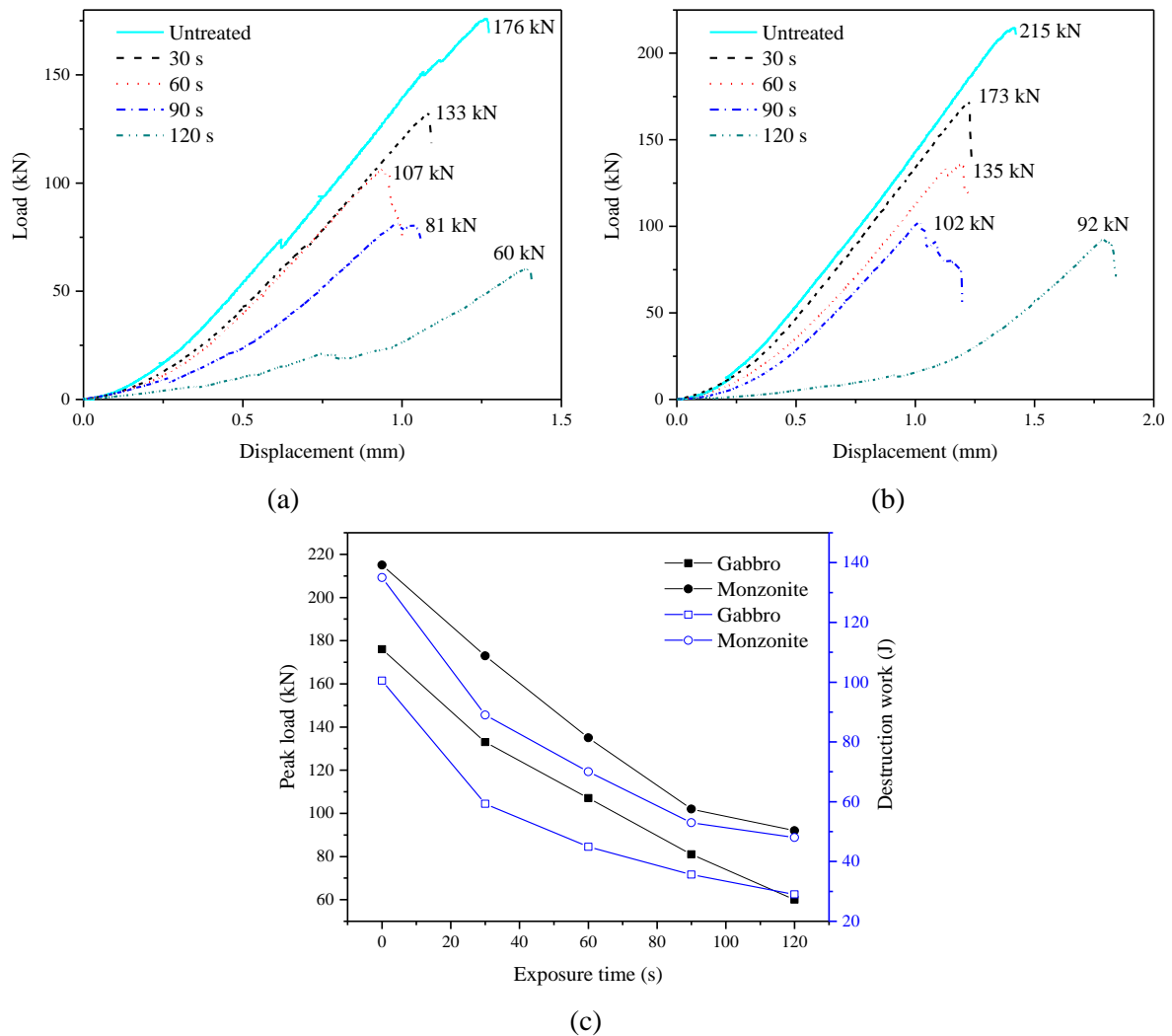


Fig. 5.22 Compression test results of gabbro and monzonite specimens treated at 2 kW. (a) Load-displacement curves of gabbro; (b) Load-displacement curves of monzonite; (c) Peak load and destruction work of gabbro and monzonite.

The destruction work under the load-displacement curve (as proposed by Thuro and Spaun (1996)) is calculated and displayed in Figure 5.22(c). It could be reduced by up to 71 % and 64 % for the gabbro

and monzonite, respectively. One should bear in mind that since cracks are generated in the top or bottom middle it is estimated that the tensile/bending strength could be reduced by over 90 %.

5.4.10 Crack pattern

As described in Section 5.2, the microwave treated specimens are first cooled off and impregnated with Araldite epoxy (K3600) mixed with fluorescent dye in a vacuum desiccator. After the epoxy hardened, the excessive fluorescent dye is removed from the surface using a grinding wheel and a flat glass with silicon carbide. The UV images are then taken by a Nikon camera to extract the cracks before thin sections are made. The thin sections are then scanned using an Epson scanner with two polarising films and observed under petrographic microscopes. The resolution of the scanner can be up to 4800 dpi. In order not to lose the fluorescent while thinning the sections, their thicknesses are kept at around 60-70 μm . Crack pattern in terms of intergranular and trans-granular are explored based on the PPL and XPL images obtained. Below the crack patterns each rock type are discussed separately.

(a) Gabbro specimens

Both macrocracks (visible with naked eyes) and microcracks are characterised on the microscopic images of gabbro thin sections. **Figures 5.23-25** illustrates macrocracks on the surfaces of specimens. It can be seen that the cracks are in the radial patterns. The initiation and coalescence of cracks is governed by the microstructures of the grain matrix and the crystallography of individual mineral grains (Chaki et al., 2008; Fredrich and Wong, 1986; Kranz, 1983). Cracks take place either inter-granular or trans-granular depending on the grain distribution and the thermal stress state. The starting points of crack are the inherent weak planes such as cleavages in orthoclase (two good cleavages intersecting at 88 degree), plagioclase (one perfect cleavage, one good cleavage intersecting at 93 degree) and the lamellar twinning planes in plagioclase and orthoclase (Nesse, 2013). Those weak planes generally control the cracking and fragmentation due to thermal stresses. They are very weak in tensile strength and shear strength. It should be noted that many of cracks developed in orthopyroxene and clinopyroxene are close to the grain boundaries whereas cracks in plagioclase are random under the heating conditions. Since pyroxenes have higher microwave absorbing capabilities than plagioclase feldspar, there are thermal stress concentrations at grain boundaries of pyroxene and feldspar.

Figure 5.26 shows the close-ups of the images in the red lined boxes in **Figures 5.23-5.25**. Cracks types are characterised and marked by arrows in the figure. All types of cracks are identified to exist. Transgranular cracks normally occurs along the cleavage planes or the twinning planes while the intergranular cracks most of the time take place along different mineral types, e.g. plagioclase-orthoclase grain boundaries and clino(ortho)pyroxene-plagioclase(orthopyroxene) grain boundaries. A statistical study will be presented in the next section.

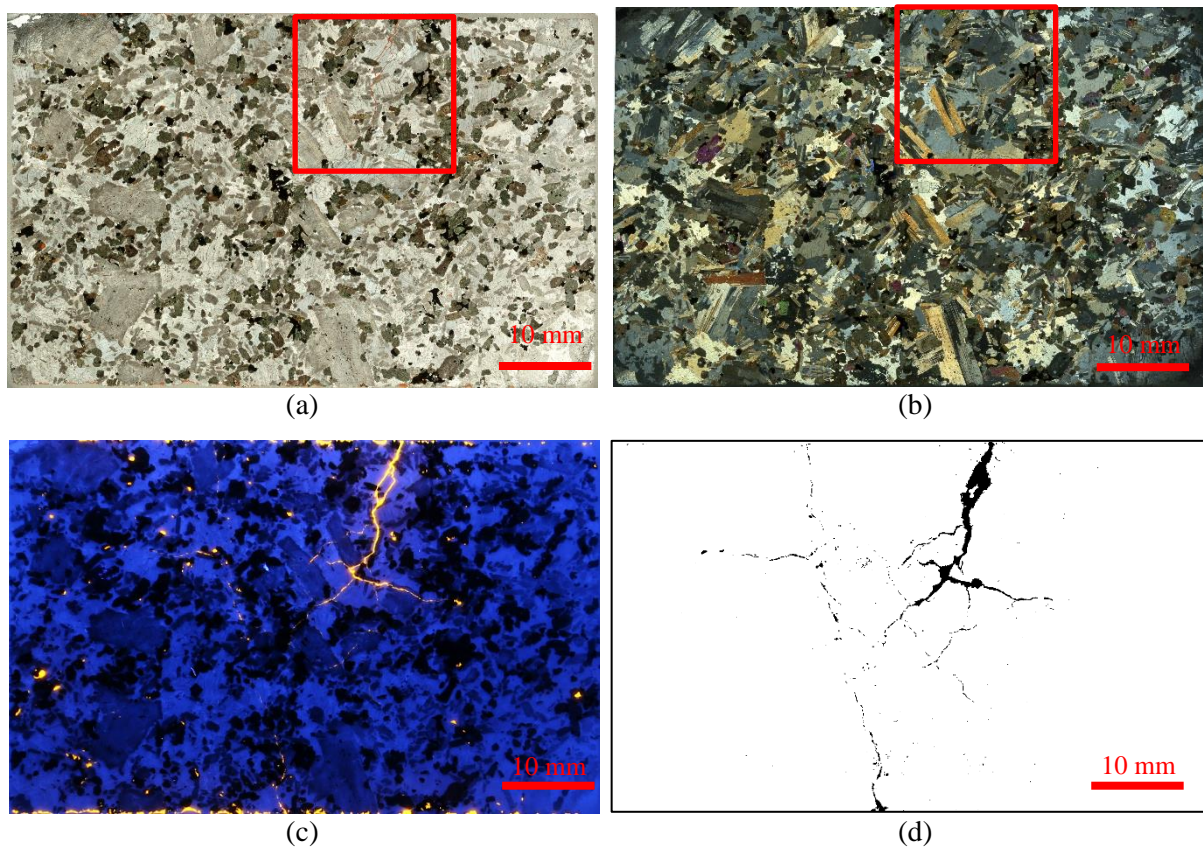
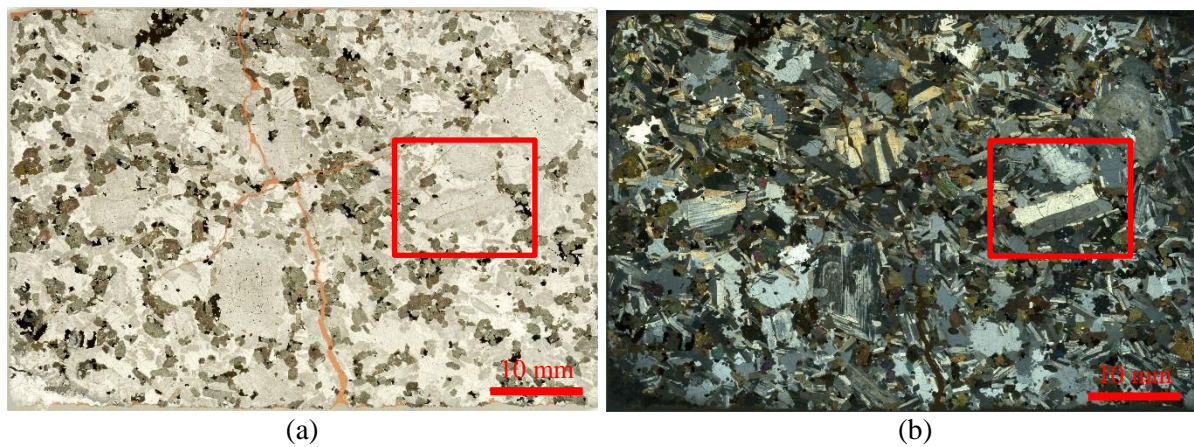


Fig. 5.23 Thin section images of Austral Black Gabbro after microwave treated at 2 kW for 30 seconds (Size of view: 60mm by 40mm). (a) Image under plane-polarised light; (b) Image under cross-polarised light; (c) Image under UV light; (d) Binarised crack extraction.



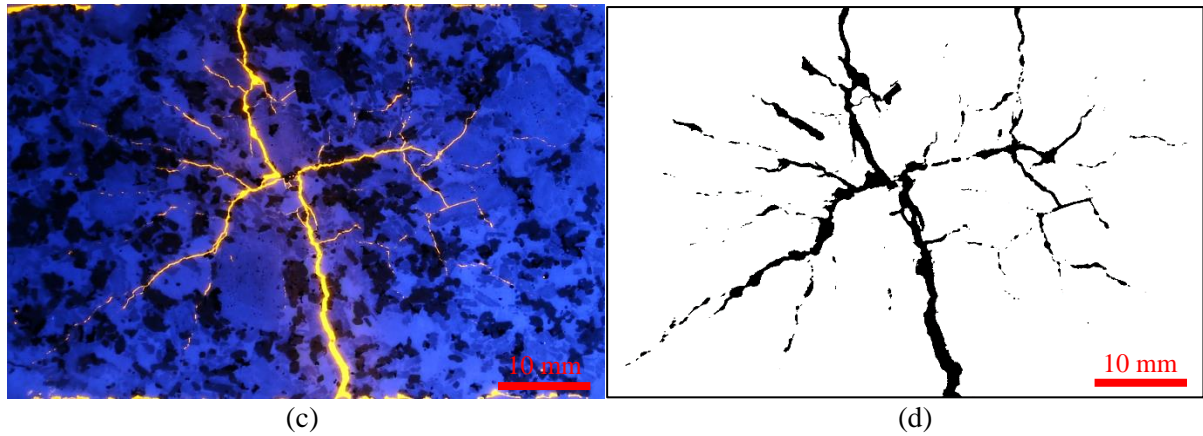


Fig. 5.24 Thin section images of Austral Black Gabbro after microwave treated at 1.5 kW for 120 seconds (Size of view: 60mm by 40mm). (a) Image under plane-polarised light; (b) Image under cross-polarised light; (c) Image under UV light; (d) Binarised crack extraction.

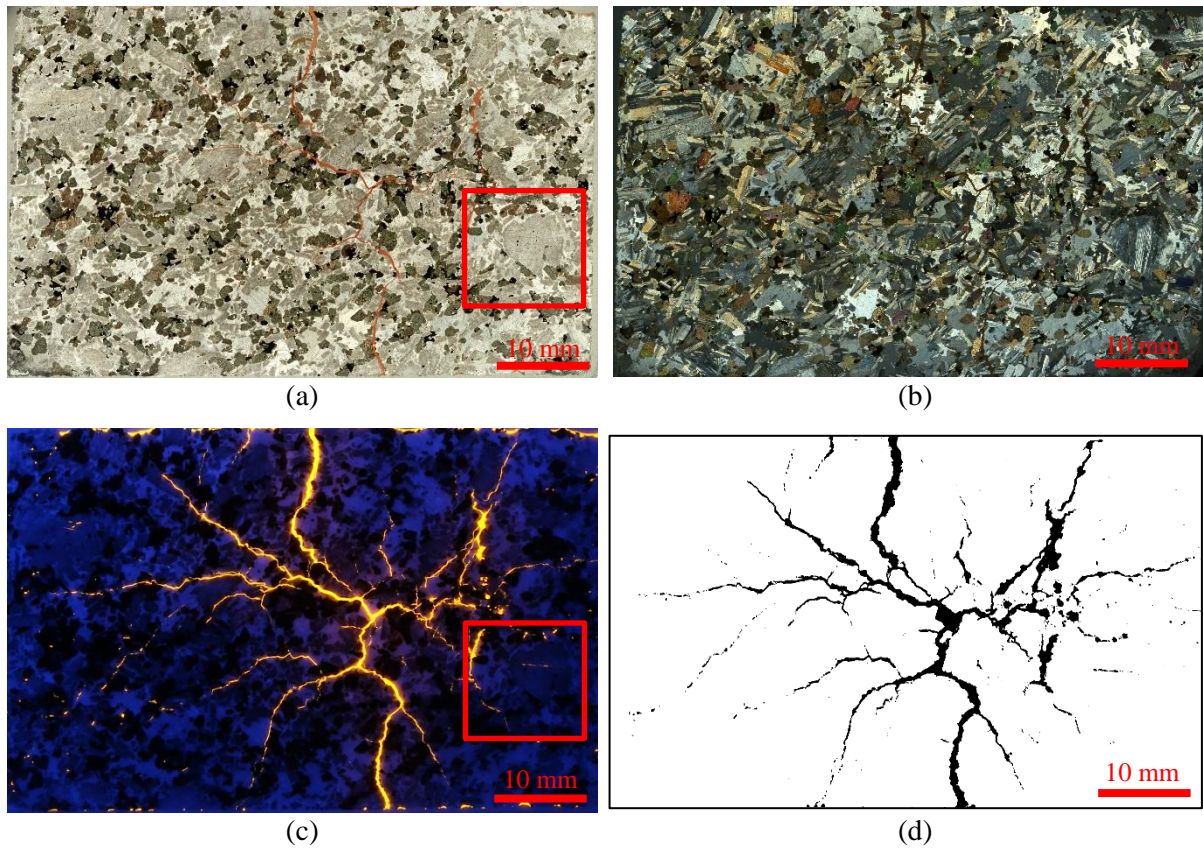


Fig. 5.25 Thin section images of Austral Black Gabbro after microwave treated at 2 kW for 90 seconds (Size of view: 60mm by 40mm). (a) Image under plane-polarised light; (b) Image under cross-polarised light; (c) Image under UV light; (d) Binarised crack extraction.

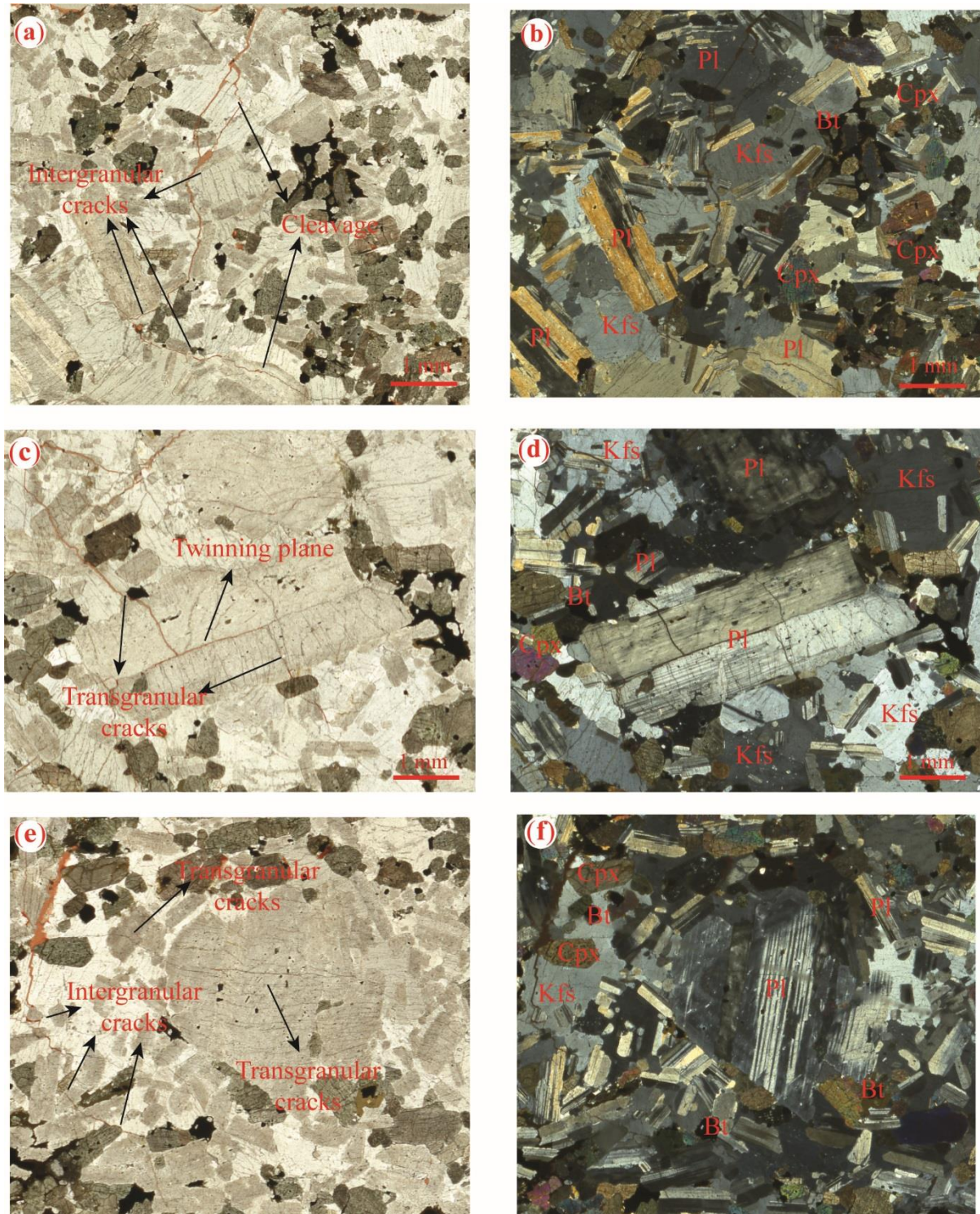


Fig. 5.26 Crack patterns of Austral Black Gabbro after microwave treatment. (a) and (b) are images of trans-granular cracks along the cleavage planes of the plagioclase and intergranular cracks along feldspar-pyroxene grain boundaries (specimens heated at 2 kW for 30 seconds); (c) and (d) are images of cracks along the lamellar twinning plane of an orthoclase and transgranular cracks under PPL and XPL (specimen heated at 1.5 kW for 120 seconds); (e) and (f) are images of inter-granular, trans-granular and intra-granular cracks under PPL and XPL (specimen heated at 1.5 kW for 90 seconds).

(b) Monzonite specimens

Figures 5.27-5.28 show the thin section images of the monzonite specimens heated at 2 kW for 90 seconds and 120 seconds respectively. Both macrocracks (visible with naked eyes) and microcracks are characterised on the microscopic images of the thin sections. Comparing to Figures 5.23-5.25, the crack numbers are significant less. Figure 5.29 illustrates close-ups of cracks in the red boxes in Figures 5.27-5.28. It can be said that most of the cracks are intergranular. The reason might be that there are fewer weak planes such as cleavages in the small-sized mineral (plagioclase and orthoclase) grains thus cracks prefers to take place at the weak-bonded grain boundaries.

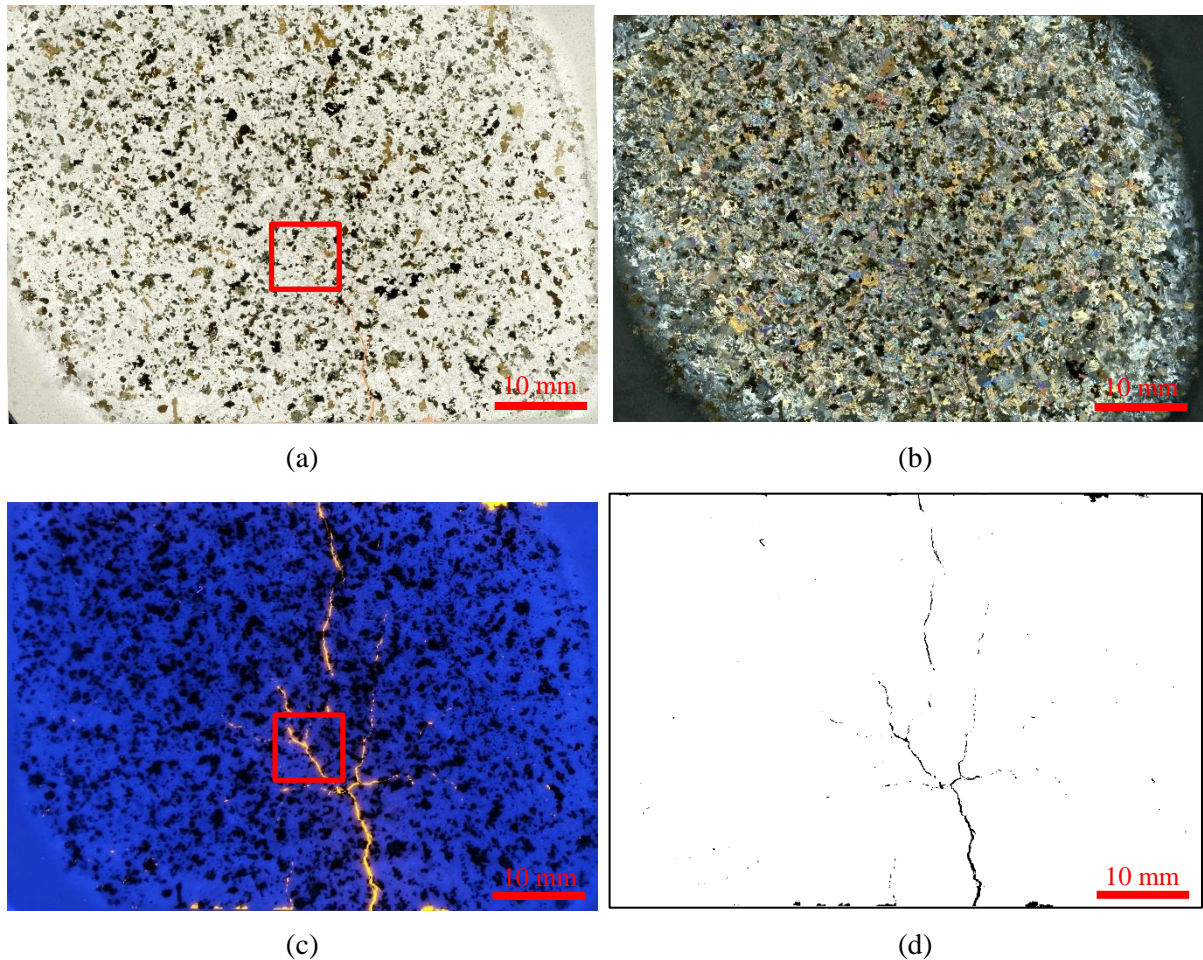


Fig. 5.27 Thin section images of a monzonite specimen after microwave treated at 2 kW for 90 seconds (Size of view: 60mm by 40mm). (a) Image under plane-polarised light; (b) Image under cross-polarised light; (c) Image under UV light; (d) Binarised crack extraction.

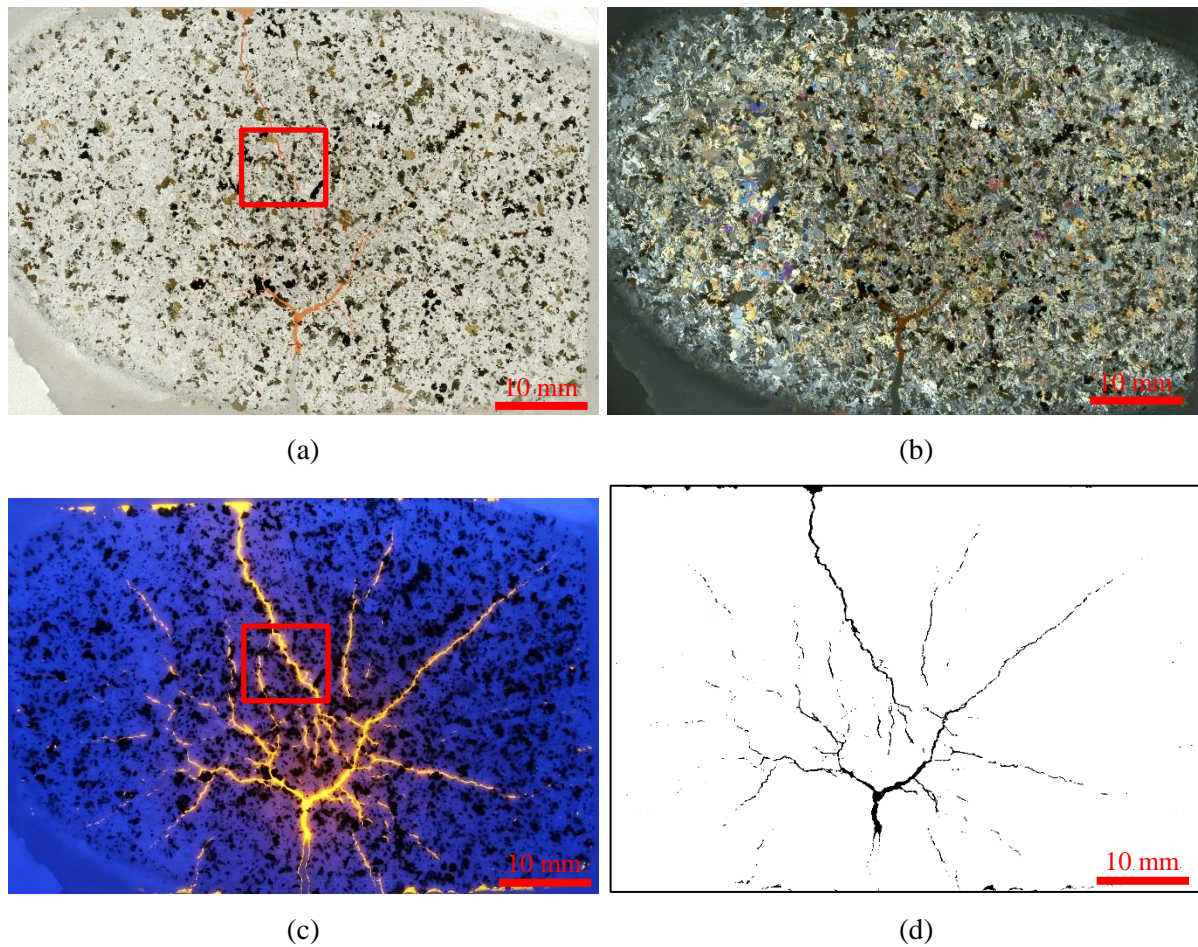


Fig. 5.28 Thin section images of a monzonite specimen after microwave treated at 2 kW for 120 seconds (Size of view: 60mm by 40mm). (a) Image under plane-polarised light; (b) Image under cross-polarised light; (c) Image under UV light; (d) Binarised crack extraction.

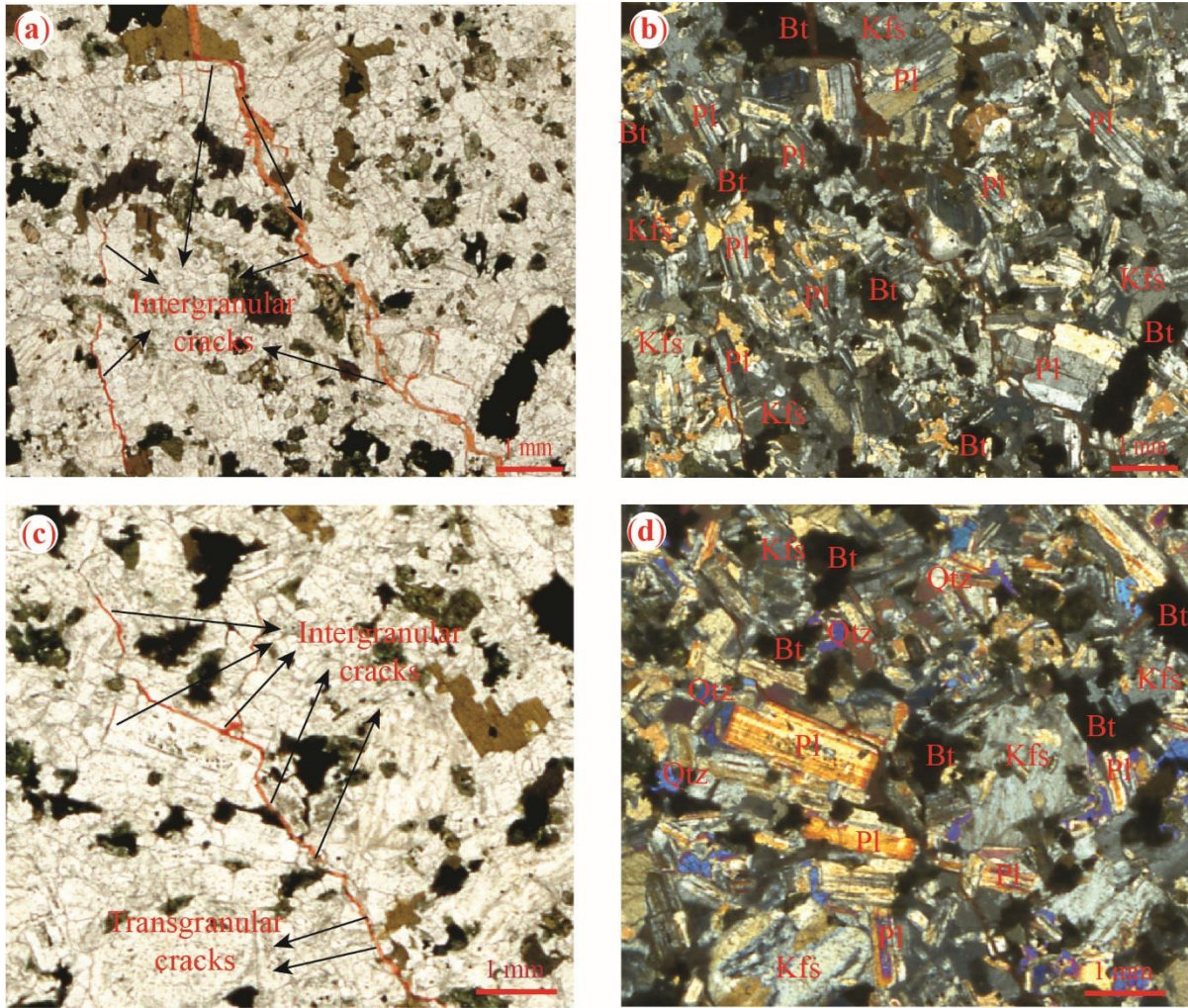


Fig. 5.29 Crack patterns in monzonite thin sections after microwave treatment. (a) and (b) are PPL and XPL images showing inter-granular cracks along feldspar-quartz grain boundaries (specimens heated at 2 kW for 90 seconds); (c) and (d) are PPL and XPL images showing the predominant intergranular cracks along the grain boundaries under (specimen heated at 1.5 kW for 120 seconds).

(c) Granite specimens

Figure 5.30 shows the thin section images of a granite specimen heated at 1 kW for 90 seconds. There is no or only a handful of cracks in the specimen's middle part due to the brittleness of granite. **Figure 5.31** shows the typical crack types in granite. Note the majority of the cracks are trans-granular with a limited number of intergranular cracks. Also a change in colour indicates the oxidation of the dark minerals.

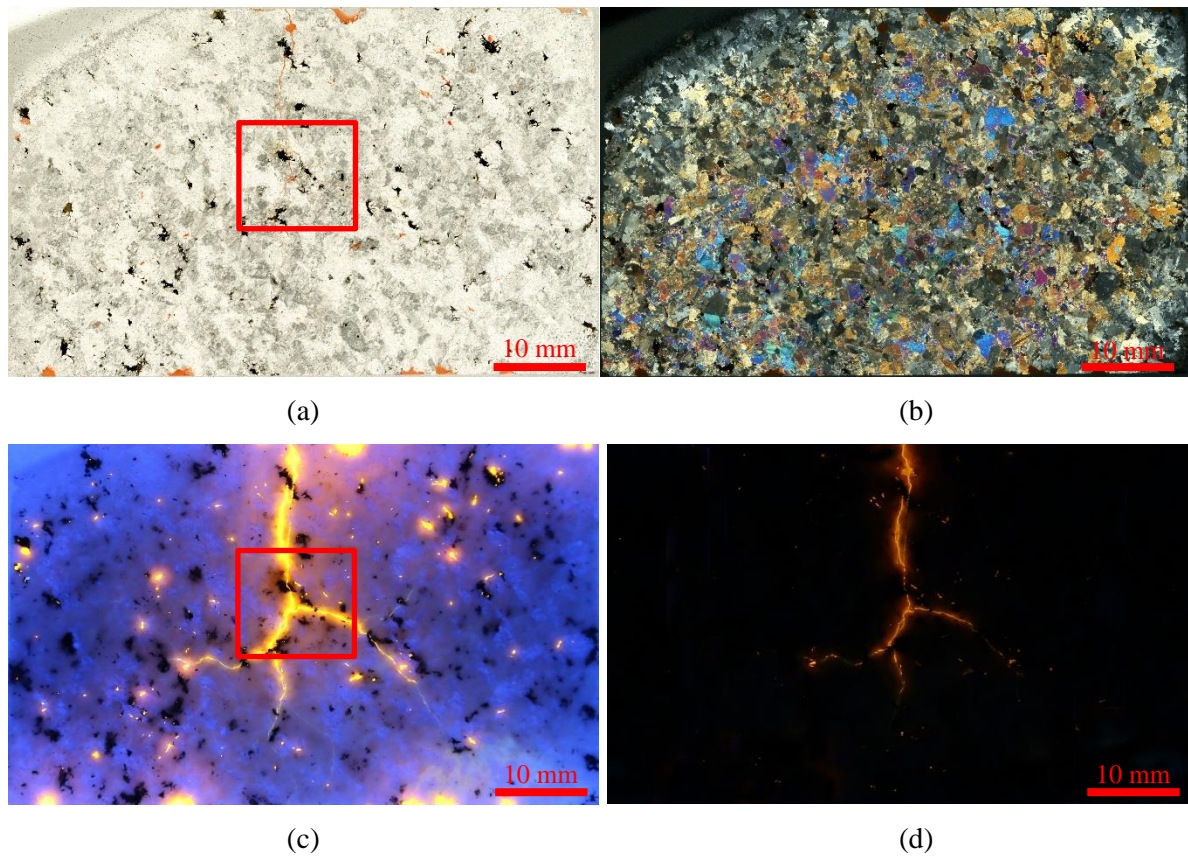
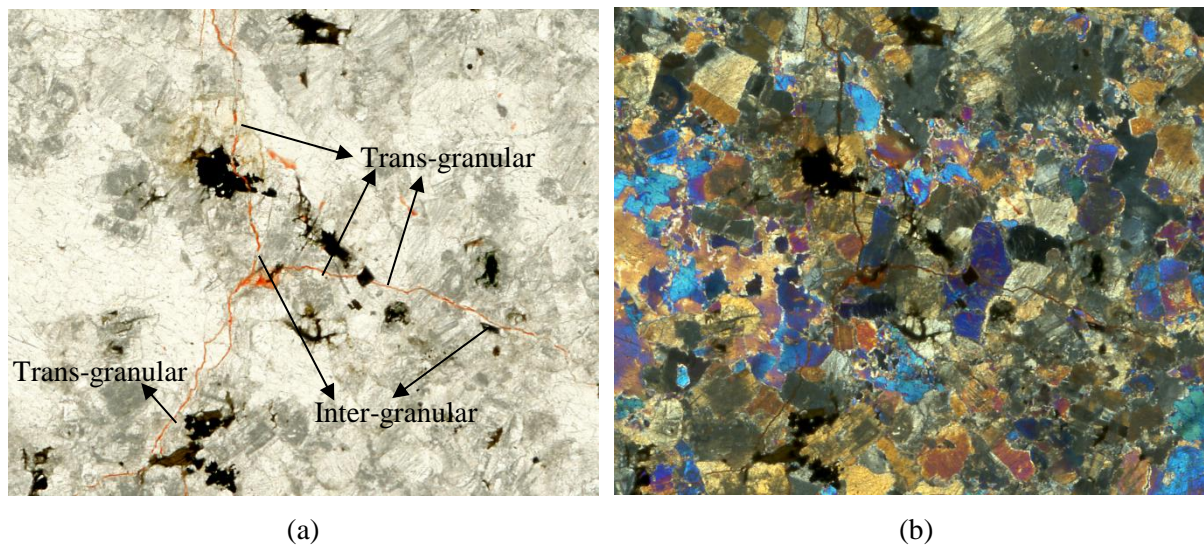


Fig. 5.30 Thin section images of a granite specimen after microwave treated at 1 kW for 90 seconds (Size of view: 60mm by 40mm). (a) Image under plane-polarised light; (b) Image under cross-polarised light; (c) Image under UV light; (d) Binarised crack extraction.



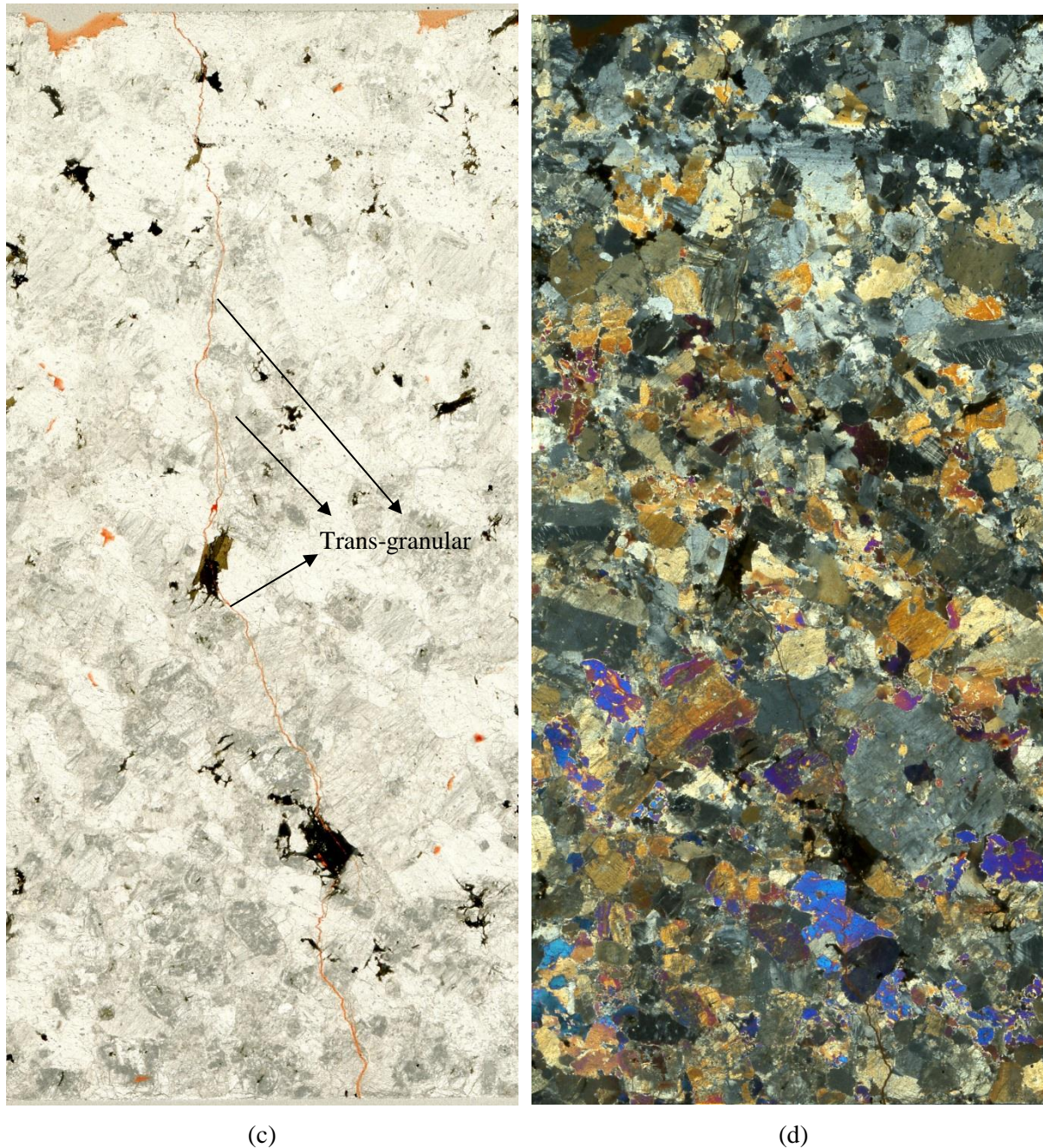


Fig. 5.31 Crack patterns in granite thin sections after microwave treatment. (a) and (b) are PPL and XPL close-up images showing transgranular cracks (specimens heated at 1 kW for 90 seconds); (c) and (d) are PPL and XPL images showing the predominant trans-granular cracks along the grain boundaries (specimen heated at 1 kW for 60 seconds).

5.4.11 Crack density

(a) Crack density based on total length

Crack density, defined as the ratio of the total crack length on the surface and total surface area are computed. The software ImageJ is used to skeletonise the binary cracks and to calculate the total crack length. **Figure 5.32 and 33** shows the skeletonised cracks of gabbro specimens heated at 0.5 kW and 2 kW, respectively.

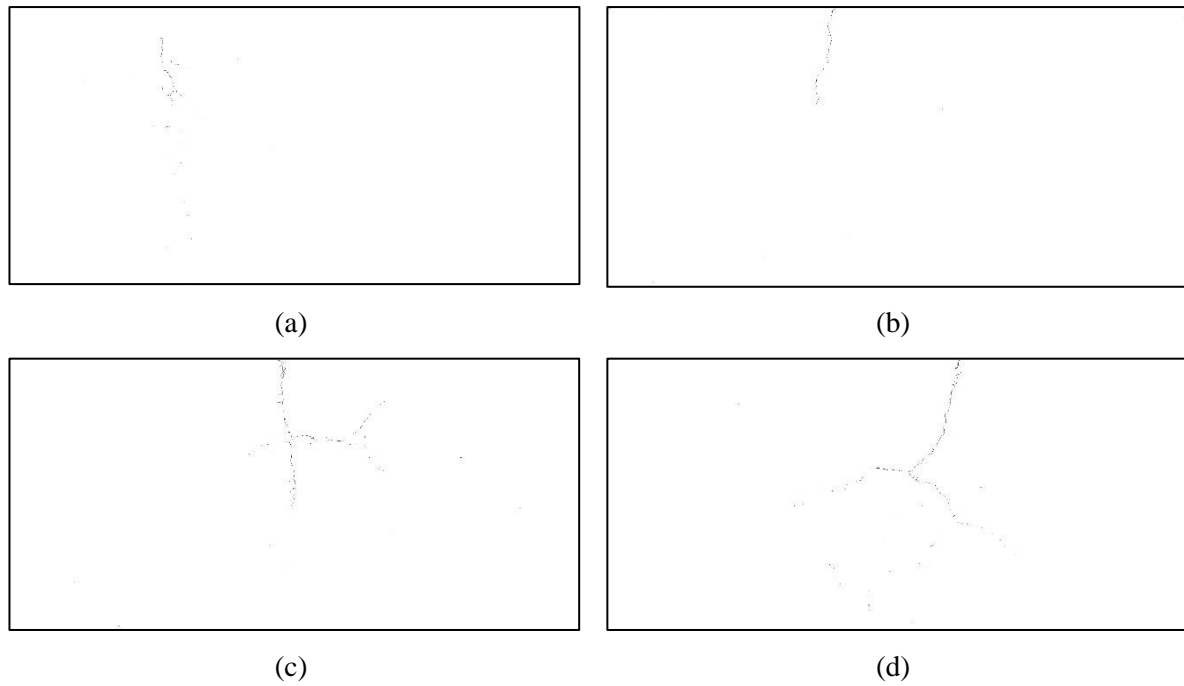


Fig. 5.32 Skeletonised cracks on microwave treated gabbro surfaces (specimens treated at 0.5 kW). (a) 30 seconds; (b) 60 seconds; (c) 90 seconds; (d) 120 seconds.

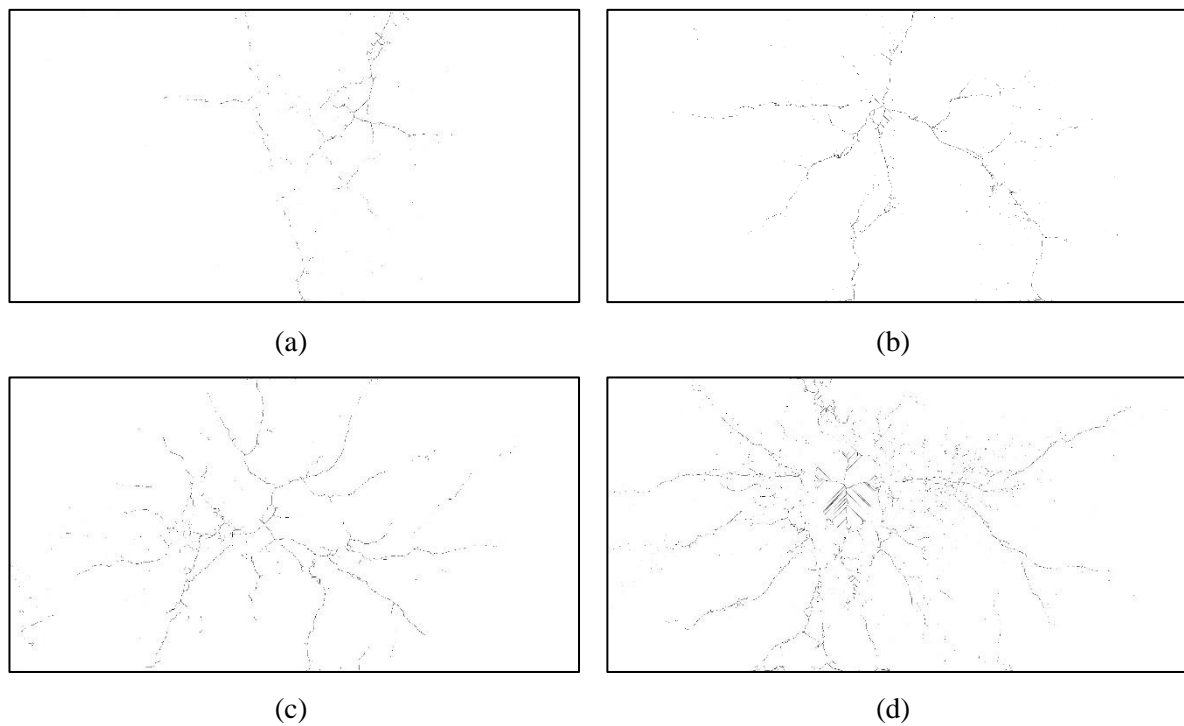


Fig. 5.33 Skeletonised cracks on microwave treated gabbro surfaces (specimens treated at 2 kW). (a) 30 seconds; (b) 60 seconds; (c) 90 seconds; (d) 120 seconds.

The crack density, expressed in mm/mm^2 , under each heating condition for the three rock types is presented **Figure 5.34**. It can be found that at lower power levels, the crack density is low as no or very few cracks are generated. However crack density can grow exponentially at high power levels as exposure time increases. Under the same heating conditions, gabbro generates the most cracks and

granite generates the least cracks. However this does not imply that microwave is not effective in weakening granite as granite specimens usually experience brittle failures.

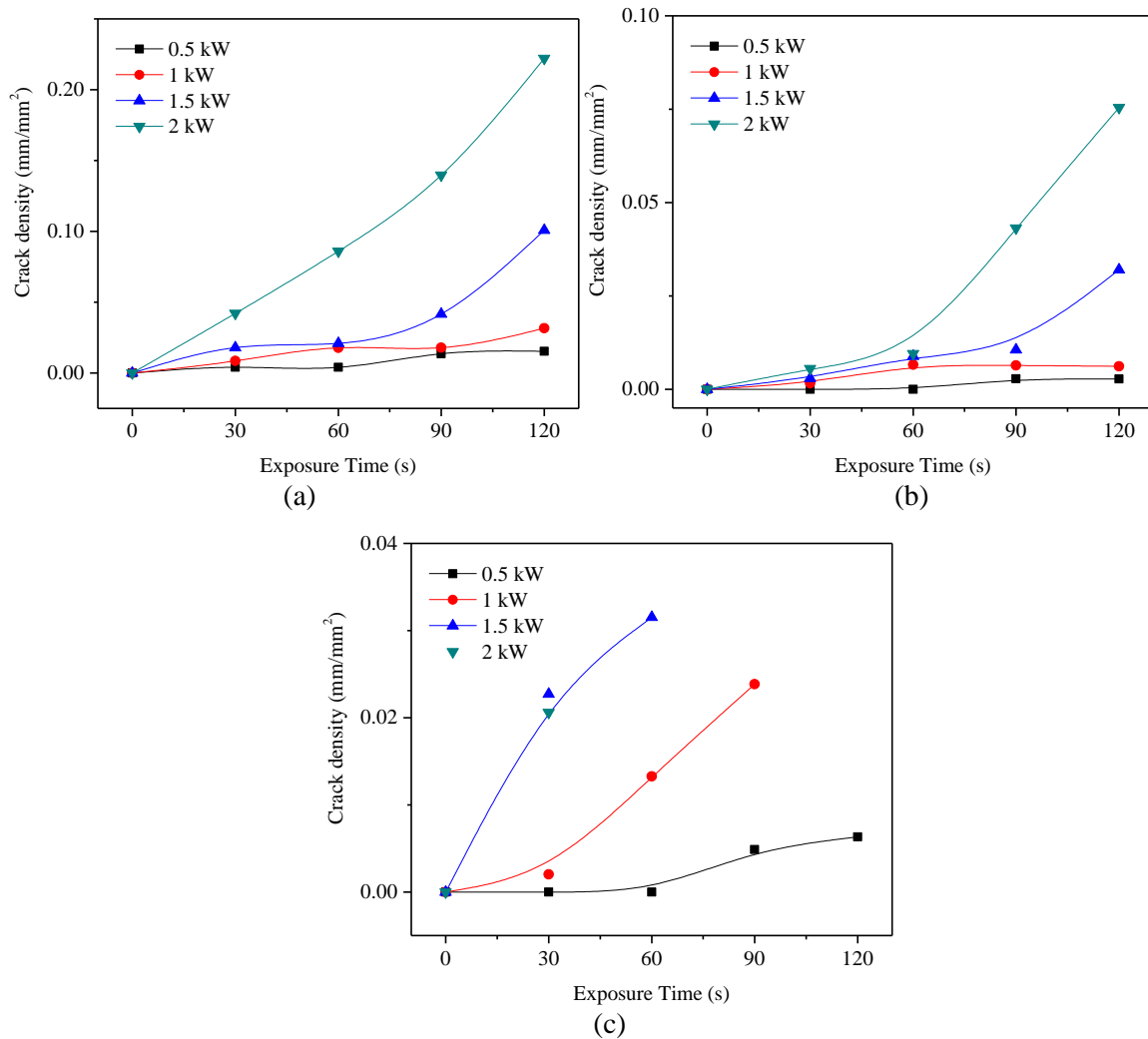


Fig. 5.34 Crack density as a function of exposure time for (a) gabbro, (b) monzonite and (c) granite.

(b) Crack density using the Underwood Method

Crack density can also be quantified using the Underwood method (Underwood, 1969) which basically involves counting the number of intersections of cracks with an equally distanced grid, as shown in Figure 5.35(a). In this section, only crack pattern and density in gabbro are quantified. During the characterisation of crack, only three types are identified, namely intergranular (pyroxene-feldspar) cracks, trans-pyroxene-granular cracks and trans-feldspar-granular cracks. The crack density of the gabbro specimens heated at 2 kW can be found in Figure 5.35(b). It is clear that the dominant crack types are intergranular cracks and transgranular cracks in feldspar. Trans-granular cracks in pyroxene only account for a small proportion of the total cracks. As exposure times increases, the cracks increased quickly first then begin to be stabilise since the heating generated is used to melt rocks rather than to induce more new cracks.

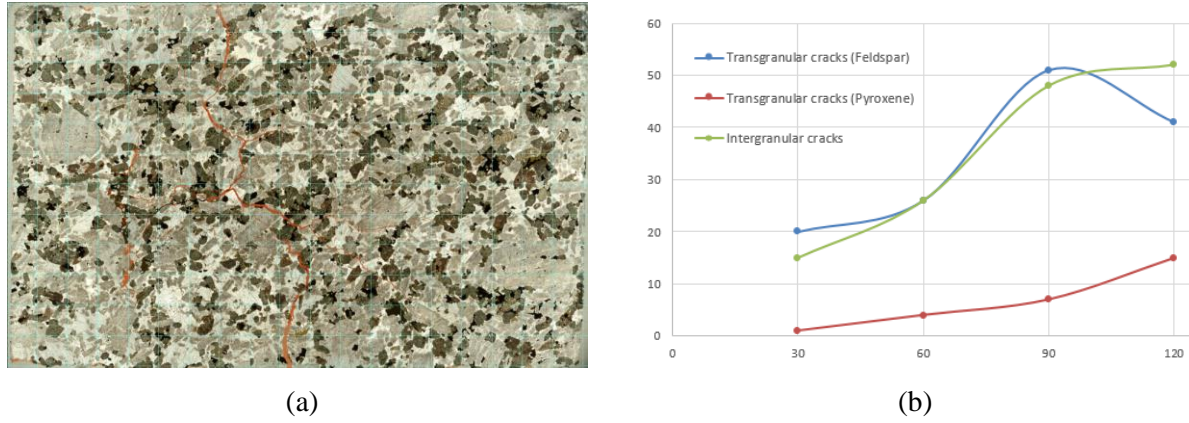


Fig. 5.35 Crack density extraction based on the Underwood Method using equivalent distance grid.

(c) Crack density estimation from P-wave velocity

From the data of P-wave velocity, the Poisson's ratio and Young's modulus of rocks, the crack density can be estimated. [David et al. \(1999\)](#) developed the following equation to calculate the crack density assuming a random distribution of dry cracks in the specimen based on [O'Connell and Budiansky \(1974\)](#) and [Hudson \(1981\)](#)'s work:

$$\eta = (\lambda_s + 2\mu_s - \rho V_p^2) / \Gamma$$

Where η is the crack density, λ_s and μ_s are the first and second Lamé elastic constants, ρ is the solid density, V_p is the P-wave velocity and Γ is the anisotropic factor. λ_s , μ_s and Γ can be calculated as:

$$\lambda_s = \frac{Ev}{(1+\nu)(1-2\nu)}, \quad \mu_s = \frac{E}{2(1+\nu)}$$

$$\Gamma = \frac{4}{27} \frac{(3\lambda_s + 2\mu_s)^2 (\lambda_s + 2\mu_s)}{\mu_s (\lambda_s + \mu_s)} + \frac{64}{135} \frac{\mu_s (\lambda_s + 2\mu_s) (9\lambda_s + 10\mu_s)}{(3\lambda_s + 4\mu_s) (\lambda_s + \mu_s)}$$

Where E and ν are the Young's Modulus and Poisson's ratio, respectively.

From the Young's Modulus (85 GPa) and Poisson's ratio (0.24) of gabbro, λ_s and μ_s are calculated as 31.6 GPa and 34.3 GPa, respectively. The estimated crack densities before and after microwave treatment are shown in [Figure 5.36](#). The crack density in the middle of specimens ([Figure 5.36\(a\)](#)) reveals that the crack density increases from zero for the intact specimen to up to 0.4 for specimens heated at 2 kW for 120 seconds. The increase rate of crack density calculated tends to decrease as the exposure time increases, which indicates that microwave heating after the first 60 seconds becomes inefficient to generate new cracks in the middle. The overall crack density of the specimen ([Figure 5.36\(b\)](#)) shows that as the heating time increases, the crack density increases almost linearly. One needs to consider the desired heating outcomes, more specifically, to weaken a certain area to generate cracks or to weaken the whole surface, before selecting which crack density should be used to evaluate the heating. In monzonite and granite ([Figures 5.36\(c\)-\(e\)](#)), similar amounts of cracks are estimated.

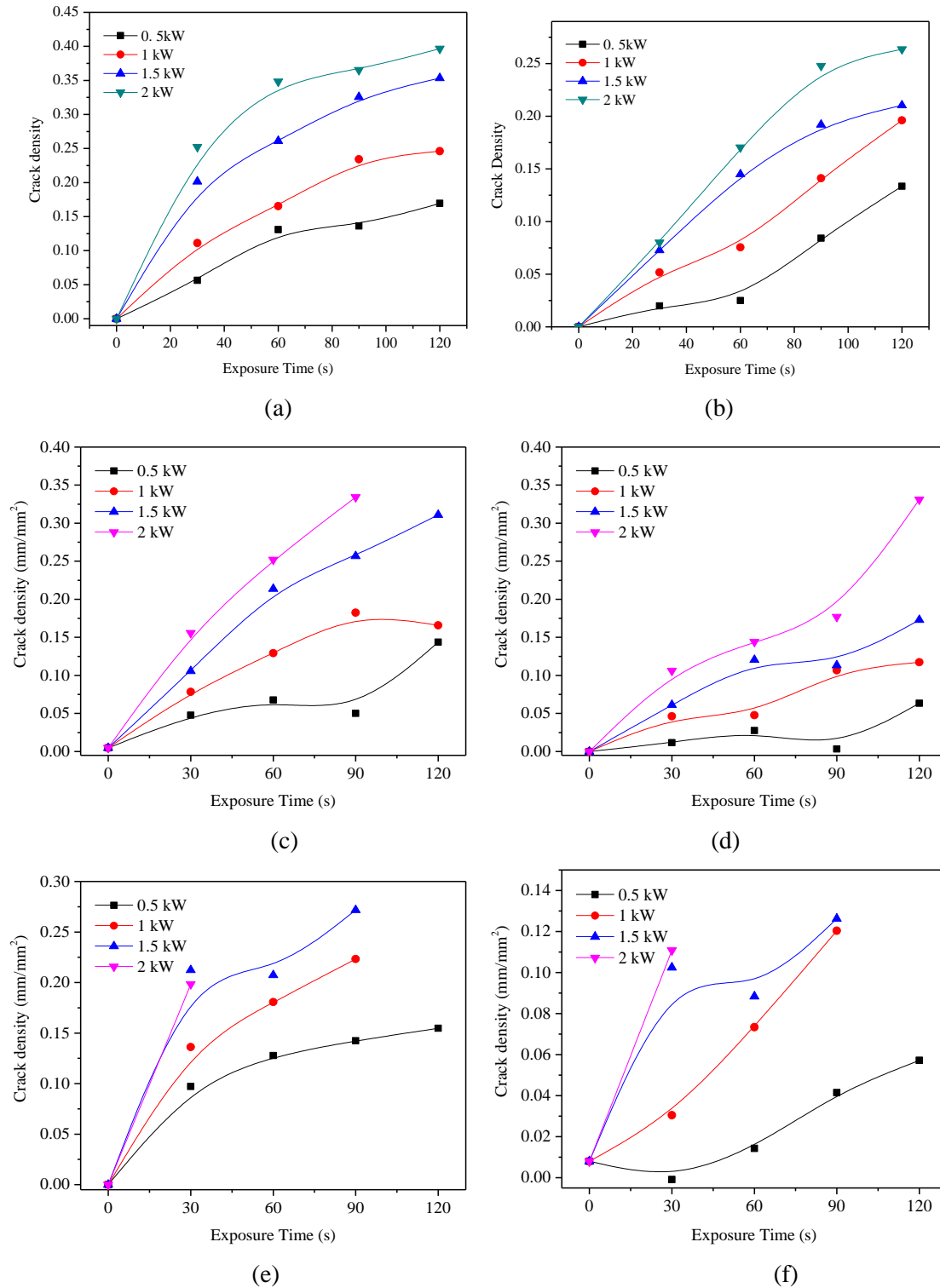


Fig. 5.36 Estimated crack density after microwave treatment. (a) in the middle of the gabbro specimens; (b) overall of gabbro specimens; (c) in the middle of the monzonite specimens; (d) overall of monzonite specimens; (e) in the middle of the granite specimens; (f) overall of granite specimens.

(d) Interior cracks

It is challenging to extract internal cracks in the specimen after microwave treatment. A Zeiss X-Ray CT is used to scan a gabbro sample treated at 2 kW for 90 seconds. Three cross sections, namely the

front surface, mid-thickness cross section (15 mm) and the back surface, with cracks are shown in **Figure 5.37**. It can be noted that there are more cracks developed on the free surfaces because of its high temperature and a lack of constraints. The cracks initiate from the top middle of the specimen where the greatest thermal gradient and thermal stress take place. The reflection of microwave on the back surface creates standing waves in the specimen, and thus improves the heating to a certain degree. The depth of thermal damage of microwave irradiation in the field needs to be further explored using an open-ended antenna and larger sized rock blocks.

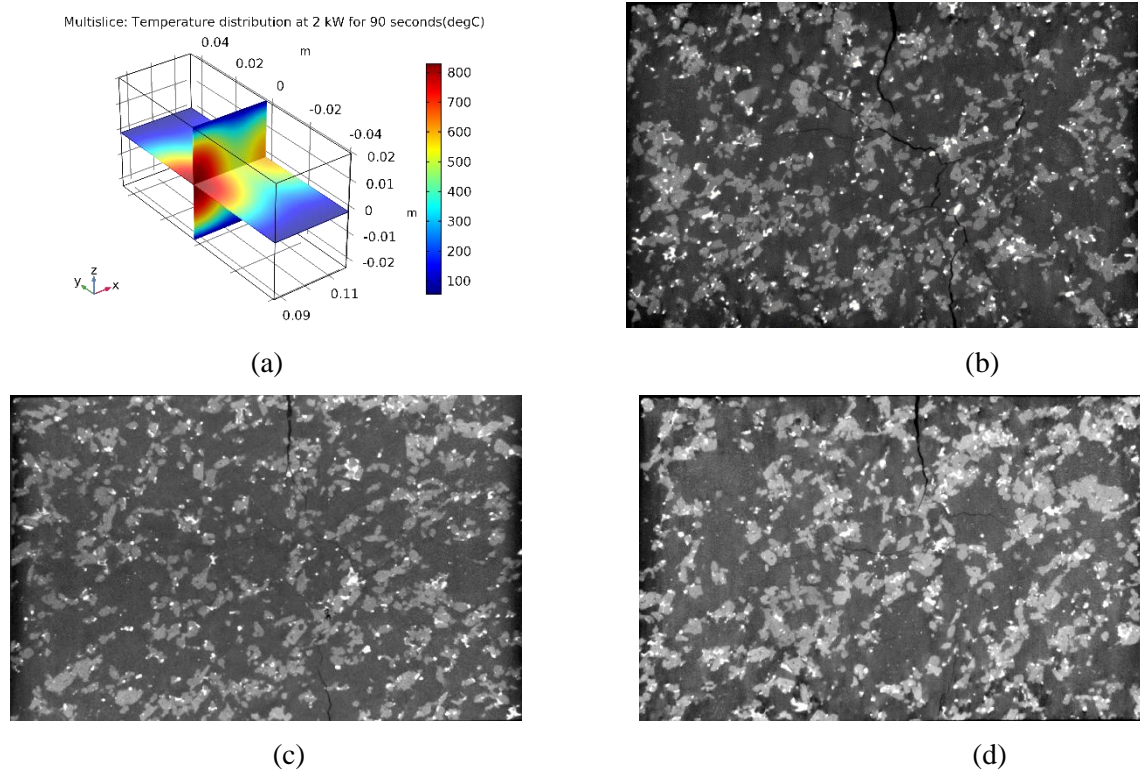


Fig. 5.37 Temperature and crack distribution of a gabbro specimen heated at 2 kW for 90 seconds. (a) Temperature distribution using multiphysics numerical simulation; (b) Cracks in the front surface; (c) Cracks in the mid-thickness cross section; (d) Cracks at the back surface.

5.4.12 Correlation between parameters

(a) Correlations between ultrasonic velocities and energy

This section tries to make correlations between the variables in an effort to dig out more information. **Figure 5.38** shows the correlation between the normalised overall velocities with the energy consumption. This is to shed light on the optimal power level and exposure time combinations. From **Figure 5.38**, it can be concluded that there is a highly linear relationship between the energy output and the P-wave velocities for gabbro and monzonite specimens. For granite the linear relationship still exists but with a lower coefficient of regression. Another finding is that for the same energy output, heating at higher power levels usually yields a better weakening result.

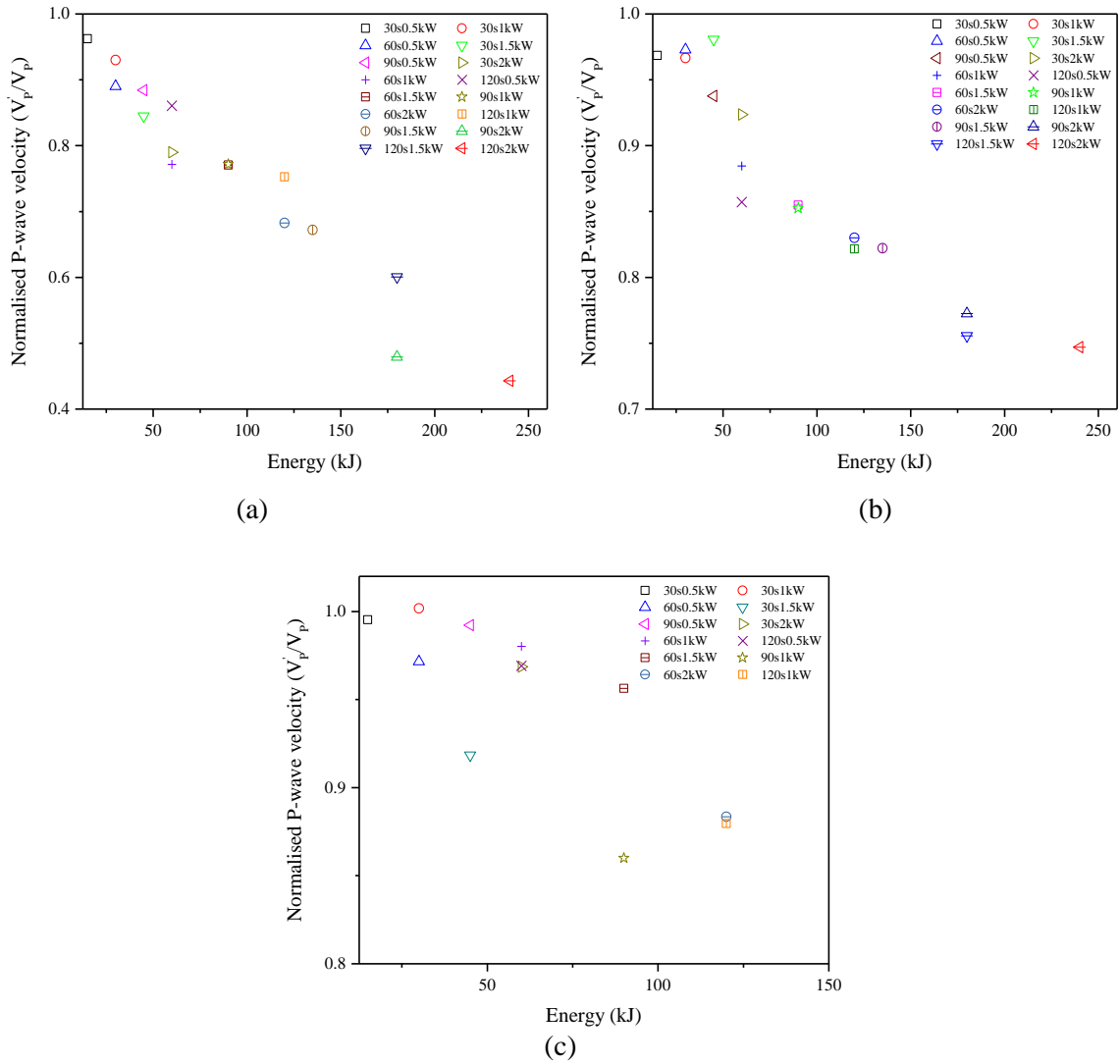


Fig. 5.38 Correlations between normalised P-wave velocity and energy output. (a) Gabbro; (b) Monzonite; (c) Granite.

(b) Correlations between ultrasonic velocities and temperature

Figure 5.39 shows the correlation between the normalised overall velocities with the average temperature of the specimen surfaces. It can be found that the reduction of the P-wave velocities, which could be defined as the degree of thermal damage, is highly linearly correlated with the average temperature for the gabbro and monzonite specimens. For the granite specimens, the regression coefficient is lower due to the nature of heterogeneity.

(c) Correlations between ultrasonic velocities and crack density

Figure 5.40 shows the relationship between the normalised Young's modulus and the measured crack density. It is clear that as the crack density increases the Young's modulus decreases. Due to the small population of data for granite specimens, the correlation of granite is not presented.

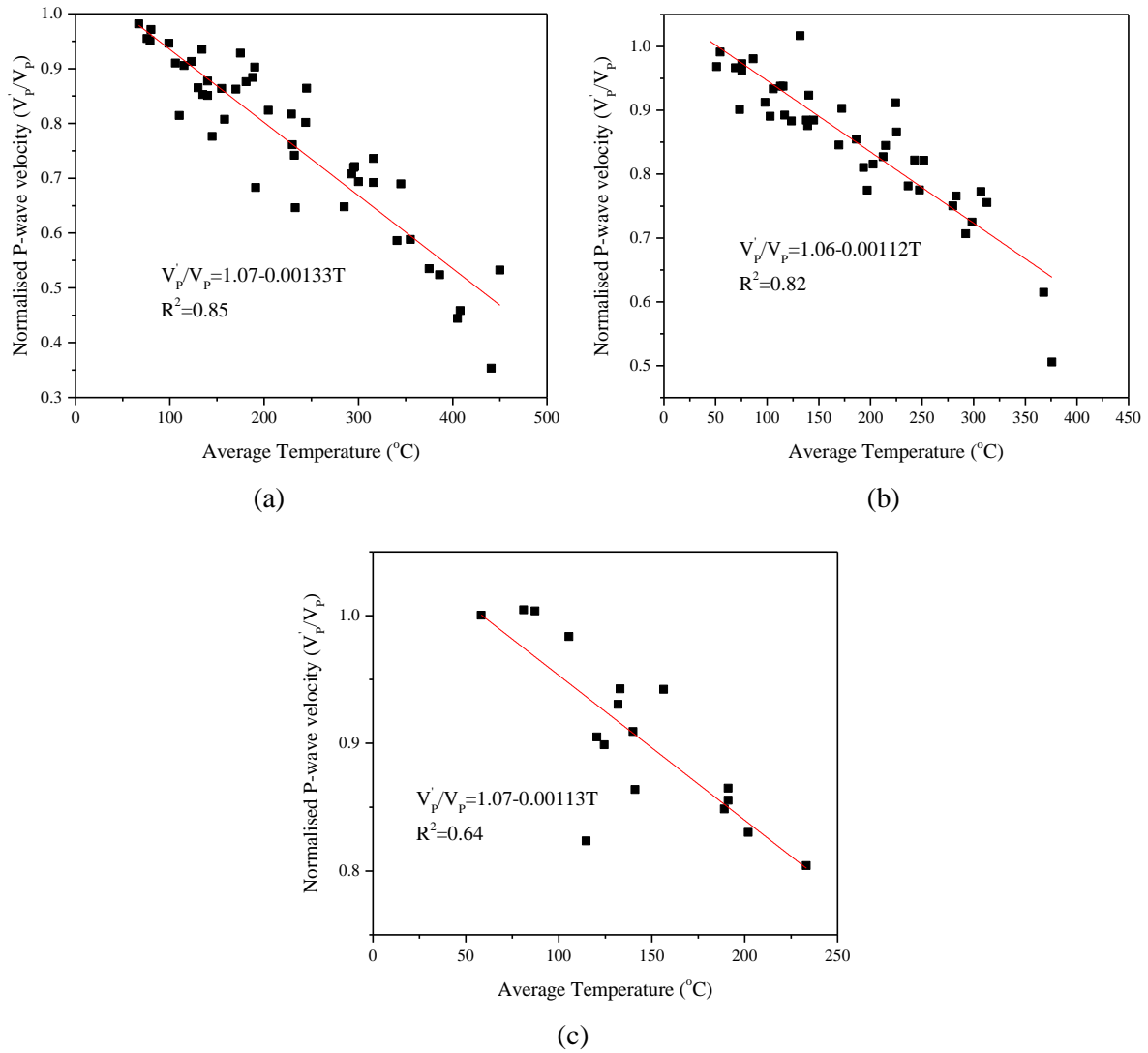


Fig. 5.39 Correlations between normalised P-wave velocity and temperature. (a) Gabbro; (b) Monzonite; (c) Granite.

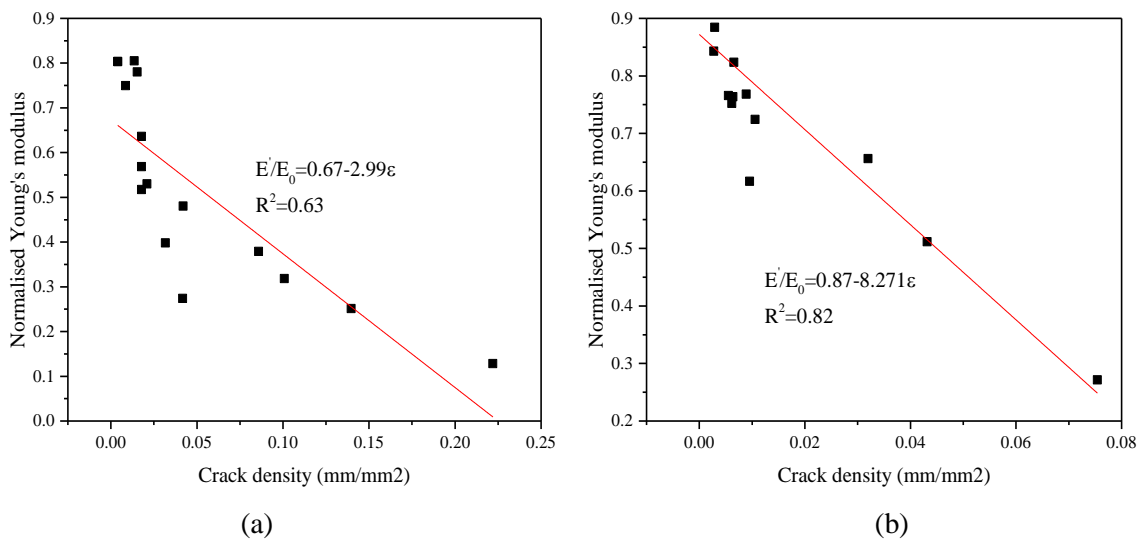


Fig. 5.40 Correlations between normalised P-wave velocity and crack density. (a) Gabbro; (b) Monzonite.

5.5 Limitation of the research

It should be noted that in the experimental tests no confinement on the specimens is applied. In case there is a confining pressure, i.e. in the field scenario, the generation of cracks will be suppressed. Future research should make efforts to account for this factor. A special loading device made of microwave transparent/isolated materials such as alumina and copper plate should be designed.

Another limitation of the research is that the thickness is not large enough to simulate the field scenario, though water load is installed at the end of the system to absorb the microwave energy transmitted through the specimens. Due to the reflection of microwave at the back surface, there exist standing waves in the specimens which could exaggerate the heating and weakening to a certain extent. This can be solved by either using thicker specimens or large rock blocks in a metallic box or by performing numerical simulations.

Although thermal cracks tended to close as the specimens cooled off, it remains unclear how many cracks are generated in the heating process and how many are generated in the cooling process. **Figure 5.41** shows the typical heating and cooling process of microwave heating process. It can be found that the cooling takes longer than the heating stage. Previous research by [Browning et al. \(2016\)](#) showed that more cracks are generated while cooling due to contraction which encourages the growth and extension of many more and larger, predominantly tensile, microcracks. Future research can probe into this using the acoustic emission measurement method.

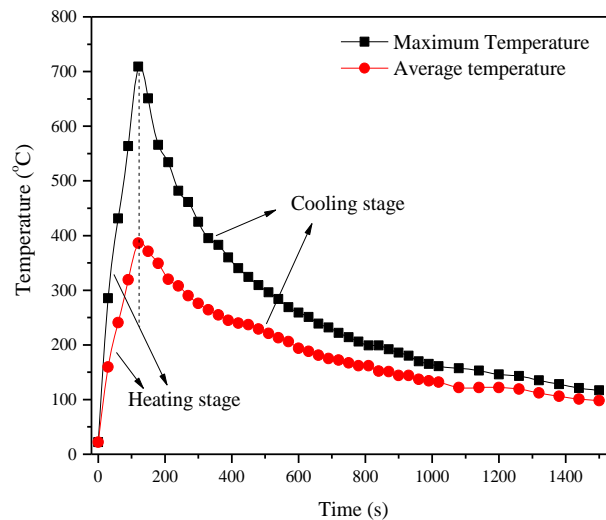


Fig. 5.41 Temperature change in the microwave heating and natural cooling process (gabbro heated at 1.5 kW for 120 seconds).

In the experiment, the maximum power output is 2 kW. Although demonstrated as satisfactorily effective in weakening the three rock types, the power level is not high enough for field application such as TBMs and roadheaders where the heating time is much shorter. As discussed in previous sections, microwave working at higher power levels is more efficient in generating rocks and weakening

hard rocks. In the future research, higher poared microwave systems should be used to simulate the field scenario.

Due to a lack of an observation window on the microwave cavity, the temperature of a specimens heated by microwave could not be continuously and real-time monitored. This is problematic for the temperature measure of granite specimens since the hot spots (biotite) could cool off very quickly after microwave heating stops. The current temperature measurement underestimated the magnitude.

5.6 Conclusions

This chapter investigates the effect of microwave treatment (power level of 0.5-2 kW, exposure time of 30-120 seconds) on the surface temperature (spatial), temperature distribution (temporal), P-wave and S-wave velocities, crack generations and loading capacities of three igneous rocks (gabbro, monzonite and granite) using a single-mode microwave system. The following conclusions could be drawn from the experiments:

- The experimental results demonstrate that microwave can effectively weaken the three rocks tested. Rocks respond differently when subjected to microwave irradiation. The gabbro and monzonite specimens are thermally cracked first then melted. By contrast, the granite specimens failed in a violent manner, especially at high power levels. The tests results indicate that microwave heating at higher power levels is preferred than heating at lower powers.
- It is found that specimen surface temperatures and heating rates increase linearly with power level. The spatial temperature distributions are in the reversed V-shape. As either power level or exposure time increases, the thermal gradient and mismatch increases. The heating rates of the three rock types could be up to 6.04, 4.51 and 3.49 °C/s, which are 1-3 orders of magnitude higher than the conventional heating rates using a furnace. The thermal gradients are in the order of tens of degree per centimetres, generating huge thermal mismatch. The thermal shock and thermal gradient together lead to the weakening of the igneous rocks.
- Ultrasonic wave velocity measurement indicates a varying degree of reduction in strength for the three rocks. Gabbro and monzonite specimens experience damage until being melted while granite specimens can failure abruptly at high power levels.
- Elastic moduli derived from the ultrasonic wave velocities show that it could be reduced to 13 % and 27 % for gabbro and monzonite specimens respectively, after microwave heated at 2 kW for 120 seconds.
- The compression tests show that after microwave treatment the loading capacity of the rock specimens decreased dramatically. The peak loads of the gabbro and monzonite specimens after microwave treatment for 120 seconds at 2 kW are reduced by 66 % and 57 %, respectively. It is estimated that the tensile strength are reduced by over 90 %.

- Petrographic microscopy studies suggest both intergranular and transgranular cracks are observed. Intergranular cracks dominate in the monzonite while trans-granular cracks dominate in gabbro and granite specimens. The crack density increases exponentially at higher power levels.
- Correlation between elastic moduli and variables such as energy output, average temperature and crack density show that there is a negatively linear relationship between them, with a relatively good coefficient of regression.

Reference

- Browning, J., Meredith, P., Gudmundsson, A., 2016. Cooling-dominated cracking in thermally stressed volcanic rocks. *Geophysical Research Letters* 43, 8417-8425.
- Chaki, S., Takarli, M., Agbodjan, W.P., 2008. Influence of thermal damage on physical properties of a granite rock: Porosity, permeability and ultrasonic wave evolutions. *Construction and Building Materials* 22, 1456-1461.
- Chen, Y.-L., Ni, J., Shao, W., Azzam, R., 2012. Experimental study on the influence of temperature on the mechanical properties of granite under uni-axial compression and fatigue loading. *International Journal of Rock Mechanics and Mining Sciences* 56, 62-66.
- David, C., Menéndez, B., Darot, M., 1999. Influence of stress-induced and thermal cracking on physical properties and microstructure of La Peyratte granite. *International Journal of Rock Mechanics and Mining Sciences* 36, 433-448.
- Fredrich, J.T., Wong, T.-f., 1986. Micromechanics of thermally induced cracking in three crustal rocks. *Journal of Geophysical Research: Solid Earth* 91, 12743-12764.
- Homand-Etienne, F., Houpert, R., 1989. Thermally induced microcracking in granites: characterization and analysis. *International Journal of Rock Mechanics and Mining Sciences & Geomechanics Abstracts* 26, 125-134.
- Hudson, J.A., 1981. Wave speeds and attenuation of elastic waves in material containing cracks. *Geophysical Journal of the Royal Astronomical Society* 64, 133-150.
- Hughes, D., Maurette, C., 1956. Variation of elastic wave velocities in granites with pressure and temperature. *Geophysics* 21, 277-284.
- Hughes, D.S., Cross, J.H., 1951. Variation of elastic wave velocities in rocks with pressure and temperature. *Geophysics* 16, 577-593.
- Insera, C., Biwa, S., Chen, Y., 2013. Influence of thermal damage on linear and nonlinear acoustic properties of granite. *International Journal of Rock Mechanics and Mining Sciences* 62, 96-104.
- Jones, C., Keaney, G., Meredith, P.G., Murrell, S.A.F., 1997. Acoustic emission and fluid permeability measurements on thermally cracked rocks. *Physics and Chemistry of the Earth* 22, 13-17.
- Keshavarz, M., Pellet, F.L., Loret, B., 2010. Damage and changes in mechanical properties of a gabbro thermally loaded up to 1,000°C. *Pure & Applied Geophysics* 167, 1511-1523.
- Kranz, R.L., 1983. Microcracks in rocks: A review. *Tectonophysics* 100, 449-480.
- Nesse, W.D., 2013. *Introduction to Optical Mineralogy*. Oxford University Press.
- Nishiyama, T., Kusuda, H., 1994. Identification of pore spaces and microcracks using fluorescent resins. *International Journal of Rock Mechanics and Mining Sciences & Geomechanics Abstracts* 31, 369-375.
- O'Connell, R.J., Budiansky, B., 1974. Seismic velocities in dry and saturated cracked solids. *Journal of Geophysical Research* 79, 5412-5426.
- Page, L., Heard, H.C., 1981. Elastic moduli, thermal expansion, and inferred permeability of Climax Quartz Monzonite and Sudbury Gabbro to 500°C and 55 MPa, The 22nd U.S. Symposium on Rock Mechanics (USRMS). American Rock Mechanics Association, Cambridge, Massachusetts, USA, pp. 97-104.
- Reuschlé, T., Gbaguidi Haore, S., Darot, M., 2006. The effect of heating on the microstructural evolution of La Peyratte granite deduced from acoustic velocity measurements. *Earth and Planetary Science Letters* 243, 692-700.

- Shao, S., Ranjith, P.G., Isantha, P.L.P., Chen, B.K., 2015. Experimental and numerical studies on the mechanical behaviour of Australian Strathbogie granite at high temperatures: An application to geothermal energy. *Geothermics* 54, 96-108.
- Thuro, K., Spaun, G., 1996. Introducing the 'destruction work' as a new rock property of toughness referring to drillability in conventional drill- and blast tunnelling, in: **Barla, G.** (Ed.), Eurock '96. International Society for Rock Mechanics, Turin, Italy, pp. 707-713.
- Underwood, E.E., 1969. Stereology, or the quantitative evaluation of microstructures. *Journal of Microscopy* 89, 161-180.
- Wang, H.F., Bonner, B.P., Carlson, S.R., Kowallis, B.J., Heard, H.C., 1989. Thermal stress cracking in granite. *Journal of Geophysical Research: Solid Earth* 94, 1745-1758.
- Yong, C., Wang, C.-y., 1980. Thermally induced acoustic emission in westerly granite. *Geophysical Research Letters* 7, 1089-1092.
- Zhou, C., Wan, Z., Zhang, Y., Gu, B., 2018. Experimental study on hydraulic fracturing of granite under thermal shock. *Geothermics* 71, 146-155.

CHAPTER 6

Application of Microwave on Tunnel Boring Machines

6.1 Introduction

As the ultimate objective of the research is to utilise microwave as a means in assisting hard rock breakage of TBMs and the effectiveness of microwave in fracturing hard rocks has been demonstrated in Chapter 5, this chapter discusses the technical considerations, which include the selection of the open-ended microwave applicators, the configurations of the applicators on the cutterhead with respect to the disc cutters, the proper working distance of the applicator, the individual and total power requirements and the expected difficulties.

6.2 Typical cutterhead designs of hard rock TBMs

Figure 6.1 shows the typical cutterhead designs of hard rock TBMs. Normally three types of disc cutters are used on the gripper and single shield TBMs, namely, twin/double disc cutters in the centre, single disc cutters on the face and gage cutters on the periphery (Rostami, 2008). The reason for using twin cutters (normally in two groups) at the centre is due to the limited space available there. The face cutters are usually set at more or less the same distance and on concentric circles from the centre. They can be randomly laid out (Figure 6.1(a)) or in several spokes (Figure 6.1(b)). The spacing of the face cutters ranges from 65 mm to 95 mm, depending on the rock strength and the cutter diameter (Maidl et al., 2008). The gage cutters are placed in a closer distance to reduce the amount of forces imposed on the cutters since they are gradually tilted outward to cut the clearance for cutter housing and body of the cutterhead (Rostami, 2008). The tilt angle is selected in such way for the cutters to be perpendicular to the surface they are cutting. This provides for less side force and helps extending cutter life in the gage area (Rostami, 2008). Besides the disc cutters, there are also openings such as mucking buckets and manholes for possible cutter inspection and replacement.

Given the internal cross sections of the rectangular microwave waveguides at 2.45 GHz and 922 MHz are 86 mm by 43 mm and 109 mm by 55 mm, respectively, they are relatively small in size compared to the disc cutters (483 mm in diameter for a 19 inch disc cutter) even when they have a flared end. Therefore, the positioning of microwave applicators on the cutterhead can be very flexible, even for TBMs as small as 3 m in diameter. They are not necessarily very close to the cutters as the cutterhead rotates at a high speed and the rock mass will be under cyclic microwave treatment. A reference can be made to Figure 2.19 where there are more infrared generators than mechanical cutters and the cutterheads are full of generators. To avoid the possible contamination and blockage of the microwave applicators by the mucks, applicators must be protected by microwave transparent ceramics such as alumina. This also helps to sustain the structural integrity of the cutterhead.

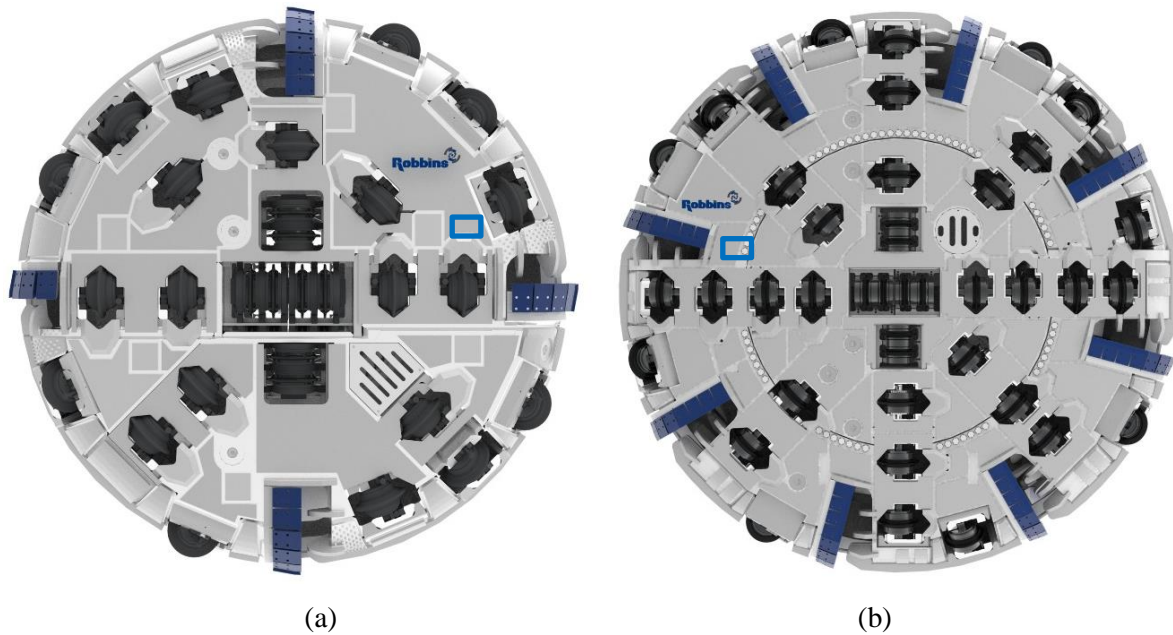


Fig. 6.1 Cutterhead designs of (a) a main beam TBM and (b) a single shield TBM (The Robbins Company). Boxes in figures illustrate the position of microwave applicators with respect to disc cutters.

Figure 6.2 illustrates the two possible configurations of the microwave applicators with respect to the TBM disc cutters. The applicators can be placed either in front of the cutters in the cutting trajectories (Figure 6.2(a)) or parallel to the cutters and offset by a certain distance (Figure 6.2(b)). Depending on the weakening effects, some cutters can be replaced by microwave applicators or the spacing of cutters can be increased. It is expected that the first configuration has a better performance as cracks initiated by microwave treatment can be further extended by the disc cutters. The second configuration may work more efficiently in rocks such as granite and quartzite where the applicators can cause more local damages such as spalling or kerfing.

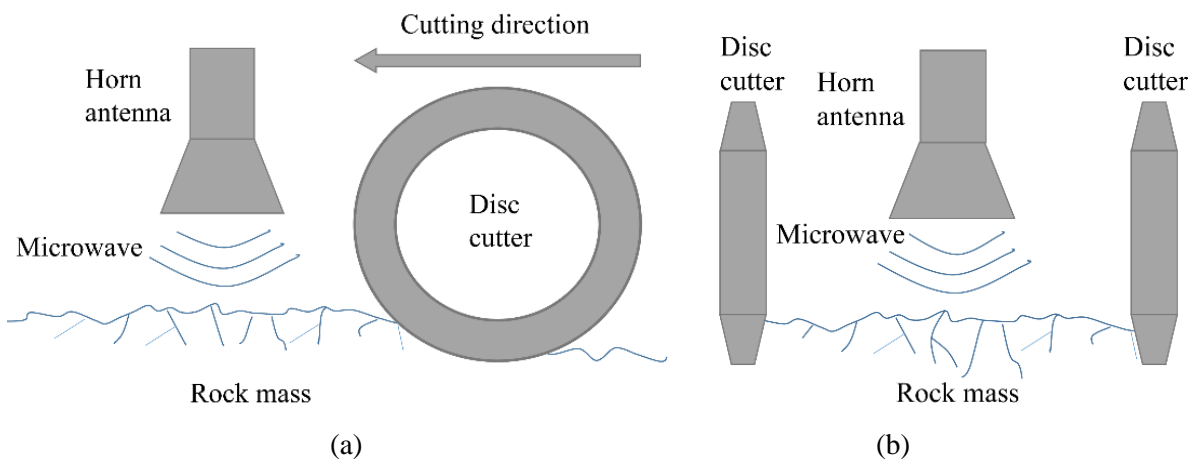


Fig. 6.2 Configurations of microwave applicators with respect to TBM disc cutters. (a) Applicators in the cutting trajectories of cutters (Hassani et al., 2016), (b) applicator parallel to disc cutter by a certain distance.

6.3 Conceptual designs of using microwave on TBMs

As shown in **Figure 6.3**, there are three available types of open-ended microwave applicators that can be installed on a TBM cutterhead to pre-weaken rocks before mechanical breakage by disc cutters. They are rectangular waveguides with or without a flange (**Figure 6.3(a)**), waveguides with a flared end (horn applicators) (**Figure 6.3(b)**) and focused waveguides with a reducing dimension in the electric direction (**Figure 6.3(c)**). Only the waveguide-type applicators are presented here since they are the most suitable applicators to carry the high power levels required for rock destruction and they are the most commercially available. Of the three applicator types, the horn applicators are more commonly used in the communications and heating industry because the horns work as an EM impedance matcher between the waveguide and the free space (377 Ohms) to maximise the energy transmission to the rock mass (Milligan, 2005). The horns also work to direct the microwave energy in the direction of propagation. The horns can be sectoral, pyramidal and conical.

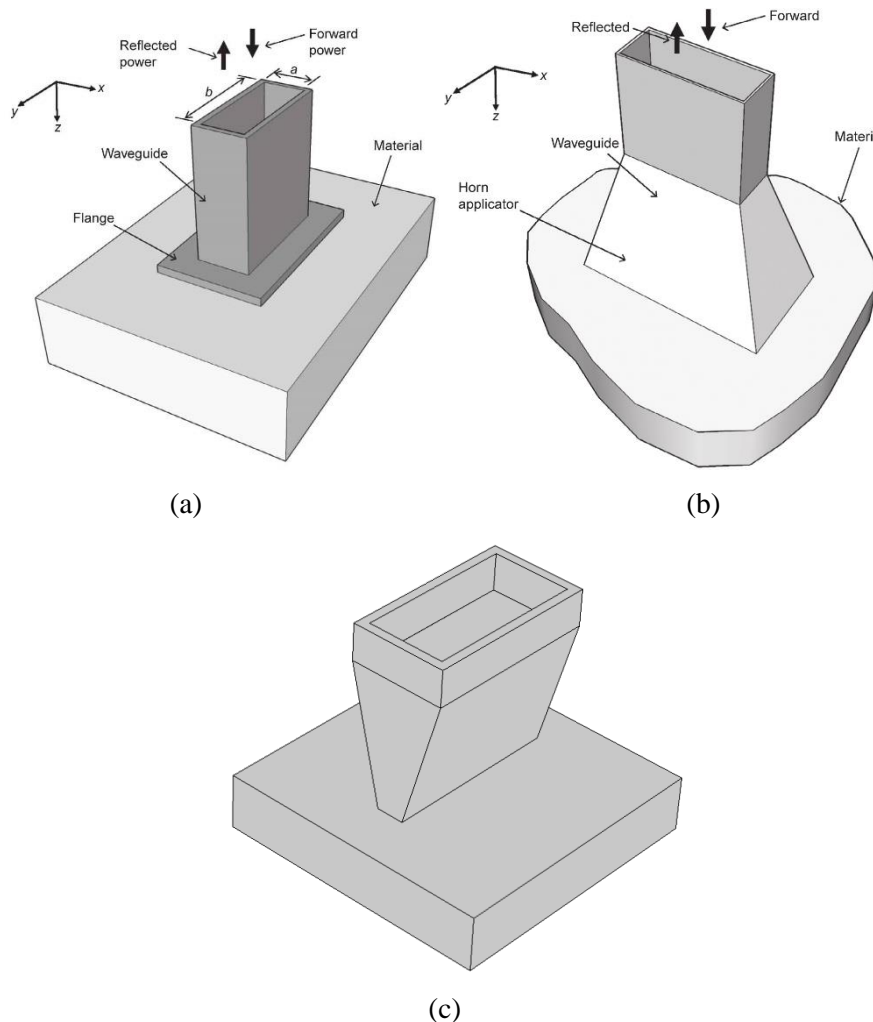


Fig. 6.3 Commercially available microwave applicator types (modified after [Mehdizadeh \(2015\)](#)). (a) Waveguide with a flange, (b) waveguide with a horn, (c) focusing waveguide.

Ideally the rock mass should be in good contact with or in the near field of the applicators (typically one wavelength of 12.24 cm) where the electric field strength is high, however, in practice it can be technically challenging, if not possible, to achieve this. **Figure 6.4** shows the distance from the excavation face to a TBM cutterhead equipped with 19 inch disc cutters. The distance is 175 mm. For 17 inch disc cutters, the distance is about 130 mm. Although special designs can be made to reduce the distance, there must be a certain distance residual to allow for mucking and to assure the safety of the microwave applicators. It is therefore reasonable to make the assumption that there will be a 5-10 cm working distance from the microwave applicators to the rock mass. It is then imperative to study the electric field strength and temperature distribution from the applicators and in the rock mass.

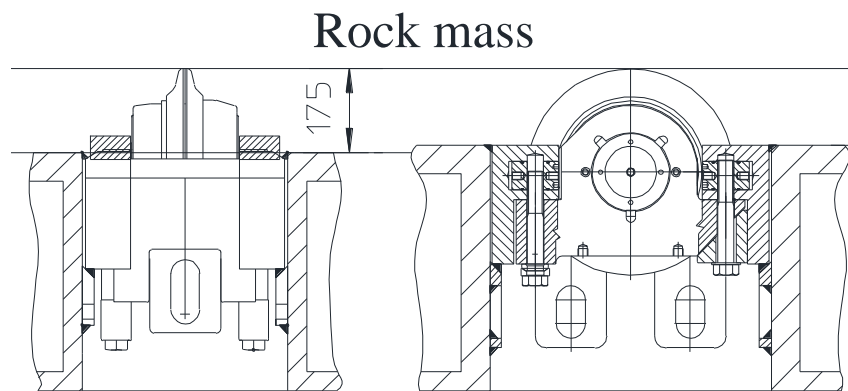


Fig. 6.4 Distance from the excavation face to the cutterhead equipped with 19 inch disc cutters.

Figures 6.5 and **6.6** show the electric field distribution at the mouth of the applicators as shown in **Figure 6.3**. The waveguides simulated are WR340 with an internal dimension of 86 mm by 43 mm. The total length of the applicators is 93 mm, with a 73 mm long transition section for the horn and focusing applicators. The apertures of the horn and focusing applicators in the electric field direction are 70 mm and 10 mm, respectively. The dimension of the computational geometry is 300 mm long by 120 mm wide by 70 mm high (90 mm high for the horn applicator). The microwave power level at the port is 2 kW, operated in the TE₁₀ mode. All the boundaries except the port are defined as scattering boundary conditions. It can be found that at the mouth of the applicators there are very strong microwave reflections due to the EM impedance mismatch between the applicators and the free space. To better illustrate the electric field distribution, only electric field strength up to 50,000 V/m are displayed for waveguide and horn applicators in **Figures 6.5** and **6.6**.

The waveguide applicator (**Figures 6.5(a)** and **6.6(a)**) has a relatively good energy transmission rate and acceptable electric field strength in the vicinity of the applicator aperture. **Figure 6.7** shows the electric field strength along the centrelines of the applicators. However, there is a high energy concentration in the applicator and a high energy dispersion at the mouth, making the electric field strength smaller at a distance of over 10 cm from the aperture when compared to the horn applicator. Due to a poor microwave directivity, the heating and weakening effect will be compromised.

The horn applicator (Figures 6.5(b) and 6.6(b)) has the highest energy transmission rate among the three applicator types. Although its electric field strength in the close vicinity of the mouth is the lowest due to the increase in the aperture dimension, the electric field strength at a distance of 10 cm from the aperture is the highest (Figures 6.7(b)). This characteristic lends itself very suitable for field applications on TBMs, considering the applicator design has not been optimised yet. Nekoovaght (2015) argued that metallic cutterhead and the rock mass at the excavation face and side walls form a virtual cavity so a higher energy transmission is desired. It can be said that the horn applicators are the most appealing design to use in the field.

The focusing applicator (Figures 6.5(c) and 6.6(c)) has the highest electric field strength at the mouth. It would work more efficiently if the rock mass and applicator are in good contact. However, its effective working distance is the smallest due to the huge energy dispersion at the mouth and high EM field concentration in the applicator due to the change in the aperture dimension. The extremely high electric field strength at the mouth may lead to a dielectric breakdown. At this stage of the research, the possibility of using focusing applicators has not been ruled out. It needs to be further investigated by a professional electrician. In the next sections, the use of horn and waveguide applicators is discussed.

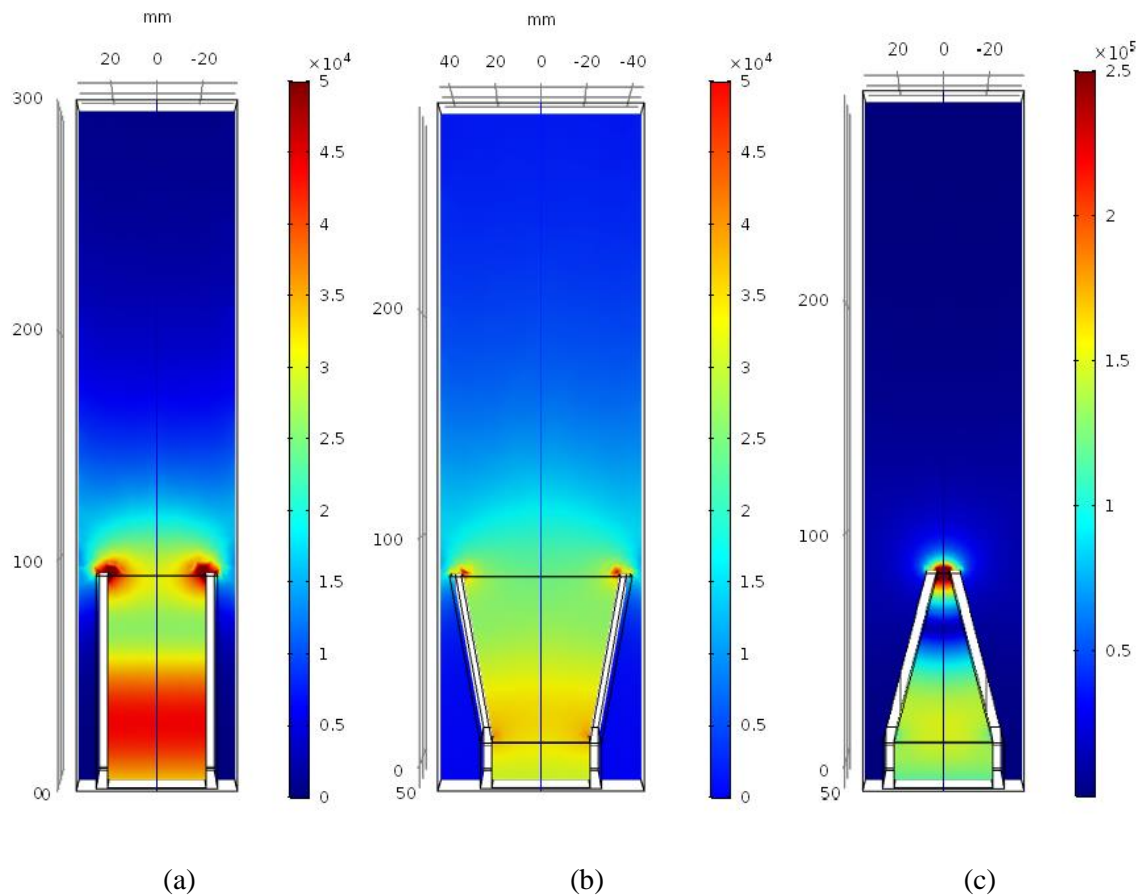


Fig. 6.5 Electric field (V/m) distribution of (a) a waveguide antenna, (b) a horn applicator and (c) a focusing antenna cut at the shorter dimension at an output power of 2 kW.

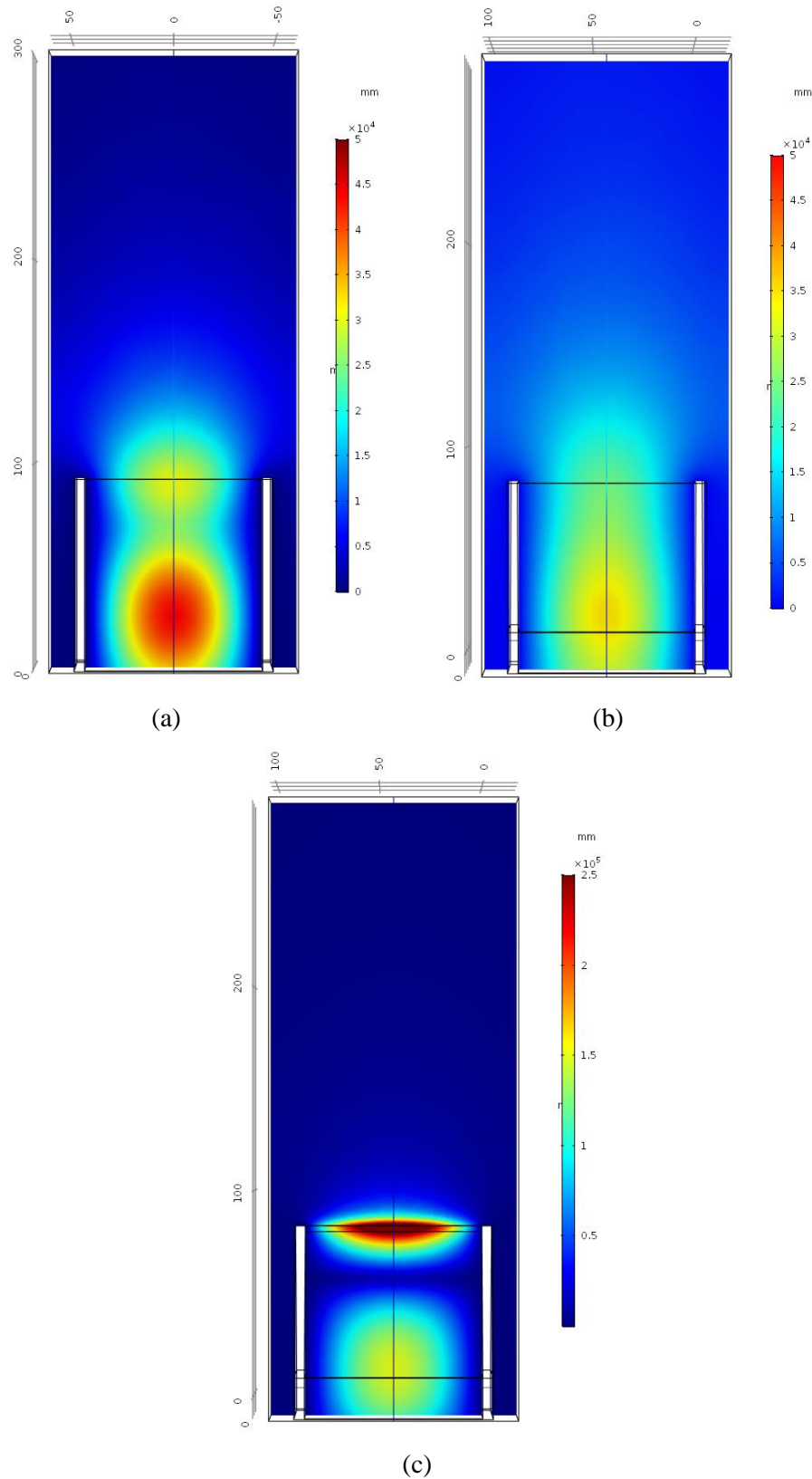


Fig. 6.6 Electric field (V/m) distribution of (a) a waveguide antenna, (b) a horn applicator and (c) a focusing antenna cut at the broader dimension at an output power of 2 kW.

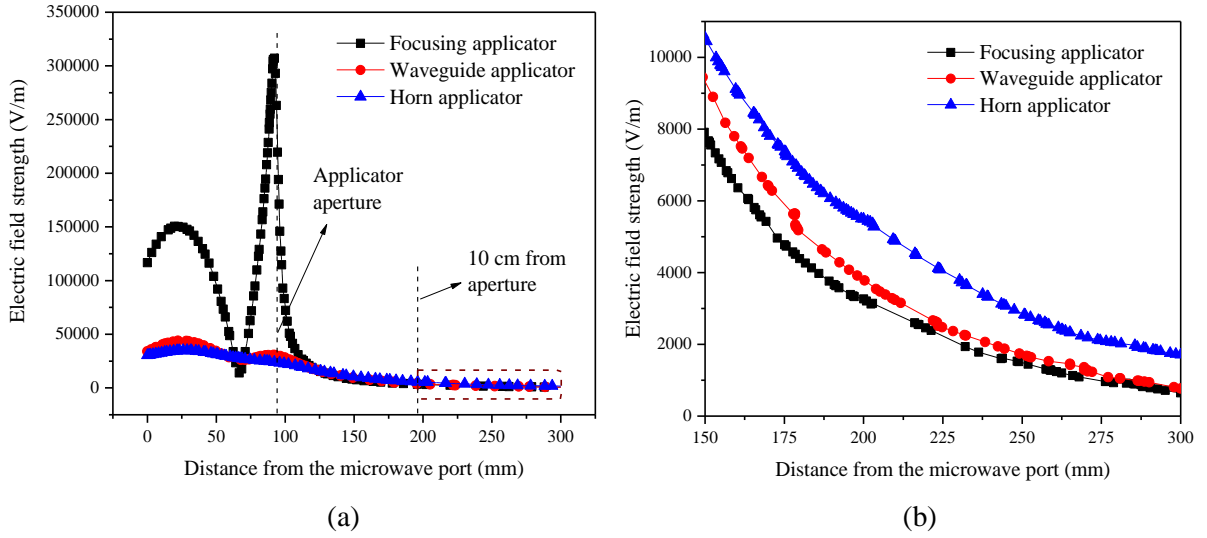


Fig. 6.7 Electric field strength along the centreline of the applicators. (a) From microwave port to a distance of 300 mm, (b) 5 cm from the aperture to 300 mm.

6.4 Study on use of open ended waveguide applicators

6.4.1 Waveguide applicators

The use of open-ended applicators in diathermia and hyperthermia has been reviewed by [Guy et al. \(1974\)](#), [Guy et al. \(1978\)](#) and [Gardioli \(1985\)](#). The closed analytical solution of open ended horn and waveguide applied to infinite medium and finite slab is investigated by [Teodoridis et al. \(1985\)](#). [Lewin \(1951\)](#) derived the admittance for a rectangular waveguide applicator radiating into a half space dielectric medium, as shown in [Figure 6.3\(a\)](#).

$$Y = G + jB = \frac{2j}{\pi ab k_1} \int_0^a \int_0^b (b-x) \left[K_2(a-y) \cos \frac{\pi y}{a} + \frac{a}{\pi} K_1 \sin \frac{\pi y}{a} \right] G_e dy dx \quad (6.1)$$

Where G and B are the conductance and susceptance of the waveguide, a and b are the height and width of the waveguide, k_1 is the TE₁₀ mode wave number, K_1 , K_2 and G_e are constants. They are computed as:

$$k_1 = \sqrt{k_0^2 - \left(\frac{\pi}{a}\right)^2}, \quad k_0 = \frac{2\pi}{\lambda_0} \quad (6.2)$$

$$K_1 = k_r^2 + \left(\frac{\pi}{a}\right)^2, \quad K_2 = k_r^2 - \left(\frac{\pi}{a}\right)^2 \quad (6.3)$$

$$k_r = k_0 \sqrt{\epsilon_r}, \quad G_e = \frac{1}{\sqrt{x^2 + y^2}} e^{-jk_r \sqrt{x^2 + y^2}} \quad (6.4)$$

Based on [Lewin \(1951\)](#), [Habash \(1994\)](#) derived the normalised electric field strength in the dielectric (body tissue) as a function of the coordinates ([Figure 6.8](#)). However, in those calculations the dielectrics are in contact with the applicator, the electric field distribution in dielectrics with a distance from the

applicator is still unknown. Numerical methods such as the finite-difference time domain techniques can be used to solve the problem (Yee, 1966).

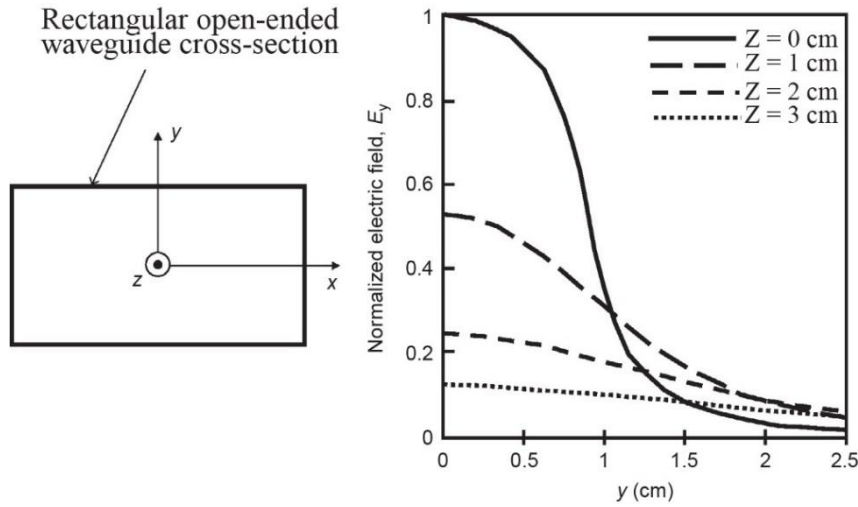


Fig. 6.8 Electric field distribution in the materials contacted with a rectangular open-ended waveguide (Habash, 1994; Mehdizadeh, 2015).

6.4.2 Horn applicators

Based on Connor (1972) and Ayappa et al. (1991), Brodie et al. (2015a) derived the electric field strength and the maximum temperature at a distance of z from the aperture. The computational geometry and the coordinate systems are shown in Figure 6.9.

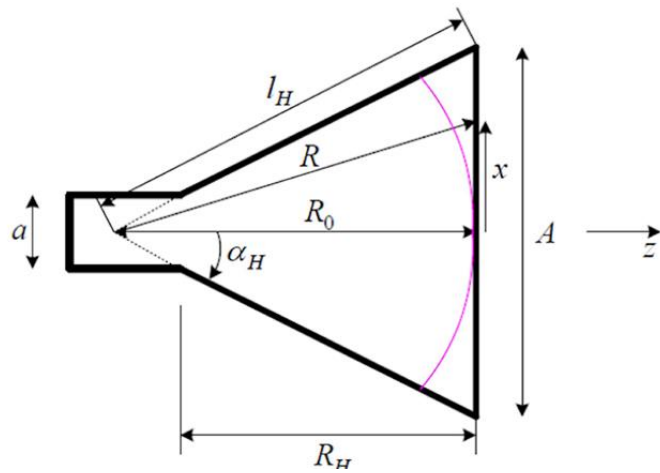


Fig. 6.9 Geometry of the horn application showing a propagating wave front in the flare (Brodie et al., 2015a).

$$\text{Electric field strength} \quad E_p = \frac{E_a}{4\pi} \int_{-\frac{A}{2}}^{\frac{A}{2}} \int_{-\frac{B}{2}}^{\frac{B}{2}} \cos\left(\frac{\pi}{A} x'\right) \frac{e^{-j\beta\left(\sqrt{(x-x')^2 + (y-y')^2 + z^2} + \sqrt{R_0^2 + (y')^2}\right)}}{\sqrt{(x-x')^2 + (y-y')^2 + z^2}} dx' dy' \quad (6.5)$$

$$\text{Electric field strength at the port} \quad E_a = E_0 \cos\left(\frac{\pi}{a} x'\right) \frac{a}{A} \quad (6.6)$$

$$\text{Maximum temperature} \quad T = \frac{n\pi f \varepsilon_0 \varepsilon''}{4k\alpha^2} (\tau E_p)^2 \left(e^{4\gamma\alpha^2 t} - 1 \right) \left(e^{-2\alpha z} + \left(\frac{h}{k} + 2\alpha \right) z e^{-\frac{z^2}{4\gamma t}} \right) \quad (6.7)$$

$$\text{Constants} \quad \alpha = \frac{2\pi f}{c} \sqrt{\frac{\varepsilon'}{2} \left(\sqrt{1 + \left(\frac{\varepsilon''}{\varepsilon'} \right)^2} - 1 \right)}, \quad \beta = \frac{2\pi f}{c} \sqrt{\frac{\varepsilon'}{2} \left(\sqrt{1 + \left(\frac{\varepsilon''}{\varepsilon'} \right)^2} + 1 \right)} \quad (6.8)$$

In Equation 6.7, n is the amplitude factor, γ is the diffusion coefficient for simultaneous heat and moisture transport of the dielectric. For moisture-free dielectrics, γ could be calculated using Equation 6.9.

$$\gamma = \frac{k}{\rho C_p} \quad (6.9)$$

Where k is the thermal conductivity (W/(m.K)), C_p is the specific heat capacity (J/(kg.K)).

Nekoovaght (2015) studied the temperature of stacked rock slabs subjected to microwave irradiation (Figure 6.10). He found that the working distance has a dominant role in the temperature distribution and that the temperature drops very quickly with depth. This thesis will study the electric field strength and temperature distribution using numerical modelling.

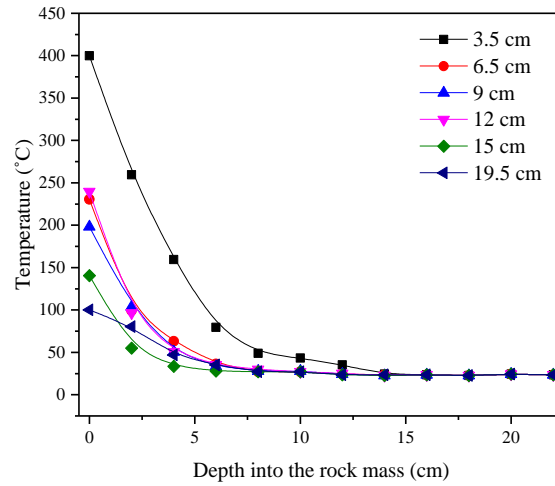


Fig. 6.10 Temperature distribution vs. depth into the stack of basalt slabs after 60s of microwave treatment at six distances from the antenna and 15 kW power (Nekoovaght, 2015).

6.5 Power requirement estimation

6.5.1 Exposure time

Once the configuration and type of microwave applicators are determined, it is necessary to estimate the requirement of the installed power of the applicators. This section tries to estimate the power requirement if a horn applicator is used. Assume that the diameter of the TBM is D (mm), the cutterhead

revolution is RPM (revolution per minute), the dimension of the microwave applicators is $W \times H \text{ cm}^2$ (width by height), and the cutter spacing is s .

The linear cutting speed at a distance R from the TBM cutterhead centre is calculated as:

$$v = \frac{\pi R}{30} \cdot RPM \quad (6.10)$$

The time of a point under microwave irradiation per revolution is:

$$t = \frac{H}{v} = \frac{30H}{\pi R \cdot RPM} \quad (6.11)$$

Given the cutterhead is rotating at the speed of RPM , the point on the rock mass is under cyclic microwave heating. The total radiation time per minute is:

$$t_m = t \cdot RPM = \frac{30H}{\pi R} \quad (6.12)$$

From Equation 6.12, it is known that the exposure time decreases from the centre to the periphery of the cutterhead. Assume the cutterhead diameter is 6 m, the dimension of the horn applicator is 86 mm by 70 mm, then microwave irradiation time per minute at the periphery is:

$$t_m = \frac{30 \cdot 0.07}{\pi \cdot 3} = 0.22s \quad (6.13)$$

This is such a short period that the temperature and thermal stress can hardly increase to a high enough value to cause any thermal damage in the rock mass. Measures must be taken to prolong the exposure time. One of the possible methods is to microwave rocks for a certain period of time before mechanical cutting. For instance, by microwaving the rock mass for 10 mins, the exposure time at the periphery of the cutterhead could be increased to 2.2 s, which may be long enough to induce thermal damages at high power levels. Another method is to increase the number of applicators on the periphery to increase the total exposure time. It should be mentioned that those methods might be used at the same time to achieve the best rock weakening effect at the minimum energy.

For the granite, the dielectric constant and loss factor are 4.5-5.5 and 0.1-0.4 respectively (see Chapter 3). Then the depth of penetration where the power drops to $1/e$ of that in the surface is calculated as:

$$D_p = \frac{c\sqrt{\epsilon'}}{2\pi f \epsilon''} = \frac{3 \times 10^8 \times \sqrt{5}}{2\pi \times 2.45 \times 10^9 \times 0.25} = 0.17m \quad (6.14)$$

For the gabbro, the penetration depth is about 8 cm. This means that a reasonable thickness of rocks behind the excavation face is heated. In the boring process, the rock behind the excavation face is continuously heated by microwave. The power level for an individual irradiator can be calculated using the specific energy method.

6.5.2 Power requirement of microwave applicators

(1) Determination of E_0

In this methodology, it is assumed that the rock mass will be effectively weakened after absorbing a certain amount of energy E_0 (Joule/cm²). E_0 is determined from the laboratory tests and it varies from rock to rock and from equipment to equipment (depending on the power level, applicator design and working distance). Knowing E_0 the power level required is calculated as:

$$P = \frac{HWE_0}{10t_m} = \frac{\pi RWE_0}{300} \quad (6.15)$$

As can be found in [Table 2.5](#), in the field tests of [Gushchin et al. \(1973\)](#) and [Gushchin et al. \(1979\)](#), the corresponding specific energy is 1.2-1.8 kJ/cm² and 1.08-1.35 kJ/cm², respectively. The total installed powers for heat generation are 450 kW and 380 kW and the applicator numbers are 16 and 32, giving an average power of the infrared radiators of 28 kW and 12 kW, respectively.

In the preliminary study stage of this thesis, the Harcourt Granite is treated by a 30 kW industrial microwave system at different power levels. The results show that the specimens failed at 5 kW after 5 seconds exposure (see [Figure 2.16](#)) and at 2.5 kW after 10 seconds ([Figure 6.11](#)). E_0 is calculated as $25/8.6/4.3=0.68$ kJ/cm². It is worth mentioning that in those tests, the overall temperature measured after microwave heating is pretty low (39 °C and 69 °C, respectively). Microwave is selectively heating the dark coloured minerals of biotite.

E_0 calculated in the experiments tests is half of the values in the field. The reason might be attributed to the fact that in the laboratory tests the electric field strength is intensified and the microwave heating is continuous. By contrast, in the field there is a large exposure area and the microwave heating is cyclic. Therefore, it is reasonable to assume that the specific energy E_0 required is about 1-2 kJ/cm².

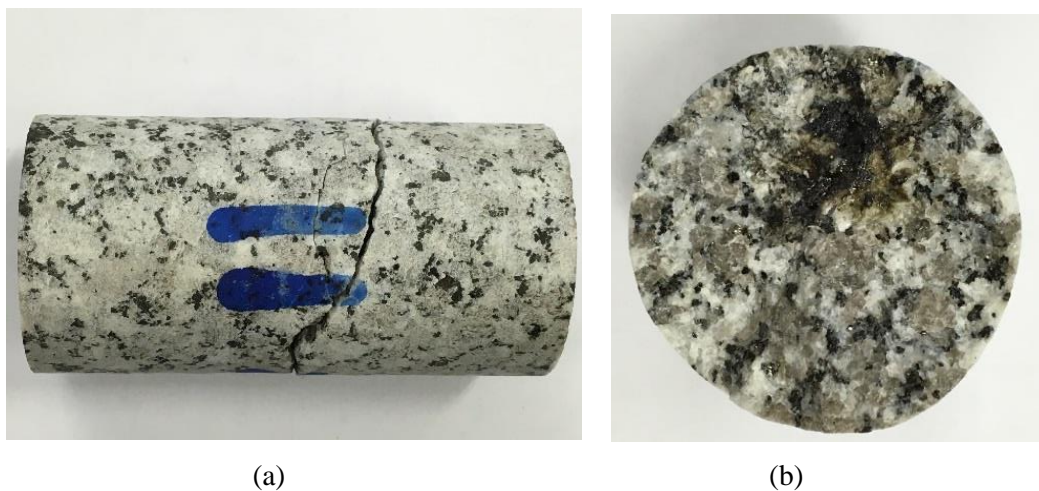


Fig. 6.11 Cracking of a 38 mm diameter 80 mm long Harcourt granite after 10 seconds of microwave heating at 2.5 kW. (a) Thermal shattering, (b) cross-section of the crack surface.

To compare the estimated power levels in this thesis with the field data of [Gushchin et al. \(1973\)](#) and [Gushchin et al. \(1979\)](#), assuming that the cutterhead diameter is 3.5 m and the pre-heating time is 10 mins, then the power level at the periphery is:

$$P = \frac{\pi \times 1.75 \times 0.086 E_0}{300} = 0.0016 E_0 \quad (6.16)$$

Substituting E_0 in the above equation by 1-2 kJ/cm² yields a power level of 16-32 kW, which is comparable to the power levels used in [Gushchin et al. \(1973\)](#) and [Gushchin et al. \(1979\)](#). It should be noted that the power level here is computed using the dimensions of the applicator aperture. In the field there is attenuation when there is a working distance. The power level is then computed using the trial and error method with the help of numerical simulation. Assume the power level is 30 kW and a working distance of 5 cm and 10 cm, the energy density is then computed below.

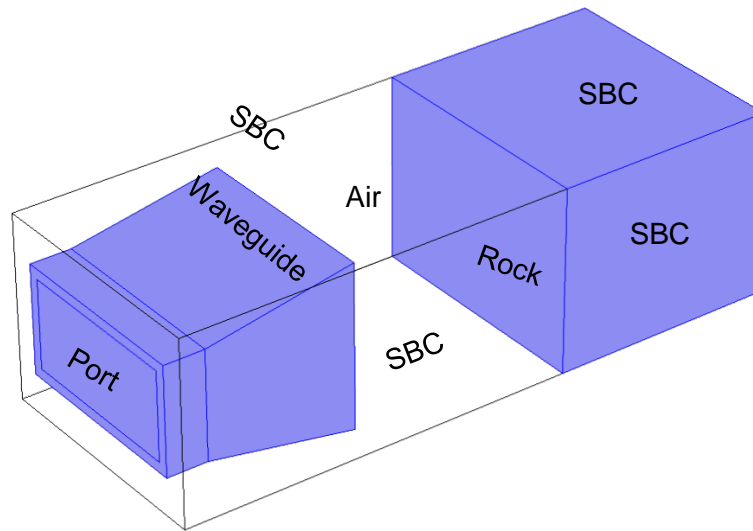


Fig. 6.12 Numerical setup with boundary conditions. SBC means scattering boundary conditions.

Figure 6.12 shows the numerical setup with boundary conditions. The computing geometry is the same as in **Figures 6.5(b)** and **6.6(b)**, which is 300 mm long by 120 mm wide by 90 mm high. Except for the applicator port, all other outer boundaries are set as scattering boundary conditions to allow 100 % microwave energy transmission. For the rock surfaces, except for the microwave facing conditions, all other surfaces are set as outflow boundary conditions. The dielectric properties of the granite in the modelling are 5 for the dielectric constant and 0.25 for the loss factor. **Figure 6.13** shows the power density on the rock mass surface and into the rock mass at a distance of 5 cm and a power level of 30 kW. The average power density on the rock mass surface is about 0.3 kW/cm². Multiplying this power density by 4 seconds (10 mins pre-heating) gives an energy density of 1.2 kJ/cm², which falls into the pre-defined energy density range of 1-2 kJ/cm².

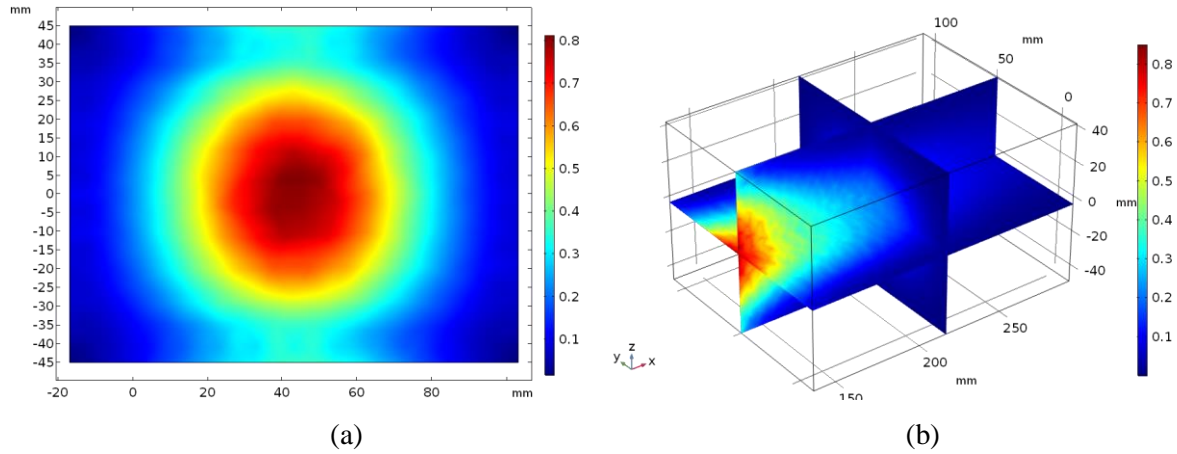


Fig. 6.13 Power density (kJ/cm^2) in the rock mass at a distance of 5 cm and a power level of 30 kW. (a) On the excavation face, (b) multi-slice in the rock mass.

However, when the working distance is 10 cm (**Figure 6.14**), the average power density drops sharply to $0.09 \text{ kW}/\text{cm}^2$, which is 30 % of that with a working distance of 5 cm. To induce enough thermal damage, either power level or exposure time must be increased, which might contribute to an unacceptable cost.

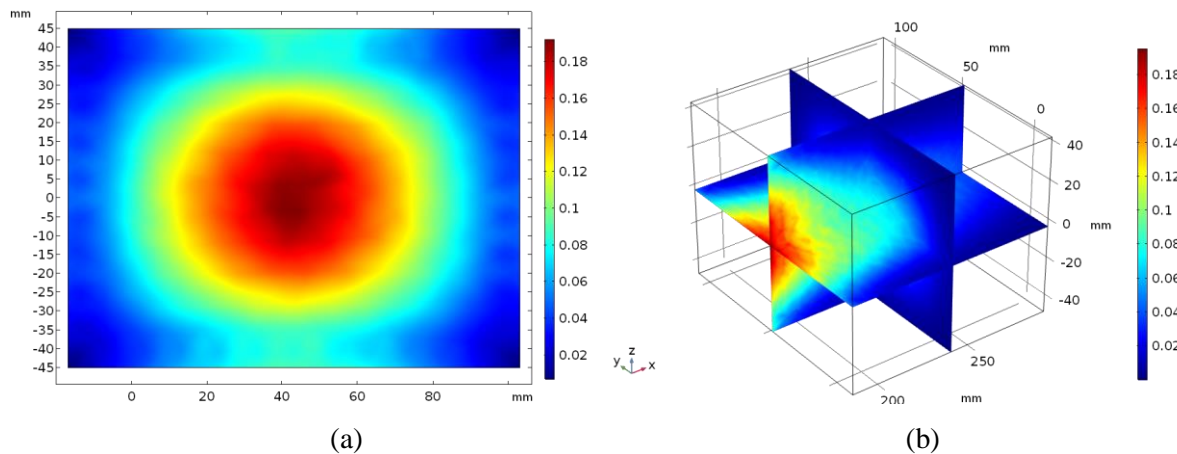


Fig. 6.14 Power density (kJ/cm^2) in the rock mass at a distance of 10 cm and a power level of 30 kW. (a) On the excavation face, (b) multi-slice in the rock mass.

Figure 6.15 shows the maximum temperature on the rock mass surface. It can be found that the working distance has a great impact on the temperature of the rock mass. Also the average temperature at a short exposure time, for instance, 4 seconds, can be very low. This is in agreement of the test observations in the field. [Gushchin et al. \(1979\)](#) measured the temperature of the roller cutters, broken rocks and the conveyor belts of the ETM machine in the field. They found that the maximum temperature of rollers could be up to 280°C ; the temperatures of the broken rocks in the ET mode could be 130°C up to but would fall to $40\text{--}60^\circ\text{C}$ in the ETM mode.

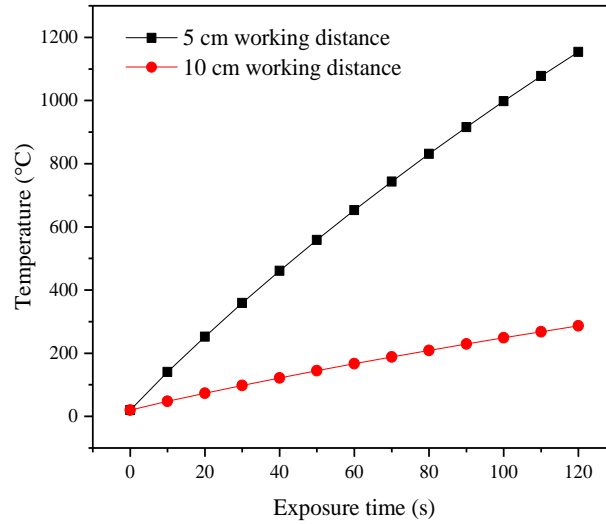


Fig. 6.15 Maximum temperature in the rock mass with a distance of 5 cm and 10 cm and at 30 kW.

Another implication is that it will be prohibitively expensive to heat the rocks to several hundred degree Celsius as the preheating takes too much energy. Microwave will lose its applicability if the rocks are too homogeneous in dielectric properties. However, for the most problematic rock types in TBM tunnelling (granite and quartzite), microwave is presumed to be efficient.

Assuming the cutter spacing is 80 mm, a 3.5 m diameter TBM is equipped with about 20 disc cutters. If every disc cutter is accompanied by a microwave applicator, then the total installed power should be 30 kW times 20 divided by 2, which is about 300 kW. This is comparable with the power levels tried in the field (Gushchin et al., 1979; Gushchin et al., 1973).

6.5.3 Conventional cutterhead

Ates et al. (2014) developed an empirical model from 72 case studies to predict the torque, thrust, number of cutters and RPM of gripper TBMs in hard rocks. Those parameters as a function of TBM diameter are expressed as:

$$\text{Thrust} \quad F = 1777R + 378 \quad (R^2 = 0.40) \quad (6.17)$$

$$\text{Torque} \quad T_q = 1089R - 4189 \quad (R^2 = 0.63) \quad (6.18)$$

$$\text{Number of disc cutter} \quad NC = 5.52R + 7.92 \quad (R^2 = 0.95) \quad (6.19)$$

$$\text{Maximum RPM} \quad RPM = 28.01R^{-0.6641} \quad (R^2 = 0.88) \quad (6.20)$$

Using the CSM model proposed by Rostami and Ozdemir (1993), the power required for the TBM cutterhead is computed as:

$$HP = \frac{\pi}{27} \times T_q \times \frac{RPM}{2} = \frac{\pi}{27} \times (1089R - 4189) \times 28.01R^{-0.6641} \quad (6.21)$$

For a gripper TBM with a diameter of 6 m, the power for the cutterhead is calculated to be 2100 kW. If microwave applicators are installed on the cutterhead, the individual and total power requirements are

calculated to be about 50 kW and 1000 kW. For the cutters on the periphery, several applicators of lower power levels can be installed. An addition of half the installed power seems to be technically and economically possible. Considering the possible reductions in thrust forces and torques of mechanical excavations after microwave treatment, the microwave power consumption is in fact well justified.

6.6 Expected difficulties

There are still some technical difficulties in using microwave to assist TBM hard rock breakage.

(a) Microwave applicator design and system integration

As discussed in Chapter 3, a microwave heating system consists of the following key components: the microwave generator, an isolator, the impedance matching tuner, an applicator and a water load. The previous sections only provide a very rough applicator that is far from optimal. However, the successful application of microwave in TBM tunnelling requires a multidisciplinary teams consisting of materials and process engineers, microwave engineers, equipment designers, and manufacturing specialists, to properly develop microwave processes and procedures (NRC, 1994). Special attention should be paid to the applicator design.

(b) Microwave heating parameters

As discussed in Chapter 5, rocks composing of different minerals respond differently when subjected to microwave irradiation. Some spall violently while others melt silently. It would be very difficult to determine the right microwave parameters for different rock types. It is imperative to do more tests to understand the behaviours of rocks under microwave irradiation.

(c) Heat problem

Microwave will heat the rocks, the TBM cutterheads and the working environment. This may pose hazards to the machine and workers and increase the demand for ventilation. However, Gushchin et al. (1979)'s field data on temperature downplayed the heat hazards. The temperature of the conveyor belts is below 30-50 °C. Temperatures of other components are raised by 10-15 °C. The air temperature of the operator's location remained practically unaltered. This means that the heat problem may not be as severe as anticipated. Nonetheless, the heat flow in the tunnel is to be properly studied to guarantee the safety of workers and the machine.

(d) Occupational health and safety

There is a chance that microwave will come out from the excavation chamber, which will bring occupational health and safety issues. The electronic devices and other components may also fail to work under microwave irradiation. Industrial standards of microwave leakage level must be met.

(e) Protection of the cutters and cutterheads

In the excavation chamber, the concentration of EM energy should be avoided. Otherwise, there may be local heating which could lead to the generation of plasma. The plasma may damage the cutters and the cutterheads. Thus, in the field applications, one of the greatest challenges is to match the impedance. This can be achieved by using automatic tuners. The applicators should also be properly designed based on the dielectric properties of the rocks and the distance from the applicator to the excavation face.

6.7 Conclusions

This chapter presents the technical considerations of applying microwave on hard rock TBMs. It is demonstrated that the cutterhead has enough space for the installation of microwave applicators. Microwave applicators can be installed either on the cutting trajectory of the disc cutters or between two adjacent cutters. For microwave to work efficiently, the applicators should be as close to the rock mass as possible. The electric field strength along the direction of propagation of three applicator types, namely, waveguide applicator, horn applicator and focusing applicator, are examined using numerical simulations. It is found that the horn applicator has the best performance thanks to the lower energy dispersion at the aperture mouth and its ability to direct the microwave energy.

The exposure time of rock mass at different locations when using horn applicators are computed. It is shown that the exposure time on the periphery of a cutterhead can be very short due to the large travelling distance of the applicators. Special measures such as microwaving rock mass for a couple of minutes before mechanical cutting and increasing the number of applicators should be adopted to allow for the temperature and stress build-up.

The temperature distribution in the rock mass subjected to microwave irradiation is numerically computed. The results indicate that microwave may work efficiently in granite and quartzite (the most challenging rock types for TBM tunnelling) which are composed of minerals with drastically different dielectric properties. However, the applicability of microwave on TBMs in more dielectrically homogeneous rocks such as basalt are in question, as there will be lower temperature difference in the grain minerals and less thermal damage at low temperatures. More experimental studies on large blocks using higher power levels should be performed to validate the numerical simulations.

Reference

- Ates, U., Bilgin, N., Copur, H., 2014. Estimating torque, thrust and other design parameters of different type TBMs with some criticism to TBMs used in Turkish tunneling projects. *Tunnelling and Underground Space Technology* 40, 46-63.
- Ayappa, K.G., Davis, H.T., Crapiste, G., Davis, E.A., Gordon, J., 1991. Microwave heating: an evaluation of power formulations. *Chemical Engineering Science* 46, 1005-1016.
- Brodie, G., Jacob, M.V., Farrell, P., 2015. *Microwave applicators, Microwave and Radio-Frequency Technologies in Agriculture An Introduction for Agriculturalists and Engineers*. De Gruyter Open, Berlin, Boston, pp. 194-217.
- Connor, F.R., 1972. *Antennas*. Edward Arnold, London.

- Gardioli, F.E., 1985. Open-ended waveguides: Principles and applications, in: Hawkes, P.W. (Ed.), *Advances in electronics and electron physics*. Academic Press, pp. 139-187.
- Gushchin, V.V., Kuznetsov, V.V., Chernikov, V.A., Merzon, A.G., Protasov, Y.I., Vartanov, G.A., 1979. Driving horizontal workings by means of an entry drifting machine with electrothermomechanical cutting. *Soviet Mining* 15, 133-137.
- Gushchin, V.V., Rzhetskii, V.V., Kuznetsov, V.V., Protasov, Y.I., Yurchenko, N.N., 1973. Driving of workings by a cutter-loader with electrothermal rock breaking. *Soviet Mining* 9, 618-622.
- Guy, A.W., Lehmann, J.F., Stonebridge, J.B., 1974. Therapeutic applications of electromagnetic power. *Proceedings of the IEEE* 62, 55-75.
- Guy, A.W., Lehmann, J.F., Stonebridge, J.B., Sorensen, C.C., 1978. Development of a 915-MHz direct-contact applicator for therapeutic heating of tissues. *IEEE Transactions on Microwave Theory and Techniques* 26, 550-556.
- Habash, R.W.Y., 1994. Non-invasive microwave hyperthermia, Faculty of Engineering. Indian Institute of Science.
- Hassani, F., Nekoovaght, P.M., Gharib, N., 2016. The influence of microwave irradiation on rocks for microwave-assisted underground excavation. *Journal of Rock Mechanics and Geotechnical Engineering* 8, 1-15.
- Lewin, L., 1951. *Advanced theory of waveguides*. Iliffe.
- Maidl, B., Schmid, L., Ritz, W., Herrenknecht, M., 2008. *Hardrock tunnel boring machines*. Wiley.
- Mehdizadeh, M., 2015. Chapter 6 - Applicators and probes based on the open end of microwave transmission lines, *Microwave/RF Applicators and Probes (Second Edition)*. William Andrew Publishing, Boston, pp. 184-218.
- Milligan, T.A., 2005. Properties of antennas, *Modern antenna design*. John Wiley & Sons, Inc., pp. 1-41.
- Nekoovaght, P.M., 2015. Physical and mechanical properties of rocks exposed to microwave irradiation: Potential application to tunnel boring, Department of Mining and Materials. McGill University.
- NRC, 1994. *Microwave processing of materials*. The National Academies Press, Washington, DC.
- Rostami, J., 2008. Hard rock TBM cutterhead modeling for design and performance prediction. *Geomechanik und Tunnelbau* 1, 18-28.
- Rostami, J., Ozdemir, L., 1993. A new model for performance prediction of hard rock TBM, in: Bowerman, L.D. (Ed.), *Rapid Excavation and Tunnelling Conference 1993*, Boston, MA, pp. 793-809.
- Teodoridis, V., Sphicopoulos, T., Gardiol, F.E., 1985. The reflection from an open-ended rectangular waveguide terminated by a layered dielectric medium. *IEEE Transactions on Microwave Theory and Techniques* 33, 359-366.
- Yee, K., 1966. Numerical solution of initial boundary value problems involving maxwell's equations in isotropic media. *IEEE Transactions on Antennas and Propagation* 14, 302-307.

CHAPTER 7

Conclusion and Future Work

7.1 Conclusions

Hard and abrasive rocks have posed great challenges to TBMs by reducing penetration rates and increasing cutter wear. In the development of TBMs, assisting methods such as waterjet, laser, infrared and microwave have been investigated to assist rock breakage. Through an extensive literature review, microwave is recognised as a promising technique due to its feature in selective heating. The objectives of this PhD research are to quantify the dielectric properties of basic rock forming minerals and rocks (which translate as the ability in absorbing microwave energy), to assess the influence of microwave treatment on the physical and mechanical properties of hard and abrasive rocks and to study the feasibility of using microwave on hard rock TBMs. The conclusions are as follows:

(1) Heating rates and loss factors of basic rock forming minerals

The heating rates of 8 rock forming minerals at four different microwave power levels (0.5 kW to 2 kW) for up to 4 mins are measured, from which the dielectric loss factors are derived using a newly proposed method that combines the effective medium theory, the electromagnetic field simulation and the heating rates. The following conclusions from this work are drawn:

- The order of the heating rates from low to high, regardless of the mass of the minerals, is olivine, quartz, muscovite, diopside, plagioclase, orthoclase, biotite and hornblende.
- The minerals can be classified into three categories: good microwave absorbers including hornblende and biotite, intermediate microwave absorber including orthoclase and poor microwave absorbers including quartz, diopside, olivine, muscovite and plagioclase. Due to the significant difference in heating rates, it is believed that for rocks in nature minerals will be selectively heated which can be favourable from the viewpoint of energy saving.
- The order of the dielectric loss factors from low to high is quartz, olivine, muscovite, diopside, plagioclase, orthoclase, biotite and hornblende.
- The effect of grain size on the heating rates and dielectric properties of minerals indicate that as grain size decreases, heating rates and dielectric properties increase.
- No significant dependence of loss factors on the chemical elements of the minerals has been found.

(2) Effect of microwave treatment on the physical and mechanical properties of rocks

A 2 kW industrial microwave system is used to treat three rock types (gabbro, monzonite and granite). The following conclusions can be drawn.

- The microwave system is effective in weakening the three rocks by inducing very high heating rates (several degree per second) and thermal gradients (tens of degree per centimetre). Rocks respond differently when subjected to microwave irradiation. The gabbro and monzonite specimens are thermally cracked first then melted. By contrast, the granite specimens failed in a violent manner, especially at high power levels. The tests results indicate that microwave heating at higher power levels is preferred than heating at lower powers.
- Specimen surface temperatures and heating rates increase linearly with power level. The spatial temperature distributions are in the reversed V-shape. As either power level or exposure time increases, the thermal gradient and mismatch increases.
- The ultrasonic wave velocities, elastic moduli and loading capacities of the three rock all decreased to a great extent after microwave treatment at 2 kW for 120 seconds.
- Both intergranular and transgranular cracks are observed. Intergranular cracks dominated in the monzonite while trans-granular cracks dominated in gabbro and granite specimens. The crack density increases exponentially at higher power levels.

(3) Use of microwave on TBMs

Technical considerations of using microwave on TBMs are explored, from aspects of selection of the open-ended microwave applicators, the configurations of the applicators on the cutterhead with respect to the disc cutters, the power requirements and the expected difficulties. The conclusions are:

- Installation of microwave applicators on the cutterhead is feasible. Microwave applicators can be installed either on the cutting trajectory of the disc cutters or between two adjacent cutters. The main challenge comes from a rotating cutterhead which results in a very short exposure time of rocks on the periphery. Special measures such as microwaving rock mass for a couple of minutes before mechanical cutting and increasing the number of applicators should be adopted to allow for the temperature and stress build-up.
- Among the waveguide applicator, horn applicator and focusing applicator, the horn applicator is proved to have the best energy directivity and is the most suitable to be installed on TBM cutterheads. Microwave density disperses quickly from the applicator aperture, thus the applicators should be as close to the rock mass as possible. The possibility of using lens antennas which can focus the microwave energy to a spot or a small area should also be explored.
- Microwave may only work efficiently in granite and quartzite (the most challenging rock types for TBM tunnelling) which are composed of minerals with drastically different dielectric properties. However, the applicability of microwave on TBMs in more dielectrically

homogeneous rocks such as basalt are in question, as there will be lower temperature difference in the grain minerals and less thermal damage at low temperatures.

7.2 Limitation and future work

As has been discussed in the previous chapters, there are some limitations in the study that need to be investigated in a more detailed manner in the future research.

(1) Understanding the effect of confinement on the thermal cracking of rocks subjected to microwave irradiation

In the experiments, the rock specimens expand after microwave heating. For the ease of removing them from the cavity, they are cut slightly smaller than the interior dimension of the cavity. This means that no confinement is applied on the specimens while microwave heating. This could have facilitated the initiation of cracks from the top/bottom middle of the specimens and the generation of the radial crack pattern at the centre of the specimens. In the field where the rock mass is confined, the thermal cracking will be suppressed. In the future research, the confinement can be taken into account by developing a special loading device which is made of microwave transparent/isolated materials such as alumina and copper plate. Alternatively, setups as shown in **Figure 6.3(a)** which involves radiating larger rock blocks can be adopted.

(2) Thermal cracking in the heating and cooling process

In this thesis, the crack pattern and density, the ultrasonic wave velocities and the mechanical strength are measured after the specimens cooled off. Some previous research has showed that in the conventional heating and cooling of rocks more cracks can be generated in the cooling stage. Even though microwave heating yields much larger thermal gradients and thermal shocks and could possibly generate more cracks in the heating stage, it is still necessary to investigate the percentage of cracks generated in each stage. This can be done by continuously measuring the acoustic emission in the whole heating and cooling process.

(3) Test on quartz-rich igneous and metamorphic rocks

As summarised in Chapter 1, the most problematic rock types encountered in TBM tunnelling are high quartz content granite and quartzite. The experimental tests in Chapter 5 show that granite fails violently at relatively before reaching high temperatures. This characteristic makes those rocks very ideal for microwave treatment when compared to more homogeneous gabbro and basalt. In the future, quartz rich rocks such as quartzite should be collected from the field.

(4) Understanding the thermal damage process by conducting numerical simulations

During the development of the thesis, attempts are made to develop an EM waves-thermal-mechanical model that considers the microstructure of the rock specimens to simulate the thermal cracking process.

Even though the former two physics are relatively reliable in the finite element model, difficulties are encountered in simulating the cracks. This made it impossible to estimate the depth of thermal damage into the rock mass. In the future, efforts should be made to develop a FEM-DEM coupling model to elucidate the thermal cracking process. The Multiphysics simulation of microwave heating rocks indicates that as the exposure time increases, the thermal mismatch (thermal gradient and heating rate) also increases. At the grain boundaries, there are stress concentrations. As the power level increases the thermal mismatch consuming the same energy also increases, implying that the higher power level is preferred for more effective rock breaking and fracturing. The numerical simulations also show that for low loss rocks, although the overall temperature and heat generation are lower, the local temperature in the relatively good microwave absorbing mineral can be higher. This implies that microwave may be more effective in weakening quartz rich granite, or even quartzite, which is of particular importance to solve the challenges faced by TBMs in the field.

(5) Validation of predication on large blocks

In the experimental tests, relatively thin rock specimens are used. Due to the unavoidable reflection of microwave on the back surface, the heating and weakening effects are larger than when an infinite thick specimen is used. In the future, the thickness of specimens should be increased to minimise this impact.

(6) Conducting linear cutting tests on microwave treated specimens

When using microwave on TBMs, reductions of TBM thrust and rolling forces are expected. Small-scale or full-scale linear cutting test should be performed on microwave treated rock blocks. The optimal applicator-cutter configurations for different rock types should also be examined. Moreover, the effect of microwave treatment on the abrasiveness of rocks should be studied by performing the CHERCHAR abrasiveness tests.

(7) Optimisation of the microwave applicators

In this thesis, the horn applicator used for analysis is not optimally designed. Given the special application, no existing applicators can be used in the field. Applicators should be designed with considerations of the dielectric properties of rocks, the working distance of the applicator, and the exposure time. Special attention should be paid to the design of focusing microwave applicators.

CURRICULUM VITAE

PERSONAL INFORMATION

Name: Yanlong Zheng

Email: [REDACTED]

Nationality: People's Republic of China

Date of Birth: 5 June 1988

Gender: Male



EDUCATION

- Monash University, Department of Civil Engineering**
 Melbourne, Australia
 PhD Candidate in Rock Mechanics Dec. 2013-present
 Research topic: *Microwave assisted hard rock breakage and fracturing*
 Advisors: Prof. Jian Zhao and Dr. Qianbing Zhang
- Tongji University, Department of Geotechnical Engineering** Shanghai, China
 Master of Engineering in Tunnelling and Underground Engineering 2010- 2013
 Dissertation: *Experimental Investigation and Solid-Gas Flow Simulation of Pneumatic Excavation and Conveying of Lunar Regolith Simulant in Hard Vacuum*
 Supervisor: Prof. Dr. **Yun Bai**
 GPA: 85.21/100 3.51/4 Ranking: 8/64
- Central South University, College of Resource and Safety Eng.** Changsha, China
 Bachelor of Engineering in Mining and Geotechnical Engineering 2006- 2010
 GPA: 87.62/100 3.61/4 Ranking: 1/106
 Major GPA: 89.46/100 3.73/4

WORKING AND INTERSHIP EXPERIENCE

- Monash University** December 2013- Present
 Research assistants, teaching assistants for Surface Mining, Rock Mechanics and Mining Asset Management
- Shanghai Yusui Eng. Management and Consulting Co., Ltd.** July 2010-July 2012
 Risk management of Shanghai Metro Line 12
- Sanshandao Gold Mine of Shandong Gold Group Co., Ltd.** March 2010-April 2010
 Optimized the mining method, designed the extension of the drainage system
- Kangjiawan Zn & Pb Mine of Hunan Nonferrous Metals Corp., Ltd.** July 2009
 Trained in the mine including the mining processes and safety procedures

SCHOLARSHIPS & HONORS

- Postgraduate Publication Award, Monash University December 2017
- Best Publication Award, Monash University November 2017
- Best Publication Award, Monash University November 2016
- Award of Excellent Graduate, Hunan Province June 2010
- Award of Outstanding Undergraduates, Central South University 2007 and 2009
- National Scholarship and Outstanding Scholarship (**Top 1 student**) 2008 and 2009
- Award of Excellent Student Leader 2008

RESEARCH EXPERIENCE

- **Microwave assisted hard rock breakage and fracturing**
November 2013- Present
The project investigates into the microwave-mineral interaction mechanisms and provides an evaluation of the applicability of industrial microwave as a tool in breaking or fracturing hard rocks for possible applications in civil, mining, oil/gas and geothermal industries.
- **Pre-feasibility Study of the China-Nepal-India Railway across the Himalayas**
November 2011- November 2013
The project aimed to select possible alternative alignments, to make social, technical and economic analysis, to identify the challenges as well as to put forward mitigation measures
- **Experimental Study of Pneumatic Excavation and Transferring of Regolith Simulant in Hard Vacuum under Earth's Gravity**
August 2011- August 2013
The objectives are to demonstrate the feasibility of pneumatic excavation on the moon and to determine main parameters affecting the excavation and conveying efficiency.

RESEARCH INTERESTS

- **Microwave assisted rock breakage in tunneling, shale/gas and geothermal energy extraction**
- **Conventional and mechanized tunnelling**
- **Rock mechanics and rock engineering**
- **Mining engineering**